Ab-initio-Berechnung von Transporteigenschaften von warmer dichter Materie

Kumulative Habilitationsschrift
an der Mathematisch-Naturwissenschaftlichen Fakultät
der Universität Rostock

vorgelegt von

Dr. rer. nat. Martin French

Rostock
Juni 2021

https://doi.org/10.18453/rosdok_id00003719

Gutachter:
Prof. Dr. Ronald Redmer, Universität Rostock, Institut für Physik
Prof. Dr. Michael Bonitz, Christian-Albrechts-Universität zu Kiel, Sektion Physik
Dr. Andreas Hermann, The University of Edinburgh, School of Physics and Astronomy

Jahr der Einreichung: 2021
Jahr der Probevorlesung: 2022
Jahr des Kolloquiums: 2022

Inhaltsverzeichnis

Kapitel 1

Einleitung

Die uns geläufigsten Formen, in denen Materie auftritt, sind gasförmige, flüssige und feste Zustände, die in der Thermodynamik auch als Phasen bezeichnet werden. Ihre physikalischen Eigenschaften werden von Art und Zusammensetzung der Stoffbausteine (Kerne und Elektronen) sowie deren elektromagnetischen Wechselwirkungen miteinander bestimmt [1]. Änderungen von thermodynamischen Zustandsgrößen wie Druck P oder Temperatur T können Phasenumwandlungen hervorrufen, z.B. Festkörper schmelzen oder sublimieren, Flüssigkeiten erstarren oder verdampfen, Gase kondensieren lassen. Insbesondere durch eine sehr starke Erhöhung der Temperatur kann Materie in den Plasmazustand übergehen [2, 3], in welchem die Bindungen zwischen Kernen und Elektronen zumindest teilweise aufgelöst sind und sich die freigesetzten Ladungsträger frei bewegen können.

Als warme dichte Materie (WDM) bezeichnet man in diesem Zusammenhang Zustände aus partiell ionisierten Atomen bzw. partiell dissoziierten Molekülen, die meist als dichtes Plasma vorliegen [4, 5, 6] aber auch festkörperartige [7] oder superionische Strukturen [8] bilden können. Typischerweise existiert WDM bei hohen Temperaturen (oftmals 10^3 K $\lesssim T \lesssim 10^6$ K) und Dichten von ca. 10^{-2} g/cm^3 $\lesssim \varrho \lesssim 10^3$ g/cm^3 [9].

1.1 Warme dichte Materie

Etwas genauer als über den oben angegebenen Dichte-Temperatur-Bereich lassen sich WDM-Zustände mit den grundlegenden Parametern aus der Plasmaphysik charakterisieren [10]. Der Kopplungsparameter Γ_a setzt die mittlere Coulomb-Wechselwirkungsenergie zwischen den Teilchen der Sorte a ins Verhältnis zu ihrer thermischen Energie k_BT über:

$$\Gamma_a = \frac{q_a^2}{4\pi\varepsilon_0 d_a k_B T} \quad , \quad \text{mit} \quad d_a = \left(\frac{3}{4\pi n_a}\right)^{1/3} \quad . \tag{1.1}$$

Hierbei sind k_B die Boltzmann-Konstante, q_a die Ladung und d_a der mittlere Teilchenabstand, der sich aus der Teilchendichte n_a ergibt. Für WDM gilt $\Gamma_a \gtrsim 1$, d.h. die Coulomb-Wechselwirkung hat maßgeblichen Einfluss, wodurch sich WDM vom Bereich der schwach gekoppelten Plasmen ($\Gamma_a \ll 1$) abgrenzt. Weiterhin definiert man den Entartungsparameter der Elektronen durch:

$$\Theta_e = \frac{k_B T}{E_F} \quad , \quad \text{mit} \quad E_F = \frac{\hbar^2}{2m_e}\left(3\pi^2 n_e\right)^{2/3} \quad , \tag{1.2}$$

mit der Planckschen Konstante $\hbar$ und der Elektronenmasse m_e. Dieser setzt die thermische Energie ins Verhältnis zur Fermi-Energie E_F und zeigt so die Bedeutung von Quanteneffekten bei der Bewegung der Elektronen an. In WDM ist $\Theta_e \approx 1$, d.h. das Elektronensystem ist teilweise entartet und kann weder als näherungsweise klassisch ($\Theta_e \gg 1$) noch als stark entartet ($\Theta_e \ll 1$) beschrieben werden. Aufgrund der deutlich größeren Masse der Ionen ($m_i \gg m_e$) spielen Quanteneffekte der Ionenbewegung in WDM eine weniger wichtige Rolle.[1]

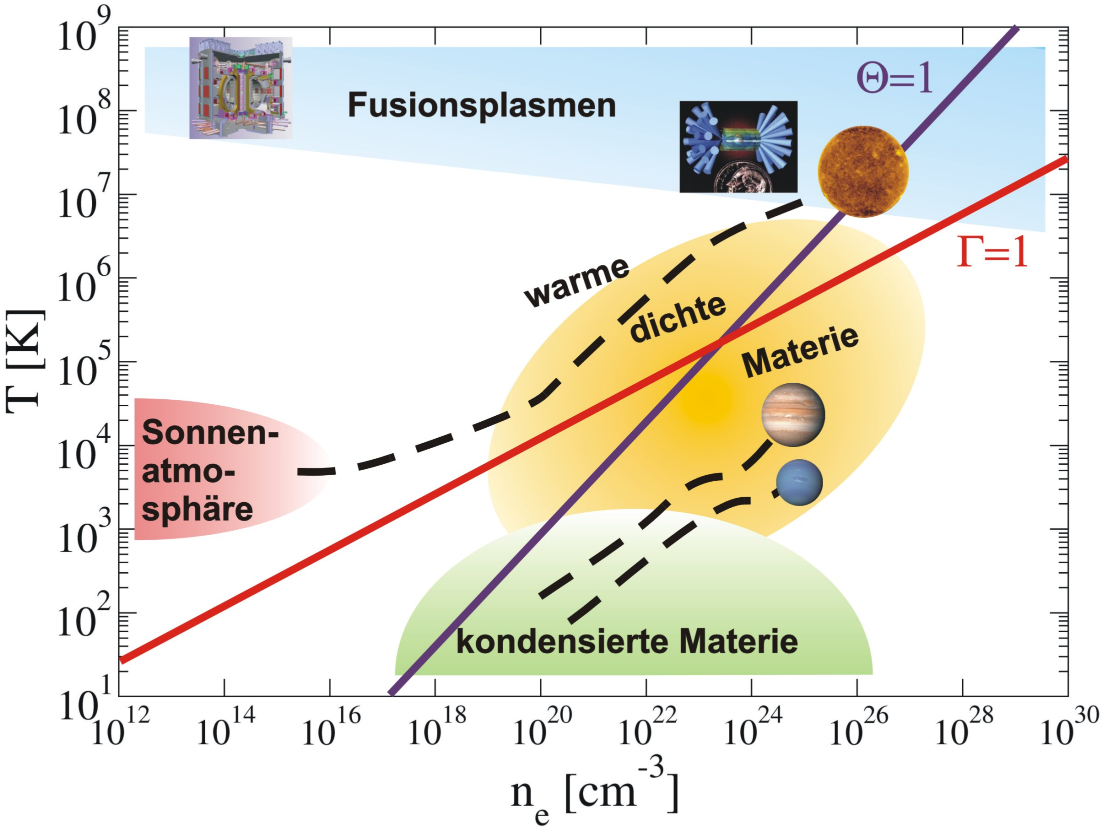

Abbildung 1.1: Elektronendichte-Temperatur-Ebene einschließlich der thermodynamischen Bedingungen in Sonne [13], Jupiter [14] und Neptun [15]. Fotoquelle: NASA, ITER, NIF. Kondensierte Materie steht hier stellvertretend für fluide (z.B. Gase und Flüssigkeiten) und feste Zustände.

Zur Veranschaulichung der Zustandsregion von WDM ist in Bild 1.1 eine Dichte-Temperatur-Ebene dargestellt. WDM kommt in der Natur typischerweise im Inneren von Planeten

---

[1] Insbesondere bei wasserstoffhaltiger Materie können sie dennoch wichtig werden [11]. Zum Beispiel beträgt die charakteristische Schwingungstemperatur eines Wasserstoffmoleküls immerhin 6332 K [12].

vor [16, 17]. Hierbei sind die Elemente Wasserstoff und Helium die häufigsten und gleichzeitig diejenigen, aus denen Gasriesen wie Jupiter und Saturn hauptsächlich bestehen [18]. Hauptbestandteile der sogenannten Eisriesen [19, 20] Uranus und Neptun sind vermutlich Wasser, Methan und Ammoniak [21, 22]. In Gesteinsplaneten wie der Erde finden sich vorwiegend Verbindungen aus Magnesium, Silizium, Sauerstoff sowie Eisen [23, 24, 25]. Spätestens die Entdeckung weiterer Typen wie Minineptune und Supererden aus der Gruppe der Exoplaneten zeigt, dass eine scharfe Klassifizierung von Planeten lediglich eine vereinfachte Vorstellung sein kann [26, 27, 28]. Planetare Materie besteht grundsätzlich aus Mischungen komplexer Stöchiometrie. Insbesondere Phasenübergänge und Entmischungsphänomene in WDM haben dabei einen großen Einfluss auf die innere Struktur der Planeten und können dort zu Schichtenbildung führen [29, 30]. Zum Beispiel enthält die Erde im Inneren einen eisenreichen Kern unterhalb eines Gesteinsmantels [31]. Der Kern ist wiederum in feste und flüssige Bereiche unterteilt, deren stöchiometrische Zusammensetzungen nur näherungsweise bekannt sind. Das Verständnis der physikalischen Eigenschaften von WDM ist daher von herausragender Bedeutung für die Planetenphysik. Nicht zuletzt legt das Innere von (Exo)planeten wichtige Rahmenbedingungen für deren mögliche Habitabilität fest [26].

Weiterhin können WDM-Zustände auch in technischen Anwendungen wie möglicher Energiegewinnung durch Trägheitsfusion [32] oder in Kernwaffenexplosionen auftreten. Die sehr heißen Fusionsplasmazustände selbst [33, 34, 35] zählt man jedoch nicht mehr zu WDM [9], siehe Abbildung 1.1. Generell sind WDM-Zustände im Labor nur schwierig herzustellen bzw. kontrolliert so zu stabilisieren, dass man deren Eigenschaften messen kann. Eine häufig verwendete Methode ist die Kompression von Stoffen in Diamantstempelzellen [36], womit man Drücke bis in den TPa-Bereich erzeugen kann [37, 38]. In Kombination mit Laserheizung lassen sich gleichzeitig Temperaturen von mehreren tausend Kelvin erzeugen [39, 40]. Das Erreichen von noch höheren Drücken und Temperaturen geschieht hingegen mittels dynamischer Kompressionstechniken [41]. Besonders verbreitet sind hierbei Stoßwellenexperimente [42], welche thermodynamische Zustände auf der Hugoniot-Kurve generieren. Daneben verwendet man sowohl komplexere Multistoßwellentechniken als auch komplett stoßfreie Verfahren, die eine nahezu isentrope Kompression ermöglichen, z.B. durch Beschuss mit speziell geformten, intensiven Laserpulsen [41].

1.2 Transporteigenschaften

Bedingt durch die starken Coulomb-Wechselwirkungen zwischen den Teilchen, aus denen das System WDM besteht, liegt es in vielen Fällen als thermodynamischer Gleichgewichtszustand vor. Demzufolge wird der Untersuchung der thermodynamischen Eigenschaften (Zustandsgleichungen, Phasendiagramme, etc.) von WDM große Aufmerksamkeit geschenkt. Wird das System jedoch durch eine kleine, äußere Störung (Onsagersche Kraft) aus dem Gleichgewicht gebracht, so bestimmen seine Transporteigenschaften, wie es darauf reagiert [43]. Generell erfolgt dann ein Stromfluss (Onsagerscher Strom), der mit Entropieproduktion einhergeht.

Transportvorgänge lassen sich mithilfe phänomenologischer Gleichungen mathematisch formulieren. Da in WDM frei bewegliche Ladungsträger vorhanden sind, ist die wichtigste Transporteigenschaft ihre elektrische Leitfähigkeit σ. Sie bestimmt, welche elektrische Stromdichte $\mathbf{j}_{el}$ bei Anlegen eines elektrischen Potentials $\mathbf{\Phi}$ (äußere Störung) fließt, und zwar über das Ohmsche Gesetz:

$$\mathbf{j}_{el} = -\sigma \nabla \mathbf{\Phi} \quad . \tag{1.3}$$

Analog definiert man die Wärmeleitfähigkeit λ, die die Wärmestromdichte $\mathbf{j}_Q$ bei Vorhandensein eines Temperaturgradienten festlegt. Mathematisch beschrieben wird dies durch das Fourier-Gesetz:

$$\mathbf{j}_Q = -\lambda \nabla T \quad . \tag{1.4}$$

Eine dritte wichtige Transportgröße ist die Scherviskosität η, die die mechanische Schubspannung τ_{xy} bei Vorhandensein von Schergeschwindigkeiten $\partial v_x / \partial y$ in Fluiden (üblicherweise Plasmen im Fall von WDM) festlegt [44]. Sie ist im Gegensatz zu den Leitfähigkeiten eine Art inverser Transportkoeffizient, d.h., sie beschreibt einen mechanischen Reibungs*widerstand*. Die entsprechende Transportgleichung ist das Newtonsche Gesetz:

$$\tau_{xy} = \eta \frac{\partial v_x}{\partial y} \quad . \tag{1.5}$$

Weitere Transportkoeffizienten erhält man als Kreuzeffekte (z.B. die thermoelektrische Kraft), denn jede Onsagersche Kraft kann prinzipiell jede Art von Strom als Antwort hervorrufen [43]. Speziell in Mehrkomponentensystemen sind auch die Interdiffusionskoeffizienten D_{ab} von Bedeutung [45]. Allgemein haben Transportgrößen einen Tensorcharakter, vereinfachen sich aber bei Abwesenheit von Magnetfeldern in kubischen und isotropen Systemen zu Skalaren. Eine sehr ausführliche Ausarbeitung der phänomenologischen Transporttheorie, basierend auf der Entropieproduktion im Nichtgleichgewicht, findet sich z.B. in dem Werk von de Groot und Mazur [43].

Die genaue Kenntnis der Transportgrößen von WDM ist von großer Bedeutung, sowohl als Mittel zur Plasmadiagnostik als auch in der Planetenphysik. So bestimmt insbesondere die elektrische Leitfähigkeit der WDM im Inneren von Planeten über die Funktion der Dynamos, die die vorwiegend dipolaren (Erde, Jupiter, Saturn) oder komplexeren (Uranus, Neptun) planetaren Magnetfelder erzeugen [46, 47, 48]. Ebenso erhofft man sich, durch das Verständnis der Konvektionsdynamik in den Gas- und Eisriesen mehr über ihren inneren Aufbau zu lernen sowie ihre Leuchtkraft erklären zu können [29, 49, 50]. Für die Entwicklung derartiger Modelle müssen neben Zustandsgleichung und Phasendiagramm u.a. Wärmeleitfähigkeit und Viskosität bekannt sein.

1.3 Messung der Transporteigenschaften von WDM

Die experimentelle Bestimmung von Transporteigenschaften von WDM ist eine große wissenschaftliche und technische Herausforderung. Nicht nur müssen WDM-Zustände kontrolliert erzeugt und thermodynamisch charakterisiert werden, sondern zusätzlich die äußere Störung ausgeübt sowie ein Stromfluss gemessen werden.

Eine vergleichsweise große Anzahl an Messungen existiert für die elektrische Leitfähigkeit. Eine häufig verwendete Messmethode dafür sind Drahtexplosionsexperimente, bei denen ein Metalldraht durch einen Stromstoß ggf. bis zur Verdampfung erhitzt und seine Ausdehnung und der elektrische Widerstand gemessen wird [51, 52, 53, 54]. Dadurch lässt sich die elektrische Leitfähigkeit von expandierten Metallen in festen, flüssigen und Plasmazuständen relativ genau ermitteln. Die Messung der Leitfähigkeit in komprimierter WDM kann in Diamantstempelzellen [55, 56] oder in dynamischen Kompressionsexperimenten mit Gaskanonen oder Sprengstoffen [57, 58, 59] erfolgen. So wurde z.B. Wasserstoff bis zum Auftreten von metallischer Leitfähigkeit ($\sigma \gtrsim 200$ S/cm [60, 61, 62, 63])[1] komprimiert [64].

Etwa um die Jahrtausendwende wurden die mechanischen Treiber (Gaskanonen) in Stoßwellenexperimenten durch Hochleistungslaser [65, 66] und magnetische Treiber wie der Z-Maschine an den Sandia National Laboratories [67, 68, 69] weitgehend verdrängt. Mit diesen neuen Technologien lassen sich höhere Hugoniot-Drücke bis in den Multimegabarbereich (1 Mbar = 100 GPa) erzeugen. Leider bedeutete dies auch das vorläufige Ende von Leitfähigkeitsmessungen mit dynamischen Kompressionsexperimenten, da die auftretenden elektromagnetischen Störfelder keine sauberen Gleichstrommessungen zulassen. Alternativ kann die Leitfähigkeit indirekt aus der Reflektivität von optischem Laserlicht, z.B. an einer Stoßfront in Hugoniot-Experimenten oder am Probenmaterial in Diamantstempelzellen, bestimmt werden [70, 71, 72, 73, 74]. Für den Gleichstromwert muss jedoch die Abhängigkeit der Leitfähigkeit von der Frequenz ω bekannt sein, was meistens nicht der Fall ist. Eine weitere indirekte Methode ist das Bestimmen der Leitfähigkeit aus einem Röntgen-Thomson-Streuspektrum [75], die wiederum zusätzliche theoretische Modellierung erfordert.

Die Messung der Wärmeleitfähigkeit von WDM ist ungleich schwieriger, da weitere unerwünschte Störfaktoren wie Konvektion und Energieverlust durch Strahlung oder Wärmeabfluss durch das Einschlussgefäß während des Experiments unterbunden werden müssen [76]. Die meisten Messungen wurden daher an gut leitenden Metallen vorgenommen [77, 78]. So wurde z.B. die Wärmeleitfähigkeit von Eisen bis in den Mbar-Bereich und Temperaturen von 3000 K in lasergeheizten Diamantstempelzellen gemessen [79]. Die Wärmeleitfähigkeit von flüssigem Wasser hingegen ist experimentell nur bis 3,5 GPa und 700 K bestimmt worden [80], wohingegen man sie für Wassereis VII bei Raumtemperatur schon bis über 20 GPa hinaus messen konnte [81]. Ein indirekter Weg zur Abschätzung der Wärmeleitfähigkeit aus der elektrischen Leitfähigkeit von nicht zu heißen Metallen ist das Wiedemann-Franz-Gesetz [82]. Hierbei wird für die Lorenz-Zahl:

$$L = \left(\frac{q_e}{k_B}\right)^2 \frac{\lambda}{T\sigma} \quad , \tag{1.6}$$

wobei $q_e = -e$ die Elektronenladung ist, der Drude-Sommerfeld-Wert von $L = \pi^2/3$ angesetzt [83]. Diese Annahme setzt jedoch Zustände mit stark entarteten Metallelektronen voraus, was bei WDM typischerweise nicht gerechtfertigt ist, siehe Abschnitt 1.1.

---

[1] Diese Zahl ist als grober Richtwert zu verstehen. Ob ein System metallisch ist oder nicht, kann prinzipiell nur am Temperaturnullpunkt eindeutig anhand der elektronischen Struktur beantwortet werden.

Es gibt nur wenige Messungen der Viskosität von WDM, fast alle mit Wasser als Probenmaterial. Neben Messverfahren mit rollenden Kügelchen in geheizten Diamantstempelzellen [84] wurden unterschiedliche Techniken für Stoßwellenexperimente probiert [85, 86, 87], z.B. mithilfe geriffelter Stoßfrontprofile oder unter Verwendung zylinderförmiger Störkörper, die von der Stoßwelle mitgerissen werden. Die verschiedenen Methoden lieferten teilweise um Größenordnungen verschiedene Werte [88], die im Fall von Wasser von mPas bis kPas reichen. Die Vergleichsanalyse von Abramson [88] lässt die Werte im mPas-Bereich am plausibelsten erscheinen. Das Messen der Viskosität von WDM ist immer noch ein weitgehend unerforschtes Gebiet, sodass entsprechende theoretische Berechnungen hier besonders wertvolle Beiträge zu deren Verständnis leisten könnten.

1.4 Theoretische Zugänge zur Berechnung von Transportgrößen von WDM

Die theoretische Beschreibung der Transporteigenschaften von WDM geschieht mit Methoden der Vielteilchenphysik. WDM ist dabei grundsätzlich als Mehrkomponentensystem aus Elektronen und Ionen zu betrachten, wobei jede Teilchensorte sowohl zum Stromfluss als auch zur Streuung der sich bewegenden Teilchen beitragen kann.

Historisch gesehen gelang die erste systematische Berechnung von Transportgrößen im Rahmen der kinetischen Theorie. Deren grundlegender Ausgangspunkt ist die Boltzmann-Gleichung [89, 90], die eine Bewegungsgleichung für die Nichtgleichgewichtsverteilungsfunktion bei Anwesenheit externer Feldkräfte darstellt. Mit dem von Boltzmann postulierten Stoßterm wird dabei der Beitrag von unkorrelierten Zweiteilchenstößen erfasst. Exakte Lösungen der Boltzmann-Gleichung erhält man z.B. für Elektronentransport in Relaxationszeitnäherung, d.h., die Elektronen streuen ausschließlich an unbeweglichen Ionen oder Atomen (adiabatische Näherung) [91]. Dies funktioniert für beliebig entartete Elektronen und führt z.B. zur Ziman-Formel für die elektrische Leitfähigkeit in Metallen [92]. Mit der Chapman-Enskog-Methode [93] lässt sich die Boltzmann-Gleichung bei bekannten Wechselwirkungspotentialen für praktisch alle Transportkoeffizienten nahezu exakt lösen, auch in Mehrkomponentensystem. Diese Methode setzt allerdings den nicht entarteten Grenzfall voraus, d.h. sie funktioniert nur für verdünnte Gase oder heiße Plasmen.

Zur Beschreibung von entarteten und stärker gekoppelten Plasmen wurden quantenstatistische Methoden entwickelt, die korrelierte Mehrteilchenwechselwirkungen, einschließlich möglicher Bindungszustände (Atome, Moleküle), mittels Störungstheorie (z.B. thermodynamische Greensche Funktionen) oder Integralgleichungstechniken behandeln [4, 5, 6, 94]. Meist wird zusätzlich das sogenannte „chemische Bild“ zu Hilfe genommen, bei dem die Konzentration relevanter Bindungs- und Streuzustände (freie Elektronen, freie Ionen, Atome, Moleküle, etc.) als Quasiteilchen im Vielteilchensystem mit Massenwirkungsgesetzen berechnet wird. Die Verwendung des „chemischen Bildes“ ist formal gerechtfertigt, soweit sämtliche Streu- und Bindungszustände berücksichtigt werden [4, 5, 6, 94]. In der Praxis ist dies jedoch nicht erreichbar, sodass zwangsläufig Näherungen für die Wechselwirkungsanteile der chemischen

Potentiale der Quasiteilchen verwendet werden müssen. Nach Bestimmung der Konzentrationen und effektiven Wechselwirkungspotentiale der chemischen Quasiteilchen erfolgt die Berechnung der Transportgrößen mit der „Linearen Response-Theorie“ (dt. Theorie der linearen Antwort) [95, 96, 97, 98, 99], speziell dem für Störungstheorie ausgelegten Zubarev-Formalismus [100, 101] als Erweiterung der Kubo-Theorie [102, 103]. Für schwach gekoppelte Plasmen lassen sich so bekannte Grenzfälle aus der kinetischen Theorie reproduzieren [104]. Insbesondere kann mit dem Zubarev-Formalismus der Einfluss von Elektron-Elektron-Stößen quantenmechanisch berechnet werden [105, 106, 107]. Dennoch sind auch diese störungstheoretischen Zugänge im WDM-Bereich aufgrund der erforderlichen Näherungen unzuverlässig. Sie können z.B. zum Auftreten von weitläufigen thermodynamischen Instabilitätsbereichen wie Plasmaphasenübergängen führen [94, 108, 109], deren Natur nach wie vor ungeklärt ist.

Mit dem Aufkommen massiv parallelisierter Großrechner ist mittlerweile die direkte quantenmechanische Berechnung der elektronischen Struktur von WDM als Coulomb-System auf der Grundlage der Schrödinger-Gleichung in guter Näherung möglich. Dadurch kann eine konsequente Beschreibung im Rahmen des „physikalischen Bildes“ erfolgen, d.h., es können alle Streu- und Bindungszustände erfasst und auf gleichem Niveau behandelt werden. Etabliert hat sich dazu eine Kombination aus Dichtefunktionaltheorie (DFT) [110, 111, 112, 113] für die Elektronen und Molekulardynamik (MD) für die Ionen [114], zusammen DFT-MD. Ein statistisches Ensemble aus ca. mehreren hundert Ionen beliebiger Sorte und entsprechend vielen Elektronen wird dabei für Pikosekundenzeiträume im Computer simuliert. Numerische Datensätze für thermodynamische und Transporteigenschaften werden danach durch statistische Mittelungen erhalten. Die notwendigen Näherungen in der DFT, hauptsächlich das sogenannte Austausch- und Korrelationsfunktional, sind relativ gut kontrollierbar und werden fortwährend verbessert [115, 116, 117]. Sie werden z.B. an gut verstandene Referenzsysteme wie dem homogenen Elektronengas [118, 119, 120] und weiterer exakt bekannter Eigenschaften des realen Elektronengases angepasst. Da keine elementspezifischen Modellannahmen erforderlich sind, kann die DFT-MD-Methode als *Ab-initio*-Methode angesehen werden. Die Kernergebnisse dieser Arbeit beruhen auf DFT-MD-Rechnungen.

Vereinfachte Varianten der DFT-MD-Methode mit verschiedenen zusätzlichen Näherungen in der elektronischen und/oder ionischen Strukturberechnung existieren ebenso, siehe z.B. [121, 122, 123]. Diese sind zwar weniger genau, haben aber aufgrund ihrer hohen numerischen Effizienz vor allem in der Plasmaphysik eine beachtliche Bedeutung erlangt [124].

1.5 Ziel und Struktur dieser Arbeit

In dieser kumulativen Habilitationsschrift werden aktuelle Fortschritte auf dem Gebiet der Berechnung von Transportgrößen von WDM mit der DFT-MD-Simulationsmethode dargestellt. Dazu werden in Kapitel 2 die DFT-MD-Methode sowie in Kapitel 3 die zur Berechnung von Transportgrößen notwendige Lineare Response-Theorie (LRT) erläutert. Kapitel 4 ist dann den elektronischen Transporteigenschaften gewidmet, während Kapitel 5 sich hauptsächlich mit den Beiträgen der schweren Teilchen (Ionen, Atome, etc.) befasst.

In die Kapitel 4 und 5 ist eine Auswahl bereits veröffentlichter Arbeiten eingebunden, die Anwendungsergebnisse zu Wasserstoff [125], Molybdän [126], Eisen [127] sowie Wasser [128, 129, 130, 131] und Wasserstoff-Helium-Gemischen [132] in WDM-Zuständen enthalten. Abschließend erfolgt ein Ausblick.

Die Ergebnisse dieser Arbeit entstanden größtenteils in Forschungsprojekten an der Universität Rostock als wissenschaftlicher Mitarbeiter in der AG „Statistische Physik“ von Prof. Redmer. Konkret waren dies das DFG-Schwerpunktprogramm 1488: „Planetarer Magnetismus“ (PlanetMag, 2011-2017) und die seit 2017 geförderte DFG-Forschungsgruppe 2440: „Materie im Inneren von Planeten – Hochdruck-, Planeten- und Plasmaphysik“. Die Ergebnisse zu Molybdän wurden während einer Anstellung als Postdoc an den Sandia National Laboratories (USA) im Jahr 2013 erarbeitet.

Zusätzlich sei angemerkt, dass der Autor während seiner Forschungsarbeiten nach seiner Dissertation im Jahre 2010 [133] zahlreiche weitere Arbeiten veröffentlicht hat [15, 73, 125, 134, 135, 136, 137, 138, 139, 140, 141, 142, 143, 144, 145, 146, 147, 148, 149], die meisten davon über thermodynamische Eigenschaften von WDM. Diese sind jedoch nicht Bestandteil dieser Habilitationsschrift.

Zusammen mit den zuvor genannten Arbeiten bedeuten die in dieser Habilitationsschrift vorgestellten Veröffentlichungen einen beachtlichen Fortschritt zum Verständnis der thermophysikalischen Eigenschaften von WDM. Sie liefern damit neue und grundlegende Erkenntnisse, die für die zukünftige Weiterentwicklung von Modellen solarer und extrasolarer Planeten von großer Bedeutung sind.

Kapitel 2

Dichtefunktionaltheorie-Molekulardynamik-Simulationen

Die Grundlage der quantenmechanischen Beschreibung von nichtrelativistischen Vielteilchensystemen ist die Schrödinger-Gleichung [150]. Deren zentrale Größe ist der Hamiltonoperator $\hat{H}$, der die kinetischen Energien aller Teilchen sowie ihre Coulomb-Wechselwirkungsenergien enthält. Der mathematische Aufwand zur Lösung der Schrödinger-Gleichung steigt jedoch exponentiell mit der Teilchenzahl und ist daher nur für Vielteilchensysteme von ca. 10 oder weniger Teilchen bewältigbar [151]. Folglich muss auf Näherungsmethoden zurückgegriffen werden, mit denen dennoch zufriedenstellende Ergebnisse unter vertretbarem numerischen Aufwand erzielt werden können. Für WDM hat sich hierbei die DFT-MD-Simulationsmethode als Standardwerkzeug etabliert. Sie ist im Vergleich zu prinzipiell exakten Quanten-Monte-Carlo-Methoden [152, 153, 154] deutlich effizienter und insbesondere für die Berechnung von Transporteigenschaften geeignet.

Die grundlegendste Näherung in der DFT-MD ist die Born-Oppenheimer-Näherung. Im Rahmen dieser lassen sich die Bewegungsgleichungen von Elektronen und Ionen aufgrund ihres großen Massenunterschieds entkoppeln [114, 155]. Das Elektronensystem (N_e-Teilchenzustand $|\Psi_n\rangle$, Energieeigenwert ϵ_n) gehorcht dann zu jedem Zeitpunkt t der folgenden zeitunabhängigen Schrödinger-Gleichung:

$$\hat{H}_e|\Psi_n\rangle = \left(\hat{K}_e + \hat{U}_{ee} + \hat{V}_{ei}\left(\{\mathbf{R}_a(t)\}\right)\right)|\Psi_n\rangle = \epsilon_n|\Psi_n\rangle \quad , \tag{2.1}$$

mit dem elektronischen Hamiltonoperator $\hat{H}_e$, der sich aus deren kinetischer Energie $\hat{K}_e$, der Elektron-Elektron-Wechselwirkungsenergie $\hat{U}_{ee}$ und der Elektron-Ion-Wechselwirkungsenergie $\hat{V}_{ei}$ zusammensetzt. Letztere enthält die Positionen der Ionen $\mathbf{R}_a(t)$ als externe Parameter.

Weiterhin ist es zweckmäßig, die Ionen als klassische Teilchen anzusehen, wodurch sich folgende Newtonsche Bewegungsgleichungen ergeben [114]:

$$m_a \frac{\mathrm{d}^2\mathbf{R}_a(t)}{\mathrm{d}t^2} = -\nabla_a U_{ii}\left(\{\mathbf{R}_a(t)\}\right) - \nabla_a \Omega_e(\{\mathbf{R}_a(t)\}) \quad . \tag{2.2}$$

Die Gradienten der ionischen Coulomb-Wechselwirkungsenergie U_{ii} und der Born-Oppenheimer-Energiefläche $\Omega_e(\{\mathbf{R}_a(t)\})$ bestimmen die Kräfte auf die Ionen, die als Hellmann-Feynman-

Kräfte bezeichnet werden.[1] Die Gleichungen (2.1) und (2.2) müssen fortan abwechselnd gelöst werden, damit sich das Coulomb-System zeitlich entwickelt. Dies entspricht einer Molekulardynamiksimulation (MD) für die Ionen, jedoch mit Kräften, die zu jedem Zeitschritt direkt aus einer quantenmechanischen Berechnung des Elektronensystems stammen. Zur Lösung der Gleichung (2.1) wird die sehr effiziente Näherungsmethode der Dichtefunktionaltheorie (DFT) verwendet, welche im folgenden Abschnitt genauer erläutert wird.

Zusammengenommen ergibt sich so die DFT-MD-Simulationsmethode, die eine konsistente Beschreibung von WDM im sogenannten „physikalischen Bild“ [4, 5, 6] erlaubt, d.h. keinerlei Trennung in Streu- und Bindungszustände erfordert. Die Methode wird gelegentlich auch anders bezeichnet wird, z.B. FT-DFT-MD (Finite-Temperature-DFT-MD) [158], QMD (Quantum-MD) [159], BOMD (Born-Oppenheimer-MD) [160], FPMD (First-Principles-MD) [161] oder AIMD (*Ab-initio*-MD) [114]. Die weit verbreitete Car-Parrinello-MD [162] ist ein eng verwandtes Verfahren, in dem jedoch nur zum Anfangszeitpunkt eine selbstkonsistente DFT-Rechnung durchgeführt wird und sich das System danach anhand der Car-Parrinello-Gleichungen zeitlich entwickelt.

Es sei angemerkt, dass klassische MD-Simulationen seit langem etablierte Standardmethoden zur numerischen Beschreibung von Vielteilchensystemen sind [163, 164]. Somit kann die DFT-MD direkt auf viele der damit gemachten Erfahrungen zurückgreifen, z.B. bezüglich periodischer Randbedingungen, numerischer Integrationsalgorithmen, Thermostaten zur Temperaturregulierung, Konvergenzanalyse, etc.

2.1 Thermische Dichtefunktionaltheorie

Die Lösung der zeitunabhängigen Schrödinger-Gleichung (2.1) erfolgt im Rahmen von DFT [113, 114, 165, 166, 167]. Mit DFT wird das Vielteilchenproblem der wechselwirkenden Elektronen in ein Einteilchenproblem für nichtwechselwirkende Quasiteilchen in einem effektiven Potential umgewandelt, das die Vielteilcheneffekte indirekt enthält.

2.1.1 Das universelle Dichtefunktional der freien Energie

Bei WDM ist es essentiell, dass im Gegensatz zur häufig verwendeten Grundzustands-DFT auch thermische Anregungen der Elektronen berücksichtigt werden. Grundlage dieser thermischen DFT sind die Theoreme von Hohenberg, Kohn [110, 168] und Mermin [112]. Nach diesen bestimmen die Positionen der Ionen (externes Potential $\hat{V}_{ei}$ für das Elektronensystem) eindeutig die Elektronendichte $n_e(\mathbf{r})$ sowie die freie Energie des Elektronensystems, das sich in einem thermischen Gleichgewichtszustand befindet. Hierzu muss ein Dichtefunktional der freien Energie $F_e(T,V,N_e) = U_e - TS_e$ bzw. des großkanonischen thermodynamischen Potentials $\Omega_e(T,V,\mu_e) = F_e - \mu_e N_e$ minimiert werden [112, 156, 157]. Hierbei sind $U_e = \langle \hat{H}_e \rangle$ die innere Energie, S_e die Entropie und μ_e das chemische Potential des Elektronensystems. Die

---

[1] Für den elektronischen Grundzustand ist $\Omega_e = \epsilon_0$. Bei einem thermisch angeregten Elektronengas mit Temperatur T ist es die Fläche des großkanonischen Potentials des Elektronensystems [156, 157].

gesamte Elektronenzahl:

$$N_e = \int \mathrm{d}^3\mathbf{r}\, n_e(\mathbf{r}) \tag{2.3}$$

ist dabei durch die Sorten und Anzahl der Ionen N_i unter Forderung globaler Ladungsneutralität im betrachteten Volumen $V = \int \mathrm{d}^3\mathbf{r}$ festgeschrieben.

Die Elektronendichte $n_e(\mathbf{r})$ als zentrale Größe der DFT entspricht einer reduzierten Einteilchenverteilungsfunktion im Ortsraum. Somit ermöglicht ihre Bestimmung mittels DFT die Transformation des Vielteilchenproblems der wechselwirkenden Elektronen auf ein Referenzsystem aus nicht wechselwirkenden Elektronen, was einem effektiven Einteilchenbild entspricht. Die antisymmetrisierte Gesamtwellenfunktion der nicht wechselwirkenden Elektronen hat dann die Form einer Slater-Determinante [150], und die thermische Besetzung der Einteilchenzustände (Kohn-Sham-Orbitale) $|\phi_n\rangle$ entspricht einer Fermi-Dirac-Verteilung:

$$f_n = \frac{1}{e^{(E_n-\mu_e)/k_BT} + 1} \quad , \tag{2.4}$$

wobei E_n die Energieeigenwerte der Kohn-Sham-Orbitale sind. Die Elektronendichte ergibt sich aus den Betragsquadraten der Einteilchenwellenfunktionen:

$$n_e(\mathbf{r}) = \sum_n f_n \langle\phi_n|\mathbf{r}\rangle\langle\mathbf{r}|\phi_n\rangle = \sum_n f_n \phi_n^*(\mathbf{r})\phi_n(\mathbf{r}) \quad . \tag{2.5}$$

Das entscheidene Problem bleibt nun das Finden des universellen und in praktischen Anwendungen zu minimierenden Dichtefunktionals der freien Energie $F_e\left[n_e(\mathbf{r})\right]$. Dieses ist leider nicht vollständig bekannt, aber es ist von folgender Struktur:

$$F_e\left[n_e(\mathbf{r})\right] = K_0 + U_{0,H}\left[n_e(\mathbf{r})\right] + V_{ei}\left[n_e(\mathbf{r})\right] - TS_0 + F_{xc}\left[n_e(\mathbf{r})\right] \quad . \tag{2.6}$$

Explizit davon bekannt sind das Dichtefunktional der Wechselwirkungsenergie der Elektronen mit den Ionen:

$$V_{ei}\left[n_e(\mathbf{r})\right] = -\sum_{a=1}^{N_i} \frac{Z_a q_e^2}{4\pi\varepsilon_0} \int \mathrm{d}^3\mathbf{r}\, \frac{n_e(\mathbf{r})}{|\mathbf{R}_a - \mathbf{r}|} \quad , \tag{2.7}$$

und die klassische Wechselwirkungsenergie (Hartree-Energie) der Elektronen untereinander:

$$U_{0,H}\left[n_e(\mathbf{r})\right] = \frac{q_e^2}{8\pi\varepsilon_0} \int \mathrm{d}^3\mathbf{r}\, n_e(\mathbf{r}) \int \mathrm{d}^3\mathbf{r}'\, \frac{n_e(\mathbf{r}')}{|\mathbf{r} - \mathbf{r}'|} \quad . \tag{2.8}$$

Weiterhin kennt man die kinetische Energie:

$$K_0 = -\frac{\hbar^2}{2m_e} \sum_n f_n \langle\phi_n|\mathbf{r}\rangle \nabla^2 \langle\mathbf{r}|\phi_n\rangle \quad , \tag{2.9}$$

sowie die Entropie des Systems aus nicht miteinander wechselwirkenden Teilchen:

$$S_0 = -k_B \sum_n \left[f_n \ln f_n + (1 - f_n)\ln(1 - f_n)\right] \quad . \tag{2.10}$$

Die in $F_e\left[n_e(\mathbf{r})\right]$ unbekannten Terme fasst man zum Austausch- und Korrelationsbeitrag:

$$F_{xc}\left[n_e(\mathbf{r})\right] = K_e\left[n_e(\mathbf{r})\right] - K_0 + U_{ee}\left[n_e(\mathbf{r})\right] - U_{0,H}\left[n_e(\mathbf{r})\right] - TS_e\left[n_e(\mathbf{r})\right] + TS_0 \tag{2.11}$$

zusammen, wobei K_e die unbekannte exakte kinetische Energie und U_{ee} die unbekannte exakte Elektron-Elektron-Wechselwirkungsenergie sind. Für F_{xc} müssen daher geeignete Näherungen gefunden werden.

Die hier vorgestellte spinentartete Variante der DFT kann zur Spin-DFT verallgemeinert werden, womit sich auch magnetische Eigenschaften des Elektronengases einschließlich der Spin-Bahn-Kopplung beschreiben lassen [169, 170]. Der entsprechende Formalismus ist komplexer und enthält zusätzlich zur Elektronendichte $n_e(\mathbf{r})$ auch die Magnetisierungsdichte $\mathbf{m}_e(\mathbf{r})$, folgt aber denselben Grundgedanken. Praktische Bedeutsamkeit hat die Spin-DFT vor allem, wenn Berechnungen für Elemente der 4. und höheren Periode durchgeführt werden sollen.

2.1.2 Das Kohn-Sham-Verfahren

Im vorangegangenen Abschnitt 2.1.1 wurde das zu minimierende Funktional der freien Energie vorgestellt. Durch dessen Variationsableitung bezüglich der Elektronendichte [111] gelangt man zu folgendem effektiven Potential für die Quasiteilchen (Kohn-Sham-Elektronen):

$$v_{eff}(\mathbf{r}) = -\sum_{a=1}^{N_i} \frac{q_e^2}{4\pi\varepsilon_0} \frac{Z_a}{|\mathbf{R}_a - \mathbf{r}|} + \frac{q_e^2}{4\pi\varepsilon_0} \int \mathrm{d}^3\mathbf{r}' \, \frac{n_e(\mathbf{r}')}{|\mathbf{r} - \mathbf{r}'|} + \frac{\delta F_{xc}\left[n_e(\mathbf{r})\right]}{\delta n_e(\mathbf{r}')} \tag{2.12}$$

für eine zeitunabhängige Schrödinger-Gleichung:

$$\left(-\frac{\hbar^2\nabla^2}{2m_e} + v_{eff}(\mathbf{r})\right)\langle\mathbf{r}|\phi_n\rangle = E_n\langle\mathbf{r}|\phi_n\rangle \tag{2.13}$$

für die nicht miteinander wechselwirkenden Elektronen. Das effektive Potential $v_{eff}(\mathbf{r})$ enthält nun indirekt sämtliche Wechselwirkungen der Elektronen untereinander, welche von der Hartree-Energie und der Austausch- und Korrelationsenergie stammen. Die Funktionalableitung von $F_{xc}\left[n_e(\mathbf{r})\right]$ wird je nach konkret verwendeter Näherung analytisch ausgeführt. Zusammen mit dem bekannten Ausdruck für die Elektronendichte:

$$n_e(\mathbf{r}) = \sum_n f_n\langle\phi_n|\mathbf{r}\rangle\langle\mathbf{r}|\phi_n\rangle \quad , \tag{2.14}$$

bezeichnet man diese drei Gleichungen als Kohn-Sham-Gleichungen [111]. Sie müssen numerisch und selbstkonsistent gelöst werden, bis eine konvergierte (minimierte) freie Energie $F_e\left[n_e(\mathbf{r})\right]$ und Elektronendichte $n_e(\mathbf{r})$ gefunden sind.

2.2 Wahl des Austausch- und Korrelationsfunktionals

Das Austausch- und Korrelationsfunktional $F_{xc}\left[n_e(\mathbf{r})\right]$ ist nicht exakt bekannt und muss daher approximiert werden. Im Laufe der letzten vier Dekaden wurde eine Vielzahl von

Näherungen dafür entwickelt, die sich in verschiedene Klassen von Funktionalen einteilen lassen [113, 117]. Je nach physikalischer Problemstellung kann daher auf einfachere oder komplexere, aber dafür umso rechenzeitintensivere zurückgegriffen werden.

In der thermischen DFT ist es immer noch üblich, das Austausch- und Korrelationsfunktional für die freie Energie durch eines aus der Grundzustands-DFT anzunähern [171, 172, 173, 174], $F_{xc} \approx E_{xc}$, und so einen Teil der Temperatureffekte zu vernachlässigen. Der Hauptgrund ist, dass explizit temperaturabhängige Funktionale lange nicht verfügbar waren und ihnen erst seit wenigen Jahren stärkere Aufmerksamkeit zugewandt wird [175, 176, 177]. Darüber hinaus ist durch viele Vergleiche mit Experimenten mittlerweile bekannt, dass beliebte Grundzustandsfunktionale wie PBE [119] und AM05 [178] thermodynamische Eigenschaften von WDM durchaus gut beschreiben können [73, 172, 179, 180]. Effekte durch temperaturabhängige Austausch- und Korrelationsbeiträge treten zwar genau in dem für WDM bedeutsamen Temperaturbereich $k_BT \approx E_F$ auf, sind aber relativ klein. Sie führen z.B. in warmem dichtem Wasserstoff zu Druckabweichungen im einstelligen Prozentbereich [181, 182].

Die im Rahmen dieser Arbeit am häufigsten verwendeten Austausch- und Korrelationsfunktionale $E_{xc}[n_e(\mathbf{r})]$ sind das von Perdew, Burke und Ernzerhof (PBE) [119] und das von Armiento und Mattsson (AM05) [178]. Diese sogenannten GGA (engl. generalized gradient approximation, dt. verallgemeinerte Gradientennäherung)-Funktionale hängen von der lokalen Dichte $n_e(\mathbf{r})$ und ihrem lokalen Gradienten $\nabla n_e(\mathbf{r})$ ab. Sie bieten eine deutlich bessere Beschreibung von elektronischen Bindungsenergien, molekularen Dissoziationsenergien [113, 167], Gitterkonstanten von Festkörpern [183, 184] sowie Wasserstoffbrückenbindungen [185, 186] als die lokale Dichtenäherung (engl. local density approximation: LDA) [118, 187] bei vernachlässigbar größerem Rechenaufwand. Beide Funktionale reproduzieren im Fall von verschwindendem Gradienten den Grenzfall der LDA und sind nicht an empirische Werte angepasst. Sie wurden derart konstruiert, dass sie im Einklang mit möglichst vielen der formal bekannten Eigenschaften der Austausch- und Korrelationsenergie stehen [113, 167]. Das AM05-Funktional stellt hierbei den Versuch dar, die Austausch- und Korrelationsenergie des Airy-Elektronengases als Referenzsystem möglichst gut abzubilden, analog zur Parametrisierung des LDA-Funktionals anhand des homogenen Elektronengases [118, 120].

Sowohl das PBE- als auch das AM05-Funktional haben größere Defizite bei der korrekten Beschreibung von van-der-Waals-Kräften und unterschätzen die fundamentale elektronische Bandlücke [188, 189, 190, 191] deutlich. Meta-GGA-Funktionale [192, 193, 194] wie das SCAN-Funktional [195] als Erweiterung der GGA enthalten eine zusätzliche Abhängigkeit von der kinetischen Energiedichte $\sim \sum_n f_n |\nabla \phi_n|^2$, können die genannten Defizite aber nicht beheben [196, 197]. Sogenannte van-der-Waals-Funktionale [198, 199], welche nichtlokale Korrelationsenergien berücksichtigen, können die Beschreibung von van-der-Waals-Kräften beachtlich verbessern, sind aber rechenzeitaufwendiger.

Für genaue Berechnungen der elektronischen Leitfähigkeit von Nichtmetallen ist eine gute Vorhersagekraft der fundamentalen Bandlücke durch DFT äußerst wichtig. Bei zu kleiner Bandlücke werden die Leitungsbänder zu hoch besetzt bzw. können Halbleiter fälschlicherweise komplett metallisch sein, sodass deren Ionisationsgrad überschätzt wird [153].

Für solche nichtmetallischen Systeme bietet hier das Funktional von Heyd, Scuseria und Ernzerhof (HSE) [200, 201] Abhilfe, das eine Weiterentwicklung des PBE-Funktionals darstellt. Dieses Funktional gehört in die Klasse der Hybridfunktionale und enthält neben der PBE-Korrelationsenergie E_c^{PBE} einen Teil der nichtlokalen Fock-Austauschenergie der Kohn-Sham-Zustände:

$$E_x^F = -\frac{q_e^2}{8\pi\varepsilon_0} \sum_n \sum_m f_n f_m \int \mathrm{d}^3\mathbf{r} \int \mathrm{d}^3\mathbf{r}' \, \frac{\phi_n^*(\mathbf{r})\,\phi_m(\mathbf{r})\,\phi_m^*(\mathbf{r}')\,\phi_n(\mathbf{r}')}{|\mathbf{r}-\mathbf{r}'|} \quad . \tag{2.15}$$

Die numerische Auswertung dieses Doppelintegrals bedeutet insbesondere auf periodischen Randbedingungen einen erheblichen Rechenaufwand [202]. Der Fock-Austauschterm trägt jedoch vor allem über kurze Distanzen $r = |\mathbf{r}-\mathbf{r}'|$ bei. Deshalb wird im HSE-Funktional der gesamte Austauschterm in einen kurz- und einen langreichweitigen Anteil zerlegt. Der kurzreichweitige Anteil wird zu einem Viertel durch den Fock-Term $E_x^{F,S}$ und zu drei Vierteln durch den PBE-Austausch $E_x^{PBE,S}$ bestimmt. Für den langreichweitigen Anteil wird ausschließlich der PBE-Austauschterm $E_x^{PBE,L}$ verwendet. Die HSE-Austausch- und Korrelationsenergie setzt sich daher wie folgt zusammen:

$$E_{xc}^{HSE} = E_c^{PBE} + \frac{3}{4}E_x^{PBE,S} + \frac{1}{4}E_x^{F,S} + E_x^{PBE,L} \quad . \tag{2.16}$$

Die Unterteilung in kurzreichweitige $S(r)$ und langreichweitige $L(r)$ Anteile wird durch folgende Mischungsfunktion erreicht:

$$1 = S(r) + L(r) = \mathrm{erfc}(\mu_s r) + \mathrm{erf}(\mu_s r) \quad , \tag{2.17}$$

die anteilsweise unter dem Doppelintegral in Gleichung (2.15) und ebenso bei dem PBE-Austausch [119] eingefügt wird.[2] Der Abschirmparameter $\mu_s = 0,2\ \text{Å}^{-1}$ legt die Reichweite beider Anteile fest [201]. Das HSE-Funktional geht im Grenzfall verschwindender Abschirmung in das PBE0-Funktional [203] über. Ausführliche Untersuchungen hatten gezeigt, dass DFT mit dem HSE-Funktional die Bandlücke von vielen Halbleiterkristallen mit einer Genauigkeit von ca. 10% vorhersagen kann [204].

2.3 Ebene Wellen und Pseudopotentiale

Die Lösung der in den vorangegangenen Abschnitten beschriebenen Gleichungen erfordert numerisch effiziente Verfahren. Konkret befinden sich die Elektronen aufgrund der periodischen Randbedingungen in einem gitterperiodischen Potential und daher in Bloch-Zuständen [205] mit den Quantenzahlen[3] $n = (\mathbf{k}, \nu, \alpha)$: Wellenzahl $\mathbf{k}$, Bandindex ν und Spinausrichtung α.

---

[2] Es sind $\mathrm{erf}(\mu_s r)$ die Fehlerfunktion und $\mathrm{erfc}(\mu_s r)$ ihr Komplementäranteil.

[3] In der spinentarteten DFT ergeben verbleibende Summen über den Spin einfach den Faktor 2.

Wegen der periodischen Randbedingungen ist es für die numerische Lösung der Kohn-Sham-Gleichungen zweckmäßig, den Bloch-Faktor $u_{\mathbf{k}\nu\alpha}(\mathbf{r})$ der elektronischen Wellenfunktion nach ebenen Wellen zu entwickeln [113, 114]:

$$\langle \mathbf{r}|\mathbf{k}\nu\alpha\rangle = \phi_{\mathbf{k}\nu\alpha}(\mathbf{r}) = \frac{1}{\sqrt{V}} e^{i\mathbf{k}\cdot\mathbf{r}} u_{\mathbf{k}\nu\alpha}(\mathbf{r}) = \frac{1}{\sqrt{V}} e^{i\mathbf{k}\cdot\mathbf{r}} \sum_{\mathbf{G}} C_{\mathbf{k}\nu\alpha}(\mathbf{G})\, e^{i\mathbf{G}\cdot\mathbf{r}} \quad . \tag{2.18}$$

In der Praxis muss die Summation über die Wellenzahlen $\mathbf{G}$ bei einem Grenzwert abgebrochen werden. Diese Abbruchbedingung ist durch die sogenannte Cutoff-Energie E_{cut} festgelegt, und zwar über die Beziehung:

$$E_{cut} > \frac{\hbar^2}{2m_e} |\mathbf{k}+\mathbf{G}|^2 \quad . \tag{2.19}$$

Die Cutoff-Energie ist somit ein entscheidender Parameter für die Konvergenz der DFT-Rechnungen. Gleichermaßen transformiert man die Kohn-Sham-Gleichung (2.13) in den Raum der ebenen Wellen [113], wodurch sich ein Gleichungssystem für die Entwicklungskoeffizienten $C_{\mathbf{k}\nu\alpha}(\mathbf{G})$ ergibt:

$$\sum_{\mathbf{G}'} \left(\frac{\hbar^2}{2m_e} |\mathbf{k}+\mathbf{G}|^2 \delta_{\mathbf{G},\mathbf{G}'} + v_{eff}(\mathbf{G}-\mathbf{G}') \right) C_{\mathbf{k}\nu\alpha}(\mathbf{G}') = E_{\mathbf{k}\nu\alpha} C_{\mathbf{k}\nu\alpha}(\mathbf{G}) \quad . \tag{2.20}$$

Das $\mathbf{k}$-Punktgitter in der ersten Brillouinzone und die Zahl der Bänder sind hier weitere Parameter, die groß genug zu wählen sind, sodass man gut konvergierte Ergebnisse erhält. Die Fourier-Transformierte des gitterperiodischen Kohn-Sham-Potentials $v_{eff}(\mathbf{r})$ lautet:

$$v_{eff}(\mathbf{G}-\mathbf{G}') = \frac{1}{V} \int \mathrm{d}^3\mathbf{r}\, v_{eff}(\mathbf{r})\, e^{-i(\mathbf{G}-\mathbf{G}')\cdot\mathbf{r}} \quad . \tag{2.21}$$

Es ist prinzipiell möglich, die Kohn-Sham-Gleichungen mit den ebenen Wellen als Basis so wie hier beschrieben zu lösen. Dabei zeigt sich jedoch, dass enorm hohe Cutoff-Energien erforderlich sind, um die stark oszillierende Wellenfunktion in der Nähe der Kerne hinreichend gut konvergiert berechnen zu können [113, 114]. Dieses Problem vergrößert sich mit steigender Kernladungszahl. Es lässt sich umgehen, wenn man sogenannte Pseudopotentiale einführt und damit das System auf zweierlei Arten manipuliert:

Einerseits betrachtet man die energetisch tief gebundenen Elektronen, welche für viele chemische und optische Eigenschaften unbedeutsam sind, als stark gebunden und fasst sie mit dem Coulomb-Potential des Kerns zusammen (auch Frozen-Core-Approximation genannt). Dadurch wird das Kernpotential abgeschirmt, und die äußeren Elektronen finden ein weicheres Potential vor. Außerdem definiert man um die Kerne einen Radius r_{PP}, innerhalb dessen die stark oszillierende Wellenfunktion durch eine glatte, knotenfreie Pseudowellenfunktion ersetzt wird, welche numerisch leichter zu handhaben ist.

Die Theorie der Pseudopotentiale ist hoch entwickelt [113, 114], und es haben sich Pseudopotentiale durchgesetzt, welche durch im Ortsraum nichtlokale Operatoren beschrieben werden, wie die Projector-Augmented-Wave (PAW)-Potentiale [206, 207]. PAW-Potentiale können mit einer linearen Transformation aus der Pseudowellenfunktion die exakte Wellenfunktion innerhalb von r_{PP} erzeugen. Durch die Verwendung von Pseudopotentialen werden sämtliche in diesem Kapitel vorgestellte Formeln deutlich komplizierter [206, 207, 208]. Aus Gründen der Übersichtlichkeit wird auf die genauere Darstellung dieses Sachverhalts verzichtet. Dennoch sei betont, dass die Pseudopotentiale ein Hilfsmittel zur rein numerischen Effizienzsteigerung zu verstehen sind und keine weitere physikalische Näherung darstellen [114, 209]. Ihre Erzeugung und Verwendung sind vollkommen beherrschbare Angelegenheiten, soweit sie darauf überprüft werden, ob bzw. inwieweit sie die Ergebnisse im Vergleich zu Rechnungen ohne Pseudopotentiale verfälschen [114]. Dies trifft speziell auf Berechnungen stark komprimierter Systeme zu, in denen sich zwei benachbarte Ionen a und b näher als $r_{a,PP} + r_{b,PP}$ kommen können. Systematische Vergleiche mit härteren Pseudopotentialen (solche mit kleinerem r_{PP}) sind daher für DFT-MD-Simulationen von WDM unabdingbar.

2.4 VASP als Implementation der Methode

Die DFT-MD-Simulationsmethode ist heutzutage in verschiedenen Programmpaketen implementiert, z.B. VASP [210], ABINIT [211], QUANTUM ESPRESSO [212], CP2K [213]. Die Rechnungen zur vorliegenden Arbeit wurden ausschließlich mit dem Programmpaket Vienna-*Ab-initio*-Simulation-Package (VASP) [214, 215, 216] durchgeführt. Das VASP enthält die thermische DFT als Standardmethode der elektronischen Strukturberechnung und hat sich seit Jahrzehnten als zuverlässiges Werkzeug erwiesen. Ein allgemeines Ablaufschema für die DFT-MD-Simulationen mit dem VASP ist in Abbildung 2.1 gezeigt. Alle DFT-MD-Rechnungen aus dieser Arbeit wurden auf parallelisierten Hochleistungsrechnern (z.B. dem HLRN) durchgeführt.

Das VASP stellt eine große Datenbank an generierten und vorgetesteten Pseudopotentialen für jedes Element zur Verfügung, aus denen ausgewählt werden kann. Zur Diagonalisierung der Matrixgleichung (2.20) ist der RMM-DIIS-Algorithmus implementiert [216]. Dieser skaliert für Systeme mit ca. 1000 oder weniger Elektronen näherungsweise quadratisch, darüber etwa kubisch. In den DFT-Schritten werden mehrmals Fourier-Transformationen ausgeführt, da sich in der Basis der ebenen Wellen viele Terme im reziproken Raum relativ schnell auswerten lassen [113, 114]. Die Hartree-Energie $U_{0,H}$ und die Coulomb-Energie der Ionen U_{ii} berechnet das VASP mit einer Ewald-Summation [218]. Der Drucktensor P wird mit dem quantenmechanischen Virialsatz [113, 114, 219, 220, 221, 222] berechnet. Die Bewegungsgleichung für die Ionen (2.2) wird mit einem Verlet-Algorithmus [163, 164] integriert. Zur Simulation eines quasi-kanonischen Ensembles kann die Temperatur z.B. mit dem Nosé-Hoover-Thermostaten [223, 224] geregelt oder in jedem Zeitschritt skaliert werden.

An dieser Stelle bringen wir die Kerngedanken der DFT-MD noch einmal auf den Punkt:

- Alle Teilchen werden nichtrelativistisch betrachtet.
- Die Born-Oppenheimer-Näherung separiert die Bewegungsgleichungen der leichten Elektronen von denen der schweren Ionen.

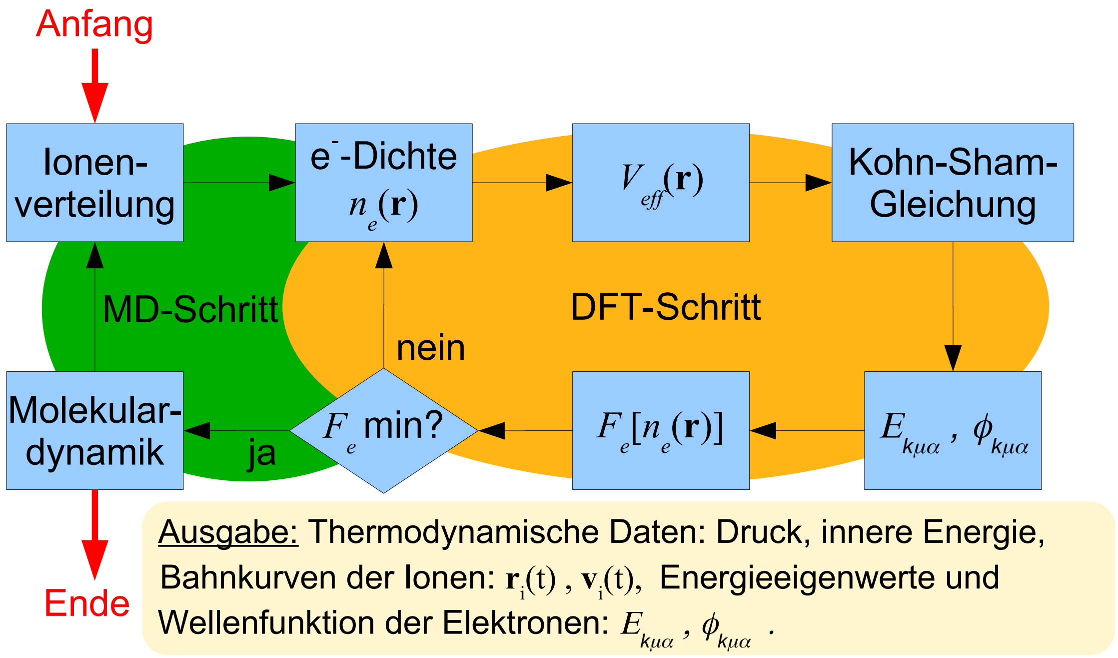

Abbildung 2.1: Schema der DFT-MD (nach B. Holst [217], überarbeitet). In jedem MD-Schritt werden mehrere DFT-Schritte durchlaufen, bis eine konvergierte freie Energie, Wellenfunktion und dazugehörige Energieeigenwerte erzeugt sind. Danach werden die Hellmann-Feynman-Kräfte auf die Ionen sowie die innere Energie und der Drucktensor berechnet. Abschließend werden die Ionen weiterbewegt, und ein neuer MD-Schritt startet.

- Die Elektronen werden quantenstatistisch im Rahmen der thermischen DFT behandelt. Das Austausch- und Korrelationsfunktional muss dabei approximiert werden.
- Die Ionen propagieren als klassische Teilchen mit den Hellmann-Feynman-Kräften aus der DFT.

Dazu sei Folgendes angemerkt: Es ist möglich, spinpolarisierte DFT-Rechnungen [169, 170, 225, 226] mit dem VASP durchzuführen, wie z.B. bei der Berechnung der Leitfähigkeit von Eisen [127] notwendig wurde, siehe Abschnitt 4.3. Bei der Pseudopotentialerzeugung werden relativistische Effekte der tiefgebundenen Elektronen in schweren Elementen berücksichtigt [113].

Kapitel 3

Lineare Response-Theorie

Mit der im Kapitel 2 vorgestellten DFT-MD-Methode lassen sich thermodynamische Gleichgewichtszustände beschreiben. Thermodynamische Mittelwerte werden durch Zeitmittel in der Gleichgewichtssimulation $\langle \ldots \rangle_0$ berechnet. Die Berechnung von Transportgrößen erfordert jedoch eine Erweiterung der theoretischen Beschreibung auf das Nichtgleichgewicht. Wird das Gleichgewicht nur schwach gestört, reagiert das System mit einer zur Störung direkt proportionalen Antwort, was zu linearen Transportgleichungen führt, siehe Abschnitt 1.2. In solchem Fall bestimmen allein die Fluktuationen der Gleichgewichtsgrößen über die Transportvorgänge im Nichtgleichgewicht, wie man durch das Fluktuations-Dissipations-Theorem [227] allgemein begründen kann. Die im Folgenden dargestellte „Lineare Response-Theorie“ (LRT, dt. Theorie der linearen Antwort) liefert hierbei das mathematische Werkzeug, mit dem man Transportgrößen mittels DFT-MD-Simulationen im Gleichgewicht berechnen kann.

3.1 Kubo-Theorie für den statistischen Operator des Nichtgleichgewichts

Transportvorgänge sind irreversible Prozesse [43]. Zu ihrer Beschreibung braucht man folglich eine Bewegungsgleichung für den statistischen Operator des Nichtgleichgewichts $\hat{\varrho}(t)$, die nicht invariant bezüglich Zeitumkehr ist [100, 101, 228]. Deswegen addiert man zur von-Neumann-Gleichung, der Bewegungsgleichung für den statistischen Operator des Gleichgewichts $\hat{\varrho}_0$, folgenden Quellterm:

$$\frac{\partial \hat{\varrho}(t)}{\partial t} + \frac{i}{\hbar}\left[\hat{H}(t), \hat{\varrho}(t)\right] = -\lim_{t-t_0\to\infty} \frac{\hat{\varrho}(t) - \hat{\varrho}_0}{t - t_0} \quad . \tag{3.1}$$

Für sehr große Zeitdifferenzen $t-t_0$ verschwindet dieser Quellterm, d.h., das System kann langfristig in einen Zustand relaxieren, der durch die gewöhnliche von-Neumann-Gleichung beschrieben wird. In der Kubo-Theorie [97, 102] ist dies der thermodynamische Gleichgewichtszustand [100, 101]. Damit ist eine Anfangsbedingung (hier Endbedingung) für die

Differentialgleichung (3.1) festgelegt,

$$\lim_{t\to\infty} \hat{\varrho}(t) = \hat{\varrho}_0 \quad , \tag{3.2}$$

und gleichermaßen die unmittelbare Anknüpfungsmöglichkeit an die Gleichgewichtsbeschreibung mit DFT-MD eröffnet.[1] Der Hamiltonoperator $\hat{H}(t) = \hat{H}_0 + \hat{H}_1(t)$ enthält sowohl den Gleichgewichtsanteil $\hat{H}_0$ als auch einen im Allgemeinen zeitabhängigen Störanteil $\hat{H}_1(t)$. Das bedeutet, dass die o.g. Anfangsbedingung nur eine sinnvolle Annahme ist, wenn $\hat{H}_1(t) \ll \hat{H}_0$ ist, d.h. die Störung klein ist. Der Grenzübergang $t - t_0 \to \infty$ darf erst nach dem thermodynamischen Limes (Ensemblemittelung) ausgeführt werden, sodass der Quellterm für die Zeitentwicklung des statistischen Operators beibehalten wird [100, 101].

Die formale Lösung der Gleichung (3.1) lautet damit [100]:

$$\hat{\varrho}(t) = \frac{1}{t - t_0} \int_{t_0}^{t} \mathrm{d}t' \, \hat{U}(t,t') \hat{\varrho}_0 \hat{U}^\dagger(t,t') \quad . \tag{3.3}$$

Für die Zeitentwicklungsoperatoren gelten folgende Bewegungsgleichungen:

$$\frac{\partial \hat{U}(t,t')}{\partial t} = -\frac{i}{\hbar} \hat{H}(t) \hat{U}(t,t') \quad , \quad \frac{\partial \hat{U}^\dagger(t,t')}{\partial t} = \frac{i}{\hbar} \hat{U}^\dagger(t,t') \hat{H}(t) \quad , \tag{3.4}$$

$$\frac{\partial \hat{U}(t,t')}{\partial t'} = \frac{i}{\hbar} \hat{U}(t,t') \hat{H}(t') \quad , \quad \frac{\partial \hat{U}^\dagger(t,t')}{\partial t'} = -\frac{i}{\hbar} \hat{H}(t') \hat{U}^\dagger(t,t') \quad . \tag{3.5}$$

Mit den Ersetzungen $\tau = t - t_0$ und $t'' = t' - t$ kann man den statistischen Operator schreiben als:

$$\hat{\varrho}(t) = \lim_{\tau\to\infty} \frac{1}{\tau} \int_{-\tau}^{0} \mathrm{d}t'' \, \hat{U}(t, t''+t) \hat{\varrho}_0 \hat{U}^\dagger(t, t''+t) \quad , \tag{3.6}$$

und ihn dann mit dem Abelschen Theorem [101] umformen zu:

$$\hat{\varrho}(t) = \lim_{\varepsilon\to 0} \varepsilon \int_{-\infty}^{0} \mathrm{d}t'' \, e^{\varepsilon t''} \hat{U}(t, t''+t) \hat{\varrho}_0 \hat{U}^\dagger(t, t''+t) \quad . \tag{3.7}$$

Der Grenzübergang $\varepsilon \to 0$ darf wiederum erst nach dem thermodynamischen Limes ausgeführt werden. Um das voranstehende ε zu eliminieren, integrieren wir partiell mit:

$$\int u'v = uv| - \int uv' \quad , \tag{3.8}$$

---

[1] Eine noch allgemeinere Beschreibung bietet der Zubarev-Formalismus [100, 101], bei dem der statistische Operator stattdessen gegen einen relevanten statistischen Operator strebt, $\lim_{t\to\infty} \hat{\varrho}(t) = \hat{\varrho}_{rel}(t)$, der durch zusätzliche Variablen gekennzeichnet ist und einen Nichtgleichgewichtszustand charakterisiert. Der Zubarev-Formalismus als Erweiterung der Kubo-Theorie ist insbesondere für eine störungstheoretische Beschreibung der Wechselwirkungen innerhalb der Transporttheorie bedeutsam [97].

wobei

$$u' = \varepsilon e^{\varepsilon t''} \quad \text{und} \quad u = e^{\varepsilon t''} \quad \text{und} \quad v = \hat{U}(t, t'' + t)\hat{\varrho}_0 \hat{U}^{\dagger}(t, t'' + t) \tag{3.9}$$

sind sowie

$$v' = \hat{U}(t, t'' + t)\left(\frac{i}{\hbar}\left[\hat{H}(t'' + t), \hat{\varrho}_0\right]\right)\hat{U}^{\dagger}(t, t'' + t) \quad . \tag{3.10}$$

Da außerdem $\hat{H}_0$ mit $\hat{\varrho}_0$ kommutiert, ergibt sich für $\hat{\varrho}(t)$:

$$\hat{\varrho}(t) = \hat{\varrho}_0 - \lim_{\varepsilon \to 0} \int\limits_{-\infty}^{0} \mathrm{d}t''\, e^{\varepsilon t''} \hat{U}(t, t'' + t) \frac{i}{\hbar}\left[\hat{H}_1(t'' + t), \hat{\varrho}_0\right] \hat{U}^{\dagger}(t, t'' + t) \quad . \tag{3.11}$$

Der statistische Operator des Nichtgleichgewichts hat einen Gleichgewichtsterm und einen Zusatzterm, der die externe Störung enthält. An dieser Stelle ist es sinnvoll, $\hat{\varrho}(t)$ bezüglich der Störung zu linearisieren. Dadurch verschwindet der Störanteil in den Zeitentwicklungsoperatoren, welche sich vereinfachen zu:

$$\hat{U}_0(t, t') = \exp\left\{-\frac{i}{\hbar}\hat{H}_0(t - t')\right\} \quad \text{und} \quad \hat{U}_0^{\dagger}(t, t') = \exp\left\{\frac{i}{\hbar}\hat{H}_0(t - t')\right\} \quad . \tag{3.12}$$

Für den Feldanteil setzen wir folgende periodische Zeitabhängigkeit an:

$$\hat{H}_1(t) = \hat{H}_1 e^{i\omega t} \quad . \tag{3.13}$$

Es folgt nach Umbenennen von $t'' = t'$ aus (3.11):

$$\hat{\varrho}(t) = \hat{\varrho}_0 - \lim_{\varepsilon \to 0} e^{i\omega t} \int\limits_{-\infty}^{0} \mathrm{d}t' e^{(\varepsilon + i\omega)t'} \hat{U}_0(-t', 0) \frac{i}{\hbar}\left[\hat{H}_1, \hat{\varrho}_0\right] \hat{U}_0^{\dagger}(-t', 0) \quad . \tag{3.14}$$

Nach konkreter Festlegung von $\hat{H}_1$ können mit diesem statistischen Operator Mittelwerte von Antwortgrößen (z. B. Strömen) berechnet werden. Dabei entstehen lineare Transportgleichungen, die die gesuchten Transportkoeffizienten in Form von Zeitkorrelationsfunktionen in dem gewählten Gleichgewichtsensemble enthalten.

3.2 Quantenmechanische Transportgleichungen

Für die quantenstatistische Berechnung von Transportkoeffizienten verwendet man günstigerweise das großkanonische Ensemble. Für ein Einkomponentensystem (hier die DFT-Elektronen) lautet der statistische Operator des Gleichgewichts [100]:

$$\hat{\varrho}_0 = \frac{1}{Z_0} e^{-\beta(\hat{H}_0 - \mu_e \hat{N}_e)} \quad , \tag{3.15}$$

mit der großkanonischen Zustandssumme Z_0 und $\beta = 1/k_B T$. Für die Berechnung des Kommutators wenden wir die folgende Kuboidentität an [100, 101]:

$$\left[\hat{B}, e^{-\beta\hat{A}}\right] = e^{-\beta\hat{A}} \int\limits_0^\beta \mathrm{d}\tau\, e^{\hat{A}\tau} \left[\hat{A}, \hat{B}\right] e^{-\hat{A}\tau} \quad . \tag{3.16}$$

Der Teilchenzahloperator kommutiert mit allen anderen Operatoren, und wir finden:

$$\hat{\varrho}(t) = \hat{\varrho}_0 - \lim_{\varepsilon\to 0} e^{i\omega t} \int\limits_{-\infty}^0 \mathrm{d}t'\, e^{(\varepsilon+i\omega)t'} \int\limits_0^\beta \mathrm{d}\tau\, \hat{\varrho}_0\, e^{\frac{i}{\hbar}(t'-i\hbar\tau)\hat{H}_0} \frac{i}{\hbar} \left[\hat{H}_0, \hat{H}_1\right] e^{-\frac{i}{\hbar}(t'-i\hbar\tau)\hat{H}_0} \quad . \tag{3.17}$$

Dabei tritt die Zeitableitung des Störoperators $\hat{H}_1$, welche die durch die Störung ins System eingetragene Leistung beschreibt, als Heisenberg-Operator auf:

$$\dot{\hat{H}}_1(t' - i\hbar\tau) = e^{\frac{i}{\hbar}(t'-i\hbar\tau)\hat{H}_0} \frac{i}{\hbar} \left[\hat{H}_0, \hat{H}_1\right] e^{-\frac{i}{\hbar}(t'-i\hbar\tau)\hat{H}_0} \quad . \tag{3.18}$$

Beispiel: Elektrische Leitfähigkeit im Einkomponentensystem aus Elektronen

Für ein homogenes elektrisches Feld $\mathbf{E} = -\nabla\Phi$ in x-Richtung lauten der Hamiltonoperator der Störung und seine Zeitableitung:

$$\hat{H}_1 = -\sum_{i=1}^{N_e} q_e E_x \hat{x}_i = -q_e E_x \hat{X} \quad ,\text{bzw.} \quad \dot{\hat{H}}_1 = \frac{i}{\hbar}\left[\hat{H}_0, \hat{H}_1\right] = -q_e E_x \dot{\hat{X}} \quad . \tag{3.19}$$

Berechnet man damit den quantenstatistischen Mittelwert der elektrischen Stromdichte, so liefert der Gleichgewichtsanteil keinen Beitrag, und es bleibt übrig:

$$\begin{aligned}
\left\langle \hat{j}_{el,x}(\omega) \right\rangle &= \frac{q_e}{V} \mathrm{Tr}\left\{\hat{\varrho}(t)\dot{\hat{X}}\right\} && (3.20)\\
&= \lim_{\varepsilon\to 0} \frac{q_e^2}{V} \int\limits_{-\infty}^0 \mathrm{d}t'\, e^{(\varepsilon+i\omega)t'} \int\limits_0^\beta \mathrm{d}\tau\, \mathrm{Tr}\left\{\varrho_0 \dot{\hat{X}}(t'-i\hbar\tau)\dot{\hat{X}}\right\} E_x e^{i\omega t} && (3.21)\\
&\overset{!}{=} \frac{q_e^2}{V} \left\langle\!\!\left\langle \dot{\hat{X}}(t-i\hbar\tau)\dot{\hat{X}} \right\rangle\!\!\right\rangle_0 E_x e^{i\omega t} = \frac{1}{V} \left\langle\!\!\left\langle \hat{J}_{el,x}(t-i\hbar\tau)\hat{J}_{el,x} \right\rangle\!\!\right\rangle_0 E_x e^{i\omega t} && (3.22)\\
&= \sigma_{xx}(\omega) E_x e^{i\omega t} = -\sigma_{xx}(\omega)\nabla\Phi e^{i\omega t} \quad . && (3.23)
\end{aligned}$$

Dies ist das Ohmsche Gesetz (1.3), und durch einen Koeffizientenvergleich findet man die dynamische Leitfähigkeit $\sigma_{xx}(\omega)$ als xx-Komponente des Leitfähigkeitstensors. Alle anderen räumlichen Komponenten folgen analog. Die weitere Auswertung der quantenstatistischen Strom-Strom-Korrelationsfunktion $\langle\!\langle \ldots \rangle\!\rangle_0$ aus (3.22) in Besetzungszahldarstellung von

Kohn-Sham-Zuständen [125, 133] ist langwierig und führt letztendlich zur frequenzabhängigen Kubo-Greenwood-Formel [102, 229].[2] Genaueres dazu wird in Kapitel 4 erörtert und gleichermaßen auf die elektronische Wärmeleitfähigkeit und die Thermokraft angewendet.

3.3 Klassische Transportgleichungen

Der Übergang zur klassischen Physik erfolgt formal über die Wigner-Darstellung des statistischen Operators [100, 230]. Der folgende, vereinfachte Übergang liefert jedoch dieselben Ergebnisse. Die statistischen Operatoren $\hat{\varrho}(t)$ und $\hat{\varrho}_0$ werden dabei durch die klassischen Verteilungsfunktionen $f(t)$ und f_0 ersetzt. Der Grenzwert $\varepsilon \to 0$ lässt sich nun ausführen, da effektiv eine Spurbildung in der Wigner-Darstellung stattgefunden hat. Alle hermiteschen Operatoren werden zu den entsprechenden klassischen dynamischen Variablen bestehend aus Orten $\mathbf{r}_i$ und Impulsen $\mathbf{p}_i$ der Teilchen. Der Kommutator wird durch die Poissonklammer:

$$-\frac{i}{\hbar}\left[\hat{A},\hat{B}\right] \to \{A,B\} = \sum_{k=1}^{3N}\left(\frac{\partial A}{\partial r_k}\frac{\partial B}{\partial p_k} - \frac{\partial A}{\partial p_k}\frac{\partial B}{\partial r_k}\right) \tag{3.24}$$

ersetzt, die sämtliche Orts- und Impulskoordinaten r_k und p_k enthält. Die Zeitentwicklungsoperatoren werden zum klassischen Liouville-Operator, der lediglich das Zeitargument t' der Poissonklammer festlegt. Weiterhin ist es in der klassischen Kubo-Theorie üblich, die Zeit $t' \to -t'$ umzukehren. Damit folgt für die klassische Nichtgleichgewichtsverteilungsfunktion:

$$f(t) = f_0 + e^{i\omega t}\int_0^\infty \mathrm{d}t'\, e^{-i\omega t'}\left\{H_1, f_0\right\}(t') \quad . \tag{3.25}$$

Als Gleichgewichtsensemble verwenden wir nun die kanonische Gesamtheit, deren Verteilung gegeben ist als:

$$f_0 = \frac{1}{Z_0}e^{-\beta H_0} \quad , \tag{3.26}$$

mit der kanonischen Zustandssumme Z_0. Man kann leicht zeigen, dass gilt:

$$\left\{H_1, f_0\right\} = -\beta f_0\left\{H_1, H_0\right\} = -\beta f_0 \dot{H}_1 \quad . \tag{3.27}$$

Damit erhält man für die Nichtgleichgewichtsverteilung den Ausdruck:

$$f(t) = f_0 - \beta f_0 e^{i\omega t}\int_0^\infty \mathrm{d}t'\, e^{-i\omega t'}\left\{H_1, H_0\right\}(t') \quad , \tag{3.28}$$

---

[2] In den konkreten Herleitungen in [125, 133] wurde von der Formel (5.1.19) aus [101] ausgegangen. Diese entspricht nicht exakt dem Ausdruck (3.22). Beide Formeln liefern zwar dasselbe Ergebnis für den Realteil (Kubo-Greenwood-Formel), aber entgegengesetzte Vorzeichen für den Imaginärteil der Leitfähigkeit. Alternativ kann der Imaginärteil auch aus dem Realteil über eine Kramers-Kronig-Transformation berechnet werden. Ein numerischer Vergleich ergibt, dass das korrekte Vorzeichen für den Imaginärteil mit Formel (3.22) erhalten wird.

mit dem man die klassischen Green-Kubo-Formeln [102, 231] für diverse Transportkoeffizienten herleiten kann. Im Folgenden werden die wichtigsten davon vorgestellt. Quantenkorrekturen zu den Green-Kubo-Formeln sind aus Gleichung (3.14) durch Reihenentwicklung von Operatoren nach Ordnungen von $\hbar^2$ in der Wigner-Darstellung herleitbar [230, 232].

3.3.1 Elektrische Leitfähigkeit

Die Hamiltonfunktion der Störung lautet für N Teilchen beliebiger Sorte in einem homogenen elektrischen Feld in x-Richtung:

$$H_1 = -\sum_{i=1}^{N} q_i x_i E_x \quad . \tag{3.29}$$

Dann folgt für die Verteilungsfunktion des Nichtgleichgewichts:

$$f(t) = f_0 + \beta f_0 e^{i\omega t} E_x \int_0^\infty \mathrm{d}t'\, e^{-i\omega t'} \sum_{i=1}^{N} q_i \dot{x}_i(t') \quad . \tag{3.30}$$

Berechnen wir mit dieser Verteilungsfunktion die elektrische Stromdichte, verschwindet der Gleichgewichtsterm, und wir erhalten:

$$\begin{aligned} \langle j_{el,x}(\omega)\rangle &= \frac{1}{V}\left\langle \sum_{j=1}^{N} q_j \dot{x}_j \right\rangle & (3.31)\\ &= \frac{1}{V k_B T}\int_0^\infty \mathrm{d}t'\, e^{-i\omega t'} \left\langle \sum_{i=1}^{N} q_i \dot{x}_i(t') \sum_{j=1}^{N} q_j \dot{x}_j \right\rangle_0 e^{i\omega t} E_x & (3.32)\\ &= \sigma_{xx}(\omega) e^{i\omega t} E_x \quad . & (3.33) \end{aligned}$$

Durch einen Koeffizientenvergleich mit dem Ohmschen Gesetz finden wir nach der Umbenennung $t' = t$ die Green-Kubo-Formel [102]:

$$\sigma(\omega) = \frac{1}{V k_B T}\int_0^\infty \mathrm{d}t\, e^{-i\omega t} \left\langle \sum_{i=1}^{N} q_i \dot{x}_i(t) \sum_{j=1}^{N} q_j \dot{x}_j(0) \right\rangle_0 \quad . \tag{3.34}$$

Kern dieses Ausdrucks ist eine Autokorrelationsfunktion der mikroskopischen elektrischen Ströme:[3]

$$J_{el,x}(t) = \sum_{i=1}^{N} q_i \dot{x}_i(t) = \sum_{i=1}^{N} q_i v_{x,i}(t) \tag{3.35}$$

im thermodynamischen Gleichgewichtsensemble, über deren Korrelationszeitraum integriert wird. Die Berechnung der weiteren Komponenten des Leitfähigkeitstensors erfolgt analog. In dreidimensionalen isotropen Systemen kann man eine Richtungsmittelung vornehmen und schreiben:

$$\sigma(\omega) = \frac{1}{3 V k_B T}\int_0^\infty \mathrm{d}t\, e^{-i\omega t} \left\langle \mathbf{J}_{el}(t) \cdot \mathbf{J}_{el}(0) \right\rangle_0 \quad . \tag{3.36}$$

---

[3] Laut Einheit ($[\mathbf{J}_{el}]$=Am) ist $\mathbf{J}_{el}$ streng genommen kein elektrischer Strom, aber es ist $\mathbf{j}_{el} = \mathbf{J}_{el}/V$ die physikalische Stromdichte mit $[\mathbf{j}_{el}]$=A/m^2.

3.3.2 Wärmeleitfähigkeit im Einkomponentensystem

Die Störung des Systems (Temperaturgradient) wird nicht durch ein externes Feld hervorgerufen, sondern sie ist nichtmechanisch. Der entsprechende Störanteil H_1 wird durch eine Betrachtung lokaler Inhomogenitäten in der Verteilungsfunktion erhalten [97, 101, 233]. Diese Inhomogenitäten können in der kanonischen Verteilung (3.26) wie folgt linearisiert werden:[4]

$$\begin{aligned} f_0(-\beta H_0) \to f_0\left(-\int \mathrm{d}^3\mathbf{r}\, \beta(\mathbf{r})\, h_0(\mathbf{r})\right) &\approx f_0\left(-\beta H_0 - \int \mathrm{d}^3\mathbf{r}\, h_0(\mathbf{r})\, \mathbf{r}\cdot\nabla\beta\right) && (3.37)\\ &\approx -f_0(-\beta H_0)\left(\mathbf{R}_E - \langle\mathbf{R}_E\rangle_0\right)\cdot\nabla\beta && (3.38)\\ &= f_0(-\beta H_0)\beta H_1 \quad , && (3.39)\end{aligned}$$

mit dem Energieschwerpunkt:

$$\mathbf{R}_E = \int \mathrm{d}^3\mathbf{r}\, h_0(\mathbf{r})\, \mathbf{r} \tag{3.40}$$

und der lokalen Energiedichte $h_0(\mathbf{r})$. Durch Vergleich findet man für die Störung:

$$H_1 = -\frac{1}{\beta}\left(\mathbf{R}_E - \langle\mathbf{R}_E\rangle_0\right)\cdot\nabla\beta \quad . \tag{3.41}$$

Als Hamiltonfunktion H_0 nehmen wir beispielsweise punktförmige Teilchen mit radialer Paarwechselwirkung an:

$$H_0 = \sum_{i=1}^{N}\varepsilon_i = \sum_{i=1}^{N}\left(\frac{\mathbf{p}_i^2}{2m_i} + \frac{1}{2}\sum_{\substack{j=1\\ j\neq i}}^{N} V_{ij}(r_{ij})\right) \quad . \tag{3.42}$$

Damit lässt sich der mikroskopische Energieschwerpunkt schreiben als:

$$\mathbf{R}_E = \sum_{i=1}^{N}\varepsilon_i\mathbf{r}_i = \sum_{i=1}^{N}\left(\frac{\mathbf{p}_i^2}{2m_i} + \frac{1}{2}\sum_{\substack{j=1\\ j\neq i}}^{N} V_{ij}(r_{ij})\right)\mathbf{r}_i \quad . \tag{3.43}$$

Aus diesem berechnet man mit einer Zeitableitung den Energiestrom:

$$\dot{\mathbf{R}}_E(t) = \mathbf{J}_E(t) = \sum_{i=1}^{N}\varepsilon_i(t)\mathbf{v}_i(t) + \frac{1}{2}\left(\sum_{\substack{i,j=1\\ j\neq i}}^{N}\mathbf{F}_{ij}(r_{ij}(t))\cdot\mathbf{v}_i(t)\right)\mathbf{r}_{ij}(t) \quad . \tag{3.44}$$

Damit lautet die Nichtgleichgewichtsverteilungsfunktion:

$$f(t) = f_0 + f_0 e^{i\omega t}\int_0^\infty \mathrm{d}t'\, e^{-i\omega t'}\mathbf{J}_E(t')\cdot\nabla\beta \quad . \tag{3.45}$$

---

[4] Konkret wird dies schon vor Gleichung (3.11) getan, sodass der entsprechende Kommutator bzw. die Poisson-Klammer richtig entsteht. Der Term $\sim \langle\mathbf{R}_e\rangle_0$ entsteht aus der Linearisierung der Zustandssumme, enthält aber keine dynamischen Variablen und verschwindet später bei der Zeitableitung.

Die Frequenzabhängigkeit ist üblicherweise uninteressant und wird nun auf $\omega = 0$ gesetzt. Den Wärmeleitfähigkeitstensor berechnet man über den Mittelwert der Wärmestromdichte $\mathbf{j}_Q$, die aufgrund von Massenschwerpunktserhaltung im Gleichgewichtsensemble mit der Energiestromdichte $\mathbf{j}_E$ übereinstimmt [43, 234]:

$$\begin{aligned} \langle \mathbf{j}_Q \rangle = \langle \mathbf{j}_E \rangle &= \frac{1}{V} \langle \mathbf{J}_E \rangle && (3.46) \\ &= -\frac{1}{V k_B T^2} \int\limits_0^\infty \mathrm{d}t \, \langle (\mathbf{J}_E(t) \cdot \nabla T) \mathbf{J}_E(0) \rangle_0 \quad . && (3.47) \end{aligned}$$

Durch Koeffizientenvergleich mit dem phänomenologischen Fourier-Gesetz (1.4) findet man den Wärmeleitfähigkeitstensor [233]:

$$\lambda = \frac{1}{V k_B T^2} \int\limits_0^\infty \mathrm{d}t \, \langle \mathbf{J}_E(t) \otimes \mathbf{J}_E(0) \rangle_0 \quad . \tag{3.48}$$

Ebenso funktioniert bei isotropen Systemen die Richtungsmittelung über die Diagonalkomponenten:

$$\lambda = \frac{1}{3 V k_B T^2} \int\limits_0^\infty \mathrm{d}t \, \langle \mathbf{J}_E(t) \cdot \mathbf{J}_E(0) \rangle_0 \quad . \tag{3.49}$$

Die Berechnung der Wärmeleitfähigkeit in Mehrkomponentensystemen ist komplexer, da auch die Massenströme der einzelnen Sorten berücksichtigt werden müssen, siehe z.B. [234, 235] sowie den Anhang von [130]. Des Weiteren lassen sich je nach konkreter physikalischer Situation bzw. konkretem experimentellen Aufbau unterschiedliche phänomenologische Gleichungen definieren, zu denen verschiedene Wärmeleitfähigkeiten gehören [43].

Dazu sei angemerkt, dass in der Literatur vielfach unterschiedliche (teilweise falsche) Definitionen von Wärme- und Energieströmen zu finden sind, die nicht miteinander übereinstimmen [235, 236], genauer gesagt sich durch linear addierte Massen- bzw. Teilchenstromterme unterscheiden, und so zu Unklarheiten führen. Die Wärmeleitfähigkeit λ aus einem Experiment im stationären Zustand, in dem alle Massenströme verschwunden sind und nur der Wärmestrom fließt (und nur diese Wärmeleitfähigkeit), ist jedoch invariant gegenüber solchen linearen Transformationen [43, 235].

3.3.3 Viskositäten

Der Störanteil der Hamiltonfunktion, der die Energieänderung durch irreversible mechanische Verformungen liefert [237], hat neun Komponenten und kann bei kleinen Verzerrungsraten $\nabla \otimes \mathbf{v}$ (äußere Störung) mithilfe der Betrachtung einer inhomogenen kinetischen Energiedichte $k(\mathbf{r}) = n(\mathbf{r}) m \mathbf{v}^2(\mathbf{r})/2$ und Linearisierung von $\mathbf{v}(\mathbf{r}) \to \mathbf{v} + \partial \mathbf{v}/\partial \mathbf{r} \cdot \mathbf{r}$ erhalten werden:

$$H_1 \approx \int \mathrm{d}^3\mathbf{r} \, n(\mathbf{r}) \, (\mathbf{r} \otimes \mathbf{p}) : (\nabla \otimes \mathbf{v}) = R_p : (\nabla \otimes \mathbf{v}) \quad , \tag{3.50}$$

wobei der Impulsschwerpunktstensor:

$$R_p = \int \mathrm{d}^3\mathbf{r}\, n(\mathbf{r})\, (\mathbf{r} \otimes \mathbf{p}) = \sum_{i=1}^{N} \mathbf{r}_i \otimes \mathbf{p}_i \tag{3.51}$$

die dynamischen Größen der Teilchen enthält. Seine Zeitableitung liefert über den Virialsatz [90] folgende Verbindung zum Drucktensor P [237]:

$$\dot{R}_p = \sum_{i=1}^{N} (m_i \mathbf{v}_i \otimes \mathbf{v}_i + \mathbf{r}_i \otimes \mathbf{F}_i) = (P - \langle P \rangle_0)\, V \quad . \tag{3.52}$$

Hierbei wurden die Kräfte $\mathbf{F}_i$ aufgrund des festgelegten endlichen Volumens in innere und äußere Anteile zerlegt. Aus letzteren entsteht der Gleichgewichtsterm $-\langle P \rangle_0$ [237, 238], während die inneren Kräfte zusammen mit dem kinetischen Term den Druck P im System ergeben. Damit findet man für die Zeitableitung von H_1 den aus der Nichtgleichgewichtsthermodynamik bekannten Ausdruck für die durch viskose Strömungen eingetragene Leistung [43]:

$$\dot{H}_1 = V \Pi : (\nabla \otimes \mathbf{v}) \quad , \tag{3.53}$$

wobei $\Pi = P - \langle P \rangle_0$ der viskose Drucktensor ist. Der Drucktensor des hydrostatischen Gleichgewichts $\langle P \rangle_0$ ist diagonal. Berechnet man mit der Nichtgleichgewichtsverteilung (3.28) für $\omega = 0$ komponentenweise die Mittelwerte von Π, so findet man die Newtonschen Gesetze, z.B. Gleichung (1.5), und durch Koeffizientenvergleich die Viskositäten. Für den Spannungstensor gilt dabei: $\tau = -P$ [44].

Aus den Nichtdiagonalkomponenten $\Pi_{xy} = \Pi_{yx}$, $\Pi_{yz} = \Pi_{zy}$ und $\Pi_{zx} = \Pi_{xz}$ folgt nach Richtungsmittelung die Scherviskosität:[5]

$$\eta = \frac{V}{3k_B T} \int_0^\infty \mathrm{d}t \sum_{n=xy,yz,zx} \langle \Pi_n(t) \Pi_n(0) \rangle_0 \quad . \tag{3.54}$$

Gleichermaßen folgt aus den Diagonalkomponenten Π_{xx}, Π_{yy} und Π_{zz} die longitudinale Viskosität η', die gegeben ist durch:

$$\eta' = \frac{V}{3k_B T} \int_0^\infty \mathrm{d}t \sum_{n=xx,yy,zz} \langle \Pi_n(t) \Pi_n(0) \rangle_0 \quad . \tag{3.55}$$

Die longitudinale Viskosität spielt eine wichtige Rolle bei der Schallabsorption [240] und beeinflusst zusammen mit der Scherviskosität die Dicke von Stoßwellenfronten in kompressiblen Fluiden [241, 242, 243].

---

[5] Obwohl der hydrostatische Gleichgewichtsdrucktensor $\langle P \rangle_0$ formal keine Nichtdiagonalkomponenten hat, ist dies in praktischen DFT-MD-Simulationen oft nicht exakt erfüllt, insbesondere bei Verwendung von asymmetrischen **k**-Punktsätzen wie dem Baldereschi-Punkt [239]. Daher ist es sinnvoll, diesen Term bei Berechnungen der Scherviskosität mit DFT-MD-Simulationen grundsätzlich mitzunehmen und so möglicherweise divergente Korrelationsfunktionen zu vermeiden.

3.3.4 Diffusionskoeffizienten

In Mehrkomponentensystemen führen Konzentrationsgradienten bzw. Gradienten in den chemischen Potentialen μ_a zu Diffusionsströmen. Die Hamiltonfunktion für diese Störung H_1 lässt sich im großkanonischen Ensemble durch gleichartige Betrachtungen wie bei der Berechnung der Wärmeleitfähigkeit direkt herleiten [97, 101]. Im kanonischen Ensemble funktioniert dies nicht so, aber es ist legitim, die Hamiltonfunktion um einen Anteil chemischer Energie zu erweitern (Eichfreiheit) und darin die Inhomogenitäten in $\mu_a(\mathbf{r})$ zu linearisieren:

$$\begin{aligned} H_1 = \sum_a \int \mathrm{d}^3\mathbf{r}\, \mu_a(\mathbf{r}) n_a(\mathbf{r}) &\approx \sum_a \mu_a N_a + \sum_a \nabla\mu_a \cdot \int \mathrm{d}^3\mathbf{r}\, n_a(\mathbf{r})\, \mathbf{r} && (3.56) \\ &= \sum_a \mu_a N_a + \sum_a \nabla\mu_a \cdot \mathbf{R}_a \quad . && (3.57) \end{aligned}$$

Bei der Zeitableitung verschwindet die mittlere chemische Energie, da sie keine dynamischen Variablen enthält.

Interdiffusion im Zweikomponentensystem

In einem Zweikomponentensystem mit den Sorten a und b kann man aus der Gibbsschen Fundamentalgleichung zusammen mit der Gibbs-Duhem-Gleichung bei konstantem Druck und konstanter Temperatur folgende Relation ableiten [43]:

$$N_b(\nabla\mu_b)_{P,T} = -N_a(\nabla\mu_a)_{P,T} \quad . \tag{3.58}$$

Damit vereinfacht sich die Zeitableitung der Hamiltonfunktion zu:

$$\dot{H}_1 = x_a\left(\frac{\dot{\mathbf{R}}_a}{x_a} - \frac{\dot{\mathbf{R}}_b}{x_b}\right) \cdot (\nabla\mu_a)_{P,T} \quad , \quad \text{mit} \quad \dot{\mathbf{R}}_a = \sum_{i=1}^{N_a} \mathbf{v}_i \tag{3.59}$$

und den Molenbrüchen x_a und x_b. Berechnet man mit der Nichtgleichgewichtsverteilung (3.28) bei $\omega = 0$ den Mittelwert des gegenläufigen Teilchenstromes:

$$\mathbf{J}_{ab} = x_a x_b \left(\frac{\dot{\mathbf{R}}_a}{x_a} - \frac{\dot{\mathbf{R}}_b}{x_b}\right) = x_b \sum_{i=1}^{N_a} \mathbf{v}_i - x_a \sum_{i=1}^{N_b} \mathbf{v}_i \quad , \tag{3.60}$$

so findet man die Maxwell-Stefan-Gleichung [45]:

$$\beta x_a d_{ab} (\nabla\mu_a)_{P,T} = \frac{x_a x_b}{N}\left(\frac{\dot{\mathbf{R}}_b}{x_b} - \frac{\dot{\mathbf{R}}_a}{x_a}\right) = \frac{-\mathbf{J}_{ab}}{N} \quad , \tag{3.61}$$

und durch Koeffizientenvergleich sowie Richtungsmittelung den Maxwell-Stefan-Diffusionskoeffizienten:

$$d_{ab} = \frac{1}{3N x_a x_b} \int_0^\infty \mathrm{d}t\, \langle \mathbf{J}_{ab}(t) \cdot \mathbf{J}_{ab}(0) \rangle_0 \quad . \tag{3.62}$$

Der Übergang zum experimentell zugänglichen Fickschen Diffusionskoeffizienten D_{ab} geschieht über die Relation [45]:

$$D_{ab} = d_{ab} Q = d_{ab} \frac{x_a}{k_B T} \left(\frac{\partial \mu_a}{\partial x_a} \right)_{P,T,x_b} \quad . \tag{3.63}$$

Für stark verdünnte Lösungen sowie ideale Mischungen ist der thermodynamische Faktor $Q = 1$, da:

$$\mu_a(P,T) = \mu_a(P_0,T_0) + k_B T \ln x_a \quad . \tag{3.64}$$

In Stoffen mit mehr als zwei Sorten sind die phänomenologischen Gleichungen für alle auftretenden Maxwell-Stefan-Diffusionskoeffizienten deutlich komplizierter [244, 245, 246]. Der Übergang zu den jeweiligen Fickschen Diffusionskoeffizienten erfolgt dann durch eine lineare Transformation, die jedoch nicht eindeutig umkehrbar ist [45, 247, 248].

Tracerdiffusion und Selbstdiffusion als Grenzfälle

Angenommen, es ist in einem Zweikomponentensystem nur ein einziges Teilchen der Sorte b vorhanden ($N_b = 1$). Damit sind $N \approx N_a$, $x_a \approx 1$ und $x_b \approx 1/N \ll x_a$ und auch $Q = 1$. Der Ausdruck für den gegenläufigen Teilchenstrom vereinfacht sich sofort zu:

$$\mathbf{J}_{ab}(t) = -\mathbf{v}_b(t) \quad . \tag{3.65}$$

Der daraus folgende Interdiffusionskoeffizient wird somit zum Tracer- bzw. Spurenstoffdiffusionskoeffizienten:

$$D_{ab}^{(T)} = \frac{1}{3} \int_0^\infty \mathrm{d}t \, \langle \mathbf{v}_b(t) \cdot \mathbf{v}_b(0) \rangle_0 \quad , \tag{3.66}$$

der allein durch eine Autokorrelationsfunktion der Geschwindigkeiten gegeben ist. Falls nun die Sorte b gleich der Sorte a ist, beschreibt die obige Gleichung die Selbstdiffusion für ein Teilchen der Sorte a:

$$D_{aa}^{(T)} = \frac{1}{3} \int_0^\infty \mathrm{d}t \, \langle \mathbf{v}_a(t) \cdot \mathbf{v}_a(0) \rangle_0 \quad . \tag{3.67}$$

Da alle Teilchen der Sorte a im Prinzip ununterscheidbar sind, kann man entsprechend mitteln und findet die bekannte Formel für die Selbstdiffusionskoeffizienten [163]:

$$D_a = \frac{1}{3N_a} \sum_{i=1}^{N_a} \int_0^\infty \mathrm{d}t \, \langle \mathbf{v}_i(t) \cdot \mathbf{v}_i(0) \rangle_0 \quad . \tag{3.68}$$

Aufgrund der statistischen Mittelung über alle Teilchen lassen sich Selbstdiffusionskoeffizienten mit deutlich höherer Genauigkeit berechnen als die anderen bisher vorgestellten Transportkoeffizienten. Die obige Green-Kubo-Formel lässt sich übrigens zu einer Reichweitenformel (Einstein-Formel) umformen, die statt der Geschwindigkeiten die quadratische

Bewegungsweite der Teilchen enthält [227]:

$$D_a = \lim_{t\to\infty} \frac{1}{6N_a t} \sum_{i=1}^{N_a} \left\langle (\mathbf{r}_i(t) - \mathbf{r}_i(0))^2 \right\rangle_0 \quad . \tag{3.69}$$

Äquivalente Ausdrücke gibt es auch für die anderen Green-Kubo-Formeln [238].

Darken-Relation und Nernst-Einstein-Formel

Mithilfe von Selbstdiffusionskoeffizienten lassen sich Näherungsformeln für einige weitere Transportkoeffizienten angeben, indem man die Kreuzkorrelationen zwischen verschiedenen Teilchen vernachlässigt. Für den Interdiffusionskoeffizienten (3.63) einer zweikomponentigen idealen Mischung ($Q = 1$) findet man so die Darken-Relation [245, 249]:

$$D_{ab}^{(D)} = x_b D_a + x_a D_b \quad . \tag{3.70}$$

Genauso erhält man aus der elektrischen Gleichstromleitfähigkeit (3.36) die Nernst-Einstein-Formel für verdünnte Elektrolyte [250]:

$$\sigma^{(NE)} = \sum_a \frac{q_a^2 N_a D_a}{V k_B T} \quad . \tag{3.71}$$

3.4 Weitere Anmerkungen zur LRT

Neben den bislang betrachteten Transportkoeffizienten, die sich aus Autokorrelationsfunktionen von Strömen bzw. Drücken berechnen, sind auch Kreuzeffekte [43] auf die gleiche Art und Weise herleitbar. Von praktischer Bedeutung sind davon vor allem die Thermokraft und die Thermodiffusionskoeffizienten in Mehrkomponentensystemen. Die zugehörigen Formeln enthalten entsprechende Kreuzkorrelationsfunktionen zweier verschiedener Ströme [233]. Auch Ausdrücke für magnetische Transportkoeffizienten wie dem Hall-Widerstand lassen sich mithilfe der LRT gewinnen [251, 252]. Optische Eigenschaften sind aus der frequenzabhängigen Leitfähigkeit berechenbar [134, 159].

Weiterhin besteht eine Verbindung der LRT zum hydrodynamischen Grenzfall des dynamischen Strukturfaktors $S(\mathbf{k}, \omega)$ [250], aus welchem prinzipiell die gleichen in diesem Kapitel vorgestellten Transportkoeffizienten berechnet werden können. Für Systeme mit kleinen Teilchenzahlen, wie sie in DFT-MD-Simulationen praktisch handhabbar sind, ist die Berechnung des Grenzfalls $\mathbf{k} \to 0$ von $S(\mathbf{k}, \omega)$ jedoch schwierig, sodass in der Praxis den LRT-Ausdrücken der Vorzug gegeben wird.

In der DFT-MD-Simulationsmethode werden die Elektronen als quantenmechanische und die Ionen als klassische Teilchen betrachtet, deren Dynamik durch die Born-Oppenheimer-Näherung zeitlich voneinander getrennt wird. Damit werden bei der Auswertung der LRT-Formeln für elektrische und Wärmeleitfähigkeit sowie Viskosität zwangsläufig die zeitlichen Korrelationen zwischen Elektronen- und Ionenbewegung vernachlässigt. Darüber hinaus bedeutet die Beschreibung der Elektronen mit DFT eine rein statische Betrachtungsweise dieser

Teilchensorte. Prinzipiell ließen sich diese Probleme mit zeitabhängiger DFT [253, 254] umgehen. Jedoch sind die Zeiträume, die damit simulierbar sind, um Größenordnungen zu klein, als dass eine für die Auswertung der LRT-Korrelationsfunktionen ausreichende Konvergenz der Elektron-Ionen-Dynamik erreicht wird.

Im Rahmen der hier verwendeten DFT-MD ist es dennoch möglich, elektronische und ionische Anteile zum elektrischen Strom, Wärmestrom und zum Drucktensor sinnvoll zu definieren, sodass sich entsprechend additive Beiträge zu den Transportkoeffizienten berechnen lassen, z.B. $\sigma = \sigma_e + \sigma_i$. Die folgenden Kapitel 4 und 5 befassen sich jeweils mit der konkreten Berechnung dieser Beiträge von Elektronen bzw. Ionen und enthalten genauere Erläuterungen dazu.

Kapitel 4

Elektronische Transportkoeffizienten

In WDM liefern frei bewegliche Elektronen aufgrund des oftmals hohen Ionisationsgrades wichtige Beiträge zur elektrischen und zur Wärmeleitfähigkeit. Die Viskosität wird hingegen kaum von freien Elektronen beeinflusst, da die schwereren Ionen grundsätzlich für den Hauptteil des Impulstransports verantwortlich sind, der den mechanischen Reibungswiderstand ausmacht [255]. Die Berechnung der elektronischen Beiträge zur elektrischen Leitfähigkeit σ_e, Wärmeleitfähigkeit λ_e und zur Thermokraft α_e mithilfe der DFT-MD-Methode ist Gegenstand der folgenden Abschnitte.

4.1 Kubo-Greenwood-Formalismus

In der DFT-MD befindet sich das Elektronensystem zu jedem Zeitschritt der MD in einem thermischen Gleichgewichtszustand im Schwerpunktsystem der Ionen und ist durch die Kohn-Sham-Zustände $|\mathbf{k}\nu\alpha\rangle$ und die Eigenwerte $E_{\mathbf{k}\nu\alpha}$ charakterisiert. Die Berechnung der elektronischen Transportkoeffizienten geschieht mithilfe der LRT, wobei quantenstatistische Strom-Strom-Korrelationsfunktionen (3.22) mit den Operatoren des elektrischen Stromes bzw. des Wärmestromes ausgewertet werden müssen.

Detailliertere Informationen hierzu befinden sich im Kapitel 3 aus dem Artikel [125]: „Electronic transport coefficients from ab initio simulations and application to dense liquid hydrogen“ von B. Holst, M. French und R. Redmer, Phys. Rev. B **83**, 235101 (2011), siehe auch Anhang I.
Eigener Anteil: Mitarbeit an den analytischen Herleitungen, bei der Diskussion der Ergebnisse und beim Schreiben des Artikels.

Die Herleitungen in [125] führen zu folgenden Realteilen der Onsager-Koeffizienten:

$$\begin{aligned} L_n(\omega) &= \frac{\pi q_e^{2-n}}{3V\omega} \sum_{\mathbf{k}\nu\mu\alpha} |\langle \mathbf{k}\nu\alpha|\hat{\mathbf{v}}|\mathbf{k}\mu\alpha\rangle|^2 (f_{\mathbf{k}\nu\alpha} - f_{\mathbf{k}\mu\alpha}) \\ &\cdot \left(\frac{E_{\mathbf{k}\mu\alpha} + E_{\mathbf{k}\nu\alpha}}{2} - h_e\right)^n \delta(E_{\mathbf{k}\mu\alpha} - E_{\mathbf{k}\nu\alpha} - \hbar\omega) \quad , \end{aligned} \tag{4.1}$$

mit der Enthalpie pro Elektron $h_e = \mu_e + Ts_e$. Die Matrixelemente mit dem Geschwindigkeitsoperator $\langle \mathbf{k}\nu\alpha|\hat{\mathbf{v}}|\mathbf{k}\mu\alpha\rangle$ werden aus den von VASP intern berechneten Matrixelementen des Ortsoperators [256] über $\langle \mathbf{k}\nu\alpha|\hat{\mathbf{v}}|\mathbf{k}\mu\alpha\rangle = i(E_{\mathbf{k}\nu\alpha} - E_{\mathbf{k}\mu\alpha})\langle \mathbf{k}\nu\alpha|\hat{\mathbf{r}}|\mathbf{k}\mu\alpha\rangle/\hbar$ berechnet, die ausgelesen werden können.[1] Die Onsager-Koeffizienten gehören zu folgenden phänomenologischen Gleichungen:[2]

$$\mathbf{j}_{el} = L_0\mathbf{E}_e - \frac{L_1}{T}\nabla T = \sigma_e\mathbf{E}_e - \sigma_e\alpha_e\nabla T \quad , \tag{4.2}$$

$$\mathbf{j}'_Q = L_1\mathbf{E}_e - \frac{L_2}{T}\nabla T = T\sigma_e\alpha_e\mathbf{E}_e - \left(\lambda_e + T\sigma_e\alpha_e^2\right)\nabla T \quad , \tag{4.3}$$

mit der elektrochemischen Feldstärke $\mathbf{E}_e = \mathbf{E} - (\nabla\mu_e)_{P,T}/q_e$ und der verallgemeinerten Wärmestromdichte $\mathbf{j}'_Q = \mathbf{j}_Q - h_e\mathbf{j}_{el}/q_e$. Somit sind die gesuchten elektronischen Transportkoeffizienten wie folgt durch die Onsagerkoeffizienten (4.1) ausdrückbar:[3]

$$\sigma_e(\omega) = L_0(\omega) \quad , \quad \alpha_e(\omega) = \frac{L_1(\omega)}{TL_0(\omega)} \quad , \quad \lambda_e(\omega) = \frac{1}{T}\left(L_2(\omega) - \frac{L_1^2(\omega)}{L_0(\omega)}\right) \quad . \tag{4.4}$$

Der für die Berechnung der Gleichstromwerte wichtige Grenzwert $\omega \to 0$ lässt sich formal ausführen, wodurch die bekannten Kubo-Greenwood- [229] bzw. Chester-Thellung-Formeln [258] entstehen. Aufgrund der endlichen Teilchenzahl bzw. des endlichen Simulationsvolumens sind diese Grenzwertformeln jedoch in der Praxis nicht auswertbar, da der minimale Abstand zwischen allen berechneten Energieeigenwerten $E_{\mathbf{k}\mu\alpha}$ endlich ist, wodurch unterhalb einer gewissen Frequenz keine Werte mehr für die Transportkoeffizienten (4.1) berechenbar sind. Stattdessen werden sie mit einer zur Gauß-Funktion[4] leicht verbreiterten δ−Funktion frequenzabhängig berechnet und die noch sinnvollen Werte bei kleinen Frequenzen zu $\omega \to 0$ extrapoliert. Durch sorgfältige Konvergenzuntersuchungen bezüglich der Wahl dieses Verbreiterungsparameters und der in der Simulation verwendeten Teilchenzahl lassen sich so

---

[1] Dies funktioniert so nur für die nichtdiagonalen Matrixelemente. Allerdings werden die diagonalen Matrixelemente (Elektronengeschwindigkeiten) nicht gebraucht, da sie in Gleichung. (4.1) nicht beitragen. Die Matrixelemente der `OPTIC`-Datei aus früheren VASP-Versionen [257] funktionieren auch, sollten aber nicht benutzt werden, wenn Hybridfunktionale oder PAW-Pseudopotentiale [206, 207] mit Projektoren für Drehimpulse $l > 2$ verwendet werden, da die zugehörigen nichtlokalen Anteile darin nicht berechnet werden.

[2] Die entsprechenden Gleichungen (1) und (2) in [125] sind nicht korrekt.

[3] In Rechnungen mit anisotropen Simulationszellen muss die Tensorstruktur der L_n bei den Multiplikationen entsprechend beachtet werden [129].

[4] In den Herleitungen tritt formal eine Lorentz-Funktion statt einer Gauß-Funktion auf, aber für die numerische Auswertung ist dies unerheblich.

numerisch konvergierende Gleichstromwerte berechnen. Die statistischen Mittelwerte für σ_e, α_e und λ_e werden letztendlich durch Mittelung über ca. 10-100 LRT-Rechnungen mit verschiedenen Ionenkonfigurationen aus einer DFT-MD-Simulation im thermischen Gleichgewicht gewonnen.

Physikalisch gesehen bestimmen die Wechselwirkungen (z. B. Streuprozesse) der Elektronen mit den Ionen und anderen Elektronen die Leitfähigkeit. Die Wechselwirkung mit den Ionen ist in der DFT nahezu exakt berücksichtigt, wobei aufgrund der Born-Oppenheimer-Näherung allerdings kein Impulsübertrag auf die Ionen stattfindet und somit keine Phononenanregungen oder dynamischen Abschirmungseffekte [259, 260] auftreten können. Die Wechselwirkungen der Elektronen untereinander werden indirekt durch den Hartree-Term und das Austausch- und Korrelationsfunktional beschrieben. Die in Gleichung (4.1) enthaltene Stoßkinematik entspricht jedoch der von adiabatischen Elektron-Ion-Stößen in dem effektiven Kohn-Sham-Potential (2.12). Somit ist keine Elektron-Elektron-Stoßkinematik [105] an sich enthalten. Elektron-Elektron-Stöße ändern zwar nicht den Gesamtimpuls (und damit auch nicht den transportierten Nettoladungsstrom) beider Stoßpartner, wohl aber deren Nettoenergiestrom [261]. Des Weiteren verändern Elektron-Elektron-Stöße die Geschwindigkeitsverteilung der Elektronen und haben somit einen indirekten Effekt auf die stattfindenden Elektron-Ion-Stöße [99, 261, 262]. Der Einfluss der Elektron-Elektron-Wechselwirkungen ist im nichtentarteten Grenzfall am größten und verschwindet aufgrund des Pauli-Verbots im entarteten Grenzfall [105].

Nachtrag Juni 2022: Inzwischen wurde in zwei Arbeiten [263] und [264] gezeigt, dass die DFT im Rahmen des Kubo-Greenwood-Formalismus keine Elektron-Elektron-Stöße erfasst. Frühere DFT-Rechnungen hierzu von Desjarlais *et al.* [261] waren nicht konvergiert und ergaben daher zu niedrige Werte für die elektrische und die Wärmeleitfähigkeit [264].

Inwieweit mit den Gleichungen (4.1) die Beiträge chemischer Ionisationsreaktionen zur Wärmeleitfähigkeit [265, 266, 267] korrekt erfasst werden, ist hingegen noch nicht klar. Im Vergleich mit experimentellen Messungen zeigen mit DFT-MD-Simulationen berechnete Transportkoeffizienten flüssiger und fester Metalle [53, 126, 127, 142, 268, 269, 270] jedoch eine gute Übereinstimmung, wie in den beiden folgenden Abschnitten gezeigt werden wird.

4.2 Thermoelektrische Transportkoeffizienten von Molybdän

Das gut leitende Refraktärmetall Molybdän ist aufgrund seiner technologischen Bedeutung und des einfachen Phasendiagramms mit nur einer bekannten Festkörperphase (kubisch raumzentriertes Ionengitter) ein hervorragender Kandidat für die Anwendung der DFT-MD-Methode. Der konkrete Hintergrund für diese Rechnungen war dessen geplanter Einsatz als Treibermaterial an der Z-Maschine der Sandia National Laboratories für neuartige Messungen der Fließgrenze von dynamisch komprimierten Feststoffen [271]. Hierfür wurden genaue Werte für die elektrische Leitfähigkeit von Molybdän im Mbar-Bereich benötigt.

Detailliertere Informationen hierzu befinden sich im Artikel [126]: „Thermoelectric transport coefficients of molybdenum from ab initio simulations“ von M. French und T. R. Mattsson, Phys. Rev. B **90**, 165113 (2014), siehe auch Anhang II.
Eigener Anteil: Durchführung der Berechnungen. Hauptsächliche Diskussion der Ergebnisse und Schreiben des Artikels.

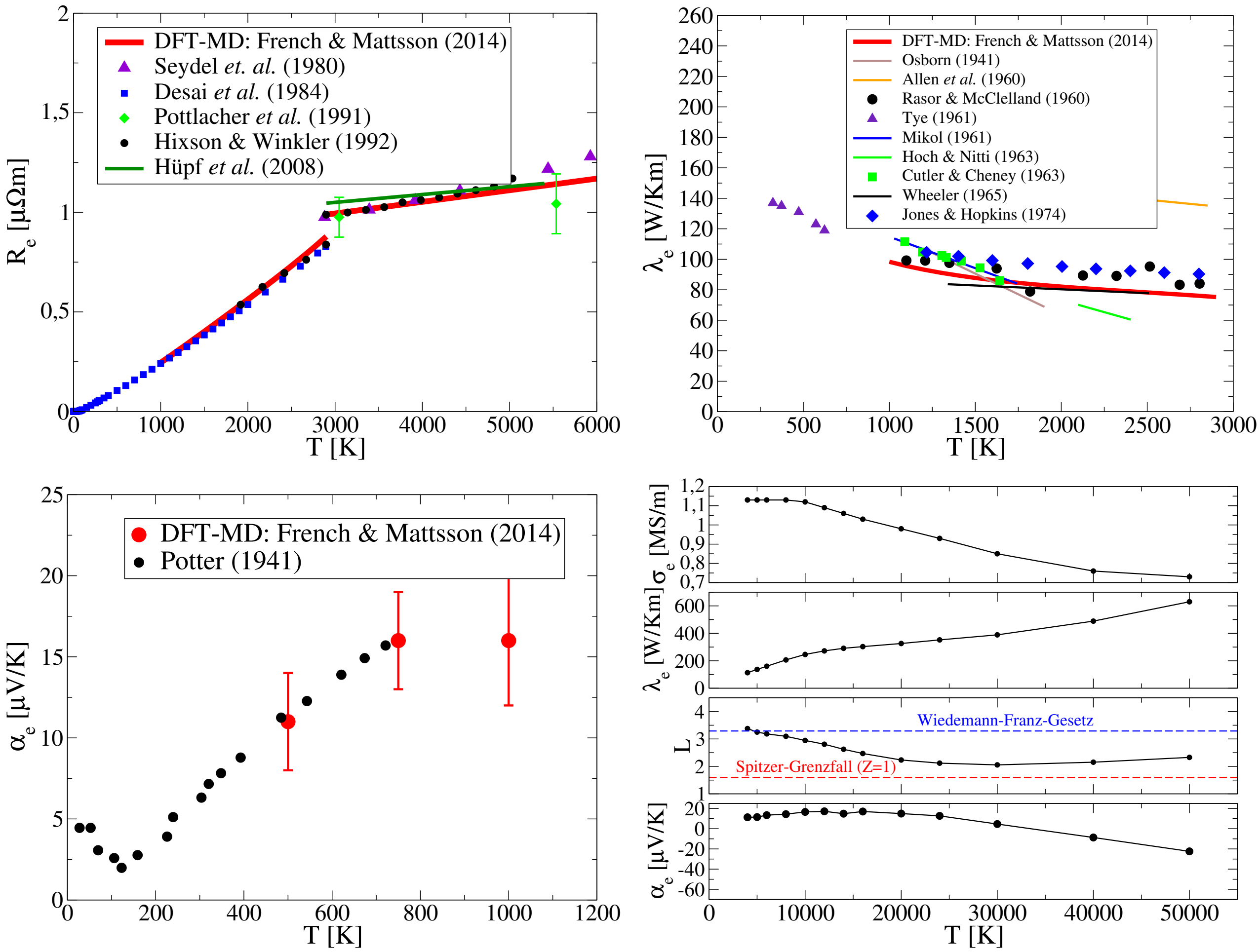

Abbildung 4.1: Mit DFT-MD berechneter spezifischer Widerstand $R_e = \sigma_e^{-1}$ (links oben), Wärmeleitfähigkeit λ_e (rechts oben) und Thermokraft α_e (links unten) von Molybdän im Vergleich mit Experimenten. Selbige thermoelektrische Transportkoeffizienten einschließlich der Lorenz-Zahl L, siehe Gleichung (1.6), entlang der 10 g/cm^3-Isochore (rechts unten). Alle Bilder wurden [126] entnommen und angepasst.

Im Zuge der ausführlichen numerischen Untersuchungen wurden σ_e, λ_e und α_e von Molybdän mit vorhanden experimentellen Datensätzen verglichen, siehe Abbildung 4.1. Hierbei wurde eine sehr gute Übereinstimmung zwischen den DFT-MD-Ergebnissen und den Experimenten für sowohl die Festkörperphase als auch die Flüssigkeit erzielt. Besonders bemerkenswert ist hierbei, dass die DFT-MD auch das positive Vorzeichen der Thermokraft von festem Molybdän reproduziert. Dies deutet darauf hin, dass die komplizierte elektronische Struktur von Molybdän durch DFT akkurat wiedergegeben wird. In Plasmen mit unkorrelierter Elektronenstruktur ist die Thermokraft negativ, bzw. sie verschwindet im vollständig entarteten Elektronengas ganz [104].

In Abbildung 4.1 sind auch die berechneten Transportkoeffizienten von Molybdänplasma entlang einer Isochore bei etwa Normaldichte gezeigt, in der man die für Metalle typische Abnahme der elektrischen Leitfähigkeit bei zunehmender Temperatur erkennt. Die Lorenz-Zahl sinkt ausgehend von dem Wiedemann-Franz-Grenzwert von $L = \pi^2/3$ mit der Temperatur, erreicht jedoch nicht den Spitzer-Grenzwert [104, 262] für einfach ionisierte Plasmen. Dies ist plausibel, da das Plasma noch teilweise entartet ist und außerdem innere Elektronen ionisiert werden können. Das Vorzeichen der Thermokraft kehrt sich bei ca. 30 000 K um und bleibt bei hohen Temperaturen erwartungsgemäß negativ.

4.3 Elektrische und Wärmeleitfähigkeit von flüssigem Eisen

Als Hauptbestandteil des Erdkerns ist Eisen von herausragender geophysikalischer Bedeutung. Das Verständnis der Magnetfelderzeugung mit dem Geodynamo erfordert genaue Kenntnisse über die elektrische und die Wärmeleitfähigkeit von festem und flüssigem Eisen in WDM-Zuständen, die bislang nicht experimentell zugänglich sind. Diese Transportgrößen wurden von zwar schon von anderen Autoren mit der DFT-MD-Methode berechnet [272, 273, 274], aber die von ihnen gefundene Abweichung zu gemessenen Referenzwerten bei Normalbedingungen war unzufriedenstellend. Hier konnte die damals vernachlässigte selbstkonsistene Betrachtung des Elektronenspins in der DFT-MD als Ursache für diese Abweichungen ausgemacht werden.

Detailliertere Informationen hierzu befinden sich im Artikel [127]: „Paramagnetic-to-Diamagnetic Transition in Dense Liquid Iron and Its Influence on Electronic Transport Properties“ von J.-A. Korell, M. French, G. Steinle-Neumann und R. Redmer, Phys. Rev. Lett. **122**, 086601 (2019), siehe auch Anhang III.
Eigener Anteil: Mitarbeit bei der Durchführung der Berechnungen, bei der Diskussion der Ergebnisse und beim Schreiben des Artikels.

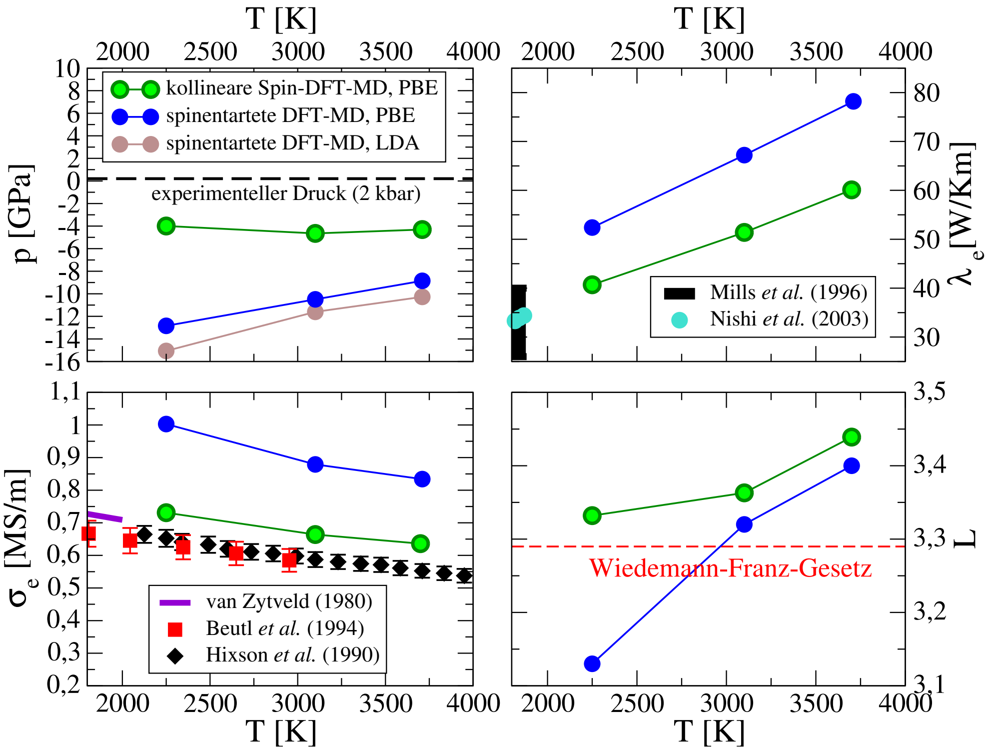

Abbildung 4.2: Mit DFT-MD berechneter Druck (links oben), elektrische Leitfähigkeit σ_e (links unten), Wärmeleitfähigkeit λ_e (rechts oben) und Lorenz-Zahl (rechts unten) für Dichten entlang der experimentell vermessenen 2 kbar-Isobare im Vergleich zu den gemessenen Werten. Alle Bilder wurden [127] entnommen und angepasst.

Mit kollinearen Spin-DFT-MD-Simulationen[5] kann das Auftreten von atomaren Paramagnetismus im flüssigen Eisen in guter Näherung erfasst werden. Die Abbildung 4.2 zeigt, dass Druck, elektrische und Wärmeleitfähigkeit mit Berücksichtigung des Spins in der DFT im Vergleich mit den Messungen an flüssigem Eisen deutlich genauer berechnet werden als mit der spinentarteten Variante. Die Reduzierung der Leitfähigkeiten kann hauptsächlich durch die Erhaltung der Spinausrichtung bei der Elektronenstreuung erklärt werden, die in die Matrixelemente $\langle \mathbf{k}\nu\alpha|\hat{\mathbf{v}}|\mathbf{k}\mu\alpha\rangle$ eingeht.

Weiterführende Berechnungen zeigten, dass der Paramagnetismus in flüssigem Eisen mit steigender Temperatur und steigendem Druck schwächer wird und zwischen 20 und 50 GPa schließlich verschwindet. Bei Erdkernbedingungen spielt der Magnetismus von Eisen folglich keine Rolle mehr, und die mit spinentarteter DFT-MD berechneten Leitfähigkeitswerte [272, 273, 274] sollten für geophysikalische Anwendungen brauchbar sein.

---

[5] Die kollineare Näherung bedeutet, dass der Vektor der Magnetisierungsdichte an jedem Ort immer in die gleiche Richtung zeigt, d.h. $\mathbf{m}(\mathbf{r}) = (0, 0, m(\mathbf{r}))$. In nicht kollinearen Rechnungen wird diese Einschränkung nicht gemacht, aber die numerische Konvergenz der Kohn-Sham-Gleichungen ist in ungeordneten Systemen mit der nicht kollinearen Variante der DFT-MD extrem schwierig zu erreichen. Selbst in der nicht kollinearen Beschreibung können nichtadiabatische Elektron-Magnon-Streuprozesse [275, 276] nicht erfasst werden.

Die Bedeutung der Leitfähigkeit von Eisen auf das Kühlverhalten und die Magnetfelderzeugung im Erdkern bleibt dennoch Gegenstand aktueller Forschungen. Magnetohydrodynamische Modelle des Erdkerns ergeben, dass die berechnete Wärmeleitfähigkeit möglicherweise zu hoch ist, sodass die für den Dynamo notwendige Konvektion durch Wärmeleitung unterbunden werden könnte [277, 278]. Das Verstehen der Löslichkeit von leichteren und schweren Elementen in dem eisenreichen Erdkern und ihr Einfluss auf dessen Transporteigenschaften könnte hier weitere Erkenntnisse zur Erforschung des Geodynamos liefern [279].

4.4 Thermoelektrische Transportkoeffizienten von warmem dichtem Wasserstoff

Wasserstoff ist als einfachstes Element des Periodensystems das Paradebeispiel der Plasmaphysik und wegen seiner großen Häufigkeit im Universum von herausragender Bedeutung, so als Hauptbestandteil von Sternen, Braunen Zwergen und von Gasplaneten wie Jupiter und Saturn. Der erste konsistent mit DFT-MD berechnete dichte- und temperaturabhängige Datensatz für die thermoelektrischen Transportkoeffizienten von Wasserstoffplasma wird nun vorgestellt.

Detailliertere Informationen hierzu befinden sich den Kapiteln 1, 2, 4 und 5 aus dem Artikel [125]: „Electronic transport coefficients from ab initio simulations and application to dense liquid hydrogen“ von B. Holst, M. French und R. Redmer, Phys. Rev. B **83**, 235101 (2011), siehe auch Anhang I.
Eigener Anteil: Mitarbeit an den analytischen Herleitungen, bei der Diskussion der Ergebnisse und beim Schreiben des Artikels.

Die Abbildung 4.3 zeigt die thermoelektrischen Transportkoeffizienten von Wasserstoffplasma in Abhängigkeit von Dichte und Temperatur. Klar zu erkennen ist das Auftreten thermischer Ionisation bei kleinen Dichten, die die Leitfähigkeiten ansteigen lässt. Der Effekt der Druckionisation unterhalb von 1 g/cm^3 führt zum abrupten Anstieg in der Leitfähigkeit mit der Dichte und zur Metallisierung, was deutlich an der Umkehr der temperaturabhängigkeit von σ_e zu sehen ist. Dieser Metall-Nichtmetall-Übergang ist noch immer Gegenstand lebhafter Diskussionen [280, 281, 282, 283, 284]. Die genaue Berechnung seiner Lage mit DFT-MD-Simulationen ist stark abhängig vom verwendeten Austausch- und Korrelationsfunktional [153, 182, 285, 286]. In DFT-MD- und Quanten-Monte-Carlo-Simulationen ist er ähnlich wie in chemischen Modellen von einer thermodynamischen Instabilität begleitet [153, 182, 285, 286, 287], jedoch nur in einem sehr engen (in Abbildung 4.3 nicht aufgelöstem) Dichtebereich und unterhalb einer relativ niedrigen kritischen Temperatur von ca. 2000 K. Bezüglich seiner Lage im Phasendiagramm widersprechen sich auch die wenigen bisher gemachten Experimente [64, 281, 282, 288].

Bei hohen Dichten reproduziert die DFT-MD-Methode den bekannten Grenzfall für die Thermokraft ($\alpha_e = 0$) [91] sowie das Wiedemann-Franz-Gesetz. Die bei kleinen Dichten auftretenden starken Abweichungen der Lorenz-Zahl vom Wiedemann-Franz-Gesetz zeigen, dass

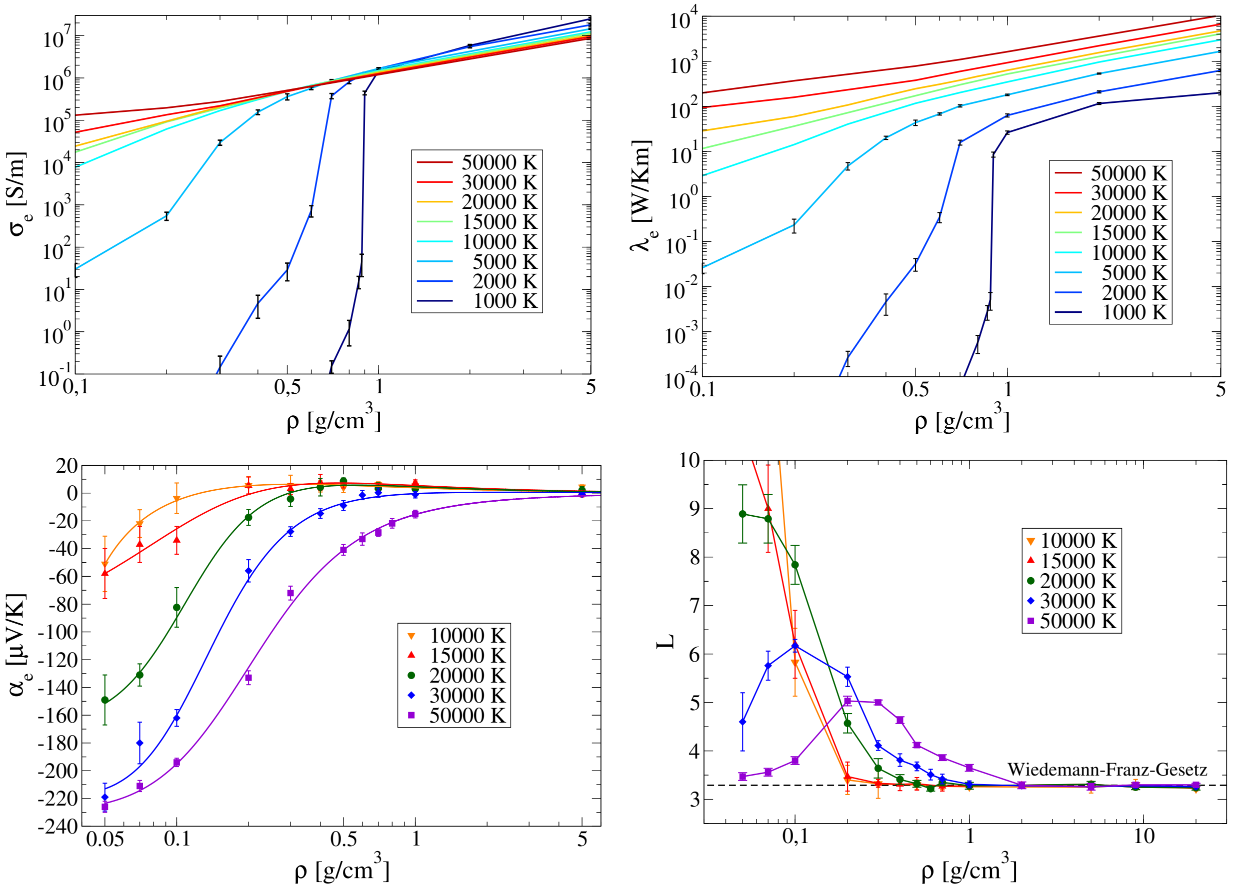

Abbildung 4.3: Mit DFT-MD berechnete elektrische Leitfähigkeit σ_e (links oben), Wärmeleitfähigkeit λ_e (rechts oben), Thermokraft α_e (links unten) und Lorenz-Zahl (rechts unten) von Wasserstoffplasmen. Alle Bilder wurden [125] entnommen und angepasst.

diese einfache Relation im nichtmetallischen Bereich nicht anwendbar ist. Der mit abnehmender Dichte und zunehmender Temperatur stark steigende Rechenaufwand für die DFT-MD-Simulationen macht eine ähnliche Untersuchung der Grenzfälle im nichtentarteten Bereich leider sehr schwierig.

4.5 Elektronische Leitfähigkeiten des Wasserstoff-Helium-Gemisches in Jupiter

Mit der erstmaligen Verfügbarkeit von DFT-MD-Zustandsgleichungsdatensätzen für Wasserstoff und Helium wurden große Fortschritte bei Modellierung des inneren Aufbaus des Planeten Jupiter erzielt [289, 290], da diese Zustandsgleichungen nun nicht mehr auf chemische Ionisationsmodelle für Wasserstoff-Helium-Plasmen angewiesen waren. Als konsistente Ergänzung dieser Strukturmodelle sind zusätzlich zu den thermodynamischen Eigenschaften auch die mit DFT-MD zugänglichen Transportgrößen entlang des Planetenprofils von großem Interesse. Insbesondere wird der Verlauf der elektrischen Leitfähigkeit für die direkte Anwendung in magnetohydrodynamischen Simulationen des Jupiterdynamos benötigt, da er entscheidenden Einfluss auf Form und Stärke des erzeugten Magnetfeldes hat.

Detailliertere Informationen hierzu befinden sich im Artikel [132]: „Ab Initio Simulations For Material Properties Along The Jupiter Adiabat“ von M. French, A. Becker, W. Lorenzen, N. Nettelmann, M. Bethkenhagen, J. Wicht und R. Redmer, Astrophys. J. Suppl. Ser. **202**, 5 (2012), siehe auch Anhang IV.
Eigener Anteil: Hauptsächliche Berechnung der Transporteigenschaften. Mitarbeit bei der Diskussion der Ergebnisse und beim Schreiben des Artikels.

Das in Abbildung 4.4 dargestellte elektrische Leitfähigkeitsprofil entlang der Jupiteradiabate zeigt im stark ionisierten Inneren nur eine schwache Abnahme nach außen hin. Erst bei ca. 0,9 Jupiterradien R_J setzt vermehrt die Atom- und Molekülbildung ein, die den sehr starken Abfall der Leitfähigkeit im äußeren Bereich verursacht. Im Fall der Wärmeleitfähigkeit sinkt der elektronische Beitrag dort unter den der schweren Teilchen ab, die die Wärme im äußeren Bereich durch Atom- und Molekülstöße transportieren.

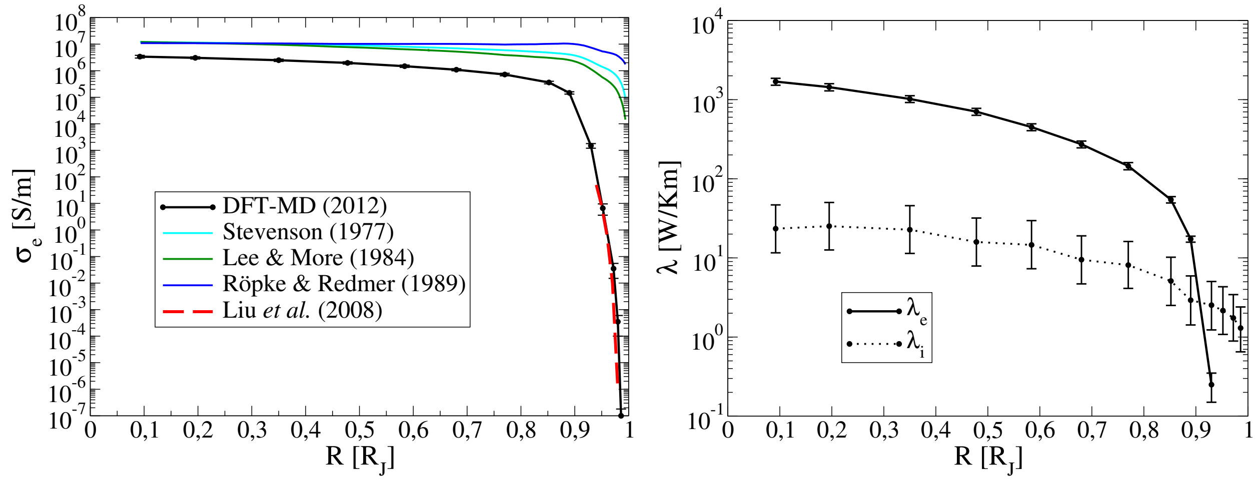

Abbildung 4.4: Mit DFT-MD berechnete elektrische Leitfähigkeit σ_e (links) und Wärmeleitfähigkeit λ_e (rechts) im Inneren von Jupiter im Vergleich zu früheren Modellen für reinen Wasserstoff und einem Ionisationsmodell für die äußere Schicht [291]. Für die Wärmeleitfähigkeit wurde hier auch der Beitrag der schweren Teilchen λ_i ähnlich wie in Kapitel 5.2 abgeschätzt, allerdings mit vereinfachten Kraftfeldern (aus Invertierung der Hochtemperaturnäherung für die ionischen Paarverteilungsfunktionen) [132]. Alle Bilder wurden [132] entnommen und angepasst.

Die der DFT-MD zugrundeliegende elektronische Strukturbeschreibung erfasst den Einfluss von Dissoziation und Ionisation auf die Leitfähigkeit deutlich genauer, als es Ionisations- und Leitfähigkeitsmodelle im „chemischen Bild“ vermögen, da Bindungs- und Streuzustände auf gleichem Niveau beschrieben werden und keine Trennung zwischen diesen erfolgen muss. Darüber hinaus stellt die Möglichkeit, das reale Wasserstoff-Helium-Gemisch direkt und ohne weitere Näherungen in der Mehrkomponentenbeschreibung zu simulieren, einen großen Vorteil der DFT-MD-Methode dar.

Das berechnete elektrische Leitfähigkeitsprofil wurde inzwischen in mehreren magnetohydrodynamischen Simulationen verwendet, in denen das dipolare Magnetfeld sowie teilweise die Struktur der zonalen Winde in Jupiter im Einklang mit Beobachtungsdaten reproduziert werden konnten [292, 293, 294, 295, 296]. Aus der intensiven Kollaboration mit Magnetfeldmodellierern im Rahmen des DFG-SPP „Planetarer Magnetismus“ entstand ein Buchkapitel [297], in dem diese Fortschritte ausführlicher dokumentiert sind. Die genauere Vermessung des Jupiter-Magnetfeldes durch die Juno-Mission [298, 299] zeigt allerdings auch, dass das Magnetfeld komplexer ist als vorher bekannt war, sodass eine weitere Verfeinerung der bisherigen Struktur- und Magnetfeldmodelle von Jupiter auch in Zukunft notwendig sein wird.

4.6 Elektronische Transportkoeffizienten von Wasserplasmen

Neben Wasserstoff und Helium kommt Wasser als dritthäufigster Stoff im Universum eine enorme Bedeutung in der Planetenphysik zu [300]. Das Verständnis der Leitfähigkeit von Wasserplasmen über einen großen Dichte- und Temperaturbereich ist insbesondere wichtig für die wasserreichen Planeten Neptun und Uranus, welche besonders komplizierte (multipolare) Magnetfeldgeometrien haben [47, 48, 301]. Ebenso kann die Wärmeleitfähigkeit des planetaren Plasmas einen Einfluss auf das Abkühlverhalten dieser Planeten haben [50, 302].

Detailliertere Informationen hierzu befinden sich im Artikel [129]: „Electronic transport in partially ionized water plasmas“ von M. French und R. Redmer, Phys. Plasmas **24**, 092306 (2017), siehe auch Anhang V.
Eigener Anteil: Berechnung der Transportgrößen mit DFT-MD. Hauptsächliche Ausarbeitung des MCCM, Diskussion der Ergebnisse und Schreiben des Artikels.

Die mit DFT-MD-Simulationen berechnete elektrische und Wärmeleitfähigkeit von Wasserplasmen ist in Abbildung 4.5 dargestellt. Beide Größen zeigen ein ähnliches Dichte-Temperatur-Verhalten wie reiner Wasserstoff (Abbildung 4.3). Allerdings sind die Zahlenwerte insgesamt geringer, und die Druckionisation verläuft hier ausschließlich kontinuierlich.

Strukturelle Analysen der DFT-MD-Simulationen ergeben, dass im partiell ionisierten Wasserplasma eine Vielzahl unterschiedlicher chemischer Spezies auftaucht (z.B. H_2O-, OH-, H_2-, O_2-Moleküle, Atome und Ionen), an denen die Elektronen streuen können. Die DFT-MD-Leitfähigkeiten stellen wichtige Referenzwerte dar, die für die Weiterentwicklung von chemischen Transportmodellen für dichte Plasmen mit komplexer Zusammensetzung verwendet werden können. Es wurde daher versucht, ein leicht handhabbares Leitfähigkeitsmodell passend zu einem chemischen Ionisationsmodell [136] für das verdünnte (nahezu ideale) Plasma zu entwickeln und mit den DFT-MD-Ergebnissen zu vergleichen. Hier zeigt sich je-

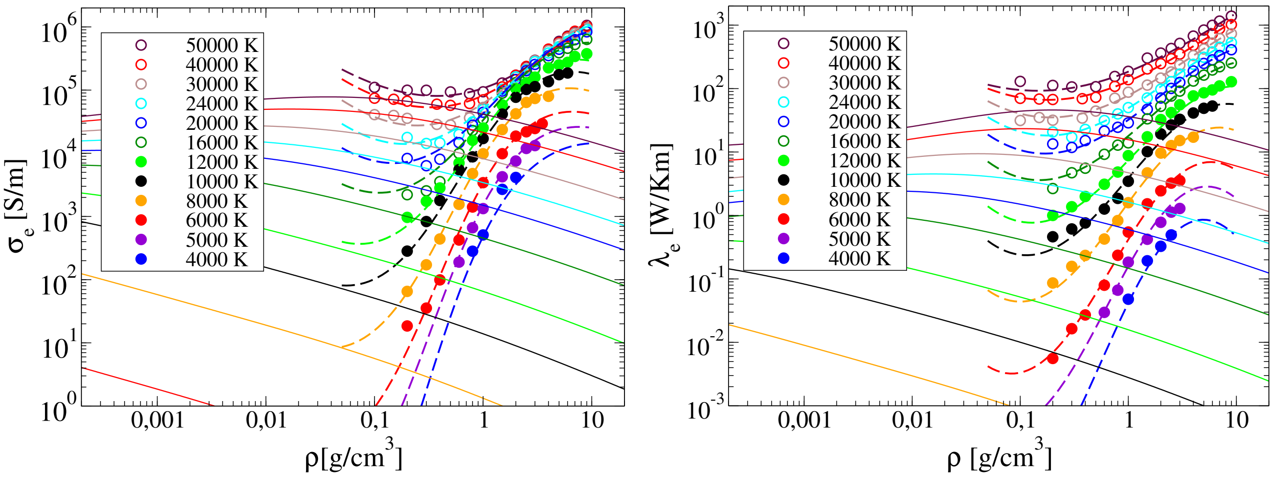

Abbildung 4.5: Mit DFT-MD (Punkte und gestrichelte Linien) berechnete elektrische Leitfähigkeit σ_e (links) und Wärmeleitfähigkeit λ_e (rechts) von Wasserplasmen im Vergleich zu einem einfachen Modell im „chemischen Bild“ (durchgezogene Linien) mit rein thermischer Ionisation. Alle Bilder wurden [129] entnommen und angepasst.

doch, dass das sehr einfache chemische Modell aufgrund vernachlässigter Druckdissoziation und -ionisation der Wasserteilchen noch keinen ausreichend guten Anschluss an die DFT-MD-Ergebnisse liefert, insbesondere für die Wärmeleitfähigkeit.

Die elektronischen Beiträge σ_e und λ_e beschreiben besonders im Fall von Wasser nur einen Anteil zu den jeweiligen Transportgrößen σ und λ. Durch Autoprotolyse erzeugte ionische Ladungsträger liefern bei kleinen Temperaturen, bei denen der Ionisationsgrad niedrig ist, den Hauptbeitrag zum Ladungstransport [158, 303, 304]. Ebenso wird die Wärme bei kleinen Temperaturen bevorzugt durch Molekül- und Atomstöße übertragen [255, 305]. Wie auch diese Beiträge mit der DFT-MD-Methode berechnet werden können, wird im folgenden Kapitel dargestellt.

Kapitel 5

Transportkoeffizienten der schweren Teilchen

Die Beiträge der schweren Teilchen werden laut Kapitel 3 über die klassischen Green-Kubo-Formeln berechnet. Speziell für die Leitfähigkeiten kommt hier das fundamentale Problem der Entkopplung der Elektron-Ion-Dynamik durch die Born-Oppenheimer-Näherung wie folgt zum Tragen: Es bleibt unklar, welche effektive Ladung bzw. wieviel elektronische Bindungsenergie jedes Ion zum mikroskopischen elektrischen (3.35) bzw. Wärmestrom (3.44) beisteuert, da die elektronische Abschirmwolke, von der es einen Teil mit sich ziehen sollte, zu jedem MD-Zeitschritt statisch bleibt. Eine Unterteilung der Elektronenzustände $|\mathbf{k}\nu\alpha\rangle$ in an Ionen gebundene und ungebundene Zustände entspräche der Verwendung eines „chemischen Bildes“ und ist bekanntermaßen in einem Vielteilchensystem nicht ohne Willkür möglich [4]. Für den Fall, dass das gesamte System im elektronischen Grundzustand und nichtmetallisch ist, kann solch eine effektive Ladungszuordnung jedoch mithilfe von Polarisationstheorie exakt erfolgen, wie im nächsten Abschnitt erläutert wird. Als Anwendungsbeispiel soll hier ausschließlich Wasser als typischer Vertreter für ein nicht zu komplexes und gleichzeitig für die Planetenphysik relevantes Mehrkomponentensystem dienen.

5.1 Elektrische Leitfähigkeit der Ionen

Als Ausgangspunkt dient der bekannte Zusammenhang, dass die zeitliche Änderung der elektrischen Polarisation $\mathbf{P}_{el}$ eines elektronischen Isolators einem Stromfluss entspricht. Diese Polarisationsänderung soll sich aus Einzelbeiträgen der sich im System umherbewegenden N_i Ionen mit den Positionen $\mathbf{r}_a$ zusammensetzen:

$$\mathbf{J}_{el}(t) = \frac{\mathrm{d}\mathbf{P}_{el}(\{\mathbf{r}_a(t)\})}{\mathrm{d}t} = \sum_{a=1}^{N_i} \frac{\partial \mathbf{P}_{el}}{\partial \mathbf{r}_a} \cdot \frac{\partial \mathbf{r}_a}{\partial t} = \sum_{a=1}^{N_i} q_a^{eff}(t) \cdot \mathbf{v}_a(t) \quad . \tag{5.1}$$

Die hier auftretenden effektiven Ladungen q_a^{eff} sind die aus der Festkörperphysik bekannten Bornschen Polarisationsladungstensoren [306, 307, 308]. Sie setzen sich zusammen aus der unabgeschirmten skalaren Ladung des Ions q_a und einem elektronischen Polarisationsanteil und können geschrieben werden als [309, 310]:

$$q_a^{eff} = Z_a|q_e| = q_a\mathbb{1} + q_e \sum_{v,c} \left(\left\langle \frac{\partial \phi_v}{\partial \mathbf{r}_a} \middle| \phi_c \right\rangle \otimes \langle \phi_c | \hat{\mathbf{r}} | \phi_v \rangle + c.c. \right) \quad , \tag{5.2}$$

wobei v die besetzten Valenzzustände ($E_v < \mu_e$) und c die unbesetzten Leitungszustände ($E_c > \mu_e$) kennzeichnen. Die effektiven Bornschen Ladungen können mithilfe von Dichtefunktionalstörungstheorie [309, 311] berechnet werden, die auch in VASP implementiert ist [256]. Hier treten u.a. dieselben elektronischen Matrixelemente aus Kapitel 4 auf. Es ist zwar möglich, alle Polarisationsbeiträge zusammenzufassen und so einen adiabatischen Strom aus Beiträgen der unabgeschirmten Ionen und dem gesamten elektronischen Polarisationsstrom zu definieren [310], jedoch eröffnet die Untersuchung der Bornschen Ladungen interessante Möglichkeiten zur mikroskopischen Interpretation des Ladungstransports.

Detailliertere Informationen hierzu befinden sich im Artikel [128]: „Dynamical Screening and Ionic Conductivity in Water from Ab Initio Simulations“ von M. French, S. Hamel und R. Redmer, Phys. Rev. Lett. **107**, 185901 (2011), siehe auch Anhang VI.
Eigener Anteil: Erabeitung der Methode. Hauptsächliche Durchführung der numerischen Rechnungen, Diskussion der Ergebnisse und Schreiben des Artikels.

Am Beispiel von Wasser zeigt sich, dass die effektiven Bornschen Ladungen eine breite statistische Verteilung mit nicht ganzzahligen Mittelwerten haben, siehe Abbildung 5.1. Berechnet man die ionische Gleichstromleitfähigkeit σ_i mit den zeitabhängigen Bornschen Ladungen und sucht nach einer mittleren Ionenladung für jede Sorte, die dieselben Leitfähigkeitswerte liefert, so gelingt dies nicht mit den gemittelten Bornschen Ladungen, sondern stattdessen mit den ganzzahligen Ladungszahlen $Z_H = 1$ für Wasserstoff und $Z_O = -2$ für Sauerstoff. Dieser rein numerisch gefundene Zusammenhang, dass jedes Ion eine ganzzahlige Nettoladung transportiert, kann mit der Topologie der elektronischen Struktur von gitterperiodischen Isolatoren tiefer begründet werden [312, 313]. Praktisch bedeutet dies, dass die sehr zeitintensiven Berechnungen der Bornschen Ladungen vermieden werden können, falls man die Ladungszahlen aus den chemischen Oxidationszuständen der Ionen in der Simulation richtig bestimmen kann.[1] Die Kenntnis dieser topologisch quantisierten Ladungszahlen hilft jedoch nicht bei der Berechnung der Wechselstromleitfähigkeit (3.36), da die Zeitabhängigkeit der Strom-Strom-Korrelationsfunktion explizit in die Fouriertransformation eingeht. Abbildung 5.1 zeigt, dass sich diese Autokorrelationsfunktion deutlich verändert, wenn statt der zeitabhängigen Bornschen Ladungen die Ladungszahlen $Z_H = 1$ und $Z_O = -2$ angesetzt werden.

Im Hinblick auf WDM bietet die hier vorgestellte Berechnungsmethode noch keine befriedigende Lösung, da sie auf ionisierte Materialien formal nicht anwendbar ist. In der Praxis

---

[1] Dies sollte in der Praxis dennoch nicht ohne Testrechnungen mit Bornschen Ladungen gehen, da formal auch jedes ganzzahlige Vielfache erlaubt wäre. Inwieweit einfaches Raten von Oxidationszuständen über die chemische Intuition bei Systemen mit mehr als zwei Komponenten ausreichend ist, bleibt zu zeigen.

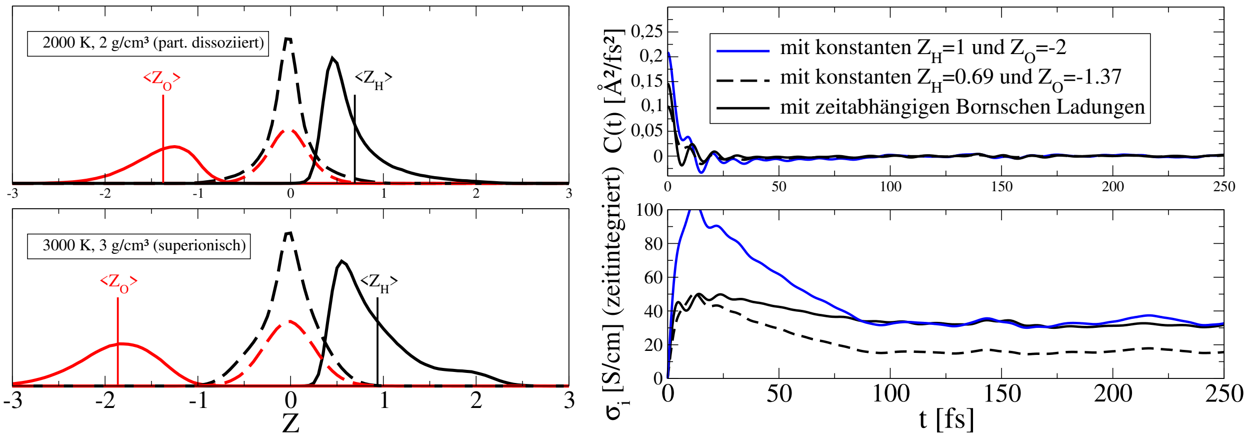

Abbildung 5.1: Häufigkeitsverteilung der Bornschen Ladungen für teilweise dissoziiertes (links oben) und superionisches Wasser (links unten). Ionische Leitfähigkeit σ_i bei 2000 K und 2 g/cm^3 berechnet mit verschiedenen Werten für die effektiven Ladungen (rechts). Alle Bilder wurden [128] entnommen und angepasst.

erhält man bei schwacher elektronischer Anregung dennoch sinnvolle Werte für die Bornschen Ladungen. Zusätzlich übersteigt die elektronische Leitfähigkeit σ_e schon bei relativ schwacher Ionisation die ionische Leitfähigkeit σ_i deutlich [158], sodass die Gesamtleitfähigkeit $\sigma = \sigma_e + \sigma_i$ von WDM bis auf in einem kleinen Bereich wo $\sigma_e \approx \sigma_i$ mit guter Genauigkeit durch DFT-MD-Simulationen berechenbar sein sollte.

Allgemein erfordert das Erreichen von numerischer Konvergenz bei der Auswertung der Green-Kubo-Formel (3.36) sehr lange Simulationen der Größenordnung 100 000 Zeitschritte. Daher gibt es bislang nur sehr wenige Arbeiten, die die Methode aufgegriffen haben [310, 314, 313, 315].[2] Alternativ können ionische Leitfähigkeitsmodelle entwickelt werden, die wie die Nernst-Einstein-Formel (3.71) allein auf Selbstdiffusionskoeffizienten basieren [304, 317]. Zum Beispiel gelingt es mit dem Modell von Mattsson und Desjarlais [304] für Protonenleitfähigkeit, experimentelle Leitfähigkeitswerte von teilweise dissoziiertem Wasser entlang der Hugoniot-Kurve zu reproduzieren [158]. Gleichzeitig kann dieses Modell durch Vergleich mit Green-Kubo-Ergebnissen validiert werden [128, 314].[3]

---

[2] Rosza *et al.* [314] verwenden statt Bornschen Ladungen die Polarisation aus elektronischen Wannierzentren [316]. Beide Verfahren sind im Prinzip äquivalent. Das Verwenden der Polarisation $\mathbf{P}_{el}$ selbst kann jedoch problematisch sein, da diese (genau wie der Ort) auf periodischen Randbedingungen nur bis auf Vielfache der Periodizitätslänge definiert ist [307, 308, 310]. Bornsche Ladungen sind grundsätzlich wohldefiniert, da sie aus Ableitungen der Polarisation gewonnen werden.

[3] Für die Protonenleitfähigkeit von superionischem Wasser funktioniert das Modell jedoch nicht [128], da es keine positiven Kreuzkorrelationsbeiträge zwischen den Teilchen beinhaltet, sondern ausschließlich negative, welche die Leitfähigkeitsminderung aufgrund von Bindung an Sauerstoffionen beschreiben.

5.2 Wärmeleitfähigkeit der schweren Teilchen

Die Gedankengänge aus dem vorigen Abschnitt lassen sich größtenteils auf die Wärmeleitfähigkeit übertragen. Der für die Green-Kubo-Formel (3.49) benötigte Energiestrom lässt sich über die zeitliche Ableitung des Energieschwerpunktes aus der DFT-MD berechnen. Dies führt zu einer energetischen Polarisationstheorie, die von Marcolongo *et al.* [318] ausgearbeitet wurde. Auch diese Theorie ist nur für elektronische Isolatoren gültig. Diese Einschränkung stellt sich in bei Berechnungen der Wärmeleitfähigkeit als deutlich gravierender heraus, als es bei der elektrischen Leitfähigkeit der Fall ist. Der Grund ist, dass der Beitrag der schweren Teilchen zur Wärmeleitfähigkeit λ_i den der Elektronen λ_e auch noch bei signifikanter Ionisation übersteigen kann. Gerade chemische Dissoziationsreaktionen, die in WDM-Zuständen natürlicherweise vorkommen, liefern besonders hohe Beiträge zur Wärmeleitfähigkeit [267].

Um diese konzeptionellen Schwierigkeiten und gleichfalls die sehr aufwendigen Berechnungen der energetischen Polarisationstheorie zu vermeiden, kann der Wärmestrom alternativ durch Anpassung von Kraftfeldern an DFT-MD-Simulationen berechnet werden. Als einfachste Möglichkeit bieten sich hier radiale Paarwechselwirkungspotentiale an, wie sie beispielsweise in Gleichung (3.44) verwendet wurden. Diese müssen selbstverständlich für jeden Punkt in der Dichte-Temperatur-Ebene neu angepasst werden, was aber mit den Kräften aus derselben DFT-MD-Simulation geschehen kann, mit deren Ionentrajektorien die Green-Kubo-Formel (3.49) ausgewertet wird. Dieser Ansatz wurde am Beispiel von Wasser unter Berücksichtigung der erforderlichen Beschreibung als Mehrkomponentensystem verfolgt.

Detailliertere Informationen hierzu befinden sich im Artikel [130]: „Thermal conductivity of dissociating water – an ab initio study“ von M. French, New. J. Phys. **21**, 023007 (2019), siehe auch Anhang VII.

Trotz der erheblichen Vereinfachungen, die die Annahme von rein radialen Paarwechselwirkungskräften mit sich bringt, liefert die in [130] beschriebene DFT-MD+GKFF-Methode eine Übereinstimmung mit experimentellen Wärmeleitfähigkeitsdaten. Offensichtliche Verbesserungsmöglichkeiten der Methode für die Anwendung auf komplexere Systeme ergäben sich durch die Verwendung von realistischeren Potentialmodellen, z.B. mit Ansätzen, die auf dem Tight-Binding-Modell [319] oder auf maschinellem Lernen [320, 321] basieren.

Neben der fluiden Phase von Wasser ist für das Innere der Planeten Uranus und Neptun auch die superionische Phase relevant, die aus einem festen Sauerstoffgitter und beweglichen Protonen besteht [8, 15, 139, 322]. Diese hat eine hohe protonische aber relativ niedrige elektronische Leitfähigkeit [158, 304], sodass auch die Wärmeleitfähigkeit hauptsächlich durch die Protonendiffusion bestimmt wird. Die DFT-MD+GKFF-Methode ist ohne Einschränkung auch für superionische Phasen und Festkörper einsetzbar.

Als Ergänzung zu den Ergebnissen aus [130] wird nun die ionische Wärmeleitfähigkeit der kubisch raumzentrierten superionischen Phase berechnet, die in Abbildung 5.2 gezeigt ist. Diese Wärmeleitfähigkeit zeigt einen nahezu linearen Anstieg mit der Dichte und keine si-

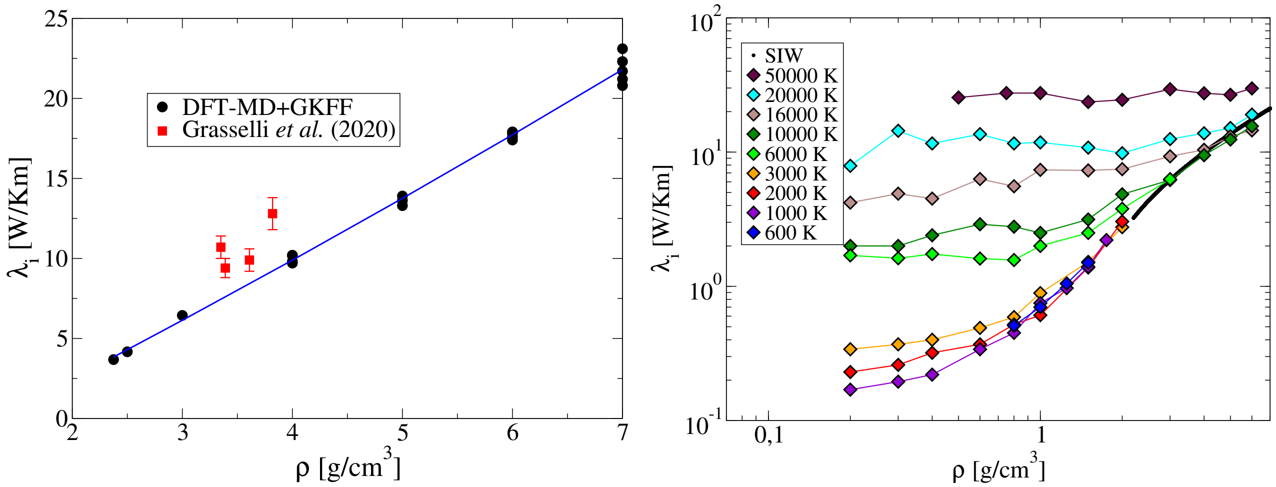

Abbildung 5.2: Ionische Wärmeleitfähigkeit in superionischem Wasser mit kubisch raumzentriertem Sauerstoffgitter (links) im Vergleich zu den Daten von Grasselli *et al.* [315]. Ionische Wärmeleitfähigkeit in warmem dichtem Wasser (rechts). Das rechte Bild wurde [128] entnommen und die Wärmeleitfähigkeit der superionischen Phase aus dem linken Bild zu den Datenpunkten für die fluide Phase mit eingetragen (SIW, schwarze Linie).

gnifikante Temperaturabhängigkeit.[4] Die numerischen Werte können wie folgt parametrisiert werden:

$$\lambda_i^{SIW}\,[\mathrm{W/Km}] = -4,4815 + 3,3784\,\varrho\,[\mathrm{g/cm^3}] + 0,053726\,\left(\varrho\,[\mathrm{g/cm^3}]\right)^2 \quad . \tag{5.3}$$

Sie sind im Vergleich zu den Ergebnissen von Grasselli *et al.* [315], die mit energetischer Polarisationstheorie berechnet wurden, etwas kleiner, zeigen jedoch deutlich geringere statistische Schwankungen. Eine definitive Erklärung für diese Abweichungen kann momentan nicht gegeben werden. Der in Abbildung 5.2 gezeigte Vergleich mit den Werten aus der fluiden Phase zeigt einen nahtlosen Anschluss bei dem Phasenübergang nahe 2 g/cm^3. Dies steht im Einklang mit der Beobachtung, dass auch die Protonendiffusionskoeffizienten keine Sprünge an dieser Phasengrenze haben [158]. Die Gitterstruktur der Sauerstoffionen hat zudem kaum Einfluss auf die Protonendiffusionskoeffizienten [139], sodass diese Wärmeleitfähigkeitswerte für superionisches Wasser allgemein repräsentativ sein sollten.

Die Wärmeleitfähigkeit von Wasser bzw. des planetaren Gemisches aus Wasser, Ammoniak, Methan, Wasserstoff und Helium wird für die Entwicklung von Struktur- und Evolutionsmodellen von Uranus und Neptun benötigt, welche die sehr großen Unterschiede in der Leuchtkraft dieser beiden ansonsten sehr ähnlichen Planeten erklären sollen [50, 323, 324]. Aktuelle Arbeiten dazu zielen auf die Modellierung thermischer Grenzschichten im Inneren

---

[4] Insgesamt wurden 20 Datenpunkte im Stabilitätsgebiet der kubisch raumzentrierten superionischen Phase berechnet. Die Simulationsparameter waren identisch zu denen aus [130]. Die etwas größeren statistischen Schwankungen bei der höchsten Dichte zeigten keine systematische Abhängigkeit von der Temperatur.

dieser Planeten ab [325]. Deren Lage, Dicke und Stabilität wird von mehreren Transporteigenschaften, wie Wärmeleitfähigkeit und Strahlungsdurchlässigkeit, aber auch Viskosität und Diffusionskoeffizienten planetarer WDM bestimmt [49, 50].

5.3 Viskosität und Prandtl-Zahl

Die Scherviskosität η beschreibt die Zähflüssigkeit eines Materials und beeinflusst somit die Geschwindigkeit möglicher Konvektionsströmungen. Sie geht z.B. in mehrere der für planetare Dynamosimulationen und Konvektionsmodelle essentielle hydrodynamische Kennzahlen ein [46, 47]. Die Berechnung der Scherviskosität von Fluiden ist mit DFT-MD-Simulationen über die Gleichung (3.54) ohne prinzipielle Schwierigkeiten möglich, da der dafür nötige Drucktensor direkt in der DFT-MD zugänglich ist und zu jedem Zeitschritt berechnet wird.[5]

Detailliertere Informationen hierzu befinden sich im Artikel [131]: „Viscosity and Prandtl Number of Warm Dense Water as in Ice Giant Planets“ von M. French und N. Nettelmann, Astrophys. J. **881**, 81 (2019), siehe auch Anhang VIII.
Eigener Anteil: Berechnung der Viskosität und der Prandtl-Zahl. Mitarbeit bei der Diskussion der Ergebnisse und beim Schreiben des Artikels.

Die in Abbildung 5.3 gezeigte Scherviskosität von Wasser zeigt bei kleinen Dichten einen für Gase typischen Anstieg mit der Temperatur. Dieses Temperaturverhalten verschwindet bei höheren Dichten bzw. kehrt sich um. Insgesamt bleiben die Zahlenwerte in der Größenordnung mPas und somit nahe bei den für flüssiges Wasser bei Normalbedingungen geltenden Werten.

Eine wichtige hydrodynamische Kennzahl, die nun für die WDM-Zustände von Wasser berechnt werden kann, ist die Prandtl-Zahl:

$$\mathrm{Pr} = \frac{\eta c_p}{\lambda} \quad , \tag{5.4}$$

mit der spezifischen Wärmekapazität c_p. Die Prandtl-Zahl hat maßgeblichen Einfluss auf das Konvektionsverhalten einer Flüssigkeit [326, 327] und ist in Abbildung 5.3 entlang der Druckprofile von drei Uranusmodellen gezeigt. In einem heißen Modell mit thermischer Grenzschicht [50] ist die Prandtl-Zahl aufgrund der starken Ionisation deutlich kleiner als in den isentropen, voll konvektiven Modellen [15, 141]. Da in den hier verwendeten Planetenmodellen die Rückkopplungen zwischen Temperaturprofil und Konvektionsmechanismus nicht berücksichtigt wurden, können die gezeigten Verläufe lediglich als Richtwerte dienen. Dennoch eröffnen sich mit Kenntnis der Prandtl-Zahl neue Möglichkeiten, in Zukunft realistischere Planetenmodelle für Uranus und Neptun zu entwickeln, die nicht konvektive oder teilkonvektive thermische Grenzschichten enthalten.

---

[5] Dies geschieht über den quantenmechanischen Virialsatz und beinhaltet auch Beiträge der freien Elektronen [113, 114, 219, 220, 221, 222]. Letztere kompensieren sich jedoch im viskosen Drucktensor Π weitgehend bzw. beeinflussen die Viskosität nicht merklich.

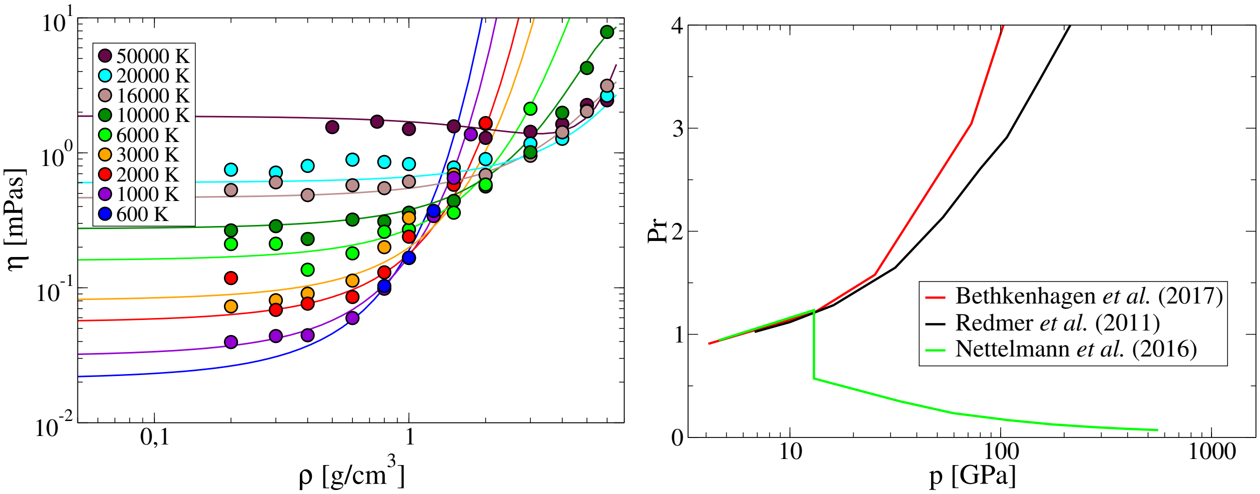

Abbildung 5.3: Scherviskosität von warmem dichtem Wasser (links). Prandtl-Zahl für Wasser in drei verschiedenen Modellen für Uranus [15, 50, 141] (rechts). Alle Bilder wurden [131] entnommen und angepasst.

Selbstverständlich bestehen Uranus und Neptun nicht aus reinem Wasser, sondern sind mit einer Vielzahl leichterer und schwerer Elemente angereichert. Die zwangsläufig dadurch auftretenden Konzentrationsgradienten der Elemente erhöhen die Komplexität der Transportvorgänge der planetaren Mischung immens. So können z.B. starke Konzentrationsgradienten die Konvektion behindern und zu doppelt diffusiven Schichten führen, möglicherweise ähnlich denen in den salzhaltigen Gewässern der Erde [328, 329, 330]. Um auch solche Vorgänge zu beschreiben, sind neben Wärmeleitfähigkeit und Scherviskosität die Diffusionskoeffizienten [45] des planetaren Stoffgemischs nötig. Diese sind mit den Gleichungen (3.62) und (3.63) prinzipiell mit DFT-MD berechenbar. Dies ist wiederum sehr aufwendig, da die Bestimmung der thermodynamischen Faktoren die Kenntnis der Konzentrationsabhängigkeit der chemischen Potentiale erfordert.[6] Einfachere Abschätzungen mithilfe von Selbstdiffusionskoeffizienten und der Darken-Relation (3.70) deuten aber bislang darauf hin, dass doppelt diffusive Konvektionsbereiche in Uranus und Neptun unwahrscheinlich sind [131]. Genauere Berechnungen der dieses Verhalten mitbestimmenden Schmidt-Zahl [327][7]

$$\mathrm{Sc} = \frac{\eta}{\varrho D_{ab}} \quad , \tag{5.5}$$

sind noch der Zukunft vorbehalten, ebenso wie die Entwicklung planetarer Modelle, die solch komplexe hydrodynamische Phänomene konsistent erfassen können.

---

[6] Dies ist ein rein thermodynamisches Problem, das z.B. durch die Berechnung der freien Enthalpie als thermodynamisches Potential gelöst werden kann. Das dies mit DFT-MD-Simulationen machbar ist, zeigen aktuelle Untersuchungen zum Entmischungsdiagramm planetarer Wasserstoff-Helium-Mischungen [331, 332].

[7] Das zu diesem Zweck in [131] verwendete Kriterium R_{crit} kann ebenso in Abhängigkeit von Pr und Sc angegeben werden.

Kapitel 6

Zusammenfassung und Ausblick

In dieser Arbeit wurde ein systematischer Überblick über aktuelle Entwicklungen und grundlegende Fortschritte bei der *Ab-initio*-Berechnung der Transporteigenschaften von warmer dichter Materie gegeben. Es wurde umfassend dargestellt, wie mit einer Kombination aus Dichtefunktionaltheorie, Molekulardynamik und Linearer Response-Theorie die relevanten elektronischen und ionischen Beiträge zu elektrischer Leitfähigkeit, Wärmeleitfähigkeit und Viskosität berechnet werden können. Insbesondere die quantenstatistische Beschreibung der Elektronen durch thermische Dichtefunktionaltheorie bietet eine effiziente und gleichzeitig genaue Berechnung der Elektronenstruktur von Vielteilchensystemen mit Coulomb-Wechselwirkung. Die klassische Betrachtung der Ionendynamik ist aufgrund der hohen Temperatur der warmen dichten Materiezustände gleichermaßen angemessen. Die Lineare Response-Theorie vermittelt letztlich den Anschluss an die für die Berechnung der Transporteigenschaften notwendige Nichtgleichgewichtsphysik. Das Zusammenführen dieser drei Methoden erfordert allerdings weitere Näherungen, die ihren hauptsächlichen Ursprung in der Born-Oppenheimer-Näherung haben, welche die Elektronen- und Ionendynamik entkoppelt. Details hierzu und wurden in der Arbeit eingehend dargestellt.

Mit zahlreichen Anwendungen auf astrophysikalisch bzw. technisch bedeutsame Materialien wie Wasser, Eisen und Molybdän wurde die hohe Vorhersagekraft der verwendeten Berechnungsmethode anhand direkter Vergleiche mit experimentellen Daten belegt. Darüber hinaus wurden erste umfangreiche Datensätze für die Transporteigenschaften von Wasser und Wasserstoff-Helium-Gemische für die extremen Bedingungen im Inneren von großen Planeten erstellt. Die Verfügbarkeit solcher gut fundierten, neuen Materialdatensätze ermöglicht es fortan, deutlich genauere und realistischere Struktur-, Entwicklungs- und Magnetfeldmodelle für Planeten wie Jupiter, Saturn, Uranus und Neptun sowie von Exoplaneten zu entwickeln. Damit eröffnen sich neue Möglichkeiten, das Forschungsgebiet der Planetenphysik in zahlreichen Schlüsselfragestellungen voranzutreiben, mit denen die Entstehung, der Aufbau und die Entwicklung von Planeten sowie Planetensystemen als Ganzes besser verstanden werden können.

Im Angesicht dieser Erfolge bleiben dennoch einige methodische Fragestellungen offen, z.B. bezüglich Möglichkeiten der direkten Erfassung von Elektron-Elektron-Stößen im Kubo-

Greenwood-Formalismus. Weiterhin müssen exakte Ausdrücke für die ionischen Stromdichten in elektronisch leitfähigen Systemen abgeleitet werden, die nicht auf die bislang verwendeten Näherungen auf Grundlage von effektiven Kraftfeldern, effektiven Ladungen bzw. Polarisationstheorie angewiesen sind. Man darf vermuten, dass diese exakten Ausdrücke existieren, sie jedoch abseits von Polarisationstheorie zu finden sind, auch wenn diese Methode für elektronische Isolatoren prinzipiell korrekte Ergebnisse liefern kann. Des Weiteren wird auch die fortlaufende Weiterentwicklung der Austausch- und Korrelationsfunktionale für die Dichtefunktionaltheorie einen wichtigen Beitrag zur weiteren Verbesserung der Methode führen. Dies ist insbesondere für eine genauere Lokalisierung und Klassifizierung des Metall-Nichtmetall-Übergangs in warmem dichtem Wasserstoff zwingend erforderlich. Zusätzlich könnte die Verwendung von Quantenkorrekturen bzw. semiklassischen Näherungen bei der Auswertung der Korrelationsfunktionen für die bislang rein klassisch betrachten Ionen die Genauigkeit der Ergebnisse weiter erhöhen. Auch die Verwendung von Pfadintegralmethoden statt der rein klassischen Molekulardynamik für die Ionen kann insbesondere für kühlere Zustände im Übergangsbereich zur kondensierten Materie weitere wertvolle Einsichten liefern.

Insgesamt stellen die breiten Anwendungsmöglichkeiten der DFT-MD-Methode aber schon jetzt einen enormen Fortschritt gegenüber früheren Zugängen aus dem „chemischen Bild“ dar, da Streu- und Bindungszustände sämtlicher Teilchen mit demselben Formalismus behandelt werden, was einer konsequenten Verwendung des „physikalischen Bildes“ entspricht. Insbesondere können Mehrkomponentensysteme mit nahezu beliebiger Stöchiometrie berechnet werden, ohne dass die gesamte Methodik dafür wesentlich verkompliziert werden muss. Dies ist für praktische Anwendungen enorm wichtig, insbesondere wiederum für die Planetenmodellierung, bei der man auf die Verfügbarkeit genauer Datensätze von Transporteigenschaften von warmer dichter Materie angewiesen ist. Die in dieser Arbeit aufgezeigten Grundlagen und Anwendungen auf relativ einfache Materialien können direkt als Leitfaden für die Untersuchung weitaus komplexerer Gemische dienen, die z.B. den realen Stoffgemischen im Inneren von Planeten deutlich näher entsprechen. Aktuelle Fragen bezüglich möglicher Schichtenbildung oder Kernerosion in den solaren Planeten, die in Zusammenhang mit großskaligen Konzentrationsgradienten von Elementen stehen, werden somit in Zukunft deutlich genauer beantwortet werden können.

Literaturverzeichnis

[1] V. E. Fortov, *Thermodynamics and Equations of State for Matter, From Ideal Gas to Quark-Gluon Plasma* (World Scientific, New Jersey, 2016).

[2] V. E. Fortov, *Extreme States Of Matter* (Springer, Heidelberg, 2011).

[3] U. Stroth, *Plasmaphysik, Phänomene, Grundlagen und Anwendungen* (Springer, Berlin, 2018).

[4] W. Ebeling, W. D. Kraeft und D. Kremp, in *Theory of Bound States and Ionization Equilibrium in Plasmas and Solids*, edited by R. Rompe und M. Steenbeck (Akademie-Verlag, Berlin, 1976).

[5] W.-D. Kraeft, D. Kremp, W. Ebeling und G. Röpke, *Quantum Statistics of Charged Particle Systems* (Akademie-Verlag, Berlin, 1986).

[6] D. Kremp, M. Schlanges und W.-D. Kraeft, *Quantum Statistics of Nonideal Plasmas* (Springer, New York, 2005).

[7] R. Boehler, *Rev. Geophys.* **38**, 221 (2009).

[8] C. Cavazzoni *et al.*, *Science* **283**, 44 (1999).

[9] F. Graziani, M. P. Desjarlais, R. Redmer und S. B. Trickey, *Frontiers and Challenges in Warm Dense Matter* (Springer, Cham, 2014).

[10] S. Ichimaru, *Statistical Plasma Physics, Volume II: Condensed Plasmas* (Addison Wesley, Menlo Park, California, 1994).

[11] M. A. Morales, J. M. McMahon, C. Pierleoni und D. M. Ceperley, *Phys. Rev. Lett.* **110**, 065702 (2013).

[12] K. K. Irikura, *J. Phys. Chem. Ref. Data* **36**, 389 (2007).

[13] J. Christensen-Dalsgaard *et al.*, *Science* **272**, 1286 (1996).

[14] N. Nettelmann, A. Becker, B. Holst und R. Redmer, *Astrophys. J.* **750**, 52 (2012).

[15] R. Redmer, T. R. Mattsson, N. Nettelmann und M. French, *Icarus* **211**, 798 (2011).

[16] T. Guillot, *Annu. Rev. Earth Planet. Sci.* **33**, 493 (2005).

[17] J. J. Fortney und N. Nettelmann, *Space Sci. Rev.* **152**, 423 (2010).

[18] T. Guillot, *Science* **286**, 72 (1999).

[19] L. N. Fletcher *et al.*, *Planet. Space Sci.* **191**, 105030 (2020).

[20] M. Blanc *et al.*, *Space Sci. Rev.* **217**, 3 (2021).

[21] W. B. Hubbard, *Science* **214**, 145 (1981).

[22] R. Helled, N. Nettelmann und T. Guillot, *Space Sci. Rev.* **216**, 38 (2020).

[23] H. Wänke und G. Dreibus, *Phil. Trans. R. Soc. Lond. A* **325**, 545 (1988).

[24] K. Righter und D. P. O'Brien, *Proc. Natl. Acad. Sci. U.S.A.* **108**, 19165 (2011).

[25] C. Dorn *et al.*, *Astron. Astrophys.* **577**, A83 (2015).

[26] T. V. Hoolst, L. Noack und A. Rivoldini, *Adv. Phys. X* **4**, 1630316 (2019).

[27] L. Zeng *et al.*, *Proc. Natl. Acad. Sci. U.S.A.* **116**, 9723 (2019).

[28] O. Mousis *et al.*, *Astrophys. J. Lett.* **896**, L22 (2020).

[29] D. J. Stevenson und E. E. Salpeter, *Astrophys. J. Suppl. Ser.* **35**, 239 (1977).

[30] C. R. Mankovich und J. J. Fortney, *Astrophys. J.* **889**, 51 (2020).

[31] A. M. Dziewonski und D. L. Anderson, *Phys. Earth Planet. Inter.* **25**, 297 (1981).

[32] J. D. Lindl *et al.*, *Phys. Plasmas* **11**, 339 (2004).

[33] D. Meade, *Nucl. Fusion* **50**, 014004 (2009).

[34] E. I. Moses *et al.*, *Phys. Plasmas* **16**, 041006 (2009).

[35] B. A. Remington *et al.*, *Proc. Natl. Acad. Sci. U.S.A.* **116**, 18233 (2019).

[36] T. Yagi, T. Sakai, H. Kadobayashi und T. Irifune, *High Press. Res.* **40**, 148 (2020).

[37] L. Dubrovinsky *et al.*, *Nature* **525**, 226 (2015).

[38] E. F. O'Bannon *et al.*, *Rev. Sci. Instrum.* **89**, 111501 (2018).

[39] N. V. C. Shekar, P. C. Sahu und K. G. Rajan, *J. Mater. Sci. Technol.* **19**, 518 (2003).

[40] S. Anzellini und S. Boccato, *Crystals* **10**, 459 (2020).

[41] T. S. Duffy und R. F. Smith, *Front. Earth Sci.* **7**, 23 (2019).

[42] Y. B. Zel'dovich und Y. P. Raizer, in *Physics of Shock Waves and High-Temperature Hydrodynamic Phenomena*, edited by W. D. Hayes und R. F. Probstein (Dover Publications Inc., Mineola, NY, 2002).

[43] S. R. de Groot und P. Mazur, *Non-Equilibrium Thermodynamics* (Dover Publications Inc., New York, 1984).

[44] M. Rütten, *Verallgemeinerte newtonsche Fluide: Thermische und viskose Strömungseigenschaften* (Springer Vieweg, Berlin, 2019).

[45] R. Krishna und J. A. Wesselingh, *Chem. Eng. Sci.* **52**, 861 (1997).

[46] J. Wicht und A. Tilgner, *Space Sci. Rev.* **152**, 501 (2010).

[47] G. Schubert und K. M. Soderlund, *Phys. Earth Planet. Inter.* **187**, 92 (2011).

[48] K. M. Soderlund und S. Stanley, *Phil. Trans. R. Soc. A* **378**, 20190479 (2020).

[49] J. Leconte und G. Chabrier, *Astron. Astrophys.* **540**, A20 (2012).

[50] N. Nettelmann *et al.*, *Icarus* **275**, 107 (2016).

[51] J. Haun *et al.*, *Phys. Rev. E* **65**, 046407 (2002).

[52] C. Cagran und G. Pottlacher, in *Recent Advances, Techniques and Applications*, Vol. 5 of *Handbook of Thermal Analysis and Calorimetry*, edited by M. E. Brown und P. K. Gallagher (Elsevier Science B.V., Amsterdam, 2008), pp. 299 – 342.

[53] J. Clérouin *et al.*, *Phys. Plasmas* **19**, 082702 (2012).

[54] V. I. Oreshkin und R. B. Baksht, *IEEE Trans. Plasma Sci.* **48**, 1214 (2020).

[55] E. Sugimura *et al.*, *J. Chem. Phys.* **137**, 194505 (2012).

[56] K. Ohta *et al.*, *Nature* **534**, 95 (2016).

[57] A. C. Mitchell und W. J. Nellis, *J. Chem. Phys.* **76**, 6273 (1982).

[58] V. V. Yakushev, V. I. Postnov, V. E. Fortov und T. I. Yakysheva, *J. Exp. Theor. Phys.* **90**, 617 (2000).

[59] R. Chau, S. Hamel und W. J. Nellis, *Nat. Commun.* **2**, 203 (2011).

[60] N. F. Mott, *Int. Rev. Phys. Chem.* **4**, 1 (1985).

[61] F. Hensel und W. W. Warren, *Fluid Metals: The Liquid-Vapor Transition of Metals* (Princeton University Press, Princeton, 1999).

[62] P. P. Edwards, M. T. J. Lodge, F. Hensel und R. Redmer, *Phil. Trans. R. Soc. A* **368**, 941 (2010).

[63] *Metal-to-Nonmetal Transitions*, edited by R. Redmer, F. Hensel und B. Holst (Springer, Heidelberg, 2010).

[64] S. T. Weir, A. C. Mitchell und W. J. Nellis, *Phys. Rev. Lett.* **76**, 1860 (1996).

[65] G. W. Collins *et al.*, *Science* **281**, 1178 (1998).

[66] N. Ozaki *et al.*, *Phys. Plasmas* **11**, 1600 (2004).

[67] M. D. Knudson *et al.*, *J. Appl. Phys.* **94**, 4420 (2003).

[68] M. D. Knudson *et al.*, *Phys. Rev. B* **69**, 144209 (2004).

[69] D. B. Sinars *et al.*, *Phys. Plasmas* **27**, 070501 (2020).

[70] H. M. Milchberg, R. R. Freeman, S. C. Davey und R. M. More, *Phys. Rev. Lett.* **61**, 2364 (1988).

[71] V. Mintsev und Y. B. Zaporogets, *Contrib. Plasma Phys.* **29**, 493 (1989).

[72] P. M. Celliers *et al.*, *Phys. Plasmas* **11**, L41 (2004).

[73] M. D. Knudson *et al.*, *Phys. Rev. Lett.* **108**, 091102 (2012).

[74] M. Zaghoo und I. F. Silvera, *Proc. Natl. Acad. Sci. U.S.A.* **114**, 11873 (2017).

[75] S. H. Glenzer und R. Redmer, *Rev. Mod. Phys.* **81**, 1625 (2009).

[76] R. G. Ross, P. Andersson, B. Sundqvist und G. Backström, *Rep. Prog. Phys.* **47**, 1347 (1984).

[77] K. C. Mills, B. J. Monaghan und B. J. Keene, *Int. Mater. Rev.* **41**, 209 (1996).

[78] A. McKelvey *et al.*, *Sci. Rep.* **7**, 7015 (2017).

[79] Z. Konôpková, R. S. McWilliams, N. Gómez-Pérez und A. F. Goncharov, *Nature* **534**, 9 (2016).

[80] E. H. Abramson, J. M. Brown und L. J. Slutsky, *J. Chem. Phys.* **115**, 10461 (2001).

[81] B. Chen *et al.*, *Phys. Rev. B* **83**, 132301 (2011).

[82] G. Wiedemann und R. Franz, *Ann. Phys.* **165**, 497 (1853).

[83] A. Sommerfeld und H. Bethe, *Elektronentheorie der Metalle* (Springer, Berlin, 1967).

[84] E. H. Abramson, *Phys. Rev. E* **76**, 051203 (2007).

[85] V. N. Mineev und R. M. Zaĭdel', *J. Exp. Theor. Phys.* **27**, 874 (1968).

[86] G. Kim, *J. Appl. Mech. Tech. Phys.* **25**, 692 (1984).

[87] G. H. Miller und T. J. Ahrens, *Rev. Mod. Phys.* **63**, 919 (1991).

[88] E. H. Abramson, *Shock Waves* **25**, 103 (2015).

[89] E. A. Uehling und G. E. Uhlenbeck, *Phys. Rev.* **43**, 552 (1933).

[90] J. O. Hirschfelder, C. F. Curtiss und R. B. Bird, *The Molecular Theory of Gases and Liquids* (Wiley, New York, 1954).

[91] Y. T. Lee und R. M. More, *Phys. Fluids* **27**, 1273 (1984).

[92] T. E. Faber, *Introduction To The Theory Of Liquid Metals* (Cambridge University Press, Cambridge, 1972).

[93] S. Chapman und T. G. Cowling, *The Mathematical Theory of Non-Uniform Gases* (Cambridge University Press, Cambridge, 1972).

[94] W. Ebeling, V. E. Fortov und V. Filinov, *Quantum Statistics of Dense Gases and Nonideal Plasmas* (Springer, Cham, 2017).

[95] G. Röpke und V. Christoph, *J . Phys. C: Solid State Phys.* **8**, 3615 (1975).

[96] W. Ebeling *et al.*, *Transport Properties of Dense Plasmas* (Akademie-Verlag, Berlin, 1984).

[97] V. Christoph und G. Röpke, *phys. stat. sol. (b)* **131**, 11 (1985).

[98] H. Reinholz, R. Redmer und S. Nagel, *Phys. Rev. E* **52**, 5368 (1995).

[99] G. Röpke, *Nonequilibrium Statistical Physics* (Wiley-VCH, Weinheim, 2013).

[100] D. Zubarev, V. Morozov und G. Röpke, *Statistical Mechanics of Nonequilibrium Processes* (Akademie-Verlag, Berlin, 1996), Band I.

[101] D. Zubarev, V. Morozov und G. Röpke, *Statistical Mechanics of Nonequilibrium Processes* (Akademie-Verlag, Berlin, 1997), Band II.

[102] R. Kubo, *J. Phys. Soc. Jpn.* **12**, 570 (1957).

[103] R. Kubo, M. Toda und N. Hashitsume, *Statistical Physics II: Nonequilibrium Statistical Mechanics* (Springer, Berlin, 1991).

[104] R. Redmer, *Phys. Rep.* **282**, 35 (1997).

[105] H. Reinholz, R. Redmer und D. Tamme, *Contrib. Plasma Phys.* **29**, 395 (1989).

[106] G. Röpke und R. Redmer, *Phys. Rev. A* **39**, 907 (1989).

[107] H. Reinholz, G. Röpke, S. Rosmej und R. Redmer, *Phys. Rev. E* **91**, 043105 (2015).

[108] D. Saumon und G. Chabrier, *Phys. Rev. Lett.* **62**, 2397 (1989).

[109] G. Norman, *Contrib. Plasma Phys.* **41**, 127 (2001).

[110] P. Hohenberg und W. Kohn, *Phys. Rev.* **136**, B864 (1964).

[111] W. Kohn und L. J. Sham, *Phys. Rev.* **140**, A1133 (1965).

[112] N. D. Mermin, *Phys. Rev.* **137**, A1441 (1965).

[113] J. Kohanoff, *Electronic Structure Calculations for Solids and Molecules* (Cambridge University Press, Cambridge, 2006).

[114] D. Marx und J. Hutter, *Ab Initio Molecular Dynamics* (Cambridge University Press, Cambridge, 2009).

[115] K. Burke, *J. Chem. Phys.* **136**, 150901 (2012).

[116] R. O. Jones, *Rev. Mod. Phys.* **87**, 897 (2015).

[117] N. Mardirossian und M. Head-Gordon, *Mol. Phys.* **115**, 2315 (2017).

[118] D. M. Ceperley und B. J. Alder, *Phys. Rev. Lett.* **45**, 566 (1980).

[119] J. P. Perdew, K. Burke und M. Ernzerhof, *Phys. Rev. Lett.* **77**, 3865 (1996).

[120] T. Dornheim, S. Groth und M. Bonitz, *Phys. Rep.* **744**, 1 (2018).

[121] C. E. Starrett, J. Daligault und D. Saumon, *Phys. Rev. E* **91**, 013104 (2015).

[122] C. E. Starrett, *High Energy Density Phys.* **19**, 58 (2016).

[123] J. Daligault *et al.*, *Phys. Rev. Lett.* **116**, 075002 (2016).

[124] P. E. Grabowski *et al.*, *High Energy Density Phys.* **37**, 100905 (2020).

[125] B. Holst, M. French und R. Redmer, *Phys. Rev. B* **83**, 235120 (2011).

[126] M. French und T. R. Mattsson, *Phys. Rev. B* **90**, 165113 (2014).

[127] J.-A. Korell, M. French, G. Steinle-Neumann und R. Redmer, *Phys. Rev. Lett.* **122**, 086601 (2019).

[128] M. French, S. Hamel und R. Redmer, *Phys. Rev. Lett.* **107**, 185901 (2011).

[129] M. French und R. Redmer, *Phys. Plasmas* **24**, 092306 (2017).

[130] M. French, *New J. Phys.* **21**, 023007 (2019).

[131] M. French und N. Nettelmann, *Astrophys. J.* **881**, 81 (2019).

[132] M. French *et al.*, *Astrophys. J. Suppl. Ser.* **202**, 5 (2012).

[133] M. French, Dissertation, Universität Rostock, (2010).

[134] M. French und R. Redmer, *Phys. Plasmas* **18**, 043301 (2011).

[135] M. Bethkenhagen, M. French und R. Redmer, *J. Chem. Phys.* **138**, 234504 (2013).

[136] M. Schöttler, R. Redmer und M. French, *Contrib. Plasma Phys.* **53**, 336 (2013).

[137] M. French und T. R. Mattsson, *J. Appl. Phys.* **116**, 013510 (2014).

[138] M. French und R. Redmer, *Phys. Rev. B* **91**, 014308 (2015).

[139] M. French, M. P. Desjarlais und R. Redmer, *Phys. Rev. E* **93**, 022140 (2016).

[140] M. Schöttler, M. French, D. Cebulla und R. Redmer, *J. Phys.: Condens. Matter* **28**, 145401 (2016).

[141] M. Bethkenhagen *et al.*, *Astrophys. J.* **848**, 67 (2017).

[142] B. B. L. Witte *et al.*, *Phys. Plasmas* **25**, 056901 (2018).

[143] B. B. L. Witte *et al.*, *Phys. Rev. E* **99**, 047201 (2019).

[144] M. Guarguaglini *et al.*, *Sci. Rep.* **9**, 10155 (2019).

[145] A. Ravasio *et al.*, *Phys. Rev. Lett.* **126**, 025003 (2021).

[146] A. Bergermann, M. French, M. Schöttler und R. Redmer, *Phys. Rev. E* **103**, 013307 (2021).

[147] A. Bergermann, M. French und R. Redmer, *Phys. Chem. Chem. Phys.* **23**, 12637 (2021).

[148] S. Kumar *et al.*, *Phys. Rev. E* **103**, 063203 (2021).

[149] Z. Chen *et al.*, *Matter Radiat. Extrem.* **6**, 054401 (2021).

[150] F. Schwabl, *Quantenmechanik* (Springer, Berlin, 1998).

[151] W. Kohn, *Rev. Mod. Phys.* **71**, 1253 (1999).

[152] B. Militzer und D. M. Ceperley, *Phys. Rev. Lett.* **85**, 1890 (2000).

[153] C. Pierleoni *et al.*, *Proc. Natl. Acad. Sci. U.S.A.* **113**, 4953 (2016).

[154] F. Lin *et al.*, *Phys. Rev. Lett.* **103**, 256401 (2009).

[155] M. Born und R. Oppenheimer, *Ann. Phys.* **389**, 457 (1927).

[156] M. Weinert und J. W. Davenport, *Phys. Rev. B* **45**, 13709 (1992).

[157] R. M. Wentzcovitch, J. L. Martins und P. B. Allen, *Phys. Rev. B* **45**, 11372 (1992).

[158] M. French, T. R. Mattsson und R. Redmer, *Phys. Rev. B* **82**, 174108 (2010).

[159] L. A. Collins *et al.*, *Phys. Rev. B* **63**, 184110 (2001).

[160] S. Yoo, X. C. Zeng und S. S. Xantheas, *J. Chem. Phys.* **130**, 221102 (2009).

[161] E. Schwegler, M. Sharma, F. Gygi und G. Galli, *Proc. Natl. Acad. Sci, U.S.A.* **105**, 14779 (2008).

[162] R. Car und M. Parrinello, *Phys. Rev. Lett.* **55**, 2471 (1985).

[163] M. P. Allen und D. J. Tildesley, *Computer Simulation of Liquids* (Oxford University Press, Oxford, 1989).

[164] R. Haberlandt, S. Fritzsche, G. Peinel und K. Heinzinger, *Molekulardynamik* (Vieweg, Braunschweig/Wiesbaden, 1995).

[165] R. G. Parr und W. Yang, in *Density-Functional Theory of Atoms and Molecules*, edited by B. Breslow, J. B. Goodenough, J. Halpern und J. S. Rowlinson (Oxford University Press, New York, 1989).

[166] R. M. Dreizler und E. K. U. Gross, *Density Functional Theory* (Springer, Berlin, 1990).

[167] W. Koch und M. C. Holthausen, *A Chemist's Guide to Density Functional Theory* (Wiley-VCH, Weinheim, 2000).

[168] W. Kohn, *Phys. Rev. Lett.* **51**, 1596 (1983).

[169] R. Zeller, in *Computational Nanoscience: Do It Yourself!*, Vol. 31 of *NIC Series*, edited by J. Grotendorst, S. Blügel und D. Marx (John von Neumann Institute for Computing, Jülich, 2006), p. 419.

[170] G. Bihlmayer, in *Computational Nanoscience: Do It Yourself!*, Vol. 31 of *NIC Series*, edited by J. Grotendorst, S. Blügel und D. Marx (John von Neumann Institute for Computing, Jülich, 2006), p. 447.

[171] M. P. Desjarlais, *Phys. Rev. B* **68**, 064204 (2003).

[172] T. R. Mattsson *et al.*, *Phys. Rev. B* **81**, 054103 (2010).

[173] B. Boates und S. A. Bonev, *Phys. Rev. Lett.* **102**, 015701 (2009).

[174] H. F. Wilson und B. Militzer, *Phys. Rev. Lett.* **104**, 121101 (2010).

[175] A. Pribram-Jones, P. E. Grabowski und K. Burke, *Phys. Rev. Lett.* **116**, 233001 (2016).

[176] S. Groth *et al.*, *Phys. Rev. Lett.* **119**, 135001 (2017).

[177] V. V. Karasiev, J. W. Dufty und S. B. Trickey, *Phys. Rev. Lett.* **120**, 076401 (2018).

[178] R. Armiento und A. E. Mattsson, *Phys. Rev. B* **72**, 085108 (2005).

[179] S. Root *et al.*, *Phys. Rev. Lett.* **115**, 198501 (2015).

[180] M. D. Knudson und M. P. Desjarlais, *Phys. Rev. Lett.* **118**, 035501 (2017).

[181] V. V. Karasiev, S. X. Hu, M. Zaghoo und T. R. Boehly, *Phys. Rev. B* **99**, 214110 (2019).

[182] K. Ramakrishna, T. Dornheim und J. Vorberger, *Phys. Rev. B* **101**, 195129 (2020).

[183] P. Haas, F. Tran und P. Blaha, *Phys. Rev. B* **79**, 085104 (2009).

[184] G. I. Csonka *et al.*, *Phys. Rev. B* **79**, 155107 (2009).

[185] D. R. Hamann, *Phys. Rev. B* **55**, R10157 (1997).

[186] A. E. Mattsson und T. R. Mattsson, *J. Chem. Theory Comput.* **5**, 887 (2009).

[187] J. P. Perdew und A. Zunger, *Phys. Rev. B* **23**, 5048 (1981).

[188] J. P. Perdew und M. Levy, *Phys. Rev. Lett.* **51**, 1884 (1983).

[189] L. J. Sham und M. Schlüter, *Phys. Rev. Lett.* **51**, 1888 (1983).

[190] V. Vlček *et al.*, *Phys. Rev. B* **91**, 035107 (2015).

[191] P. Borlido *et al.*, *Npj Comput. Mater.* **6**, 96 (2020).

[192] J. Tao, J. P. Perdew, V. N. Staroverov und G. E. Scuseria, *Phys. Rev. Lett.* **91**, 146401 (2003).

[193] F. Zahariev, S. S. Leang und M. S. Gordon, *J. Chem. Phys.* **138**, 244108 (2013).

[194] F. Tran *et al.*, *Phys. Rev. B* **102**, 024407 (2020).

[195] J. Sun, A. Ruzsinszky und J. P. Perdew, *Phys. Rev. Lett.* **115**, 036402 (2015).

[196] F. Tran, J. Stelzl und P. Blaha, *J. Chem. Phys.* **144**, 204120 (2016).

[197] Z.-h. Yang, H. Peng, J. Sun und J. P. Perdew, *Phys. Rev. B* **93**, 205205 (2016).

[198] D. C. Langreth *et al.*, *Int. J. Quantum Chem.* **101**, 559 (2005).

[199] J. Klimeš, D. R. Bowler und A. Michaelides, *Phys. Rev. B* **83**, 195131 (2011).

[200] J. Heyd, G. E. Scuseria und M. Ernzerhof, *J. Chem. Phys.* **118**, 8207 (2003).

[201] J. Heyd, G. E. Scuseria und M. Ernzerhof, *J. Chem. Phys.* **124**, 219906 (2006).

[202] J. Paier *et al.*, *J. Chem. Phys.* **124**, 154709 (2006).

[203] J. P. Perdew, M. Ernzerhof und K. Burke, *J. Chem. Phys.* **105**, 9982 (1996).

[204] J. Heyd, J. E. Peralta, G. E. Scuseria und R. L. Martin, *J. Chem. Phys.* **123**, 174101 (2005).

[205] C. Kittel, *Einführung in die Festkörperphysik* (Oldenbourg, München, 1989).

[206] P. E. Blöchl, *Phys. Rev. B* **50**, 17953 (1994).

[207] G. Kresse und D. Joubert, *Phys. Rev. B* **59**, 1758 (1999).

[208] M. Marsman und G. Kresse, *J. Chem. Phys.* **125**, 104101 (2006).

[209] M. Teter, *Phys. Rev. B* **48**, 5031 (1993).

[210] J. Hafner, *J. Comput. Chem.* **29**, 2044 (2008).

[211] X. Gonze *et al.*, *Comput. Mater. Sci.* **25**, 478 (2002).

[212] P. Giannozzi *et al.*, *J. Phys.: Condens. Matter* **21**, 395502 (2009).

[213] T. D. Kühne *et al.*, *J. Chem. Phys.* **152**, 194103 (2020).

[214] G. Kresse und J. Hafner, *Phys. Rev. B* **47**, 558 (1993).

[215] G. Kresse und J. Hafner, *Phys. Rev. B* **49**, 14251 (1994).

[216] G. Kresse und J. Furthmüller, *Phys. Rev. B* **54**, 11169 (1996).

[217] B. Holst, Dissertation, Universität Rostock, (2011).

[218] P. P. Ewald, *Ann. Phys.* **64**, 253 (1921).

[219] O. H. Nielsen und R. M. Martin, *Phys. Rev. Lett.* **50**, 697 (1983).

[220] O. H. Nielsen und R. M. Martin, *Phys. Rev. B* **32**, 3780 (1985).

[221] O. H. Nielsen und R. M. Martin, *Phys. Rev. B* **32**, 3792 (1985).

[222] G. Kresse, Dissertation, Technische Universität Wien, (1993).

[223] S. Nosé, *J. Chem. Phys.* **81**, 511 (1984).

[224] W. G. Hoover, *Phys. Rev. A* **31**, 1695 (1985).

[225] U. von Barth und L. Hedin, *J. Phys. C: Solid State Phys.* **5**, 1629 (1972).

[226] D. Hobbs, G. Kresse und J. Hafner, *Phys. Rev. B* **62**, 11556 (2000).

[227] R. Kubo, *Rep. Prog. Phys.* **29**, 255 (1966).

[228] G. Röpke, *Theor. Math. Phys.* **194**, 74 (2018).

[229] D. A. Greenwood, *Proc. Phys. Soc.* **71**, 585 (1958).

[230] B. Pietrass, *Physica* **46**, 587 (1970).

[231] M. S. Green, *J. Chem. Phys.* **22**, 398 (1954).

[232] K. İmre, E. Özizmir, M. Rosenbaum und P. F. Zweifel, *J. Math. Phys.* **8**, 1097 (1967).

[233] R. Kubo, M. Yokota und S. Nakajima, *J. Phys. Soc. Jpn.* **12**, 1203 (1957).

[234] J. J. Erpenbeck, *Phys. Rev. A* **39**, 4718 (1989).

[235] R. Bertossa, F. Grasselli, L. Ercole und S. Baroni, *Phys. Rev. Lett.* **122**, 255901 (2019).

[236] G. D. Mahan, in *Many-Particle Physics*, edited by J. T. Devreese *et al.* (Plenum Press, New York, 1981).

[237] W. G. Hoover *et al.*, *Phys. Rev. A* **22**, 1690 (1980).

[238] E. Helfand, *Phys. Rev.* **119**, 1 (1960).

[239] A. Baldereschi, *Phys. Rev. B* **7**, 5212 (1973).

[240] F. Jaeger, O. K. Matar und E. A. Müller, *J. Chem. Phys.* **148**, 174504 (2018).

[241] R. E. Graves und B. M. Argrow, *J. Thermophys. Heat Tr.* **13**, 337 (1999).

[242] G. Emanuel und B. M. Argrow, *Phys. Fluids* **6**, 3203 (1994).

[243] A. Chikitkin, B. Rogov, G. Tirsky und S. Utyuzhnikov, *Appl. Numer. Math.* **93**, 47 (2015).

[244] J. Trullàs und J. A. Padró, *J. Chem. Phys.* **99**, 3983 (1993).

[245] X. Liu *et al.*, *Int. J. Thermophys.* **34**, 1169 (2013).

[246] A. J. White *et al.*, *Phys. Rev. E* **100**, 033213 (2019).

[247] S. Rehfeldt, Dissertation, Technische Universität München, (2009).

[248] T. Janzen und J. Vrabec, *Ind. Eng. Chem. Res.* **57**, 16508 (2018).

[249] R. Krishna und J. M. van Baten, *Ind. Eng. Chem. Res.* **44**, 6939 (2005).

[250] J. P. Hansen und I. R. McDonald, *Theory Of Simple Liquids* (Academic Press, London, 1976).

[251] R. Kubo, H. Hasegawa und N. Hashitsume, *J. Phys. Soc. Jpn.* **14**, 56 (1959).

[252] J. R. Adams, H. Reinholz und R. Redmer, *Phys. Rev. E* **81**, 036409 (2010).

[253] E. Runge und E. K. U. Gross, *Phys. Rev. Lett.* **52**, 997 (1984).

[254] X. Andrade, S. Hamel und A. A. Correa, *Eur. Phys. J. B* **91**, 229 (2018).

[255] J. Aubreton, M. F. Elchinger und J. M. Vinson, *Plasma Chem. Plasma Process.* **29**, 149 (2009).

[256] M. Gajdoš *et al.*, *Phys. Rev. B* **73**, 045112 (2006).

[257] B. Adolph, J. Furthmüller und F. Bechstedt, *Phys. Rev. B* **63**, 125108 (2001).

[258] G. V. Chester und A. Thellung, *Proc. Phys. Soc.* **77**, 1005 (1961).

[259] R. A. Redmer, G. Röpke, F. Morales und K. Kilimann, *Phys. Fluids B* **2**, 390 (1990).

[260] V. S. Karakhtanov, R. Redmer, H. Reinholz und G. Röpke, *Contrib. Plasma Phys.* **53**, 639 (2013).

[261] M. P. Desjarlais *et al.*, *Phys. Rev. E* **95**, 033203 (2017).

[262] L. Spitzer und R. Härm, *Phys. Rev.* **89**, 977 (1953).

[263] G. Röpke, M. Schörner, R. Redmer und M. Bethkenhagen, *Phys. Rev. E* **104**, 045204 (2021).

[264] M. French *et al.*, *Phys. Rev. E* **105**, 065204 (2022).

[265] J. N. Butler und R. S. Brokaw, *J. Chem. Phys.* **26**, 1636 (1957).

[266] R. S. Brokaw, *J. Chem. Phys.* **32**, 1005 (1960).

[267] K. Behringer und N. van Cung, *Appl. Phys.* **22**, 373 (1980).

[268] M. P. Desjarlais, J. D. Kress und L. A. Collins, *Phys. Rev. E* **66**, 025401(R) (2002).

[269] M. Pozzo, M. P. Desjarlais und D. Alfè, *Phys. Rev. B* **84**, 054203 (2011).

[270] K. Migdal *et al.*, *Appl. Surf. Sci.* **478**, 818 (2019).

[271] C. S. Alexander, J. R. Asay und T. A. Haill, *J. Appl. Phys.* **108**, 126101 (2010).

[272] N. de Koker, G. Steinle-Neumann und V. Vlček, *Proc. Natl. Acad. Sci. U.S.A.* **109**, 4070 (2012).

[273] M. Pozzo, C. Davies, D. Gubbins und D. Alfè, *Nature* **485**, 355 (2012).

[274] M. Pozzo, C. Davies, D. Gubbins und D. Alfè, *Phys. Rev. B* **87**, 014110 (2013).

[275] G. Bergmann und P. Marquardt, *Phys. Rev. B* **17**, 1355 (1978).

[276] R. Richter, M. Wolf und F. Goedsche, *phys. stat. sol. (b)* **95**, 473 (1979).

[277] P. Olson, *Science* **342**, 431 (2013).

[278] S. Labrosse, *Phys. Earth Planet. In.* **247**, 36 (2015).

[279] M. Pozzo, C. Davies, D. Gubbins und D. Alfè, *Phys. Rev. X* **9**, 041018 (2019).

[280] J. M. McMahon, M. A. Morales, C. Pierleoni und D. M. Ceperley, *Rev. Mod. Phys.* **84**, 1607 (2012).

[281] M. D. Knudson *et al.*, *Science* **348**, 1455 (2015).

[282] P. M. Celliers *et al.*, *Science* **361**, 677 (2018).

[283] M. Zaghoo, R. J. Husband und I. F. Silvera, *Phys. Rev. B* **98**, 104102 (2018).

[284] R. Helled, G. Mazzola und R. Redmer, *Nat. Rev. Phys.* **2**, 562 (2020).

[285] M. A. Morales, C. Pierleoni, E. Schwegler und D. M. Ceperley, *Proc. Natl. Acad. Sci. U.S.A.* **107**, 12799 (2010).

[286] W. Lorenzen, B. Holst und R. Redmer, *Phys. Rev. B* **82**, 195107 (2010).

[287] H. Y. Geng, Q. Wu, M. Marqués und G. J. Ackland, *Phys. Rev. B* **100**, 134109 (2019).

[288] M. Zaghoo, R. J. Husband und I. F. Silvera, *Phys. Rev. B* **98**, 104102 (2018).

[289] N. Nettelmann *et al.*, *Astrophys. J.* **683**, 1217 (2008).

[290] B. Militzer *et al.*, *Astrophys. J.* **688**, L45 (2008).

[291] J. Liu, P. Goldreich und D. Stevenson, *Icarus* **196**, 653 (2008).

[292] T. Gastine *et al.*, *Geophys. Res. Lett.* **41**, 5410 (2014).

[293] C. Jones, *Icarus* **241**, 148 (2014).

[294] J. Wicht, T. Gastine und L. D. V. Duarte, *J. Geophys. Res.-Planets* **124**, 837 (2019).

[295] J. Wicht, T. Gastine, L. D. V. Duarte und W. Dietrich, *Astron. Astrophys.* **629**, A125 (2019).

[296] J. Wicht und T. Gastine, *Nat. Commun.* **11**, 2886 (2020).

[297] J. Wicht *et al.*, *Magnetic Fields in the Solar System* (Springer, Astrophysics and Space Science Library, Cham, 2018), Band 448, pp. 7–82.

[298] K. M. Moore *et al.*, *Nature* **561**, 76 (2018).

[299] C. Jones, *Nature* **561**, 36 (2018).

[300] T. Encrenaz, *Annu. Rev. Astron. Astrophys.* **46**, 57 (2008).

[301] S. Stanley und J. Bloxham, *Nature* **428**, 151 (2004).

[302] M. Podolak, R. Helled und G. Schubert, *Mon. Notices Royal Astron. Soc.* **487**, 2653 (2019).

[303] C. J. T. de Grotthuss, *Ann. Chim.* **LVIII**, 54 (1806).

[304] T. R. Mattsson und M. P. Desjarlais, *Phys. Rev. Lett.* **97**, 017801 (2006).

[305] M. L. Huber *et al.*, *J. Phys. Chem. Ref. Data* **41**, 033102 (2012).

[306] M. Born und K. Huang, *Dynamical Theory of Crystal Lattices* (Oxford University Press, Oxford, 1954).

[307] R. Resta, *Ferroelectrics* **136**, 51 (1992).

[308] R. Resta, *Rev. Mod. Phys.* **66**, 899 (1994).

[309] S. Baroni, S. de Gironcoli, A. Dal Corso und P. Giannozzi, *Rev. Mod. Phys.* **73**, 515 (2001).

[310] T. Sun und R. M. Wentzcovitch, *Chem. Phys. Lett.* **554**, 15 (2012).

[311] P. Giannozzi, S. de Gironcoli, P. Pavone und S. Baroni, *Phys. Rev. B* **43**, 7231 (1991).

[312] D. J. Thouless, *Phys. Rev. B* **27**, 6083 (1983).

[313] F. Grasselli und S. Baroni, *Nat. Phys.* **15**, 967 (2019).

[314] V. Rozsa, D. Pan, F. Giberti und G. Galli, *Proc. Natl. Acad. Sci. U.S.A.* **115**, 6952 (2018).

[315] F. Grasselli, L. Stixrude und S. Baroni, *Nat. Commun.* **11**, 3605 (2020).

[316] R. D. King-Smith und D. Vanderbilt, *Phys. Rev. B* **47**, 1651 (1993).

[317] D. Soyuer, F. Soubiran und R. Helled, *Mon. Notices Royal Astron. Soc.* **498**, 621 (2020).

[318] A. Marcolongo, P. Umari und S. Baroni, *Nat. Phys.* **12**, 80 (2016).

[319] J. C. Slater und G. F. Koster, *Phys. Rev.* **94**, 1498 (1954).

[320] V. Botu, R. Batra, Chapman und R. Ramprasad, *J. Phys. Chem. C* **121**, 511 (2016).

[321] L. Zhang *et al.*, *Phys. Rev. Lett.* **120**, 143001 (2018).

[322] M. French, T. R. Mattsson, N. Nettelmann und R. Redmer, *Phys. Rev. B* **79**, 054107 (2009).

[323] L. Scheibe, N. Nettelmann und R. Redmer, *Astron. Astrophys.* **632**, A70 (2020).

[324] M. Podolak, R. Helled und G. Schubert, *Mon. Notices Royal Astron. Soc.* **487**, 2653 (2020).

[325] L. Scheibe, N. Nettelmann und R. Redmer, *Astron. Astrophys.* **650**, A200 (2021).

[326] W. Merryfield, *Astrophys. J.* **444**, 318 (1995).

[327] P. Garaud, *Annu. Rev. Fluid. Mech.* **50**, 275 (2018).

[328] G. Walin, *Tellus XVI* **3**, 389 (1964).

[329] R. W. Schmitt, *Annu. Rev. Fluid. Mech.* **26**, 255 (1994).

[330] N. C. Shibley und M.-L. Timmermans, *J. Geophys. Res. Oceans* **124**, 1445 (2019).

[331] M. A. Morales *et al.*, *Proc. Natl. Acad. Sci. U.S.A.* **106**, 1324 (2009).

[332] M. Schöttler und R. Redmer, *Phys. Rev. Lett.* **120**, 115703 (2018).

PHYSICAL REVIEW B **83**, 235120 (2011)

Electronic transport coefficients from *ab initio* simulations and application to dense liquid hydrogen

Bastian Holst, Martin French, and Ronald Redmer
Institut für Physik, Universität Rostock, D-18051 Rostock, Germany
(Received 25 March 2011; revised manuscript received 1 May 2011; published 10 June 2011)

Using Kubo's linear response theory, we derive expressions for the frequency-dependent electrical conductivity (Kubo-Greenwood formula), thermopower, and thermal conductivity in a strongly correlated electron system. These are evaluated within *ab initio* molecular dynamics simulations in order to study the thermoelectric transport coefficients in dense liquid hydrogen, especially near the nonmetal-to-metal transition region. We also observe significant deviations from the widely used Wiedemann-Franz law, which is strictly valid only for degenerate systems, and give an estimate for its valid scope of application toward lower densities.

DOI: 10.1103/PhysRevB.83.235120 PACS number(s): 61.20.Ja, 52.25.Fi, 72.10.Bg, 72.80.−r

I. INTRODUCTION

An accurate description of dense hydrogen is of fundamental interest and has wide applications in astrophysics. Prominent examples are models of planetary interiors which consist predominantly of hydrogen and helium as in the case of Jupiter-like planets.[1–3] Special attention has been paid on the high-pressure phase diagram of hydrogen and its isotopes. Major problems in this context are the slope of the melting line[4–7] and the transition pressure to solid metallic hydrogen,[8,9] which is expected near 4 Mbar[10] at $T = 0$ K. Such extreme conditions are experimentally still not feasible yet.

Interestingly, metallic hydrogen has first been verified in the liquid at about 1.4 Mbar and few thousand kelvin.[11,12] The problem of whether this transition is of first order has been discussed for decades. While numerous models within the chemical picture predict almost invariably a pronounced first-order phase transition with a critical point at about 10 000 K–15 000 K and 0.5 Mbar,[13–18] only few *ab initio* simulations indicate such a behavior.[19–23] A first-order liquid-liquid phase transition with a critical point near 2000 K and 120 GPa has been predicted from both quantum Monte Carlo (QMC) and finite-temperature density functional theory molecular dynamics (FT-DFT-MD) simulations.[22] These results were confirmed almost simultaneously by extensive FT-DFT-MD simulations,[23] which predict a critical point at about 1400 K and 132 GPa, that is, at a somewhat lower temperature. A detailed analysis of the changes in the structural and electronic properties with density and temperature clearly shows that the nonmetal-to-metal transition in dense liquid hydrogen drives this first-order phase transition.

The transport coefficients yield valuable information on the state of the strongly correlated liquid. For instance, the conductivity changes drastically along the nonmetal-to-metal transition over many orders of magnitude which could already be verified experimentally.[11,12] These measures have the potential to accurately characterize subtle changes of the electronic structure with density and temperature and, especially, alongside the liquid-liquid phase transition in hydrogen. We therefore calculate the complete set of thermoelectric transport coefficients (electrical and thermal conductivity, thermopower) via FT-DFT-MD simulations for a wide range of densities [$\rho = (0.05\text{–}20)$ g/cm^3] and temperatures [$T = (1\text{–}50) \times 10^3$ K] and pay special attention to the nonmetal-to-metal transition region. The focus of our work is below 20 g/cm^3 since higher densities are of primary importance for the physics of inertial confinement fusion and were studied previously.[24]

The transport coefficients as well as their changes with density and temperature are again important for applications in astrophysics. For instance, a boundary between a nonconducting outer and a metallic inner envelope is usually assumed in interior models of gas giants such as Jupiter; its location should, in principle, be determined from the nonmetal-to-metal transition in hydrogen but is usually a free parameter.[25] Furthermore, it has been shown that demixing of helium from hydrogen occurs in H-He mixtures at megabar pressures due to the nonmetal-to-metal transition in the hydrogen subsystem.[26,27] The treatment of this effect is essential in order to explain the excess luminosity of Saturn and its age.[28] Knowledge on the transport coefficients of dense liquid hydrogen is furthermore required for dynamo simulations of planetary magnetic fields.[29] The dynamo is driven by convection of conducting material deep in the interior so that the electrical and thermal conductivity are important input quantities. Another interesting problem is the formation of giant planets out of a protoplanetary disk. The conductivities change by many orders of magnitude during the accretion process as a consequence of the density and temperature increase, which could affect the radiation hydrodynamics of the collapsing disk and the luminosity of the young protoplanet strongly.

There are a number of theoretical models that predict the electrical and thermal conductivity with different assumptions about the electronic and ionic structure and their mutual interaction.[16,30–38] Especially in a strongly coupled system it is difficult to calculate the transport properties accurately because the ionization degree and the effective two-particle scattering cross sections are not well defined. Strong ion-ion correlations, the dynamic nature of screening and exchange effects in the electron system as well as quantum effects such as Pauli blocking require a consistent quantum-statistical approach. Therefore, we calculate the transport coefficients within FT-DFT-MD simulations. This method has demonstrated its capacity to provide accurate data for the strongly correlated quantum regime.[39–42]

1098-0121/2011/83(23)/235120(8)

For simple metals the relation between electrical and thermal conductivity is described by the famous Wiedemann-Franz law[43] using a fixed value, the Lorenz number L_0, as proportionality constant. The benefit from this relation is the ability to obtain the thermal conductivity from the electrical conductivity very easily. For this procedure the Lorenz number $L(T,\rho)$ has to be known for a given density ρ and temperature T of the system. By calculating the Lorenz number *ab initio* the region where the original Wiedemann-Franz law is valid can be identified.

Our paper is organized as follows. We outline the FT-DFT-MD method in Sec. II. A generalization of the Kubo-Greenwood formula to calculate the Onsager coefficients L_{ik} is given in Sec. III. The results for the electrical and thermal conductivity, the thermopower, and the Lorenz number in dense liquid hydrogen are presented in Sec. IV for a wide range of densities and temperatures. In particular, the behavior predicted for the nonmetal-to-metal transition region is discussed. Conclusions are given in Sec. V.

II. THEORETICAL METHOD

We use the FT-DFT-MD framework, which combines classical molecular dynamics simulations for the ions with a quantum treatment of the electrons based on FT-DFT[44–46] which is implemented in the VASP 5.2 program package.[47–49] In the FT-DFT the Coulomb interactions between the electrons and the ions are treated using the projector-augmented wave method[50,51] at densities below 9 g/cm^3 with a converged energy cutoff of 800 eV. At higher densities it was necessary to perform all calculations with the Coulomb potential which required a substantial higher cutoff of 3000 eV.

The FT-DFT algorithm is used to derive the forces that act on the ions via the Hellmann-Feynman theorem at each MD step. This procedure is repeatedly performed in a cubic simulation box with periodic boundary conditions for several thousand MD time steps of 0.1 to 1 fs duration so that the total simulation time amounts up to 10 ps. The ion temperature is controlled with a Nosé thermostat.[52]

Convergence was checked with respect to the particle numbers, which vary between 64 and 512 atoms depending on the density, the **k**-point sets used for the evaluation of the Brillouin zone, and the energy cutoff for the plane wave basis set. For the simulations we chose the Baldereschi mean value point,[53] which proved to yield well converged simulation runs.[23,41] Several test calculations showed that higher efforts are necessary only in the vicinity of the phase transition.[23]

The electronic transport coefficients are subsequently calculated by evaluating the respective transport formulas (see section below).[54] This is done for 10 to 20 ion configurations from the equilibrated MD simulation using Monkhorst-Pack **k**-point meshes[55] of $3\times3\times3$ to $6\times6\times6$ to reach the convergence.

The exchange-correlation functional is the most critical input in FT-DFT calculations. Here we use the approximation of Perdew, Burke, and Ernzerhof,[56] which is numerically efficient. This functional has been chosen in similar studies[24,57,58] and reasonable results are, in general, expected in the metallic and high-temperature plasma regime.[59,60] In the semiconducting region the obtained conductivities may be overestimated by using this functional but will yet be useful for many practical applications.

Note that the ionic contribution to the transport coefficients is out of the scope of this work and is therefore consistently neglected.

III. TRANSPORT PROPERTIES AND ONSAGER COEFFICIENTS

In linear response theory (LRT) the response of an isotropic single component system of charge carriers (electrons with charge $q=-e$ in our case) to an electric field $\mathbf{E}$ and a temperature gradient ∇T is expressed by the electric current $\mathbf{J}_e$ and the heat current $\mathbf{J}_q$ through

$$\langle \mathbf{J}_e\rangle = \frac{1}{q}\left(qL_{11}\mathbf{E}+\frac{L_{12}\nabla T}{T}\right), \tag{1}$$

$$\langle \mathbf{J}_q\rangle = \frac{1}{q}\left(qL_{21}\mathbf{E}+\frac{L_{22}\nabla T}{T}\right). \tag{2}$$

The electrical conductivity σ, thermal conductivity λ, and thermopower α are then given by the Onsager coefficients L_{mn} in the following way:

$$\sigma = L_{11},\quad \lambda = \frac{1}{T}\left(L_{22}-\frac{L_{12}^2}{L_{11}}\right),\qquad \alpha = \frac{L_{12}}{TL_{11}}. \tag{3}$$

The Lorenz number is the ratio between electrical and thermal conductivity divided by the temperature,

$$L = \frac{e^2}{k_B^2 T}\frac{\lambda}{\sigma}, \tag{4}$$

and is, according to the Wiedemann-Franz law,[43] constant in the limit of high density, where it can be calculated as $L_0=\pi^2/3$ by means of the Sommerfeld expansion.[61]

Within the framework of Kubo's quantum-statistical LRT, which is described, for instance, in Refs. 62 and 63, the following expressions are obtained for the frequency-dependent Onsager coefficients $L_{mn}(\omega)$:

$$L_{mn}(\omega) = \frac{1}{3V}\langle \hat{\mathbf{J}}_m(t-i\hbar\tau);\hat{\mathbf{J}}_n\rangle_{\omega+i\varepsilon}. \tag{5}$$

The current-current correlation functions are given as

$$\langle \hat{\mathbf{J}}_m(t-i\hbar\tau);\hat{\mathbf{J}}_n\rangle_{\omega+i\varepsilon} = \lim_{\varepsilon\to 0}\int_0^\infty \mathrm{d}t\, e^{i(\omega+i\varepsilon)t}\int_0^\beta \mathrm{d}\tau\, \mathrm{Tr}\{\hat{\varrho}_0\hat{\mathbf{J}}_m(t-i\hbar\tau)\cdot\hat{\mathbf{J}}_n\}, \tag{6}$$

where $\beta=(k_BT)^{-1}$ is the inverse thermal energy. The limit $\varepsilon\to 0$ has to be taken after the calculation of the thermodynamic limit, which is done by evaluating the trace. The statistical operator of the equilibrium $\hat{\varrho}_0$ contains the Kohn-Sham Hamilton operator $\hat{H}_{\mathrm{KS}}$.

The time-dependent current operators within the Heisenberg picture are defined as

$$\hat{\mathbf{J}}_m(t-i\hbar\tau) = e^{\frac{i}{\hbar}(t-i\hbar\tau)\hat{H}_{\mathrm{KS}}}\hat{\mathbf{J}}_m e^{-\frac{i}{\hbar}(t-i\hbar\tau)\hat{H}_{\mathrm{KS}}}. \tag{7}$$

The electric current operator $\hat{\mathbf{J}}_e = \hat{\mathbf{J}}_1$ and the heat current operator $\hat{\mathbf{J}}_q = \hat{\mathbf{J}}_2$ read in second quantization of spin degenerate Bloch states:

$$\hat{\mathbf{J}}_m = \sum_{\mathbf{k}\mathbf{k}'\nu\nu'} \langle \mathbf{k}\nu|\hat{\mathbf{j}}_m|\mathbf{k}'\nu'\rangle \hat{a}^{\dagger}_{\mathbf{k}\nu}\hat{a}_{\mathbf{k}'\nu'}. \tag{8}$$

Here $\mathbf{k}$ is the wave number and ν the band index. The electric and heat current operators are given as

$$\hat{\mathbf{j}}_1 = \frac{q}{m_e}\hat{\mathbf{p}}, \tag{9}$$

$$\hat{\mathbf{j}}_2 = \frac{1}{m_e}\frac{\hat{H}\hat{\mathbf{p}} + \hat{\mathbf{p}}\hat{H}}{2} - h_e\hat{\mathbf{p}}, \tag{10}$$

where h_e is the enthalpy per electron (see Ref. 64 for further information on the definition of the currents).

The eigenvalues of the Hamiltonian can be evaluated so that Eq. (8) can be simplified,

$$\hat{\mathbf{J}}_m = \frac{q^{2-m}}{m_e} \sum_{\mathbf{k}\mathbf{k}'\nu\nu'} \langle \mathbf{k}\nu|\hat{\mathbf{p}}|\mathbf{k}'\nu'\rangle \epsilon^{m-1}_{\mathbf{k}\nu\mathbf{k}'\nu'} \hat{a}^{\dagger}_{\mathbf{k}\nu}\hat{a}_{\mathbf{k}'\nu'}, \tag{11}$$

where

$$\epsilon_{\mathbf{k}\nu\mathbf{k}'\nu'} = \left(\frac{E_{\mathbf{k}\nu} + E_{\mathbf{k}'\nu'}}{2} - h_e\right) \tag{12}$$

is used. After inserting Eq. (11) into Eq. (6) and some operator algebra the trace can be evaluated according to Wick's theorem as

$$\begin{aligned}\mathrm{Tr}\{\hat{\varrho}_{eq}\hat{a}^{\dagger}_{\mathbf{k}\nu}\hat{a}_{\mathbf{k}'\nu'}\hat{a}^{\dagger}_{\mathbf{p}\mu}\hat{a}_{\mathbf{p}'\mu'}\} &= f_{\mathbf{k}\nu}\delta_{\mathbf{k},\mathbf{k}'}\,\delta_{\nu,\nu'}\,f_{\mathbf{p}\mu}\delta_{\mathbf{p},\mathbf{p}'}\,\delta_{\mu,\mu'}\\ &\quad + f_{\mathbf{k}\nu}\delta_{\mathbf{k},\mathbf{p}'}\,\delta_{\nu,\mu'}(1 - f_{\mathbf{p}\mu})\delta_{\mathbf{p},\mathbf{k}'}\,\delta_{\mu,\nu'}.\end{aligned} \tag{13}$$

The first term vanishes and the Fermi functions are defined as $f_{\mathbf{k}\nu} = (e^{\beta(E_{\mathbf{k}\nu}-\mu_e)} + 1)^{-1}$. Altogether the trace reads

$$\begin{aligned}&\mathrm{Tr}\{\hat{\varrho}_0\hat{\mathbf{J}}_m(t - i\hbar\tau)\cdot\hat{\mathbf{J}}_n\}\\ &= \frac{q^{4-m-n}}{m_e^2}\sum_{\mathbf{k}\mathbf{p}\nu\mu} e^{\frac{i}{\hbar}(t-i\hbar\tau)\Delta E} f_{\mathbf{k}\nu}(1 - f_{\mathbf{p}\mu})\langle \mathbf{k}\nu|\hat{\mathbf{p}}|\mathbf{p}\mu\rangle\\ &\quad\times \langle \mathbf{p}\mu|\hat{\mathbf{p}}|\mathbf{k}\nu\rangle \epsilon^{m-1}_{\mathbf{k}\nu\mathbf{p}\mu}\epsilon^{n-1}_{\mathbf{p}\mu\mathbf{k}\nu},\end{aligned} \tag{14}$$

with $\Delta E = E_{\mathbf{k}\nu} - E_{\mathbf{p}\mu}$. Now the τ integration can be performed:

$$\int_0^{\beta} \mathrm{d}\tau\, e^{\tau\Delta E} = \frac{e^{\beta\Delta E} - 1}{\Delta E}. \tag{15}$$

In the same way the second integral can be solved:

$$\begin{aligned}\lim_{\varepsilon\to 0}\int_0^{\infty} \mathrm{d}t e^{(-\varepsilon + i\omega + \frac{i}{\hbar}\Delta E)t} &= \hbar\pi\,\delta\,(\Delta E + \hbar\omega)\\ &\quad + i\hbar\,\mathcal{P}\left(\frac{1}{\Delta E + \hbar\omega}\right).\end{aligned} \tag{16}$$

Only the real part of this equation is considered here, since the imaginary part can be calculated more easily with a Kramers-Kronig relation. The Onsager coefficients now read

$$\begin{aligned}L_{mn} &= \frac{\hbar\pi q^{4-m-n}}{3Vm_e^2}\sum_{\mathbf{k}\mathbf{p}\nu\mu}\frac{e^{\beta\Delta E} - 1}{\Delta E} f_{\mathbf{k}\nu}(1 - f_{\mathbf{p}\mu})\\ &\quad\times \langle \mathbf{k}\nu|\hat{\mathbf{p}}|\mathbf{p}\mu\rangle\cdot\langle \mathbf{p}\mu|\hat{\mathbf{p}}|\mathbf{k}\nu\rangle\delta(\Delta E + \hbar\omega)\,\epsilon^{m-1}_{\mathbf{k}\nu\mathbf{p}\mu}\epsilon^{n-1}_{\mathbf{p}\mu\mathbf{k}\nu}.\end{aligned} \tag{17}$$

In position representation the matrix elements have the following form:

$$\langle \mathbf{k}\nu|\hat{\mathbf{p}}|\mathbf{p}\mu\rangle = \delta_{\mathbf{p},\mathbf{k}}\left(\hbar\mathbf{k}\,\delta_{\nu,\mu} + \frac{1}{V}\int_V \mathrm{d}^3\mathbf{r}\,u^*_{\mathbf{k}\nu}(\mathbf{r})\hat{\mathbf{p}}\,u_{\mathbf{k}\mu}(\mathbf{r})\right). \tag{18}$$

Here V is the volume of the simulation box and the functions $u^*_{\mathbf{k},\nu}(\mathbf{r})$ and $u_{\mathbf{k},\mu}(\mathbf{r})$ are the Bloch factors. Because of the first Kronecker symbol the matrix elements are diagonal concerning the wave number, which eliminates the $\mathbf{p}$ sum. The spin summation leads to an additional factor of two. After using a relation between Fermi functions we finally arrive at the following expression for the Onsager coefficients:

$$\begin{aligned}L_{mn}(\omega) &= \frac{2\pi q^{4-m-n}}{3Vm_e^2\omega}\sum_{\mathbf{k}\nu\mu}\langle \mathbf{k}\nu|\hat{\mathbf{p}}|\mathbf{k}\mu\rangle\cdot\langle \mathbf{k}\mu|\hat{\mathbf{p}}|\mathbf{k}\nu\rangle\\ &\quad\times\epsilon^{m+n-2}_{\mathbf{k}\nu\mathbf{k}\mu}(f_{\mathbf{k}\nu} - f_{\mathbf{k}\mu})\delta(E_{\mathbf{k}\mu} - E_{\mathbf{k}\nu} - \hbar\omega).\end{aligned} \tag{19}$$

The Onsager coefficients (19) obey the symmetry relations $L_{mn}(\omega) = L_{mn}(-\omega)$ and $L_{mn}(\omega) = L_{nm}(\omega)$. The coefficient L_{11} is known as the frequency-dependent Kubo-Greenwood formula[65,66] and has been widely applied in FT-DFT-MD simulations.[39,67,68]

Similar but not identical frequency-dependent formulas for L_{12} and L_{22} were given by Recoules *et al.*[40] but not formally derived in their work. The different formulations lead to deviations in the results for the thermopower α and in the thermal conductivity λ at nonzero frequencies. Furthermore, the heat current from Ref. 40 contains the chemical potential μ_e instead of the enthalpy h_e [see Eq. (10)]. However, it can be shown that the term proportional to the enthalpy per particle h_e has no influence on the thermal conductivity λ in one-component systems. As a consequence the numerical results of Refs. 24 and 40 could be reproduced by Eq. (19) in the limit of $\omega \to 0$ and are therefore not questioned by the current work. Differences, however, occur in the static results for the thermopower α.

The derivation in this chapter can be easily generalized to the spin-dependent form as well as to anisotropic systems.

IV. RESULTS

A. Electrical conductivity

Figure 1 shows isotherms of the electrical conductivity over a wide range of densities and temperatures. In previous work[41] it could already be shown that these theoretical results agree well with data for the reflectivity and conductivity derived from shock-wave experiments. Here we concentrate on the general behavior of the theoretical curves on a large density and temperature scale and give results especially in the vicinity of the nonmetal-to-metal transition.

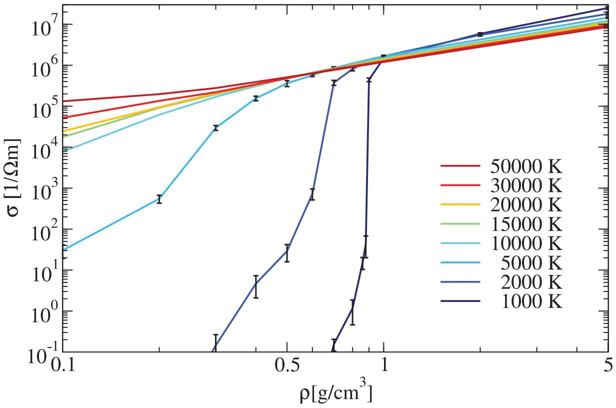

FIG. 1. (Color online) Electrical conductivity in dense hydrogen for different temperatures from the region of the liquid-liquid phase transition up to the dense plasma. At low densities the values increase with temperature and decrease with temperature at high densities.

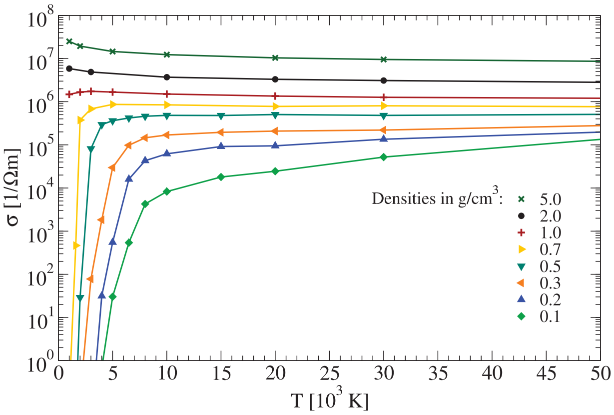

FIG. 2. (Color online) Electrical conductivity for different densities versus temperature.

In general, the conductivity rises in the whole range studied here with increasing density. On the one hand, this is the result of pressure ionization which increases the amount of conducting electrons, and on the other hand, even in the case of a fully ionized system, a rising density of electrons results in a further increase of the conductivity.

At $T = 1000$ K the liquid-liquid phase transition which was previously reported for dense hydrogen[22,23] can be identified by the steep increase of the conductivity over several orders of magnitude in a small density interval, $(0.7 - 0.9)$ g/cm^3. At temperatures higher than 1500 K the transition is continuous and the increase spreads to a larger range in density. At densities below this transition the electrical conductivity increases with temperature which is caused by thermal ionization of neutral particles. The additional free charges contribute to the conductivity.

At densities above this transition the dependence on temperature is inverted: The electrical conductivity decreases with temperature, which is typical for metals. Increasing temperature broadens the Fermi function and therefore allows additional electron scattering processes which reduce their mobility. As a result, the conductivity is lower with increasing temperature.

This behavior is also illustrated in Fig. 2, which shows the electrical conductivity along isochores for different temperatures. The conductivity decreases for temperatures above 2000 K along the isochores for densities higher than 0.9 g/cm^3, which are characteristic of the metallic phase. This indicates that most of the system is ionized and thus acts metal-like. Looking at lower densities the conductivity rises along the whole temperature range, which is due to thermal ionization. The isochores clearly show the general behavior of a rising conductivity with increasing density.

Experiments in copper plasmas[69] have indicated that the electrical conductivity becomes a function of only the coupling parameter Γ for values of $\Gamma \geqslant 10$. The plasma parameter Γ is defined by

$$\Gamma = \frac{e^2}{4\pi\varepsilon_0 k_B T}\left(\frac{4\pi n_e}{3}\right)^{\frac{1}{3}}, \tag{20}$$

where n_e is the number density of free electrons. Although such a behavior could not be confirmed later,[70] a simple functional form of the electrical conductivity at high values of Γ is still under discussion. To investigate whether such a simple scaling is valid in dense liquid hydrogen, the results for the electrical conductivity shown in Figs. 1 and 2 are plotted against Γ in Fig. 3. Only for temperatures higher than 10 000 K is the system strongly ionized. At lower temperatures the occurrence of partial ionization prevents a proper calculation of Γ within FT-DFT-MD, because the method does not distinguish between bound and free electrons. Therefore, we do not plot results for lower temperatures in Fig. 3.

The isotherms appear to be almost parallel in this logarithmic plot and are clearly separated. Even at the highest available values for $\Gamma \leqslant 60$ the isotherms do not tend to merge. We conclude that it is not possible to derive a simple temperature-independent relation for the conductivity that depends solely on the parameter Γ as it was proposed earlier for other metallic liquids.

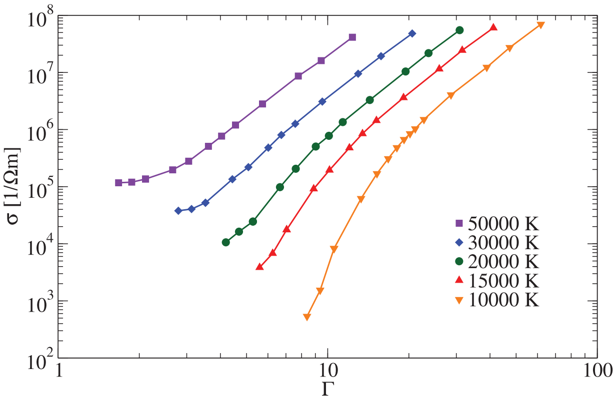

FIG. 3. (Color online) Electrical conductivity as function of the coupling parameter Γ for different temperatures. The plotted data cover a density range of (0.05–20) g/cm^3.

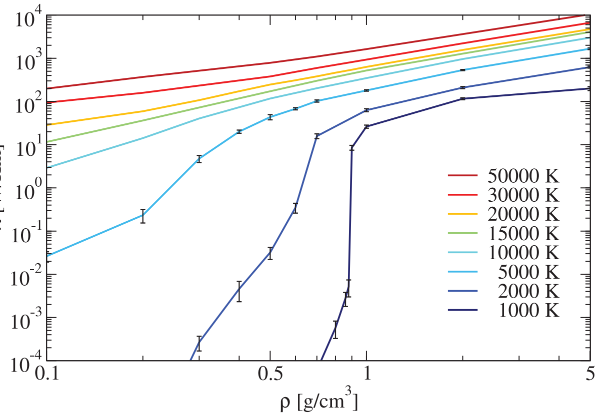

FIG. 4. (Color online) Thermal conductivity versus density for different temperatures. The values increase with temperature.

B. Thermal conductivity

The isotherms of the thermal conductivity are plotted in Fig. 4. They show a similar behavior as the electrical conductivity and indicate a sharp nonmetal-to-metal transition at a temperature below 1500 K. At this transition the thermal conductivity increases over several orders of magnitude in a narrow density range at about 0.9 g/cm^3. The increase in the thermal conductivity is due to the growing number of delocalized electrons which are produced along the phase transition. Above the critical temperature this transition becomes broader and is caused by a combination of pressure and temperature ionization.

In contrast to the behavior of the electrical conductivity, the thermal conductivity does not decrease with temperature in the metallic phase. The isotherms increase systematically with temperature for all densities.

This is also shown along the isochores of the thermal conductivity that are plotted in Fig. 5. These curves depict likewise that the thermal conductivity rises invariably with increasing density and temperature.

C. Thermopower

The thermopower α characterizes the generation of an electric field as a response to a temperature gradient. For most systems this electric field has a direction opposite to the temperature gradient, which results in a negative thermopower. The thermopower is most sensitive to changes in the electronic structure since it can be expressed as the derivative of the logarithm of the electronic conductivity with respect to the energy at the Fermi surface.[71] Such a relation, which is also known as Mott formula, follows from the Kubo-Greenwood equation (19) in the degenerate domain under strong scattering conditions.

Interestingly, large positive values for the thermopower were measured in fluid mercury[72,73] near the liquid-vapor critical point, which is located at $T_c = 1751$ K and $\varrho_c = 5.8$ g/cm^3. In this region, isotherms of the electrical conductivity near T_c show a strong increase with the density, which is steepest just at the critical density ϱ_c. This behavior was assumed to be related to fluctuations in the electron density, which are pronounced near the critical point due to critical fluctuations. In particular, a zero of the thermopower was observed exactly at the critical density. The interesting question arises as to whether a zero of the thermopower is a precursor of a first-order phase transition in dense liquids which undergo a nonmetal-to-metal transition. Wide regions with a positive thermopower have been predicted for dense hydrogen by a simple chemical model[34] but were not confirmed in an advanced chemical approach[16] by *ab initio* simulations or by experiments yet.

In Fig. 6 isotherms of the thermopower α are plotted as function of the density. The symbols represent the results from the simulations and the error bars show the statistical uncertainties. As guide to the eye, polynomial functions were fitted to the numerical results. The thermopower is mostly negative and reaches a value of about zero at high densities. At lower densities the thermopower decreases. The low density limit of $\alpha = -60.60$ μV/K is known from the Spitzer theory (see, e.g., Ref. 16). With higher temperatures the negative values become systematically larger. We expect that these values become smaller again at low densities to reach the Spitzer limit. The thermopower shows positive mean values below 20 000 K and between 0.2 g/cm^3 and 0.5 g/cm^3. These

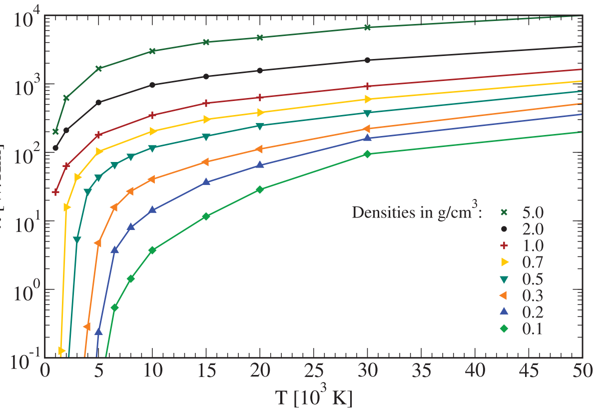

FIG. 5. (Color online) Thermal conductivity versus temperature for different densities.

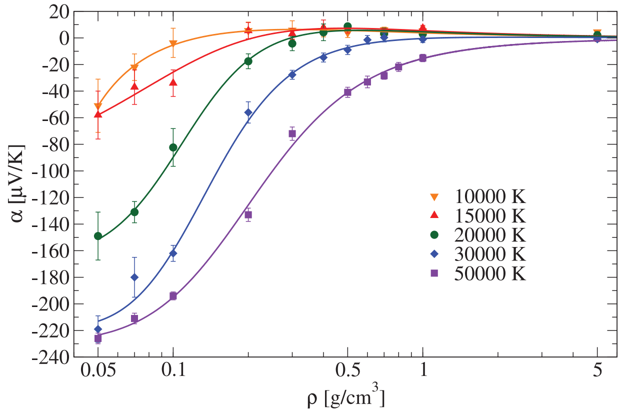

FIG. 6. (Color online) Thermopower versus density for different temperatures.

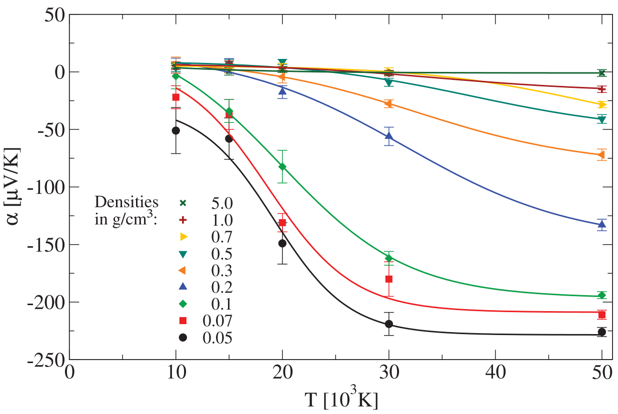

FIG. 7. (Color online) Thermopower versus temperature for different densities.

values are very small and, in fact, are about the size of the uncertainties of the respective mean values. We therefore cannot conclude definitely that significantly positive values occur within the accuracy of our *ab initio* calculations. To answer the question as to whether the zero of the thermopower occurs at the critical point of the liquid-liquid phase transition in dense hydrogen, which is predicted[22,23] at about 0.8 g/cm^3, the thermopower has to be evaluated for temperatures below 2000 K since $T_c = (1400–2000)$ K. For this region, reasonable results can be given for the electrical and thermal conductivity but not for the thermopower. This is because the values of the Onsager coefficients each decrease over orders of magnitude in systems with a majority of localized electrons, while especially the decrease of L_{12} is two orders of magnitude weaker than that of L_{11}. This behavior, on the one hand, causes the second contribution to the thermal conductivity in Eq. (3) to vanish, because L_{12} is squared in the numerator. As a result the thermal conductivity becomes proportional to L_{22}, which can be evaluated successfully in this case, as well as L_{11}. On the other hand, this leads to an enormous increase in the statistical fluctuations of the thermopower, which causes uncertainties that reach hundreds of μV/K.

In Fig. 7 isochores of the thermopower α are plotted. The thermopower decreases with higher temperature, which is more pronounced the lower the density is. Positive values appear at low temperatures, but the statistical error is too large to prove this result unambiguously.

D. Lorenz number

The Lorenz number Eq. (4) describes mainly the relation between thermal and electrical conductivity. For simple metals this relation is described via a constant and is known as the Wiedemann-Franz law. For high degeneracy this constant is $L_0 = \pi^2/3$.[61] This relation can be used to easily obtain the thermal conductivity for metals if the electrical conductivity is known. Here we calculate the Lorenz number for dense hydrogen in order to identify the region where the Wiedemann-Franz law is valid. High degeneracy occurs only at sufficiently high densities so that we expect deviations from the Wiedemann-Franz law at lower densities and higher temperatures.

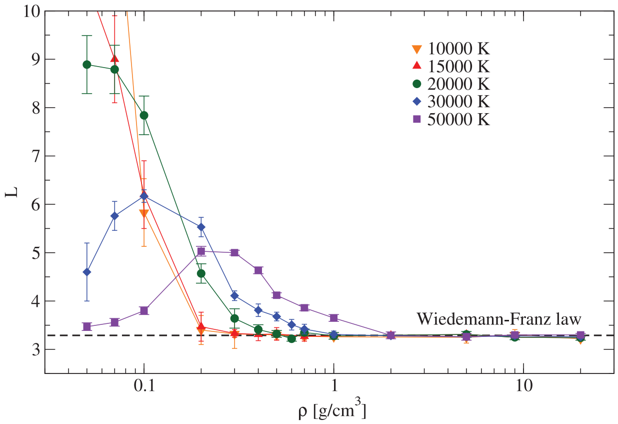

FIG. 8. (Color online) Lorenz number versus density for different temperatures. The dashed black line displays the limiting value of $L_0 = \pi^2/3$.

The Lorenz number is shown in Fig. 8 for several temperatures. At densities above 1 g/cm^3 the Lorenz number is almost constant and shows no temperature dependence, which indicates that the Wiedemann-Franz law is valid there. The value of $L_0 = \pi^2/3$, which is shown by a dashed black line, could be reproduced for each temperature at densities higher than (1–2) g/cm^3 within the statistical uncertainties. This behavior is consistent with the metalliclike properties observed already for the conductivity at high densities.

At densities below (1–2) g/cm^3 the Lorenz number shows strong deviations from the Wiedemann-Franz law with a pronounced temperature dependence. In particular, the Lorenz number rises strongly with decreasing density. This behavior becomes more pronounced at lower temperatures. On the other hand, at the lower temperatures the validity of the Wiedemann-Franz law extends to smaller densities, for example, down to 0.2 g/cm^3 at 10 000 K and 15 000 K.

Along the isotherms of 30 000 K and 50 000 K a maximum can be identified. Thus, at lower densities the Lorenz number decreases again. At 30 000 K this maximum is found at a smaller density than at 50 000 K and shows a larger value. This indicates that with decreasing temperature the maximum shifts systematically to smaller densities and increases. For temperatures below 30 000 K the maximum is not displayed. It appears to be situated at densities below 0.05 g/cm^3, which is the minimal density calculated here and which displays the current limit of our computational capabilities. However, we expect a maximum to appear for all temperatures because the Lorenz number is also known exactly at low densities from the Spitzer theory for fully ionized plasmas.[30] The latter predicts a constant low-density value of 1.5966 (see, e.g., Ref. 16).

Our results indicate that the deviations from the Wiedemann-Franz law might reach a full order of magnitude in certain regions of density and temperature. Further research will be necessary to investigate this important aspect in more detail. We also expect that certain deviations from the Wiedemann-Franz law occur in warm dense matter of arbitrary composition. In hydrogen, we predict that the Wiedemann-Franz is valid at densities above 2 g/cm^3 for temperatures below 50 000 K (see Fig. 8).

V. CONCLUSIONS

We derived formulas for the Onsager transport coefficients L_{mn} within the Kubo theory for application in *ab initio* simulations. Using these expressions we calculated the electrical and thermal conductivity as well as the thermopower of liquid hydrogen for a wide range of temperatures and densities in the megabar range. In particular, we characterize the nonmetal-to-metal transition in hydrogen by observing a rapid increase in both the electrical and the thermal conductivity. The thermopower shows a trend toward positive values in a region where the critical point of the liquid-liquid phase transition is expected, similar to the behavior of liquid mercury. At low temperatures more accurate calculations will be necessary for this transport coefficient which are beyond the scope of the currently available computer capacity. The *ab initio* calculation of the Lorenz number shows, in addition, that the validity of the original Wiedemann-Franz law is limited to the metalliclike regime of hydrogen. The theoretical framework given here can be applied to bulk material calculations for arbitrary materials within FT-DFT-MD.

ACKNOWLEDGMENTS

We thank Michael P. Desjarlais, Winfried Lorenzen, Thomas R. Mattsson, Stephane Mazevet, and Vanina Recoules for many helpful discussions. This work was supported by the Deutsche Forschungsgemeinschaft within the SFB 652 and DFG Project No. SPP 1488 (planetary magnetism) and the North-German Supercomputing Alliance (HLRN).

---

[1] T. Guillot, Science **286**, 72 (1999).

[2] N. Nettelmann, B. Holst, A. Kietzmann, M. French, R. Redmer, and D. Blaschke, Astrophys. J. **683**, 1217 (2008).

[3] J. J. Fortney and N. Nettelmann, Space Sci. Rev. **152**, 423 (2010).

[4] S. A. Bonev, E. Schwegler, T. Ogitsu, and G. Galli, Nature (London) **431**, 669 (2004).

[5] E. Gregoryanz, A. F. Goncharov, K. Matsuishi, H.-k. Mao, and R. J. Hemley, Phys. Rev. Lett. **90**, 175701 (2003).

[6] S. Deemyad and I. F. Silvera, Phys. Rev. Lett. **100**, 155701 (2008).

[7] M. I. Eremets and I. A. Trojan, JETP Lett. **89**, 174 (2009).

[8] P. Loubeyre, F. Occelli, and R. LeToullec, Nature (London) **416**, 613 (2002).

[9] C. J. Pickard and R. J. Needs, Nat. Phys. **3**, 473 (2007).

[10] M. Städele and R. M. Martin, Phys. Rev. Lett. **84**, 6070 (2000).

[11] S. T. Weir, A. C. Mitchell, and W. J. Nellis, Phys. Rev. Lett. **76**, 1860 (1996).

[12] W. J. Nellis, S. T. Weir, and A. C. Mitchell, Phys. Rev. B **59**, 3434 (1999).

[13] W. Ebeling and W. Richert, Phys. Lett. A **108**, 80 (1985).

[14] D. Saumon and G. Chabrier, Phys. Rev. Lett. **62**, 2397 (1989).

[15] M. Schlanges, M. Bonitz, and A. Tschttschjan, Contrib. Plasma Phys. **35**, 109 (1995).

[16] H. Reinholz, R. Redmer, and S. Nagel, Phys. Rev. E **52**, 5368 (1995).

[17] D. Beule, W. Ebeling, A. Förster, H. Juranek, S. Nagel, R. Redmer, and G. Röpke, Phys. Rev. B **59**, 14177 (1999).

[18] B. Holst, N. Nettelmann, and R. Redmer, Contrib. Plasma Phys. **47**, 368 (2007).

[19] V. S. Filinov, V. E. Fortov, M. Bonitz, and P. Levashov, JETP Lett. **74**, 384 (2001).

[20] S. Scandolo, Proc. Natl. Acad. Sci. USA **100**, 3051 (2003).

[21] B. Jakob, P.-G. Reinhard, C. Toepffer, and G. Zwicknagel, Phys. Rev. E **76**, 036406 (2007).

[22] M. A. Morales, C. Pierleoni, E. Schwegler, and D. M. Ceperley, Proc. Natl. Acad. Sci. USA **107**, 12799 (2010).

[23] W. Lorenzen, B. Holst, and R. Redmer, Phys. Rev. B **82**, 195107 (2010).

[24] V. Recoules, F. Lambert, A. Decoster, B. Canaud, and J. Clérouin, Phys. Rev. Lett. **102**, 075002 (2009).

[25] D. Saumon, G. Chabrier, and H. M. van Horn, Astrophys. J. Suppl. Ser. **99**, 713 (1995).

[26] W. Lorenzen, B. Holst, and R. Redmer, Phys. Rev. Lett. **102**, 115701 (2009).

[27] M. A. Morales, E. Schwegler, D. Ceperley, C. Pierleoni, S. Hamel, and K. Caspersen, Proc. Natl. Acad. Sci. USA **106**, 1324 (2009).

[28] J. J. Fortney and W. B. Hubbard, Astrophys. J. **608**, 1039 (2004).

[29] J. Wicht and A. Tilgner, Space Sci. Rev. **152**, 501 (2010).

[30] L. Spitzer and R. Härm, Phys. Rev. **89**, 977 (1953).

[31] H. Minoo, C. Deutsch, and J. Hansen, Phys. Rev. A **14**, 840 (1976).

[32] D. B. Boercker, F. J. Rogers, and H. E. DeWitt, Phys. Rev. A **25**, 1623 (1982).

[33] Y. T. Lee and R. M. More, Phys. Fluids **27**, 1273 (1984).

[34] F. Höhne, R. Redmer, G. Röpke, and H. Wegener, Physica A **128**, 643 (1984).

[35] S. Ichimaru and S. Tanaka, Phys. Rev. A **32**, 1790 (1985).

[36] G. A. Rinker, Phys. Rev. A **37**, 1284 (1988).

[37] H. Kitamura and S. Ichimaru, Phys. Rev. E **51**, 6004 (1995).

[38] R. Redmer, Phys. Rep. **282**, 35 (1997).

[39] M. P. Desjarlais, J. D. Kress, and L. A. Collins, Phys. Rev. E **66**, 025401 (2002).

[40] V. Recoules and J.-P. Crocombette, Phys. Rev. B **72**, 104202 (2005).

[41] B. Holst, R. Redmer, and M. P. Desjarlais, Phys. Rev. B **77**, 184201 (2008).

[42] L. Caillabet, S. Mazevet, and P. Loubeyre, Phys. Rev. B **83**, 094101 (2011).

[43] R. Franz and G. Wiedemann, Ann. Phys. **165**, 497 (1853).

[44] N. D. Mermin, Phys. Rev. **137**, A1441 (1965).

[45] R. M. Wentzcovitch, J. L. Martins, and P. B. Allen, Phys. Rev. B **45**, 11372 (1992).

[46] M. Weinert and J. W. Davenport, Phys. Rev. B **45**, 13709 (1992).

[47] G. Kresse and J. Hafner, Phys. Rev. B **47**, 558 (1993).

[48] G. Kresse and J. Hafner, Phys. Rev. B **49**, 14251 (1994).

[49] G. Kresse and J. Furthmüller, Phys. Rev. B **54**, 11169 (1996).

[50] P. E. Blöchl, Phys. Rev. B **50**, 17953 (1994).

[51] G. Kresse and D. Joubert, Phys. Rev. B **59**, 1758 (1999).

[52] S. Nosé, J. Chem. Phys. **81**, 511 (1984).

[53] A. Baldereschi, Phys. Rev. B **7**, 5212 (1973).

[54] The matrix elements are extracted out of the OPTIC file. It has to be ensured that all Bloch states are considered as initial and final.

[55] H. J. Monkhorst and J. D. Pack, Phys. Rev. B **13**, 5188 (1976).

[56] J. P. Perdew, K. Burke, and M. Ernzerhof, Phys. Rev. Lett. **77**, 3865 (1996).

[57] B. Boates, S. Hamel, E. Schwegler, and S. A. Bonev, J. Chem. Phys. **134**, 064504 (2011).

[58] D. A. Horner, J. D. Kress, and L. A. Collins, Phys. Rev. B **81**, 214301 (2010).

[59] S. V. Faleev, M. van Schilfgaarde, T. Kotani, F. Léonard, and M. P. Desjarlais, Phys. Rev. B **74**, 033101 (2006).

[60] M. French, T. R. Mattsson, and R. Redmer, Phys. Rev. B **82**, 174108 (2010).

[61] N. W. Ashcroft and N. D. Mermin, *Solid State Physics* (Saunders, Philadelphia, 1976).

[62] V. Christoph and G. Röpke, Phys. Status Solidi B **131**, 11 (1985).

[63] D. Zubarev, V. Morozov, and G. Röpke, *Statistical Mechanics of Nonequilibrium Processes* (Akademie-Verlag, Berlin, 1997), Vol. 2.

[64] S. R. de Groot and P. Mazur, *Non-Equilibrium Thermodynamics* (Dover, New York, 1984).

[65] R. Kubo, J. Phys. Soc. Jpn. **12**, 570 (1957).

[66] D. A. Greenwood, Proc. Phys. Soc. London **71**, 585 (1958).

[67] J. Clérouin, Y. Laudernet, V. Recoules, and S. Mazevet, Phys. Rev. B **72**, 155122 (2005).

[68] A. Kietzmann, B. Holst, R. Redmer, M. P. Desjarlais, and T. R. Mattsson, Phys. Rev. Lett. **98**, 190602 (2007).

[69] A. W. DeSilva and H.-J. Kunze, Phys. Rev. E **49**, 4448 (1994).

[70] A. W. DeSilva and J. D. Katsouros, Phys. Rev. E **57**, 5945 (1998).

[71] N. F. Mott and E. A. Davis, *Electronic Processes in Non-Crystalline Materials* (Clarendon, Oxford, 1979).

[72] W. Götzlaff, G. Schönherr, and F. Hensel, Z. Phys. Chem. Neue Folge **156**, 219 (1988).

[73] F. Hensel and W. W. Warren, *Fluid Metals* (Princeton University Press, Princeton, NJ, 1999).

PHYSICAL REVIEW B **90**, 165113 (2014)

Thermoelectric transport properties of molybdenum from *ab initio* simulations

Martin French and Thomas R. Mattsson
HEDP Theory, Sandia National Laboratories, Albuquerque, New Mexico 87185-1189, USA

(Received 2 June 2014; revised manuscript received 19 September 2014; published 10 October 2014)

We employ *ab initio* simulations based on density functional theory (DFT) to calculate the electronic transport coefficients (electrical conductivity, thermal conductivity, and thermopower) of molybdenum over a broad range of thermodynamic states. By comparing to available experimental data, we show that DFT is able to describe the desired transport properties of this refractory metal with high accuracy. Most noteworthy, both the positive sign and the quantitative values of the thermopower of solid molybdenum are reproduced very well. We calculate the electrical and thermal conductivity in the solid and the fluid phase between 1000 and 20 000 K and a wide span in density and develop empirical fit formulas for direct use in practical applications, such as magneto-hydrodynamics simulations. The influence of thermal expansion in conductivity measurements at constant pressure is also discussed in some detail.

DOI: 10.1103/PhysRevB.90.165113 PACS number(s): 31.15.A−, 72.15.Jf, 52.25.Fi

I. INTRODUCTION

Refractory metals like molybdenum are technologically important materials because of their high mechanical strength, high melting point, supreme resistance to heat and corrosion, as well as good electrical conductivity [1]. Molybdenum is commonly used in high-strength steels as well as superalloys for applications in extreme environments like turbine blades in jet engines and for components in gas turbines. A new application for molybdenum, involving even more extreme conditions in pressure and temperature, is as a drive material in pulsed-power experiments aiming to measure high-pressure yield strengths of sample materials under shear stress [2]. Understanding the physical processes involved as well as designing and optimizing the experiments rely on the use of magneto-hydrodynamic (MHD) simulations. The MHD simulations, in turn, rely on using accurate material models like an equation of state (EOS) in general and thermoelectric transport coefficients in particular. Errors in the electrical conductivity model can lead, for example, to incorrect joule heating in the simulations, driving the simulations away from the correct thermodynamic state as the simulation evolves in time. There is therefore a need to have an accurate model for the thermoelectric properties of molybdenum over a broad range of conditions, including the transition from solid state behavior to dense plasma, the warm dense matter region, a part of the phase diagram which is challenging to describe.

Molybdenum is a body-centered cubic (bcc) metal and, like many of the transition metals, it has a complex electronic structure. Three examples of effects due to the involved electronic structure are the positive signs of the thermopower [3] and Hall coefficient [4] near ambient conditions and the anomalous self-diffusion behavior at high temperature below the melting point [5]. The electrical conductivity σ in solid molybdenum is accurately known up to the melting point [6] at ambient pressure. It was also measured in the liquid phase [7–10] and in plasma states [11] using exploding wire experiments. The thermal conductivity λ of solid molybdenum was probed experimentally up to melting [12–19]. In the liquid it is typically approximated from the electrical conductivity using the Wiedemann-Franz law [20].

In this paper, we present results from extensive *ab initio* calculations for the thermoelectric transport coefficients of molybdenum that are based on finite-temperature density functional theory (FT-DFT) [21–23]. Within this framework the electronic transport coefficients are derived with expressions obtained from linear response theory (LRT) [24]. Although σ and λ are the quantities of primary practical importance, we also examine the thermopower α in some detail. This quantity does not depend directly on the concentration of free charge carriers (here best described as conduction electrons) and is very sensitive to the electronic structure. By reproducing the experimental thermopower in the solid, in addition to the conductivities in various phases, we ensure that our calculated results are of very high fidelity.

Transport properties often change significantly when phase boundaries are crossed. It is therefore important to know the location of the melt boundary. Explicit calculations of the melt boundary are not performed here, however, because of the extensive previous experimental [25–29] and theoretical [30–36] work regarding the phase diagram of molybdenum. All thermodynamic conditions of interest here (1000 to 20 000 K and up to 2 Mbar) are either in the fluid or in the bcc solid, and we thus calculate the transport properties for these two phases.

Following this Introduction is a section on the theoretical methods used, a section presenting results and extensive comparisons with available experimental data, and finally a summary and discussion. We expect the results in the article to be used to model molybdenum under high pressure and high temperature and to serve as an example on how one can approach systematic modeling of thermoelectric transport properties of materials with challenging electronic structure.

II. THEORY AND SIMULATION DETAILS

Our theoretical approach to calculate the electronic transport coefficients relies on performing FT-DFT molecular dynamics (MD) simulations in the Born-Oppenheimer approximation to obtain thermophysical properties like internal energy and pressure and an ensemble of ionic configurations at each thermodynamic state. Subsequently, static FT-DFT calculations are done for each of the ionic configurations to evaluate the LRT expressions for thermoelectrical properties. This has become a well established procedure for electronic transport calculations over the last ten years. It has been successfully applied for various materials, mostly with a focus on the electrical conductivity [24,37–42]. In this paper, in addition to conductivity, we also calculate the thermal transport properties, thus making full use of the theoretical approach. The Vienna *ab initio* simulation package (VASP) 5.3.2 [43–47], which is a plane-wave pseudopotential code, is used for both the MD simulations and transport calculations.

The calculation of the thermoelectric transport coefficients is based on the following expressions for the Onsager coefficients derived within LRT [24]:

$$L_{mn}(\omega) = \frac{2\pi(-e)^{4-m-n}}{3\Omega\omega} \sum_{\mathbf{k}\nu\mu} |\langle \mathbf{k}\nu|\hat{\mathbf{v}}|\mathbf{k}\mu\rangle|^2 (f_{\mathbf{k}\nu} - f_{\mathbf{k}\mu}) \times \left(\frac{E_{\mathbf{k}\mu}+E_{\mathbf{k}\nu}}{2} - h_e\right)^{m+n-2} \delta(E_{\mathbf{k}\mu} - E_{\mathbf{k}\nu} - \hbar\omega), \quad (1)$$

where ω is the frequency, Ω the volume of the simulation box, e the elementary charge, h_e the enthalpy per electron, $E_{\mathbf{k}\mu}$ and $f_{\mathbf{k}\mu}$ are the eigenvalue and Fermi occupation number, respectively, of the Bloch state $|\mathbf{k}\mu\rangle$, and $\langle \mathbf{k}\nu|\hat{\mathbf{v}}|\mathbf{k}\mu\rangle$ are matrix elements with the velocity operator [48]. A Gaussian function is used to slightly broaden the δ function to a finite width as necessary.

The static electrical conductivity is directly given by the coefficient $L_{11}(\omega)$, also known as the Kubo-Greenwood formula [49,50], in the limit of zero frequency:

$$\sigma = \lim_{\omega\to 0} L_{11}(\omega). \quad (2)$$

The thermal conductivity is calculated via the relation:

$$\lambda = \lim_{\omega\to 0} \frac{1}{T}\left(L_{22}(\omega) - \frac{L_{12}^2(\omega)}{L_{11}(\omega)}\right). \quad (3)$$

The thermopower is defined as

$$\alpha = \lim_{\omega\to 0} \frac{L_{12}(\omega)}{T L_{11}(\omega)}. \quad (4)$$

The zero-frequency limits are taken by making linear fits to the results from the above expressions in a narrow frequency interval, excluding the abrupt and unphysical decrease to zero in the $L_{mn}(\omega = 0)$ which occurs due to the finite number of particles in the calculations. The width of this interval is selected as narrow as possible, and it is usually different for each of the individual transport coefficients (2), (3), and (4) because of their different frequency behaviors. It also depends on density, temperature, and particle number and thus the procedure needs to be performed manually for each particular calculation.

The most important aspect of DFT calculations is the choice of the exchange-correlation functional. For Mo, the AM05 exchange-correlation functional [51,52] gives very good equilibrium density and bulk modulus [5] and was therefore used in all calculations above 4 g/cm^3. For expanded states, we used the Perdew-Burke-Ernzerhof (PBE) functional [53] instead since PBE gives good atomization energies, a property that is important in the region around the critical point. Furthermore, calculations for expanded states converge significantly better with PBE than with AM05 [54]. We verified that AM05 and PBE yield identical results for the thermoelectric transport properties in test calculations of several states above 4 g/cm^3.

Of particular importance is the fidelity of the pseudopotentials employed to reduce the number of electrons carried self-consistently in the FT-DFT calculations [55]. We exclusively use the GW-labeled 14 electron projector-augmented wave (PAW) pseudopotential [56,57] in all LRT calculations (with 300 eV cutoff energy) and in all MD simulations of the fluid (with 800 eV cutoff energy). In a recent technical report [58], it was shown that various other molybdenum pseudopotentials for VASP produce slightly less accurate results for the lattice constant and electronic density of states, even in ground-state calculations. During the construction of the GW-labeled set of pseudopotentials, special care was taken with the projectors for the (at zero temperature) unoccupied Kohn-Sham states [57]. These states become relevant when they are partially occupied at high temperatures [55] or when involved in calculating transition matrix elements.

The high accuracy of the 14 electron potential notwithstanding, the 6 electron PAW potential (with 400 eV cutoff energy) was used in the MD simulations to create the ensemble of ionic configurations of the solid, where the thermal occupation of excited states is still small. In test calculations we checked that using either of the two PAW potentials in these MD simulations did not influence the electronic transport coefficients. Importantly, the subsequent LRT calculations of thermoelectric properties were all done using the 14 electron GW-labeled PAW potential.

Achieving sound numerical convergence is a fundamental aspect in FT-DFT [59]. Depending on the phase of the system, i.e., fluid or solid, different numerical parameters were used. The relevant settings, especially the particle number and the **k**-point grids, were extensively convergence tested.

All MD simulations were made in the canonical ensemble (NVT) using a Nosé thermostat [60] and the Baldereschi **k** point [61]. Following equilibration, each thermodynamic state was run for 3000 to 20 000 time steps of lengths of 1 to 4 fs, depending on temperature using a velocity-verlet time integration algorithm.

In the fluid phase, excellent convergence of all transport coefficients could be achieved with 54 atoms at or above 5 g/cm^3 and with 24 atoms at lower densities. The respective LRT calculations (using 25–40 ionic configurations from each MD) were done with a standard 2 × 2 × 2 Monkhorst-Pack grid [62]. Table I contains two representative examples of convergence tests made for the fluid phase.

Calculating converged thermoelectric transport coefficients for the solid is much more demanding than for the fluid, especially at low temperatures. The long mean free path of the electrons requires both larger simulation boxes (with more particles) as well as denser **k**-point meshes due to the high symmetry of the ionic configurations. We illustrate this with two examples in Table I. Increasing the particle number and **k**-point grids does not necessarily lead to a uniform convergence of the transport coefficients and outliers may occur. Furthermore, full convergence of σ, λ, and α can be achieved with different simulation parameters for each of them, whereas α usually involves the lowest and λ the highest

TABLE I. Representative convergence tests for the calculated thermoelectric properties with respect to the number of atoms N and the Monkhorst-Pack **k**-point meshes [62] used in the LRT calculations. The thermodynamic states are located in the dense and expanded fluid at 10 000 K and in the solid at 1000 and 2500 K. The RW indicates that a reduced wedge of the **k**-point grid is used, generated by the projection of the full grid into the irreducible Brillouin zone of an ideal bcc lattice. Especially, the RW 2 × 2 × 2 corresponds to the Baldereschi mean-value point [61]. [Γ: Gamma point (Brillouin zone center)].

T (K)	ϱ (g/cm^3)	N	**k** points	σ (MS/m)	λ (W/Km)	α (μV/K)
10 000	5	24	Γ	0.50 ± 0.02	85 ± 3	6 ± 4
10 000	5	24	2 × 2 × 2	0.47 ± 0.01	91 ± 1	4 ± 2
10 000	5	24	3 × 3 × 3	0.47 ± 0.01	90 ± 1	3 ± 2
10 000	5	54	Γ	0.46 ± 0.01	93 ± 2	3 ± 3
10 000	5	54	2 × 2 × 2	0.46 ± 0.01	90 ± 1	3 ± 2
10 000	13	54	Γ	1.53 ± 0.02	334 ± 6	17 ± 4
10 000	13	54	2 × 2 × 2	1.49 ± 0.01	343 ± 2	13 ± 2
10 000	13	54	3 × 3 × 3	1.48 ± 0.01	342 ± 2	14 ± 2
10 000	13	128	Γ	1.49 ± 0.01	343 ± 2	12 ± 3
10 000	13	128	2 × 2 × 2	1.50 ± 0.01	344 ± 2	14 ± 2
1000	10	54	RW 4 × 4 × 4	3.6 ± 0.4	68 ± 7	40 ± 10
1000	10	54	RW 6 × 6 × 6	3.2 ± 0.3	68 ± 5	14 ± 6
1000	10	54	RW 8 × 8 × 8	3.2 ± 0.3	72 ± 5	16 ± 5
1000	10	128	RW 2 × 2 × 2	4.6 ± 0.4	89 ± 6	4 ± 8
1000	10	128	RW 4 × 4 × 4	3.6 ± 0.2	83 ± 5	21 ± 6
1000	10	128	RW 6 × 6 × 6	3.5 ± 0.1	79 ± 4	16 ± 5
1000	10	128	RW 8 × 8 × 8	3.5 ± 0.1	83 ± 4	17 ± 5
1000	10	250	RW 2 × 2 × 2	4.3 ± 0.2	84 ± 5	8 ± 7
1000	10	250	RW 4 × 4 × 4	4.0 ± 0.1	91 ± 4	16 ± 6
1000	10	250	RW 6 × 6 × 6	4.0 ± 0.1	90 ± 4	19 ± 5
1000	10	432	RW 2 × 2 × 2	4.0 ± 0.1	83 ± 5	50 ± 10
2500	13	54	RW 6 × 6 × 6	2.9 ± 0.2	176 ± 7	5 ± 5
2500	13	54	RW 8 × 8 × 8	2.9 ± 0.2	175 ± 6	5 ± 5
2500	13	128	RW 4 × 4 × 4	3.0 ± 0.1	171 ± 5	14 ± 5
2500	13	128	RW 6 × 6 × 6	2.9 ± 0.1	173 ± 5	12 ± 5
2500	13	250	RW 2 × 2 × 2	3.2 ± 0.2	172 ± 6	19 ± 6
2500	13	250	RW 4 × 4 × 4	3.0 ± 0.1	177 ± 4	14 ± 5

numerical effort. For instance, at 1000 K one can calculate a well-converged thermopower with 128 atoms, while the electrical conductivity requires at least 250 atoms. The thermal conductivity can be determined barely within a few percent at 1000 K, but this improves rapidly at higher temperature. Our second example at 2500 K shows that the higher thermal disorder in the lattice leads to a much better convergence for all transport coefficients.

As a consequence, we made extensive sets of calculations with 54, 128, and 250 atoms using different **k**-point sets for each considered density and temperature below 3000 K. All final results for the transport coefficients in the solid phase were taken from the MD simulations with 250 atoms. An irreducible wedge of the 4 × 4 × 4 **k**-point grid was used in the respective LRT calculations. This generally produced very well converged results for all transport coefficients. The occasional tendency toward an underestimation of the thermal conductivity at 1000 K did not affect the quality of the fit function derived from the complete set of results, Eq. (8).

To conclude on the methodology for calculating thermoelectric properties, we did not calculate the contribution of the phonons to the thermal conductivity of the solid. The reason is that the Wiedemann-Franz law is fulfilled within a few percent at room temperature [1,6], see subsection III C. Therefore the ionic contribution is likely to be very small and it further decreases, usually with $1/T$ behavior at elevated temperatures above the Debye temperature [63]. The phonon contribution to the thermal conductivity therefore does not need to be taken into account at the high temperatures that is the focus of the present work.

III. RESULTS

Here we present the results for the thermoelectric transport properties and compare them with available experiments. We note that the FT-DFT-MD simulations also yield the equation of state as a byproduct, with which we can estimate the critical density of molybdenum to be near 3 g/cm^3 and the critical temperature near 11 000 K. This result is close to earlier estimations from theory and experiment [64–66]. Our main data set ranges across a regular grid from 2 to 13 g/cm^3 and from 1000 to 20 000 K, excluding the thermodynamically unstable region in the subcritical fluid.

In some cases the finite number of atoms in our MD boxes allowed us to simulate both a liquid and solid phase at identical density and temperature. Having such an overlap of results is very helpful for our purposes. It significantly reduces the need to extrapolate the fit formulas when approaching the melting line.

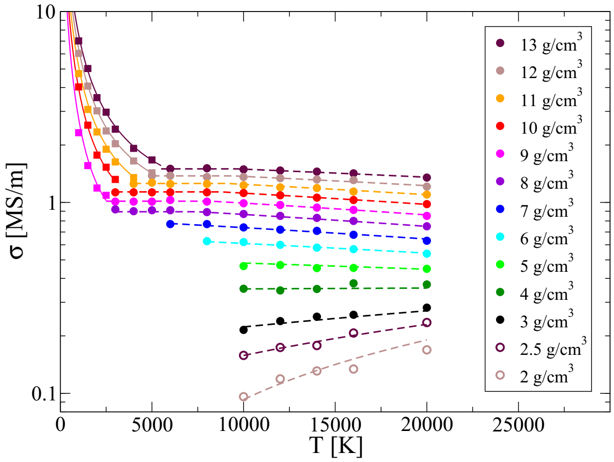

FIG. 1. (Color online) Isochores of the electrical conductivity of molybdenum. For the fluid phase the calculated values are shown as circles, whereas squares of identical color indicate results in the solid phase. The solid lines are results of Eq. (5). The dashed lines correspond to a steady connection of the Eqs. (6) and (7) for the fluid phase.

A. Electrical conductivity

We display several isochores of the electrical conductivity in Fig. 1. In both the liquid and solid phases the electrical conductivity increases roughly linearly with the density. The temperature dependence, however, is drastically different between the liquid and solid phase. While the conductivity decreases strongly with the temperature in the solid, it is almost independent of temperature in the liquid up to about 10 000 K. This is a relatively common behavior for a metallic system [6,67] and is a consequence of the drastic change in the electronic and ionic structure at melting. At higher temperatures the electrical conductivity shows a linear temperature dependence. It decreases if the density is sufficiently high but increases at lower densities, which is a well-known property of expanded metallic liquids and plasmas. This inversion of the temperature behavior occurs near 4 g/cm^3.

The following simple expression was found to lead to an excellent fit for the electrical conductivities in the solid, σ_s. It reads

$$T\sigma_s = a_0 + a_1\varrho + a_2 T + a_3 \ln T. \qquad (5)$$

TABLE II. Coefficients for the electrical σ_s (second row) and thermal conductivity λ_s (third row) of solid molybdenum. All units are chosen in a way that entering temperatures in K and densities in g/cm^3 lead to results in MS/m for σ_s or W/Km for λ_s, respectively.

	$T\sigma_s$	λ_s
a_0	1514	96.8
a_1	1204	30.4
a_2	0.796	0.0237
a_3	−1506	−47.7

TABLE III. Coefficients for the electrical conductivities σ_{f1} (second row) and σ_{f2} (third row) of fluid molybdenum. All units are chosen in a way that entering temperatures in K and densities in g/cm^3 lead to results in MS/m.

	σ_{f1}	σ_{f2}
b_0	−0.074	−0.383
b_1	0.121	0.195
b_2		-3.09×10^{-3}
b_3		2.14×10^{-5}
b_4		-6.39×10^{-6}
b_5		2.83×10^{-7}

The coefficients a_i are given in Table II. Before performing the least-squares fit, we combined our calculated conductivity results set, which does not include any data below 1000 K, with the accepted experimental data [6] between 250 and 1000 K. The fit formula is thus applicable from room temperature up to the melt line for densities between 9 and 13 g/cm^3. The volume expansion has been taken into account when processing the experimental data, see Appendix A for details. The resulting fit curves are included in Fig. 1.

Finding a closed fit formula for the electrical conductivity in the fluid phase is difficult. For simplicity, we split the expression into a temperature-independent part valid in the subcritical liquid and a part with linear temperature dependence for higher temperatures. All values in the liquid up to 8000 K can be fitted very accurately with the simple formula:

$$\sigma_{f1} = b_0 + b_1\varrho. \qquad (6)$$

The remaining results (between 10 000 K and 20 000 K) were used to parametrize the expression:

$$\sigma_{f2} = b_0 + b_1\varrho + b_2\varrho^2 + b_3 T + b_4\varrho T + b_5\varrho^2 T. \qquad (7)$$

It is very easy to make a steady connection between the above formulas. The coefficients b_i for the Eqs. (6) and (7) are collected in Table III. Figure 1 shows how the resulting fit curves match the *ab initio* results.

A comparison of our conductivities with experiments is shown in Fig. 2, which displays the electrical resistivity $R = 1/\sigma$. For the solid we find very good agreement with the values recommended by Desai *et al.* [6] and with the data from Hixson and Winkler [9]. The thermal expansion of the solid has been taken into account, see Appendix A.

The electrical resistivity of liquid molybdenum has been measured in exploding wire experiments [7–10]. The agreement of our conductivities σ_{f1} with these experiments is excellent, as can be seen from Fig. 2. We emphasize that the increase in the resistivity with temperature is caused only by the reduction in the density of the liquid. Our calculations show that the temperature has no noticeable effect on the electrical conductivity of the liquid below 8000 K when the density is kept constant, see Fig. 1.

The electrical conductivity of more widely expanded and hotter plasma states has also been measured [11]. However, there is only a partial overlap in the thermodynamic parameters between our results and those experiments. Furthermore, since the temperature of the molybdenum plasma could not be

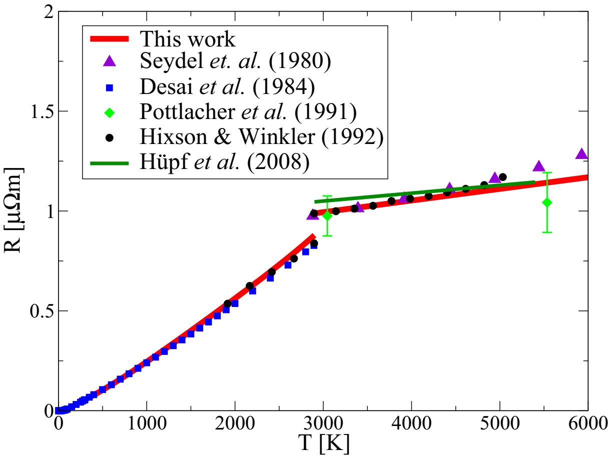

FIG. 2. (Color online) Electrical resistivity of molybdenum from Eqs. (5) and (6) in comparison with experiments [6–10]. The resistivity increases abruptly at the melt boundary (2900 K). The experiments were performed at ambient pressure. The volume expansion for the solid was calculated as described in the Appendix A. The expansion data from Hüpf *et al.* [10] was used for the liquid.

measured, the change in the internal energy was reported instead. The experimental uncertainties aside, we observe good agreement also with these experimental data when determining the respective temperatures with our calculated caloric equation of state.

B. Thermal conductivity

Our calculated thermal conductivities are shown in Fig. 3. The increase with the density is similar to what is observed also for the electrical conductivity in both the fluid and the solid phase. The temperature dependence in the fluid is strong and substantially nonlinear. In the solid its influence is much weaker and more difficult to resolve, especially between 1000 and 3000 K, due to the statistical fluctuations in our results. For temperatures above about 3000 K the thermal conductivity undoubtedly rises with the temperature.

It is experimentally known [1,14] that the thermal conductivity decreases with the temperature below 1000 K, the lowest temperature for which we have produced results. By combining our calculated results with the experimental thermal conductivities below 1000 K [14], we are able to give a very reasonable analytical fit for the thermal conductivity of solid molybdenum. Keeping in mind that the thermal conductivity naturally has a linear intrinsic temperature dependence, we choose a functional form that is analogous to Eq. (5):

$$\lambda_s = a_0 + a_1 \varrho + a_2 T + a_3 \ln T. \tag{8}$$

The respective coefficients a_i are given in Table II as well. The fit curves are displayed in Fig. 3. The shallow minimum in the thermal conductivity is located close to 2000 K.

Experiments at ambient pressure [12–18] showed that the thermal conductivity decreases with the temperature up to the melting temperature. This decrease is pronounced below 1000 K [14] but weakens at higher temperature. We compare our fit, Eq. (8), with these experiments in Fig. 4, taking into account the thermal expansion in the experiments (see Appendix A). Given the variation between all the sets of different experiments, we can infer that the theoretical results are of high fidelity. This is especially true for the slope at high temperature, which is determined by the interplay between the nonlinearities in expansion and thermal conductivity itself.

It is particularly worth noting that the effect of thermal expansion leads to a qualitatively different temperature dependence. For example, the minimum in the thermal conductivity near 2000 K at constant density does not exist at all when the pressure is held constant instead.

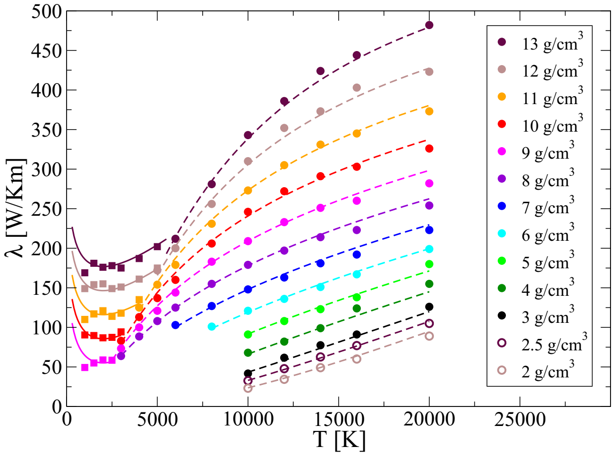

FIG. 3. (Color online) Isochores of the thermal conductivity of molybdenum. For the fluid phase the calculated values are shown as circles, whereas squares of identical color indicate values in the solid phase. The solid lines are results of Eq. (8). The dashed lines correspond to Eq. (9) for the fluid phase, respectively.

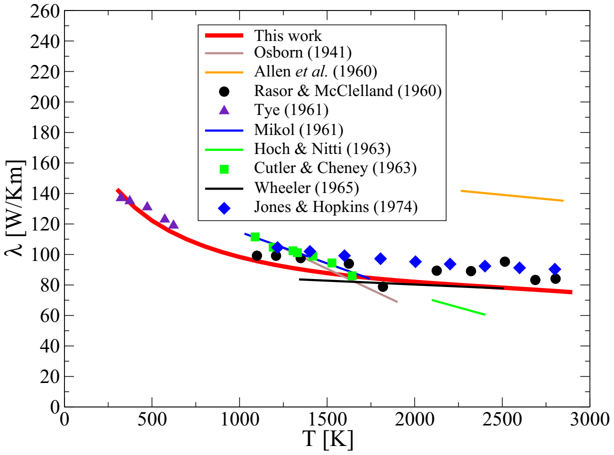

FIG. 4. (Color online) Comparison of our results for the thermal conductivity of solid molybdenum from Eq. (8) with experimental data [12–17]. The values of Mikol and of Hoch and Nitti were extracted from the paper of Jones and Hopkins [17]. The experiments were performed at ambient pressure. The respective volume expansion was calculated as described in Appendix A.

TABLE IV. Coefficients for the thermal conductivity λ_f of fluid molybdenum. All units are chosen in a way that entering temperatures in K and densities in g/cm^3 leads to results in W/Km.

c_0	−7.021
c_1	1.208
c_2	0.7929
c_3	−22 780
c_4	21 070
c_5	−2926
c_6	1.241
c_7	−0.1914
c_8	−0.056 72

For the fluid phase the thermal conductivities are fit to the following expression:

$$\ln\lambda_f = c_0 + c_1\ln\varrho + c_2\varrho + \frac{c_3}{T} + c_4\frac{\ln\varrho}{T} + c_5\frac{\varrho}{T} + c_6\ln T + c_7\ln\varrho\ln T + c_8\varrho\ln T. \tag{9}$$

This functional form is a good compromise between simplicity and numerical accuracy. The nine coefficients c_i are given in Table IV and the resulting curves are included in Fig. 3.

We are not aware of experimental measurements of thermal conductivities for fluid molybdenum. If such experiments are achieved in the future, it will be very interesting to compare them to our predictions.

C. Lorenz number

Having calculated both the electrical and thermal conductivity, it is insightful to examine the Lorenz number,

$$L = \frac{e^2\lambda}{k_B^2 T\sigma}. \tag{10}$$

In regions of high electron degeneracy this quantity takes the constant value of $L = \pi^2/3$, which is known as the Wiedemann-Franz law [20]. To explore how well this relation actually holds, we plot the Lorenz number calculated by our fit formulas, Eqs. (5) and (8) for the solid and Eqs. (6), (7), and (9) for the fluid in Fig. 5.

The left panel of Fig. 5 shows the very systematic behavior of the isochores of the Lorenz number in the solid phase. Starting with slightly higher values than $\pi^2/3$ at room temperature, it decreases to a density-dependent minimum value and then rises again. The maximum deviation from the Wiedemann-Franz law does not exceed 10% by very much in the entire region of interest.

In the fluid phase, the Lorenz number shows a much more nonlinear behavior, which is shown in the right panel of Fig. 5 along several isotherms. The deviations from the Wiedemann-Franz law are particularly strong at high temperatures, which is expected due to a decreasing electron degeneracy. There is also a particularly strong trend of a steeply rising Lorenz number toward low densities. Such behavior was already observed in earlier calculations for hydrogen [24], where a strong increase up to one order of magnitude was observed in the partially degenerate, expanded plasma.

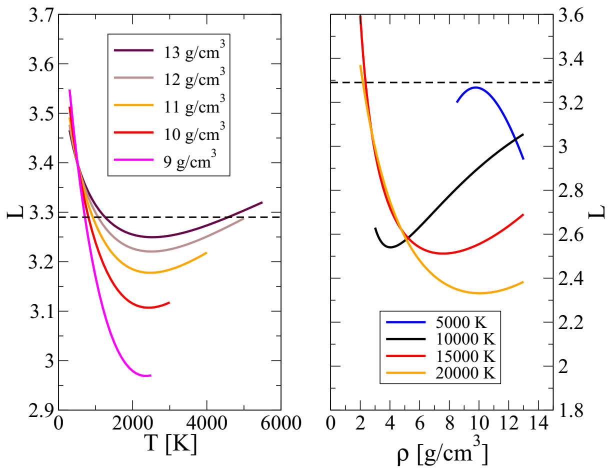

FIG. 5. (Color online) Left panel: Isochores of the Lorenz number in the solid phase. Right panel: Isotherms of the Lorenz number in the liquid phase. The dashed line indicates the Wiedemann-Franz law in both panels.

We find that, although the Wiedemann-Franz law is approximately valid for solid and liquid molybdenum, it is not to be relied upon in the low-density or high-temperature fluid regimes.

D. Thermopower

The thermopower is, like the Lorenz number, a very sensitive quantity, strongly influenced by the electronic structure. For electronic conductors it usually has a negative sign although exceptions are not uncommon, especially among the transition metals [3]. This is also the case for molybdenum.

We display our calculated values for the thermopower in Fig. 6. For densities between 8 and 13 g/cm^3 the thermopower takes a small and relatively constant value of about +15 μV/K. This number is the same for both the solid and

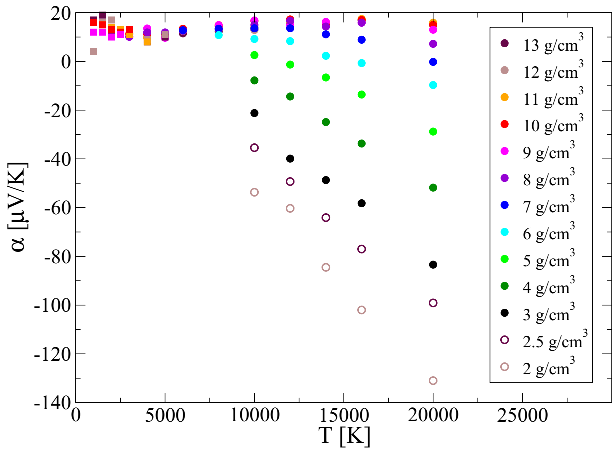

FIG. 6. (Color online) Isochores of the thermopower of molybdenum. For the fluid phase the calculated values are shown as circles, whereas squares of identical color indicate results in the solid phase.

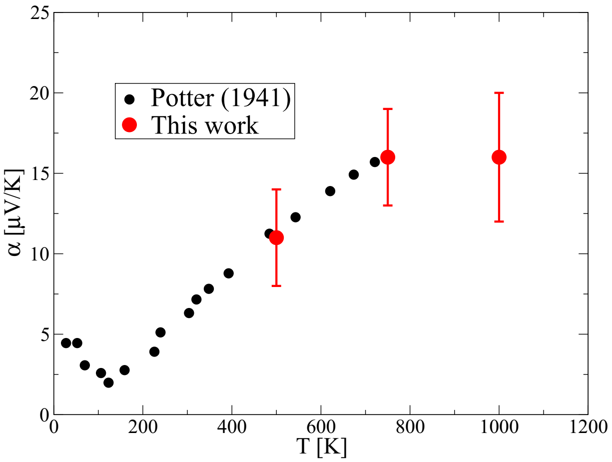

FIG. 7. (Color online) Thermopower of solid molybdenum in comparison with experimental data [3].

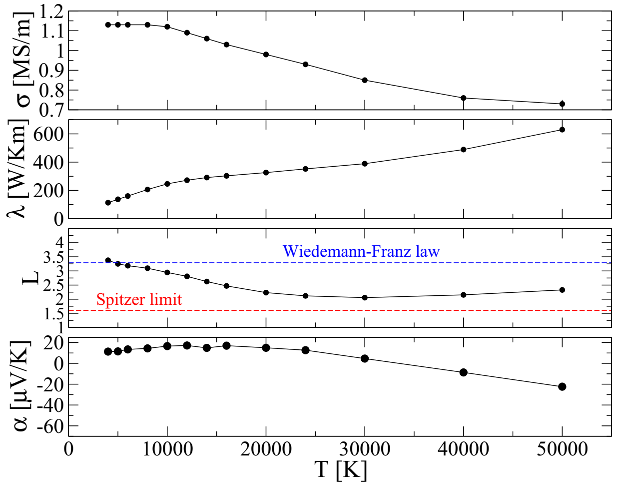

FIG. 8. (Color online) Transport properties of fluid molybdenum at 10 g/cm^3 and high temperatures.

the liquid so that, in contrast to the electrical and thermal conductivity, the thermopower has no noticeable discontinuity at the melting line. In the hot fluid the thermopower decreases with temperature and volume to reach large negative values.

Since the thermopower of fluid molybdenum is only of minor importance for practical applications, we did not attempt to write analytical expressions with optimized parameters for it.

Experimental data for the thermopower of molybdenum are very scarce and only available for the solid up to a fairly low temperature of about 700 K [3]. Our main set of results for the transport coefficients begins at 1000 K because of the significant numerical challenges in going to lower temperatures. Achieving a converged limit ($\omega \to 0$) in the evaluation of the expressions shown in Sec. II becomes very demanding for low-temperature metallic solids. The mathematical structure of Eq. (4), however, which is a quotient of two Onsager coefficients, helps to compensate these difficulties somewhat. Table I shows that the thermopower indeed converges much easier with the particle number than the conductivities do in the solid phase. With two additional sets of calculations, in which we used 200 ionic configurations each, we were able to calculate a well-converged thermopower for 500 and 750 K at the experimental density. Our theoretical results are compared to the experiment [3] in Fig. 7, with very good agreement. As noted above, we predict that the thermopower levels off and remains at a value close to 15 μV/K for higher temperatures.

E. Behavior at higher temperatures

We now present an outlook on how the behavior of the electronic transport coefficients calculated in the previous sections changes at even higher temperature, i.e., up to 50 000 K. Figure 8 shows the electrical and thermal conductivity, Lorenz number, and thermopower for the 10 g/cm^3 isochore, which roughly corresponds to the normal solid density of molybdenum.

We see that the linear decrease in the electrical conductivity between 10 000 and 30 000 K becomes weaker at higher temperature. The thermal conductivity shows a significant upwards bend at the same temperature. This is a characteristic sign for ionization of additional bound electrons. The Lorenz number, which decreases below 30 000 K, has a minimum there and starts rising again. One would not expect it to reach the Spitzer limit [68] at 50 000 K because the electron system remains partially degenerate there. The thermopower decreases and changes sign also near 30 000 K and takes standard negative values. This may indicate a significant decrease in the correlations within the electron system.

The nonlinear temperature behavior of the thermoelectric transport coefficients can be expected to continue up to much higher temperatures due to the high atomic number and, thus, possible ionization processes. Calculating the transport properties of dense molybdenum plasma for a wider parameter range is beyond the scope of this work. However, the results given here are certainly useful for developing, testing, or parametrizing plasma transport theories, e.g., like from Refs. [69–72] in the warm dense matter regime.

IV. SUMMARY AND DISCUSSION

We have shown that the thermoelectric transport properties of molybdenum, a refractory metal with complex electronic structure, can be calculated with high accuracy with density functional theory methods. Very good agreement with experiments of solid and liquid molybdenum is achieved for the electrical conductivity, thermal conductivity, and the thermopower. The significant influence of the density change due to thermal expansion in experiments performed at constant pressure is discussed in detail. We furthermore develop fit formulas that allow easy application of our conductivity results, valid from room temperature up to 20 000 K and a density range between 2 and 13 g/cm^3. The findings are of significant importance for many practical applications of molybdenum in states of warm dense matter, especially in designing and optimizing high energy-density physics experiments, for example, magnetically applied pressure-shear [2]. Furthermore, our accurate set of results can be used in the development of wide-range models for plasma transport properties that require a high fidelity also in condensed phases.

ACKNOWLEDGMENTS

We thank M. P. Desjarlais, K. Cochrane, L. Shulenburger, T. A. Haill, A. E. Mattsson, and D. G. Flicker for helpful discussions. This work was supported by the NNSA ASC/PEM program at Sandia. Sandia National Laboratories is a multiprogram laboratory managed and operated by Sandia Corporation, a wholly owned subsidiary of Lockheed Martin Corporation, for the U.S. Department of Energys National Nuclear Security Administration under Contract No. DE-AC04-94AL85000. (SAND2014-4396 J.) This work used the Extreme Science and Engineering Discovery Environment (XSEDE), which is supported by National Science Foundation Grant No. OCI-1053575. The authors acknowledge the Texas Advanced Computing Center (TACC) at The University of Texas at Austin for providing high performance computing resources that have contributed to the research results reported within this paper.

APPENDIX: THERMAL EXPANSION OF THE SOLID

The independent thermodynamic quantities in our FT-DFT-MD simulations are the density and the temperature. However, experimental measurements of transport properties in the solid are usually done at constant pressure. For direct comparisons between our theoretical and the experimental values, it is necessary to consider the thermal expansion, which becomes particularly important at high temperature.

The change in density at constant pressure can be expressed by [73]

$$\varrho(T) = \varrho_0 \exp[-3I(T)], \tag{A1}$$

where

$$\begin{aligned} I(T) = \int_{T_0}^{T} \mathrm{d}T'(&4.64 \times 10^{-6} + 6.71 \times 10^{-10} T' \\ &+ 1.24 \times 10^{-12} T'^2 - 6.43 \times 10^{-16} T'^3 \\ &+ 2.36 \times 10^{-19} T'^4). \end{aligned} \tag{A2}$$

The latter expression (temperatures to be entered in kelvin) is a fit to experimental thermal expansivity data of molybdenum displayed in the paper of Lu *et al.* [73] and is valid from room temperature up to the melting line for ambient pressure. Whenever we process or make comparisons to experimental data in the solid phase, we employ the above expressions with a reference density of $\varrho_0 = 10.228\ \mathrm{g/cm^3}$ at $T_0 = 298$ K [74]. At the melting point (2900 K) [75] the density has reduced by about 7%.

[1] C. Agte and J. Vacek, *Wolfram und Molybdän* (Akademie, Berlin, 1959).
[2] C. S. Alexander, J. R. Asay, and T. A. Haill, J. Appl. Phys. **108**, 126101 (2010).
[3] H. H. Potter, Proc. Phys. Soc. **53**, 695 (1941).
[4] V. E. Startsev, N. V. Volkenshtein, and N. A. Novoselov, Sov. Phys. JETP **24**, 882 (1967).
[5] T. R. Mattsson, N. Sandberg, R. Armiento, and A. E. Mattsson, Phys. Rev. B **80**, 224104 (2009).
[6] P. D. Desai, T. K. Chu, H. M. James, and C. Y. Ho, J. Phys. Chem. Ref. Data **13**, 1069 (1984).
[7] U. Seydel, W. Fucke, and H. Wadle, *Die Bestimmung thermophysikalischer Daten flüssiger hochschmelzender Metalle mit schnellen Pulsaufheizexperimenten* (Mannhold, Düsseldorf, 1980).
[8] G. Pottlacher, E. Kaschnitz, and H. Jäger, J. Phys.: Condens. Matter **3**, 5783 (1991).
[9] R. S. Hixson and M. A. Winkler, Int. J. Thermophys. **13**, 477 (1992).
[10] T. Hüpf, C. Cagran, G. Lohöfer, and G. Pottlacher, J. Phys. Conf. Ser. **98**, 062002 (2008).
[11] A. W. DeSilva and G. B. Vunni, Phys. Rev. E **83**, 037402 (2011).
[12] R. H. Osborn, J. Opt. Soc. Am. **31**, 428 (1941).
[13] N. S. Rasor and J. D. McClelland, J. Phys. Chem. Solids **15**, 17 (1960).
[14] R. P. Tye, J. Less-Common Met. **3**, 13 (1961).
[15] M. Cutler and G. T. Cheney, J. Appl. Phys. **34**, 1714 (1963).
[16] M. J. Wheeler, Brit. J. Appl. Phys. **16**, 365 (1965).
[17] M. Jones and M. R. Hopkins, Phys. Stat. Sol. A **21**, 507 (1974).
[18] R. D. Allen, L. F. Glasier, P. L. Jordan, J. Appl. Phys. **31**, 1382 (1960).
[19] A. Gladun, C. Gladun, and H. Vinzelberg, Phys. Stat. Sol. A **58**, 409 (1980).
[20] G. Wiedemann and R. Franz, Ann. Phys. **165**, 497 (1853).
[21] P. Hohenberg and W. Kohn, Phys. Rev. **136**, B864 (1964).
[22] W. Kohn and L. J. Sham, Phys. Rev. **140**, A1133 (1965).
[23] N. D. Mermin, Phys. Rev. **137**, A1441 (1965).
[24] B. Holst, M. French, and R. Redmer, Phys. Rev. B **83**, 235120 (2011).
[25] R. S. Hixson, D. A. Boness, J. W. Shaner, and J. A. Moriarty, Phys. Rev. Lett. **62**, 637 (1989).
[26] Y. K. Vohra and A. L. Ruoff, Phys. Rev. B **42**, 8651 (1990).
[27] R. S. Hixson and J. N. Fritz, J. Appl. Phys. **71**, 1721 (1992).
[28] D. Errandonea, B. Schwager, R. Ditz, C. Gessmann, R. Boehler, and M. Ross, Phys. Rev. B **63**, 132104 (2001).
[29] D. Santamara-Prez, M. Ross, D. Errandonea, G. D. Mukherjee, M. Mezouar, and R. Boehler, J. Chem. Phys. **130**, 124509 (2009).
[30] A. B. Belonoshko, S. I. Simak, A. E. Kochetov, B. Johansson, L. Burakovsky, and D. L. Preston, Phys. Rev. Lett. **92**, 195701 (2004).
[31] C. Cazorla, M. J. Gillan, S. Taioli, and D. Alfè, J. Chem. Phys. **126**, 194502 (2007).
[32] A. B. Belonoshko, L. Burakovsky, S. P. Chen, B. Johansson, A. S. Mikhaylushkin, D. L. Preston, S. I. Simak, and D. C. Swift, Phys. Rev. Lett. **100**, 135701 (2008).
[33] C. Cazorla, M. J. Gillan, S. Taioli, and D. Alfè, J. Phys. Conf. Ser. **121**, 012009 (2008).

[34] C. Cazorla, D. Alfè, and M. J. Gillan, Phys. Rev. B **85**, 064113 (2012).
[35] Z.-Y. Zeng, C.-E. Hu, X.-R. Chen, X.-L. Zhang, L.-C. Cai, and F.-Q. Jing, Phys. Chem. Chem. Phys. **13**, 1669 (2011).
[36] J. A. Moriarty, R. Q. Hood, and L. H. Yang, Phys. Rev. Lett. **108**, 036401 (2012).
[37] M. P. Desjarlais, Phys. Rev. B **68**, 064204 (2003).
[38] V. Recoules and J.-P. Crocombette, Phys. Rev. B **72**, 104202 (2005).
[39] T. R. Mattsson and M. P. Desjarlais, Phys. Rev. Lett. **97**, 017801 (2006).
[40] M. French, T. R. Mattsson, and R. Redmer, Phys. Rev. B **82**, 174108 (2010).
[41] D. Alfè, M. Pozzo, and M. P. Desjarlais, Phys. Rev. B **85**, 024102 (2012).
[42] J. Clérouin, P. Noiret, P. Blottiau, V. Recoules, B. Siberchicot, P. Renaudin, C. Blancard, G. Faussurier, B. Holst, and C. E. Starrett, Phys. Plasmas **19**, 082702 (2012).
[43] G. Kresse and J. Hafner, Phys. Rev. B **47**, 558 (1993).
[44] G. Kresse and J. Hafner, Phys. Rev. B **48**, 13115 (1993).
[45] G. Kresse and J. Hafner, Phys. Rev. B **49**, 14251 (1994).
[46] G. Kresse and J. Furthmüller, Phys. Rev. B **54**, 11169 (1996).
[47] J. Hafner, J. Comput. Chem. **29**, 2044 (2008).
[48] The matrix elements are extracted out of the OPTIC file. It has to be ensured that all Bloch states are considered as initial and final.
[49] R. Kubo, J. Phys. Soc. Jpn. **12**, 570 (1957).
[50] D. A. Greenwood, Proc. Phys. Soc. **71**, 585 (1958).
[51] R. Armiento and A. E. Mattsson, Phys. Rev. B **72**, 085108 (2005).
[52] A. E. Mattsson, R. Armiento, J. Paier, G. Kresse, J. M. Wills, and T. R. Mattsson, J. Chem. Phys. **128**, 084714 (2008).
[53] J. P. Perdew, K. Burke, and M. Ernzerhof, Phys. Rev. Lett. **77**, 3865 (1996).
[54] It was very challenging to converge AM05 calculations at low densities, in fact some calculations did not converge.
[55] T. R. Mattsson, S. Root, A. E. Mattsson, L. Shulenburger, R. J. Magyar, and D. G. Flicker (unpublished).
[56] P. E. Blöchl, Phys. Rev. B **50**, 17953 (1994).
[57] G. Kresse and D. Joubert, Phys. Rev. B **59**, 1758 (1999).
[58] A. E. Mattsson, Sandia National Laboratories Report No. SAND201415971, 2014 (unpublished).
[59] A. E. Mattsson, P. A. Schultz, M. P. Desjarlais, T. R. Mattsson, and K. Leung, Modell. Simul. Mater. Sci. Eng. **13**, R1 (2005).
[60] S. Nosé, J. Chem. Phys. **81**, 511 (1984).
[61] A. Baldereschi, Phys. Rev. B **7**, 5212 (1973).
[62] H. J. Monkhorst and J. D. Pack, Phys. Rev. B **13**, 5188 (1976).
[63] G. Leibfried and E. Schlömann, Nachr. Akad. Wiss. Göttingen Math.-Phys. Kl. **2**, 71 (1954).
[64] G. R. Gathers, Rep. Prog. Phys. **49**, 341 (1986).
[65] A. N. Emelyanov, A. A. Pyalling, and V. Y. Ternovoi, Int. J. Thermophys. **26**, 1985 (2005).
[66] M. French and T. R. Mattsson, J. Appl. Phys. **116**, 013510 (2014).
[67] T. E. Faber, *Introduction to the Theory of Liquid Metals* (Cambridge University Press, Cambridge, 1972).
[68] R. Redmer, Phys. Rep. **282**, 35 (1997).
[69] Y. T. Lee and R. M. More, Phys. Fluids **27**, 1273 (1984).
[70] H. Kitamura and S. Ichimaru, Phys. Rev. E **51**, 6004 (1995).
[71] M. P. Desjarlais, Contrib. Plasma Phys. **41**, 267 (2001).
[72] S. Kuhlbrodt, B. Holst, and R. Redmer, Contrib. Plasma Phys. **45**, 73 (2005).
[73] X.-G. Lu, M. Selleby, and B. Sundman, Acta Mater. **53**, 2259 (2005).
[74] K. D. Litasov, P. I. Dorogokupets, E. Ohtani, Y. Fei, A. Shatskiy, I. S. Sharygin, P. N. Gavryushkin, S. V. Rashchenko, Y. V. Seryotkin, Y. Higo, K. Funakoshi, A. D. Chanyshev, and S. S. Lobanov, J. Appl. Phys. **113**, 093507 (2013).
[75] P. D. Desai, J. Phys. Chem. Ref. Data **16**, 91 (1987).

PHYSICAL REVIEW LETTERS **122,** 086601 (2019)

Paramagnetic-to-Diamagnetic Transition in Dense Liquid Iron and Its Influence on Electronic Transport Properties

Jean-Alexander Korell,[1] Martin French,[1] Gerd Steinle-Neumann,[2] and Ronald Redmer[1]
[1]*Universität Rostock, Institut für Physik, Albert-Einstein-Strasse 23-24, D-18059 Rostock, Germany*
[2]*Bayerisches Geoinstitut, Universität Bayreuth, D-95440 Bayreuth, Germany*

(Received 3 August 2018; revised manuscript received 21 December 2018; published 1 March 2019)

The electrical σ and thermal conductivity λ of liquid iron are calculated with spin-polarized density-functional-theory-based simulations over a significant pressure and temperature range using the Kubo-Greenwood formalism. We show that a paramagnetic state is stable in the liquid up to high temperatures at ambient pressure and that the discrepancy between experimental results and spin-degenerate simulations for σ and λ of more than 30% are reduced to within 10% with lower values resulting from the spin-polarized simulations. Along the 3700 K isotherm, we explore the persistence of magnetic fluctuations toward high densities, and beyond 20–50 GPa the liquid becomes diamagnetic, which suggests the existence of a continuous paramagnetic-to-diamagnetic transition. This transition exerts a significant influence on the physical properties of liquid iron, especially on σ and λ, and is potentially of high relevance for dynamo processes in Mercury and Mars.

DOI: 10.1103/PhysRevLett.122.086601

The understanding of electrical transport properties of liquid metals has seen significant advances over the past decade as an increasing number of studies employed the Kubo-Greenwood formalism [1,2] on ionic configurations from density-functional-theory-based molecular dynamics (DFT-MD). This computational approach has successfully been applied to aluminum [1,3–6], lithium [7], sodium [8], molybdenum [9], copper [10,11], and iron [12,13].

Among those, the work on iron [12,13] and iron alloys [12,14,15] has been of great interest in geophysics, as their electrical (σ) and thermal conductivity (λ) play a significant role in assessing the efficiency of magnetic field generation and on the thermal evolution of Earth's core [16,17]. Calculations for σ of liquid Fe and Fe-Si alloys show good agreement with measurements from shock wave experiments at pressures $p > 100$ GPa [18,19] and some static experiments in the diamond anvil cell [20,21]. At lower and especially at ambient pressure, Kubo-Greenwood values for σ are significantly larger than experimental data [22–27]. This discrepancy can partly be attributed to the underlying equation of state from the DFT-MD simulations that underestimates molar volumes at ambient pressure by as much as 20% [15,28]. But even if evaluated at the correct density ρ for ambient p, the difference in σ persists.

None of the DFT-MD or Kubo-Greenwood calculations mentioned in the previous paragraph have considered spin polarization, whereas a spin Hamiltonian model predicts disordered local moments in Fe stabilized by entropy to well above the melting temperature (T_M) [29]. This model even suggests that such a paramagnetic state persists to Earth's core conditions. The presence of local moments gives rise to a spin-disordered resistivity contribution, which was computed to be in the range of 100 $\mu\Omega$ cm at ambient pressure above the Curie temperature [30] and 20 $\mu\Omega$ cm at conditions of Earth's core for bcc iron [31]. Two observations are worth pointing out: (i) Resistivity contributions due to electron-phonon scattering and spin disorder are not additive [31]; i.e., Matthiessen's rule does not apply, although it has been used in the analysis of resistivity data [32,33]; (ii) at ambient conditions, the computed spin-disorder resistivity [30] reaches values similar to the total measured resistivity [22].

Here we consider the influence of magnetism on electrical conductivity for liquid Fe directly in DFT-MD and linear response calculations for the Onsager coefficients within the Kubo-Greenwood formalism: We account for collinear magnetism in the electronic structure and, consequently, ionic configurations, using spin-polarized DFT. As Ruban, Belonoshko, and Skorodumova [29] have shown for bcc iron at ambient p, the magnetic moments resulting from such an approach are very similar to the disordered local moments from the effective Hamiltonian. We examine the influence of magnetism on both aspects of the simulations separately, i.e., DFT-MD and the Kubo-Greenwood calculations, to investigate their relative importance and assess differences to the previously published results on liquid Fe.

The molecular dynamics (MD) simulations use forces derived from finite-temperature (FT) DFT [34,35], on the basis of the Born-Oppenheimer approximation. The FT-DFT electronic structure calculations are performed within a collinear formulation of spin states [36,37] and employ the Perdew-Burke-Ernzerhof (PBE) [38] formulation for a semilocal generalized gradient (GGA) corrected exchange correlation functional. Simulations are performed with the Vienna *ab initio* simulation package (VASP) 5.4.1 [39–41], using the projector augmented wave (PAW) method and the potential file [42,43] provided with VASP ([Ar]$4s^2 3p^6$ valence configuration, labeled PAW_PBE Fe_GW) for the electron-core interaction. The plane-wave basis set is expanded to a cutoff energy E_{cut} of 1200 eV, and electronic states are calculated at the Baldereschi mean-value point [44]. The cubic cell is set up containing 70 atoms with periodic boundary conditions. With a Nosé-Hoover thermostat [45,46], we generate a canonical ensemble in which we run 2000–5000 time steps with a length of 2 fs after equilibration. All choices for numerical parameters (potential, E_{cut}, particle number, reciprocal space sampling, time steps, and total duration) are similar to those from previous studies for liquid iron [12,13] and were confirmed to be adequate by several test calculations with more stringent settings.

The electronic transport properties are subsequently computed using linear response theory (LRT) on the Kohn-Sham states [2]. Respective formulas for σ and λ are given in Supplemental Material [47], which includes Refs. [48–51]. These formulas are evaluated using ionic configurations from the MD simulations, averaged over 20–50 uncorrelated configurations per MD run. Numerical parameters for these static FT-DFT calculations are checked as well and were chosen identical to those from the MD simulations except for E_{cut}, which is reduced to 400 eV. At least 5 eV of bands with negligible occupation numbers were taken into account. The broadening parameter of the delta function was set to ≈0.005 eV. Calculations are performed consistently either spin polarized or spin degenerate for both MD and LRT, unless explicitly noted otherwise. The accuracy of our calculated values is 1%–2% for σ and 1%–4% for λ. Consequently, the Lorenz number L [47] is calculated with an accuracy of about 2%–6%. Supplemental Material [47] contains a table with our numerical results.

The total magnetic moment in the simulation cell of the DFT-MD simulations fluctuates around zero, characteristic for a paramagnetic state in the absence of an external field. The magnitude of fluctuations, illustrated by the square of the individual magnetic moments (Fig. 1), decreases systematically with both ρ and T. The most prominent effect due to the presence of magnetic fluctuations in liquid iron is therefore expected at low ρ and low T.

Local magnetic moments in the paramagnetic state can affect conductivity in both parts of the computational approach, i.e., DFT-MD and LRT. We consider the respective influences by a direct comparison of spin-polarized and spin-degenerate calculations at $\rho = 6.75\ \mathrm{g/cm^3}$ and $T = 2250$ K (Fig. 2).

The pair correlation function $g(r)$ of the spin-polarized DFT-MD configurations reveals a slight shift of interatomic distances to larger values and more pronounced maxima and minima. The nearest neighbor distance, measured as the first maximum in $g(r)$, is shifted by 0.08 Å for the spin-polarized results relative to the spin-degenerate simulations (2.47 Å), which is also reflected by a higher pressure (magnetic p) calculated for the spin-polarized case (Fig. 3).

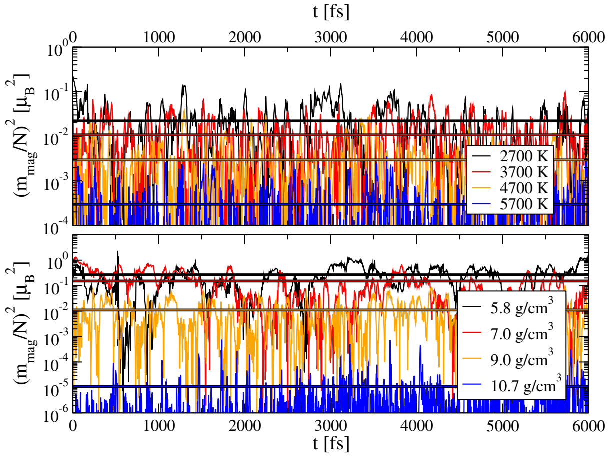

FIG. 1. Quadratic magnetic moment per atom at $\rho = 9\ \mathrm{g/cm^3}$ as a function of the simulation time for different T (upper panel) and at $T = 3700$ K for different ρ (lower panel). Horizontal lines show time averages of the moment squares.

In the LRT, spin polarization influences the electron velocity matrix elements that enter the calculation of the Onsager coefficients [2,47] and enforces a spin selection rule to take effect, due to the difference in electronic structure of the spin-up and spin-down states. Figure 2 shows the dynamic electrical conductivity calculated with

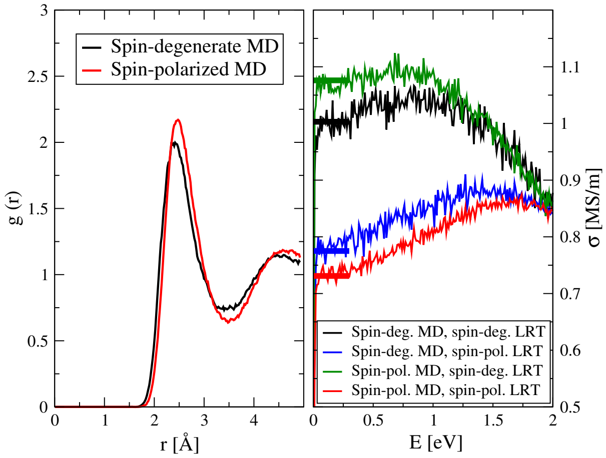

FIG. 2. Pair correlation function from a spin-degenerate and a spin-polarized DFT-MD simulation at $\rho = 6.75\ \mathrm{g/cm^3}$ and $T = 2250$ K (left panel). Frequency-dependent electrical conductivity derived at the same thermodynamic state using all four possible combinations of spin-polarized and spin-degenerate MD and LRT (right panel). dc values are indicated by thick bars of the same color.

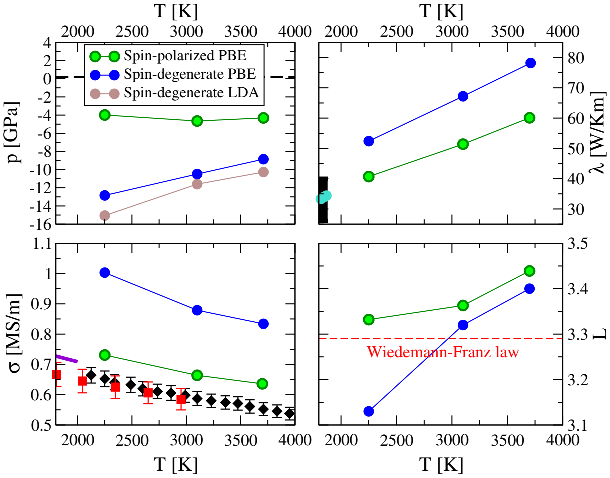

FIG. 3. Pressure and transport properties at densities and temperatures from exploding wire experiments [24]. The results from our work are represented as indicated in the legend. The thin dashed line in the upper left panel indicates the experimental pressure of 0.2 GPa [24]. Measurements of the electrical conductivity by Hixson, Winkler, and Hodgdon [24], Beutl, Pottlacher, and Jäger [25], and van Zytveld [22] are shown as diamonds, squares, and a purple line, respectively. Experimental thermal conductivities reported by Mills, Monaghan, and Keene [52] and Nishi *et al.* [53] are indicated in black and turquoise, respectively.

all four combinations of the spin-degenerate and spin-polarized approach for DFT-MD and LRT.

This comparison illustrates that the influence of spin polarization on optical conductivity through LRT is larger than that of structural changes from DFT-MD simulations. Regardless of whether the spin-polarized LRT calculations are based on configurations from spin-polarized or spin-degenerate MD simulations, zero-frequency values for σ are in the range of 0.7–0.8 MS/m, while spin-degenerate LRT yields values that exceed 1.0 MS/m.

Direct dc measurements of electrical resistivity of liquid Fe at ambient pressure with high precision are limited to 2300 K [22], and measurements at higher T require dynamic techniques [24,25]. These are exploding wire experiments that generate isobaric states (e.g., at 0.2 GPa [24]) and allow for direct measurements of ρ and T. To compare to the experimental data, we perform simulations at densities and temperatures measured in the experiments of Hixson, Winkler, and Hodgdon [24], with $\rho = 6.75$, 6.15, and 5.80 $\mathrm{g/cm^3}$ at $T = 2250$, 3100, and 3710 K, respectively. It is worth pointing out that differences in the density between the two exploding wire studies [24,25] exceed 0.1 $\mathrm{g/cm^3}$ at 3000 K and that the densities of Hixson, Winkler, and Hodgdon [24] are in closer agreement with the thermodynamic model by Komabayashi [54].

In the spin-degenerate PBE simulations, pressure from experiments is underestimated by 8–13 GPa, with the p difference decreasing with T (Fig. 3). Using the local-density approximation (LDA) to exchange and correlation leads to an additional pressure difference of 1–2 GPa. While for most nonmagnetic materials, including transition metals, LDA is known to overbind and PBE to underbind [55,56], for Fe both the LDA and GGA predict volumes that are too low for the crystalline phases [57]. Spin-polarized results, by contrast, show a significantly reduced pressure deviation of about -4 GPa that is T independent, thus correcting the failure of spin-degenerate simulations to a large extent. This behavior is in much better agreement with LDA and PBE calculations for several nonmagnetic materials that show differences in p due to the approximate exchange and correlation functionals to remain largely T independent until at least the critical point [58].

Electrical conductivity values from the spin-degenerate PBE calculations decrease with T at a higher rate and are larger by ≈30% than experimental values [22,24,25]. When spin polarization is taken into account, differences decrease to ≈10% (Fig. 3), and the T dependence becomes similar to the experimental one.

The thermal conductivity of liquid iron has been measured [52,53] only slightly above $T_M = 1808$ K [22], and significant differences exist between experiments [52]. Although we cannot equilibrate liquid states very close to the melting point in the DFT-MD simulations due to restrictions in the system size, the predicted thermal conductivity from our calculations behaves almost linearly with T along the experimental isobar and allows for a reasonable extrapolation to T_M (Fig. 3); for the spin-polarized results, the extrapolation falls within the range of experimental data. Thermal conductivity values from spin-degenerate calculations are significantly higher, and an extrapolation to T_M overshoots experimental values. The Lorenz numbers L of both spin-degenerate and spin-polarized simulations fulfill the Wiedemann-Franz law within 5% of the Drude-Sommerfeld value of $\pi^2/3$. A slight increase in L with T is similar to earlier DFT-MD results for dense hydrogen plasmas [2].

As illustrated in Fig. 1, magnetic fluctuations decrease with compression, and the differences in both the equation-of-state and transport properties are expected to vanish at high densities. As we have seen (Fig. 3), the p difference is ≈4.3 GPa at ambient volume; this difference decreases along with the magnetic fluctuations, and at $\rho = 9.0\ \mathrm{g/cm^3}$ (with magnetic fluctuations below $10^{-2}\ \mu_B^2$) the p difference has disappeared (Fig. 4). This behavior resembles predictions of the loss of magnetism in hexagonal close packed (hcp) iron in an antiferromagnetic (AFM) structure at high pressure that has been set up to model local spin fluctuations [59]. Our simulations show that the magnetic fluctuations drop most significantly in the ρ range between 8 and 9 $\mathrm{g/cm^3}$ from 0.15 to 0.033 μ_B^2, yet smoothly and without a critical loss of magnetism as predicted for other transition metals, e.g., Co [60,61]. Interestingly, the p range

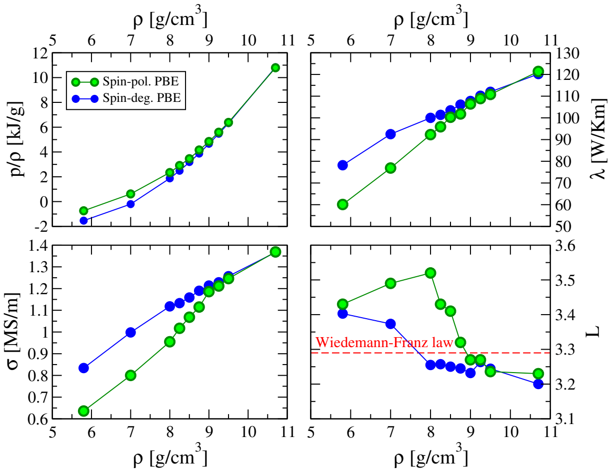

FIG. 4. Reduced pressure p/ρ and electronic transport properties as a function of densities along a 3700 K isotherm. Results from the current work (spin polarized and spin degenerate) are represented as indicated in the legend.

for the most significant decay of magnetic fluctuations (20–50 GPa) coincides with the loss of magnetism predicted in the AFM structure of hcp iron [59].

The electrical conductivity of the spin-degenerate calculations follows a smooth and simple trend (Fig. 4). The results from the spin-polarized calculations, however, display a well-pronounced increase in slope between 8 and 9 g/cm^3; at $\rho \geq 9.5$ g/cm^3, they become indistinguishable from the spin-degenerate results. A similar but less pronounced behavior occurs for the thermal conductivity. This indicates the presence of a continuous transition between paramagnetic and diamagnetic liquid states in the phase diagram of iron.

The Lorenz number of the spin-degenerate calculations decreases with ρ, and its deviation from the Wiedemann-Franz law changes from positive to negative, which occurs between 8 and 9 g/cm^3 (Fig. 4). At $\rho < 9$ g/cm^3, the L of the spin-polarized results is significantly higher than the spin-degenerate values and increases with ρ. However, deviations from the Wiedemann-Franz law do not exceed 8%.

In summary, we have shown that considering spin polarization accounts for much of the discrepancy in electrical and thermal conductivity between Kubo-Greenwood results based on DFT-MD and experiments at low p. This discrepancy has been a significant impediment in the acceptance of Kubo-Greenwood results in the high-pressure mineral physics and geophysics community, where they play a significant role in considerations of the geodynamo. Small differences to experimental values remain both for equation-of-state and transport properties, but these are within the typical range of deviations of DFT-derived properties using (semi)local approximations to the exchange and correlation functional [56,58]. A fully noncollinear treatment of magnetism could further decrease this discrepancy, but such calculations are extremely challenging to converge for disordered systems and beyond the scope of the current work.

The magnitude of magnetic fluctuations decreases with ρ and T. Along the 3700 K isotherm, a pronounced change in σ occurs in a range of $\rho = 8.0$–9.0 g/cm^3, indicating a continuous paramagnetic-to-diamagnetic transition in liquid iron. The ρ-T behavior of the magnetic fluctuations suggests that this transition has a negative slope in p-T space. With diamond anvil cell experiments, it has become possible to probe the relevant range $p = 20$–50 GPa even above the melting line [27], but higher precision in the measurements will be required to detect differences of the scale described here between spin-polarized and spin-degenerate results.

At the conditions of Earth's core, magnetic fluctuations no longer play a role, such that prior results using the Kubo-Greenwood formalism [12–14] are reproduced to within a few percent and serve as a reliable basis for geodynamic considerations [16,62]. For cores of the smaller terrestrial planets in the Solar System, Mercury and Mars, magnetic fluctuations may play a role, although alloying elements in their cores like sulfur or silicon [63,64] may influence their existence and magnitude. Because of the presence of additional scattering centers, conductivities are already reduced to different degrees depending on the nature of light elements incorporated [65]; additional magnetic contributions can potentially remedy two important existing contradictions in geophysics. (i) They may resolve contradictory inferences on the varying influence of different light elements on electrical conductivity in experiments [33] and computations [65]. (ii) Thermal conductivity at low p may be reduced to the degree that values become similar to those used previously in models that describe the thermal evolution and magnetic field generation in Mercury [66] and Mars [67]. This would render the ”new core paradox” for the energy source of a dynamo, termed by Olson [17], for the smaller planets pointless. Nevertheless, powering Earth's dynamo with high thermal conductivity remains a challenge [62].

We thank Fabian Wagle for helpful discussions. This work was supported by the Deutsche Forschungsgemeinschaft (DFG) within the FOR 2440. The *ab initio* calculations were performed at the North-German Supercomputing Alliance (HLRN) facilities and at the IT and Media Center of the University of Rostock.

[1] M. P. Desjarlais, J. D. Kress, and L. A. Collins, Phys. Rev. E **66**, 025401 (2002).
[2] B. Holst, M. French, and R. Redmer, Phys. Rev. B **83**, 235120 (2011).
[3] V. Recoules and J. P. Crocombette, Phys. Rev. B **72**, 104202 (2005).

Supplemental material to: Paramagnetic-to-diamagnetic transition in dense liquid iron and its influence on electronic transport properties

Jean-Alexander Korell, Martin French, Gerd Steinle-Neumann, Ronald Redmer
[1] *Universität Rostock, Institut für Physik, Albert-Einstein-Str. 23-24, D-18059 Rostock, Germany*
[2] *Bayerisches Geoinstitut, Universität Bayreuth, D-95440 Bayreuth, Germany*
(Dated: February 11, 2019)

This material supplements the information given in the letter "Paramagnetic-to-diamagnetic transition in dense liquid iron and its influence on electronic transport properties".

I. LINEAR RESPONSE EXPRESSIONS FOR THE TRANSPORT COEFFICIENTS

The electronic transport properties are calculated using linear response theory (LRT) on the Kohn-Sham states. In detail, the following Onsager coefficients $L_n(\omega)$ are calculated for an ensemble of ionic configurations from each of the MD simulations [1],[2]:

$$L_{\,n}(\omega) = \frac{\pi(-1)^n}{3V\omega} \sum_{\mathbf{k}\nu\mu\alpha} |\langle \mathbf{k}\nu\alpha|\hat{\mathbf{v}}|\mathbf{k}\mu\alpha\rangle|^2 (f_{\mathbf{k}\nu\alpha} - f_{\mathbf{k}\mu\alpha}) \times \left(\frac{E_{\mathbf{k}\mu\alpha} + E_{\mathbf{k}\nu\alpha}}{2} - h_e \right)^n \delta(E_{\mathbf{k}\mu\alpha} - E_{\mathbf{k}\nu\alpha} - \hbar\omega)\,, \quad (1)$$

where ω is the frequency, V the volume of the simulation box, h_e the enthalpy per electron, $E_{\mathbf{k}\mu\alpha}$ and $f_{\mathbf{k}\mu\alpha}$ are the eigenvalue and Fermi occupation number of the Bloch state $|\mathbf{k}\mu\alpha\rangle$ characterized by a reciprocal space coordinate $\mathbf{k}$, a band index μ (or ν), and a spin state α. The matrix elements $\langle \mathbf{k}\nu\alpha|\hat{\mathbf{v}}|\mathbf{k}\mu\alpha\rangle$ are calculated from the dipole transition matrix elements, $\langle \mathbf{k}\nu\alpha|\hat{\mathbf{r}}|\mathbf{k}\mu\alpha\rangle$, that are computed by the optical routines of VASP [3, 4],[5]. They contain all nonlocal contributions from the PAW pseudopotentials [3]. The delta function is broadened to a small finite width with a Gaussian representation.

The static electrical conductivity is directly given by the coefficient $L_0(\omega)$ in the limit of zero frequency, which is also known as the Kubo-Greenwood formula [6, 7]:

$$\sigma = \lim_{\omega \to 0} e^2 L_0(\omega), \quad (2)$$

where e is the elementary charge. The thermal conductivity is calculated analogously via the relation:

$$\lambda = \lim_{\omega \to 0} \frac{1}{T} \left(L_2(\omega) - \frac{L_1^2(\omega)}{L_0(\omega)} \right). \quad (3)$$

The Lorenz number is then given by:

$$L = \frac{e^2 \lambda}{k_B^2 T \sigma}, \quad (4)$$

where k_B is Boltzmann's constant.

II. CALCULATED VALUES IN TABULAR FORM

All calculated numerical values for σ and λ in the zero-frequency limit are given in Table I. The error bars are composed of a statistical uncertainty of about 1% plus an estimated systematic error (due to particle number and $\mathbf{k}$-point settings) of 1-4% estimated with several convergence tests. The systematic uncertainty is about 1% for σ and larger in case of λ, especially toward high densities. The last row in Table I includes an additional data point that reproduces a spin-degenerate calculation by Pozzo *et al.* [8] for Earth's core conditions.

---

[1] B. Holst, M. French, and R. Redmer, Phys. Rev. B **83**, 235120 (2011).
[2] A reduction of indexes is made here for simplicity.
[3] M. Gajdoš, K. Hummer, G. Kresse, J. Furthmüller, and F. Bechstedt, Phys. Rev. B **73**, 045112 (2006).
[4] M. French and R. Redmer, Phys. Plasmas **24**, 092306 (2017).
[5] This procedure is only applicable to the off-diagonal matrix elements. However, diagonal matrix elements (electron velocities) do not contribute in Eq. (1).
[6] R. Kubo, J. Phys. Soc. Jpn. **12**, 570 (1957).
[7] D. A. Greenwood, Proc. Phys. Soc. **71**, 585 (1958).
[8] M. Pozzo, C. Davies, D. Gubbins, and D. Alfè, Phys. Rev. B **87**, 014110 (2013).

TABLE I. Numerical values for electrical and thermal conductivity for spin-degenerate and spin-polarized calculations.

ϱ [g/cm^3]	T [K]	$\sigma_{\mathrm{spin-deg}}$ [MS/m]	$\lambda_{\mathrm{spin-deg}}$ [W/Km]	$\sigma_{\mathrm{spin-pol}}$ [MS/m]	$\lambda_{\mathrm{spin-pol}}$ [W/Km]
6.75	2250	1.00 ± 0.02	52.4 ± 1.1	0.73 ± 0.01	40.7 ± 0.8
6.15	2700	0.88 ± 0.01	67.2 ± 1.5	0.66 ± 0.01	51.4 ± 1.0
5.8	3710	0.83 ± 0.01	78.2 ± 1.6	0.64 ± 0.01	60.1 ± 1.2
7.0	3700	1.00 ± 0.01	92.5 ± 2.0	0.80 ± 0.01	67.9 ± 1.5
8.0	3700	1.12 ± 0.02	100.0 ± 2.5	0.96 ± 0.01	92.3 ± 2.5
8.25	3700	1.13 ± 0.02	101.4 ± 2.5	1.02 ± 0.02	95.9 ± 2.5
8.5	3700	1.16 ± 0.02	103.5 ± 2.5	1.07 ± 0.02	100.3 ± 2.5
8.75	3700	1.19 ± 0.02	106.1 ± 3.0	1.12 ± 0.02	101.8 ± 3.0
9.0	3700	1.21 ± 0.02	107.8 ± 3.0	1.19 ± 0.02	106.4 ± 3.0
9.25	3700	1.23 ± 0.02	110.2 ± 3.0	1.21 ± 0.02	108.9 ± 3.0
9.5	3700	1.26 ± 0.02	112.0 ± 3.5	1.25 ± 0.02	110.8 ± 3.5
10.69	3700	1.37 ± 0.02	120.2 ± 4.5	1.37 ± 0.02	121.4 ± 4.5
10.69	4700	1.36 ± 0.02	153.0 ± 6.0	-	-

The Astrophysical Journal Supplement Series, 202:5 (11pp), 2012 September doi:10.1088/0067-0049/202/1/5

AB INITIO SIMULATIONS FOR MATERIAL PROPERTIES ALONG THE JUPITER ADIABAT

Martin French[1], Andreas Becker[1], Winfried Lorenzen[1], Nadine Nettelmann[1],
Mandy Bethkenhagen[1], Johannes Wicht[2], and Ronald Redmer[1]
[1] Institut für Physik, Universität Rostock, D-18051 Rostock, Germany
[2] Max-Planck-Institut für Sonnensystemforschung, D-37191 Katlenburg-Lindau, Germany

Received 2012 April 10; accepted 2012 July 9; published 2012 August 24

ABSTRACT

We determine basic thermodynamic and transport properties of hydrogen–helium–water mixtures for the extreme conditions along Jupiter's adiabat via ab initio simulations, which are compiled in an accurate and consistent data set. In particular, we calculate the electrical and thermal conductivity, the shear and longitudinal viscosity, and diffusion coefficients of the nuclei. We present results for associated quantities like the magnetic and thermal diffusivity and the kinematic shear viscosity along an adiabat that is taken from a state-of-the-art interior structure model. Furthermore, the heat capacities, the thermal expansion coefficient, the isothermal compressibility, the Grüneisen parameter, and the speed of sound are calculated. We find that the onset of dissociation and ionization of hydrogen at about 0.9 Jupiter radii marks a region where the material properties change drastically. In the deep interior, where the electrons are degenerate, many of the material properties remain relatively constant. Our ab initio data will serve as a robust foundation for applications that require accurate knowledge of the material properties in Jupiter's interior, e.g., models for the dynamo generation.

Key words: conduction – diffusion – equation of state – planets and satellites: individual (Jupiter, material properties) – plasmas

1. INTRODUCTION

The detection of a great number of Jupiter-mass planets has boosted the interest in the physics of giant planets. Fundamental questions are related to their formation, evolution, and present structures including internal flow dynamics and magnetic field generation (Stevenson 1982; Guillot 2005; Jones et al. 2011). Little is known about the extrasolar planets and even our knowledge about Jupiter is still incomplete. The latter should improve considerably with the arrival of NASA's *Juno* mission at Jupiter in 2016 (Matousek 2007).

While progress has been achieved in explaining the overall shape of Jupiter's dipole-dominated field geometry (Christensen & Aubert 2006; Wicht & Tilgner 2010; Stanley & Glatzmaier 2010; Schubert & Soderlund 2011), basic properties, such as the observed flow patterns in the atmosphere (Heimpel et al. 2005; Vasavada & Showman 2005; Kaspi et al. 2009; Gastine & Wicht 2012), still await explanations that are consistent with planetary structure and dynamo models. So far, many of these models use rather gross simplifying assumptions about the interior structure and material properties, partially for numerical convenience but also because of the lack of adequate data. The knowledge of the properties of matter inside Jupiter is thus very important for both interior structure and magnetic field models.

In the past decade, enormous progress has been made in high-pressure experimental techniques (see, e.g., Knudson et al. 2004; Fortov et al. 2007; Celliers et al. 2010; Subramanian et al. 2011; Knudson et al. 2012), so that the Mbar pressure range can now be probed even for the light elements H and He. Simultaneously, the behavior of hydrogen and helium under extreme conditions has been investigated using ab initio simulations (see, e.g., Desjarlais 2003; Militzer 2006, 2009; Vorberger et al. 2007; Kietzmann et al. 2007; Holst et al. 2008, 2011; Stixrude & Jeanloz 2008; Lorenzen et al. 2009, 2010, 2011; Morales et al. 2009, 2010; Caillabet et al. 2011; Hamel et al. 2011). The predictions that can be made with the ab initio simulation technique are generally in very good agreement with experiments. Furthermore, the method allows one to examine extreme thermodynamic states deep inside Jupiter that cannot yet be generated in the laboratory.

In spite of all of the progress, no data set that has been derived consistently using a single method for the thermophysical properties, i.e., the equation of state (EOS), as well as for transport properties, is yet available for the interior conditions of Jupiter. While the chemical model EOS of Saumon et al. (1995) for H and He has had wide application in planetary physics, the electronic transport properties are usually approximated by interpolating between known limiting cases such as the fully ionized classical plasma (Spitzer & Härm 1953) and the degenerate quantum plasma (Ziman 1961). For instance, feasible interpolation formulae were given by Hubbard (1966), Lee & More (1984), Ichimaru & Tanaka (1985), and Röpke & Redmer (1989). Simple estimations for the thermal diffusivity and viscosity of hydrogen–helium mixtures exist as well (Stevenson & Salpeter 1977).

The aim of the present paper is to provide, for the first time, an accurate data set for the electrical conductivity σ, thermal conductivity λ, shear viscosity η, longitudinal viscosity η', the self-diffusion coefficients of hydrogen D_{H} and helium D_{He}, heat capacities c_p and c_v, thermal expansion coefficient α, isothermal compressibility κ_T, sound velocity c_s, and Grüneisen parameter γ at conditions along Jupiter's adiabat. Our data are obtained entirely from ab initio simulations (see Gillan et al. 2006; Hafner 2008 for reviews). This is the same method that has recently been used to calculate an improved hydrogen EOS and corresponding new Jupiter models and adiabats (Nettelmann et al. 2012).

We expect that this work will provide a robust set of material data that can be applied in models of Jupiter's magnetic field and internal flow dynamics (Kirk & Stevenson 1987; Heimpel et al. 2005). In such applications, our results would enter several of the dimensionless quantities (characteristic numbers) that can be defined, see, e.g., Table 2 in the review of Schubert & Soderlund (2011) for a compilation of those. So far, these models rely on relatively rough estimates of the quantities mentioned above.

Therefore, the derivation of consistent ab initio data for the thermodynamic and transport properties of H/He under extreme conditions is a very beneficial effort.

Our paper is arranged as follows. Sections 2 and 3 describe the ab initio simulation method for the EOS data and the interior model for Jupiter and contain results for the Jupiter adiabat, basically referring to the recent work of Nettelmann et al. (2012). Our results for the thermodynamic material properties c_p, c_v, α, κ_T, c_s, and γ are presented in Section 4. The theoretical method for computing the transport properties σ, λ, η, η', D_{H}, and D_{He} is described in Section 5 while Section 6 contains the respective results for the transport properties. We summarize our results and discuss their potential impact on future flow and dynamo models in Section 7.

2. AB INITIO SIMULATIONS FOR THE EOS DATA

In this paper, we calculate the material properties along Jupiter's adiabat. Therefore, accurate EOS data for the main components (hydrogen, helium, and heavy elements) as well as a state-of-the-art interior model are necessary. The underlying EOS data—a linear-mixture EOS of hydrogen, helium, and water—that will serve in the calculations of material properties in Section 4 have previously been used to calculate a series of Jupiter models (Nettelmann et al. 2012). Although the heavy elements, represented by water, occur only in very small quantities in Jupiter's envelope, their contribution to the total mass density ϱ must be taken into account in the complete EOS.

The EOS data for helium and water are the same as described in Nettelmann et al. (2008). The EOS of hydrogen, however, has been refined (H-REOS.2), which is explained in more detail in Nettelmann et al. (2012). For the sake of clarity, we repeat here the characteristics of the ab initio simulation method as well as numerical details of the calculations for hydrogen. Because of its high concentration in Jupiter the behavior of hydrogen dominates the properties of the complete EOS. Note that ab initio EOS data cover the pressure region above ~0.08 Mbar for H, ~0.1 Mbar for He, (Kietzmann et al. 2007), and ~0.1 Mbar for H_2O (French et al. 2009); see also Figures 1–3 in Nettelmann et al. (2008). The EOS of the mixture is obtained by the additive volume rule (Chabrier et al. 1992), implying a linear superposition of the single materials' EOS which neglects interactions between the different materials. As a result, combined data tables for the thermal and the caloric EOS were generated from which all thermodynamic quantities of interest can be gained via interpolation and differentiation.

The ab initio simulation method allows a quantum-statistical treatment of the electrons within the framework of finite-temperature density functional theory (FT-DFT) (Mermin 1965) in combination with classical molecular dynamics (MD) simulations for the ions in the Born–Oppenheimer approximation. The Vienna Ab initio Simulation Package (VASP; Kresse & Hafner 1993, 1994; Kresse & Furthmüller 1996) was used to calculate the EOS of hydrogen (Nettelmann et al. 2012). The exchange-correlation functional is the fundamental physical input in FT-DFT calculations, and the approximation of Perdew et al. (1996, hereafter PBE), which yields generally good results for the thermodynamic properties of warm dense matter, has been used; see, e.g., Holst et al. (2008), Knudson et al. (2008), Caillabet et al. (2011), and French et al. (2009).

From the FT-DFT algorithm, the forces on the ions are derived via the Hellmann–Feynman theorem at each MD time step. This procedure is repeatedly performed in a cubic simulation box with periodic boundary conditions for several thousand MD time steps. The ion temperature is controlled with a Nosé thermostat (Nosé 1984). In the case of hydrogen, typical simulations were about 5 ps long with time steps ranging from 0.1 to 1 fs.

Excellent convergence of the results was ensured with several checks with respect to the particle number, the sets used for the evaluation of the Brillouin zone, as well as the employed pseudopotentials and their respective energy cutoff for the plane-wave basis set. Projector-augmented wave (PAW) pseudopotentials (Blöchl 1994; Kresse & Joubert 1999) were used at all considered densities with a converged energy cutoff of 1200 eV. The EOS simulations for H were performed with 256 particles and the Baldereschi mean-value **k** point (Baldereschi 1973), as in earlier work (Holst et al. 2008; Lorenzen et al. 2010; Holst et al. 2011).

Since the ions are treated as classical particles within an FT–DFT–MD simulation, the heat capacities of molecular gases are usually overestimated (French & Redmer 2009), so that a quantum-mechanical correction to the caloric EOS $u(\varrho, T)$ with respect to the molecular vibrations had to be made afterward; see Nettelmann et al. (2012) for details.

The ab initio simulation method as described here is also used in the calculations for the present paper.

3. JUPITER MODELS AND ADIABAT

The work presented here relies on the linear-mixing EOS described above and on Jupiter models constructed by Nettelmann et al. (2012). Here we give only a brief summary of their key features. The Jupiter models have two adiabatic homogeneous envelopes and a core of rocks. These models reproduce the measured values of the planet mass M_J; the equatorial radius $R_{\mathrm{eq}} = 7.1492 \times 10^7$ m; the atmospheric mass abundances of helium and heavy elements; the angular velocity; the three lowest-order gravitational moments J_2, J_4, J_6; and the 1 bar temperature T_1 which determines the entropy of the outer envelope, within their observational error bars. The models have a mean He:H mass ratio $Y = M_{\mathrm{He}}/(M_{\mathrm{He}} + M_{\mathrm{H}}) = 0.275$, while the He abundance chosen in the outer envelope, $Y_1 = 0.238$, is in agreement with the measured one in the atmosphere. The two envelopes are also allowed to differ in their respective mass fractions of heavy elements Z_1 and Z_2, which are used as adjusting parameters to match J_2 and J_4, respectively.

In this paper, we select two representative models from Nettelmann et al. (2012). In particular, model J11-4a has a transition pressure between the envelopes of $P_{1-2} = 4$ Mbar, resulting in $M_{\mathrm{core}} = 7.57\, M_{\oplus}$, $Z_1 = 0.030$, $Z_2 = 0.090$, $Y_2 = 0.291$, and $R(P_{1-2}) = 0.736 R_J$, while model J11-8a has $P_{1-2} = 8$ Mbar, $M_{\mathrm{core}} = 3.56\, M_{\oplus}$, $Z_1 = 0.038$, $Z_2 = 0.128$, $Y_2 = 0.311$, and $R(P_{1-2}) = 0.629 R_J$, where $R_J = 6.9894 \times 10^7$ m is Jupiter's mean radius.

Originally, the adiabats for these models were derived via a thermodynamic integration scheme; see Nettelmann et al. (2012). Here we recalculate the adiabats with the following relation:

$$\left(\frac{\partial T}{\partial \varrho}\right)_s = \frac{T}{\varrho^2} \frac{\left(\frac{\partial P}{\partial T}\right)_\varrho}{\left(\frac{\partial u}{\partial T}\right)_\varrho} = \frac{T}{\varrho}\gamma. \tag{1}$$

When keeping all model parameters from Nettelmann et al. (2012) constant, this yields slightly different results for p and T because the procedure is more sensitive to the local derivatives of the EOS data. In addition, the new adiabat is smoother and we believe that it is more appropriate for our special purpose of

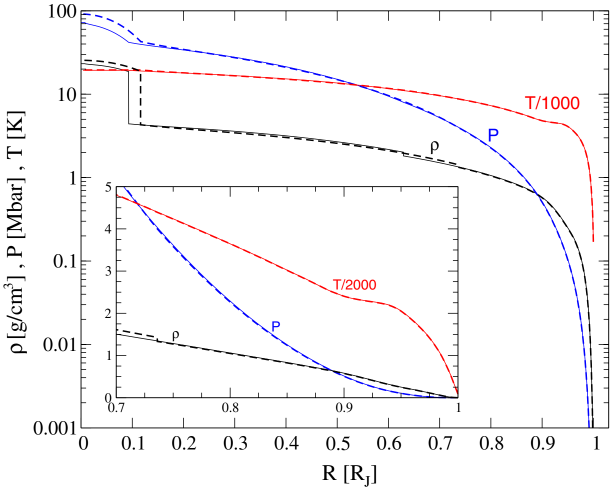

Figure 1. Interior profiles of pressure (blue), temperature (red), and mass density (black) for the two representative Jupiter models J11-4a (dashed) and J11-8a (thin solid). The density has a jump at the transition pressure between the envelopes. Inset: the transit region between the metallic inner region and the molecular outer part.

deriving material properties. The maximum deviation between the new and the original adiabats is 5% for both $P(R)$ and $T(R)$ and occurs mainly in the dissociation regime near $0.9R_J$. The density profile remains unchanged.

The internal profiles $P(R)$, $T(R)$, and $\varrho(R)$ of the respective models are shown in Figure 1. As can be seen, the pressure and temperature profiles are relatively insensitive to details of the model assumptions. This property allows us to define a general Jupiter adiabat in P–T space. Therefore, we mainly focus on the Jupiter model J11-8a in the following.

The density profiles displayed here may serve to set the average density for the flow and dynamo models which apply the Boussinesq approximation (Braginsky & Roberts 1995; Heimpel & Aurnou 2007; Wicht & Tilgner 2010) or the density gradient in the anelastic approximation of more advanced models (Kaspi et al. 2009; Stanley & Glatzmaier 2010; Jones et al. 2011; Gastine & Wicht 2012).

4. THERMODYNAMIC MATERIAL PROPERTIES

In this section, we outline the calculation of thermodynamic material properties and present the corresponding results. We have determined these quantities from the linearly mixed ab initio EOS by differentiation in the vicinity of the Jupiter adiabat. The major results are listed in Table 1.

4.1. *Definitions*

To calculate the thermal expansion coefficient α, the isothermal compressibility κ_T, the specific heat capacities for constant volume (or density), c_v, and for constant pressure, c_p, we use the following definitions:

$$\alpha = -\frac{1}{\varrho}\left(\frac{\partial \varrho}{\partial T}\right)_P = \frac{1}{\varrho}\left(\frac{\partial P}{\partial T}\right)_\varrho \left(\frac{\partial \varrho}{\partial P}\right)_T , \tag{2}$$

$$\kappa_T = \frac{1}{\varrho}\left(\frac{\partial \varrho}{\partial P}\right)_T , \tag{3}$$

$$c_v = \left(\frac{\partial u}{\partial T}\right)_\varrho , \tag{4}$$

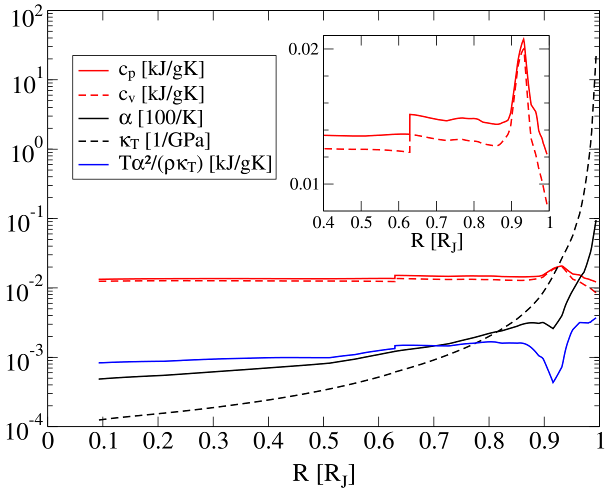

Figure 2. Thermodynamic material properties along Jupiter's adiabat for the model J11-8a: specific heat capacities c_v (red dashed) and c_p (red solid), isobaric expansion coefficient α (black solid), isothermal compressibility κ_T (black dashed), and $c_p - c_v$ (blue solid); see Equation (5). The discontinuities at 0.63 R_J are due to different material abundances in the layers.

$$c_p = c_v + \frac{T\alpha^2}{\varrho \kappa_T} . \tag{5}$$

We use cubic spline interpolations to generate smooth curves of $P(\varrho, T)$ and $u(\varrho, T)$ from the EOS data tables. The material properties are then derived via analytic differentiation of the spline polynomials.

Several other material properties can be expressed as functions of the quantities given above. For example, the sound velocity is determined from the heat capacities and the isothermal compressibility via

$$c_s = \sqrt{\left(\frac{\partial P}{\partial \varrho}\right)_s} = \sqrt{\frac{c_p}{\varrho c_v \kappa_T}} . \tag{6}$$

The Grüneisen parameter is given by

$$\gamma = \frac{1}{\varrho}\left(\frac{\partial P}{\partial u}\right)_\varrho = \frac{\alpha}{\varrho c_v \kappa_T} . \tag{7}$$

4.2. *Results*

4.2.1. *Specific Heat Capacities, Isothermal Compressibility, and Thermal Expansion Coefficient*

The numerical results for c_p, c_v, κ_T, and α are shown in Figure 2. Starting at R_J, the heat capacity c_v increases inward until reaching a maximum at $\sim 0.9R_J$ (i.e., ∼0.5 Mbar) which is caused by the dissociation of hydrogen molecules. The isobaric heat capacity c_p shows a similar behavior as c_v but is larger, as is required by a thermodynamic stability condition. For $R < 0.85R_J$, c_v and c_p remain nearly constant right down to the core–mantle boundary, except for a jump at the transition pressure (here 8 Mbar) due to the different abundances of helium and heavy elements in the layers. Although H has a larger heat capacity than He, it is less abundant in the lower layer, which leads to a smaller heat capacity of the mixture.

The thermal expansion coefficient α, together with κ_T, T, and ϱ, determines the difference between c_p and c_v; see Equation (5).

Table 1
Thermodynamic Material Properties in Jupiter (Model J11-8a)

R (R_J)	ϱ (g cm^{-3})	T (K)	P (GPa)	c_p (kJ gK^{-1})	c_v (kJ gK^{-1})	α (1 K^{-1})	κ_T (1 GPa^{-1})	c_s (km s^{-1})	γ
0.0923	4.42	19500	4180	1.33×10^{-2}	1.25×10^{-2}	4.85×10^{-6}	1.25×10^{-4}	44.03	0.705
0.196	3.99	18000	3410	1.36×10^{-2}	1.27×10^{-2}	5.43×10^{-6}	1.53×10^{-4}	41.89	0.707
0.350	3.39	16000	2460	1.36×10^{-2}	1.27×10^{-2}	6.58×10^{-6}	2.13×10^{-4}	38.64	0.737
0.478	2.80	14000	1640	1.36×10^{-2}	1.26×10^{-2}	7.82×10^{-6}	3.10×10^{-4}	35.23	0.728
0.584	2.26	12000	1030	1.37×10^{-2}	1.25×10^{-2}	1.04×10^{-5}	4.79×10^{-4}	31.83	0.782
0.629	2.02	11000	800	1.37×10^{-2}	1.24×10^{-2}	1.22×10^{-5}	6.07×10^{-4}	30.10	0.823
0.629	1.82	11000	800	1.52×10^{-2}	1.37×10^{-2}	1.22×10^{-5}	6.14×10^{-4}	31.49	0.807
0.680	1.60	10000	600	1.49×10^{-2}	1.34×10^{-2}	1.38×10^{-5}	8.08×10^{-4}	29.34	0.802
0.770	1.20	8000	300	1.49×10^{-2}	1.33×10^{-2}	1.90×10^{-5}	1.52×10^{-3}	24.82	0.781
0.852	0.824	6000	120	1.45×10^{-2}	1.29×10^{-2}	2.83×10^{-5}	3.64×10^{-3}	19.38	0.737
0.890	0.638	5000	64	1.47×10^{-2}	1.37×10^{-2}	3.09×10^{-5}	7.09×10^{-3}	15.44	0.501
0.900	0.581	4800	51	1.57×10^{-2}	1.48×10^{-2}	3.12×10^{-5}	9.11×10^{-3}	14.15	0.402
0.908	0.531	4700	42	1.73×10^{-2}	1.66×10^{-2}	2.86×10^{-5}	1.15×10^{-2}	13.04	0.292
0.918	0.464	4600	32	1.93×10^{-2}	1.88×10^{-2}	2.72×10^{-5}	1.60×10^{-2}	11.74	0.208
0.930	0.380	4500	23	2.06×10^{-2}	1.99×10^{-2}	3.76×10^{-5}	2.47×10^{-2}	10.50	0.215
0.940	0.312	4400	16	1.87×10^{-2}	1.73×10^{-2}	5.97×10^{-5}	3.57×10^{-2}	9.87	0.323
0.952	0.240	4000	9.6	1.59×10^{-2}	1.34×10^{-2}	9.27×10^{-5}	5.75×10^{-2}	9.28	0.503
0.964	0.177	3500	5.0	1.54×10^{-2}	1.22×10^{-2}	1.36×10^{-4}	1.15×10^{-1}	7.86	0.526
0.972	0.132	3000	2.7	1.40×10^{-2}	1.12×10^{-2}	1.68×10^{-4}	2.31×10^{-1}	6.41	0.498
0.980	0.0848	2500	1.2	1.34×10^{-2}	1.03×10^{-2}	2.58×10^{-4}	6.23×10^{-1}	4.97	0.494
0.986	0.0497	2000	0.45	1.29×10^{-2}	9.55×10^{-3}	3.89×10^{-4}	1.78	3.90	0.470
0.994	0.0113	1000	0.0434	1.22×10^{-2}	8.50×10^{-3}	9.50×10^{-4}	21.97	2.40	0.453

Notes. The number of digits does not necessarily correspond to the actual error bar in all cases. The double values at 11000 K are either from the inner or the outer envelope. The respective boundary is also indicated by a separating line. It is $R_J = 6.9894 \times 10^7$ m.

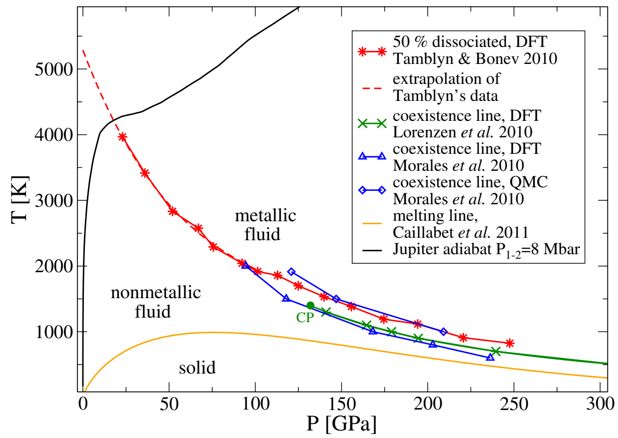

Figure 3. Phase diagram of hydrogen with the Jupiter adiabat. The data are taken from Tamblyn & Bonev (2010), Lorenzen et al. (2010), Morales et al. (2010), and Caillabet et al. (2011).

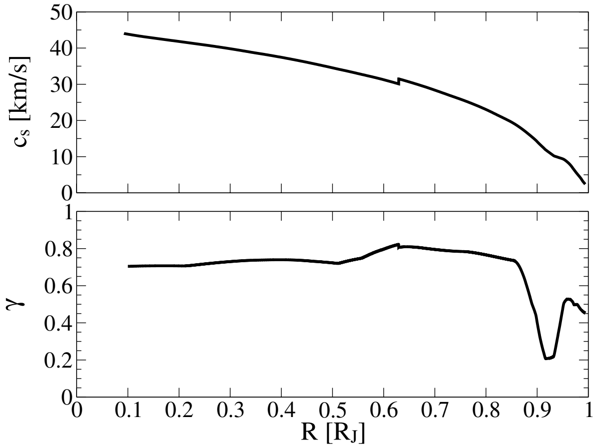

Figure 4. Sound velocity (upper panel) and Grüneisen parameter (lower panel) along Jupiter's adiabat for the model J11-8a. The discontinuities at 0.63 R_J are due to different material abundances in the layers.

The temperature and the density increase monotonously with the depth while κ_T decreases. Only the expansion coefficient α has a local extremum, which occurs exactly in the dissociation regime. There, the difference between the heat capacities becomes very small. The smooth behavior of all quantities in the second term of Equation (5) leads to compensating effects and hence to parallel slopes of c_p and c_v.

A first-order liquid–liquid phase transition has been predicted in hydrogen for temperatures below 2000 K (Morales et al. 2010; Lorenzen et al. 2010), which is accompanied by the abrupt dissociation of hydrogen molecules. While the isentrope is well above the critical point of this first-order transition, Figure 3 suggests that an extrapolation of the 50% dissociation line (Tamblyn & Bonev 2010) to higher temperatures intersects with the Jupiter adiabat. The heat capacities c_p and c_v have a maximum in that particular region, which reflects the additional energy required to break the intramolecular bonds.

4.2.2. Sound Velocity and Grüneisen Parameter: Consequences for the Adiabat

Figure 4 shows that c_s rises with depth within both envelopes as the interior becomes warmer but also increasingly degenerate. When dissociation occurs at $\sim 0.9 R_J$, c_v rises steeper than c_p, and the increase of c_s with depth is attenuated. At the internal layer boundary, the discontinuous rise in mass density maps onto a respective decrease in c_s, which can be seen in Figure 4.

In the deep interior, the value of the Grüneisen parameter is almost constant and close to the ideal Fermi-gas value of 2/3. This behavior changes drastically in the dissociation regime, where the Grüneisen parameter drops to about 0.2. The reason for this is the minimum in α and the maximum in c_v which add to each other; see Equation (7). However, the effect is only local and outside of $\sim 0.95 R_J$, the Grüneisen parameter tends to approach a value close to 0.4, which is characteristic for a classical diatomic ideal gas without vibrational excitations.

According to Equation (1), the Grüneisen parameter determines the slope of the adiabat. The flattening of the adiabat in the dissociation regime (see Figure 3) is thus a direct consequence of the pronounced minimum in γ.

5. TRANSPORT PROPERTIES: THEORY

The calculation of transport properties with the FT-DFT-MD method involves the application of linear response theory (Kubo 1957) and is much more demanding than pure EOS calculations. All transport properties are derived from FT-DFT-MD simulations for a hydrogen–helium mixture with representative concentrations. We employ again the VASP program package (Kresse & Hafner 1993, 1994; Kresse & Furthmüller 1996). The influence of heavier elements is neglected here because of their small particle abundances in the envelopes of Jupiter.

Due to the Born–Oppenheimer approximation we have to treat the contributions of the electrons and nuclei separately in the conductivity calculations. In the case of the electrical conductivity, the electronic contribution σ_e is much larger than that of the ions σ_i. The reason for this is that, once the system ionizes, the free electrons are much more mobile than the nuclei because of their large mass difference. Significant ionic conductivity, e.g., due to proton hopping as in warm dense water (French et al. 2011), can be ruled out because no charge transfer occurs between hydrogen and helium when all electrons are bound. Thus, we can safely approximate the total electrical conductivity as $\sigma = \sigma_e$.

In contrast, the electronic contribution to the thermal conductivity of the electrons λ_e is not always larger than the contributions of the ions λ_i. In particular, the molecular region of the phase diagram, where the electrons are bound and the energy is transported via intermolecular collisions, shows a very small λ_e. Therefore, the total thermal conductivity is generally given by the sum of both terms, $\lambda = \lambda_e + \lambda_i$.

5.1. *Viscosities*

The viscosities are governed by the motion of the nuclei so that the contribution of free electrons does not need to be considered for these quantities (Bertolini et al. 2007; Bernu & Vieillefosse 1978).

Both shear and longitudinal viscosities were determined from FT–DFT–MD simulations for H–He mixtures using the standard PAW pseudopotentials (Blöchl 1994; Kresse & Joubert 1999) and a cutoff energy of 1200 eV. We employ the PBE exchange-correlation functional (Perdew et al. 1996). An ensemble of 108 hydrogen and 10 helium atoms was simulated to represent the mean helium concentration of $Y = 0.275$. Depending on the density, either the $2 \times 2 \times 2$ Monkhorst–Pack **k**-point set (Monkhorst & Pack 1976) or the Balderschi point (Baldereschi 1973) was chosen to ensure the convergence of the pressure tensor.

The dynamic shear viscosity η was then derived within the standard linear response approach (Kubo et al. 1991; Allen & Tildesley 1989; Alfè & Gillan 1998) which requires the calculation of a time integral over the autocorrelation function of the off-diagonal components p_{ij} of the pressure tensor,

$$\eta = \frac{\Omega}{3k_BT}\int_0^\infty dt \sum_{ij=\{xy,yz,zx\}} \langle p_{ij}(0)p_{ij}(t)\rangle. \tag{8}$$

In the above equation, Ω is the volume of the simulation box and k_B is Boltzmann's constant. In the same way, the longitudinal viscosity η' was calculated from the autocorrelation function of the diagonal elements p_i of the pressure tensor,

$$\eta' = \frac{\Omega}{3k_BT}\int_0^\infty dt \sum_{i=\{x,y,z\}} \langle (p_i(0)-\langle p_i\rangle)(p_i(t)-\langle p_i\rangle)\rangle. \tag{9}$$

For each data point, a simulation with 80000 to 140000 time steps, with time-step sizes of 0.2 or 0.3 fs, was performed to attain a statistical uncertainty for η and η' of better than 10% in most cases. In addition, several simulations were done to test the convergence with respect to all numerical parameters listed here and to rule out potential disturbances by the thermostat.

5.2. *Electrical and Thermal Conductivity: Electronic Contribution*

5.2.1. *Onsager Coefficients*

As a first step to obtain electrical and thermal conductivities, we performed FT–DFT–MD simulations to get ensembles of equilibrated ion configurations. Then we calculated the frequency-dependent Onsager coefficients for electron transport in subsequent static FT–DFT runs for 20–100 ion configurations taken from each of the simulations. The respective results were then averaged. Expressions for the Onsager coefficients $L_{mn}(\omega)$ were derived by Holst et al. (2011) in the framework of linear response theory. They read

$$L_{mn}(\omega) = \frac{2\pi q^{4-m-n}}{3\Omega m_e^2\omega}\sum_{\mathbf{k}\nu\mu} |\langle \mathbf{k}\nu|\hat{\mathbf{p}}|\mathbf{k}\mu\rangle|^2 (f_{\mathbf{k}\nu}-f_{\mathbf{k}\mu}) \times \left(\frac{E_{\mathbf{k}\mu}+E_{\mathbf{k}\nu}}{2} - h_e\right)^{m+n-2} \delta(E_{\mathbf{k}\mu}-E_{\mathbf{k}\nu}-\hbar\omega), \tag{10}$$

where ω is the frequency, $q = -e$ and m_e are the charge and mass of an electron, h_e is the enthalpy per electron, $E_{\mathbf{k}\mu}$ and $f_{\mathbf{k}\mu}$ are the eigenvalue and Fermi occupation number of the Bloch state $|\mathbf{k}\mu\rangle$, and $\langle \mathbf{k}\nu|\hat{\mathbf{p}}|\mathbf{k}\mu\rangle$ are matrix elements with the momentum operator.

The coefficient $L_{11}(\omega)$ is also known as the frequency-dependent Kubo–Greenwood formula (Kubo 1957; Greenwood 1958). The static electrical conductivity is obtained via

$$\sigma_e = \lim_{\omega\to 0} L_{11}(\omega). \tag{11}$$

Likewise, the thermal conductivity is calculated via the relation

$$\lambda_e = \lim_{\omega\to 0}\frac{1}{T}\left(L_{22}(\omega) - \frac{L_{12}^2(\omega)}{L_{11}(\omega)}\right). \tag{12}$$

These calculations were performed with 256 electrons in the simulation box (considering several H–He ion concentrations) and, depending on the density, different **k**-point sets

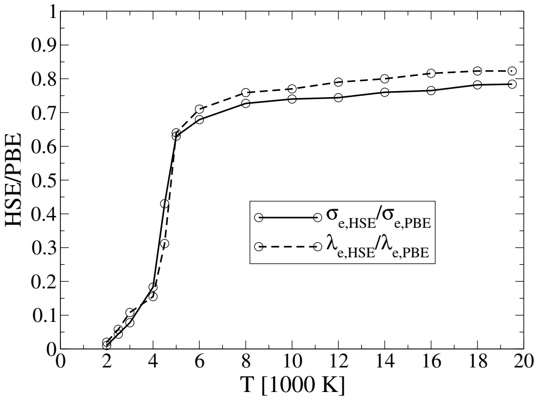

Figure 5. Ratios of the electrical (σ_e) and thermal conductivities (λ_e) along the Jupiter adiabat, obtained with the HSE and the PBE exchange-correlation functionals.

(Baldereschi 1973; Monkhorst & Pack 1976). We use the standard PAW pseudopotentials for H and He with a plane-wave cutoff energy of 400 eV or higher. Again, several tests were made to confirm that the choice of these parameters yields well-converged Onsager coefficients.

5.2.2. Exchange-correlation Functional

The selection of the exchange-correlation functional, which determines the $|\mathbf{k}\mu\rangle$ and $E_{\mathbf{k}\mu}$, is a delicate matter in electronic conductivity calculations with FT–DFT. The PBE functional, which is used in all MD simulations here, usually underestimates the fundamental electronic band gap considerably, so that the conductivities are too high. To overcome this problem, we use the hybrid functional of Heyd, Scuseria, and Ernzerhof (HSE; Heyd et al. 2003, 2006), which reproduces the band gaps of semiconductors much more accurately (Heyd et al. 2005; Paier et al. 2006), in most of the calculations of the Onsager coefficients, Equation (10). Hybrid functionals require the calculation of the nonlocal Fock-exchange integral, which involves significantly higher computational efforts. We use the HSE functional with a screening parameter of $\mu_s = 0.2$ Å^{-1}.

To illustrate the effect of the exchange-correlation functional, we plot the ratios of the conductivities that were obtained with each of these functionals (HSE vs. PBE) in Figure 5. In the molecular regime, the electronic contributions to both the electrical and the thermal conductivity are overestimated by up to two orders of magnitude using the PBE functional, whereas this effect is less important in the metallic regime. Nevertheless, the PBE functional gives the correct qualitative trends of the metal-to-nonmetal transition in the H–He mixture, similar to earlier work on high-pressure water (French et al. 2010).

5.3. Electrical and Thermal Conductivities: Ionic Contribution

The ions (nuclei) are propagated as classical particles in our simulations. Therefore, we can apply classical Green–Kubo relations, as in the viscosity calculations, to determine their contribution to the conductivities. Keeping in mind the introductory considerations of Section 5, one can estimate that the electrical conductivity of the electrons σ_e is much higher than that of the ions, σ_i, and we can neglect the latter.

In the same way, the electronic contribution to the thermal conductivity λ_e is also much higher than λ_i once ionization becomes significant. Thus, λ_i is only important in the nonmetallic region, and we can treat the ions as effectively neutral particles (due to the formation of He atoms and H_2 molecules) when calculating their contribution to the thermal conductivity. Consequently, the thermal conductivity of the ions can be calculated with the equation (Allen & Tildesley 1989)

$$\lambda_i = \frac{1}{3\Omega k_B T^2} \int_0^\infty dt \langle \boldsymbol{J}_q(0) \cdot \boldsymbol{J}_q(t) \rangle. \tag{13}$$

Regrettably, a rigorous way to express the generalized heat current $\boldsymbol{J}_q$ within FT–DFT–MD is yet unknown, so that we have to make additional but reasonable approximations here. We accomplish this by mapping the effective interactions between the nuclei in FT–DFT onto classical pair potentials. This allows us to adopt a well-known expression for J_q that is commonly applied in classical MD simulations. It is defined (Hansen & McDonald 1976; de Groot & Mazur 1984; Allen & Tildesley 1989) as

$$\boldsymbol{J}_q(t) = \sum_{k=1}^{N} (E_k(t) - \langle h_k \rangle) \boldsymbol{v}_k(t) + \frac{1}{2} \sum_{\substack{k,j=1 \\ k \neq j}}^{N} (\boldsymbol{F}_{kj}(t) \cdot \boldsymbol{v}_k(t)) \boldsymbol{r}_{kj}(t), \tag{14}$$

where N is the total number of ions, $\boldsymbol{v}_k$ and E_k are velocity and energy of the particle k, and $\langle h_k \rangle$ is its mean enthalpy, respectively. The energy per particle is given by

$$E_k(t) = \frac{1}{2} m_k \boldsymbol{v}_k^2(t) + \frac{1}{2} \sum_{\substack{j=1 \\ k \neq j}}^{N} V_{kj}(r_{kj}(t)). \tag{15}$$

The potentials V_{kj} and forces $\boldsymbol{F}_{kj}$ shall depend only on the distances $r_{kj} = |\boldsymbol{r}_{kj}|$ between the particles k and j. The last task is to obtain the effective interaction potentials between the species. Here we use a first-order approximation and express the pair potentials $V_{ab}(r)$ and forces $\boldsymbol{F}_{ab}(r)$ between the species a and b through radial pair correlation functions $g_{ab}(r)$ via

$$V_{ab}(r) = -k_B T \ln g_{ab}(r), \qquad \boldsymbol{F}_{ab}(r) = -\nabla V_{ab}(r). \tag{16}$$

All $g_{ab}(r)$ can be easily calculated from FT–DFT–MD simulation data. The mean enthalpy of a particle from the species a follows without further approximation and reads (Hansen & McDonald 1976)

$$\langle h_a \rangle = \frac{5}{2} k_B T + \sum_b \frac{2\pi N_b}{\Omega} \int_0^\infty dr\, r^2 g_{ab}(r) V_{ab}(r). \tag{17}$$

The virial contribution to $\langle h_a \rangle$ vanishes.

Such an approach, although it is not rigorously ab initio, offers significant advantages over using only the kinetic energy in the heat current or, much simpler, expressing the thermal conductivity through diffusion coefficients. Even though it has the potential to be improved, we checked that the present level is sufficient to yield reasonable thermal conductivities for the H–He mixture; at low densities they agree with extrapolated experimental data for hot gaseous hydrogen (Assael et al. 2011).

We used the same simulations that served to calculate the viscosities (108 hydrogen and 10 helium atoms, $Y \approx 0.275$) to obtain λ_i. Due to the approximations made here, we estimate that the overall accuracy of the λ_i is within a factor of two or better.

Table 2
Linear Transport Properties in Jupiter (Model J11-8a)

R (R_J)	σ (S m^{-1})	β (m^2 s^{-1})	λ (W K m^{-1})	κ (m^2 s^{-1})	η (mPa s)	ν (mm^2 s^{-1})	η' (mPa s)	$D_{\rm H}$ (mm^2 s^{-1})	$D_{\rm He}$ (mm^2 s^{-1})
0.0923	3.39×10^6	0.235	1710	2.91×10^{-5}	1.16	0.262	1.80	0.433	0.256
0.196	3.05×10^6	0.261	1470	2.70×10^{-5}	1.06	0.266	1.69	0.428	0.272
0.350	2.48×10^6	0.321	1040	2.26×10^{-5}	0.955	0.282	1.55	0.436	0.251
0.478	1.97×10^6	0.404	721	1.89×10^{-5}	0.830	0.296	1.30	0.450	0.254
0.584	1.48×10^6	0.538	465	1.50×10^{-5}	0.666	0.295	1.08	0.458	0.247
0.680	1.09×10^6	0.730	283	1.19×10^{-5}	0.500	0.313	0.92	0.468	0.229
0.770	7.20×10^5	1.11	153	8.56×10^{-6}	0.410	0.342	0.77	0.481	0.200
0.852	3.60×10^5	2.21	59.6	4.99×10^{-6}	0.297	0.360	0.49	0.471	0.179
0.890	1.46×10^5	5.45	20.2	2.16×10^{-6}	0.234	0.367	0.49	0.369	0.172
0.930	1.5×10^3	5.3×10^2	2.78*	3.55×10^{-7}*	0.140	0.368	0.99	0.274	0.260
0.952	6.6×10^0	1.2×10^5	2.18*	5.71×10^{-7}*	0.090	0.378	1.36	0.349	0.330
0.972	3.5×10^{-2}	2.3×10^7	1.74*	9.42×10^{-7}*	0.046	0.348	...	0.410	0.400
0.980	3.5×10^{-4}	2.3×10^9	1.50*	1.32×10^{-6}*	0.033	0.392	...	0.437	0.430
0.986	10^{-7}	8×10^{12}	1.30*	2.03×10^{-6}*	0.023	0.460	...	0.610	0.550

Notes. The number of digits does not necessarily correspond to the actual error bar in all cases, see figures and the text for details. Note that our data set for the longitudinal viscosities does not contain values for all radii. The values marked with "*" indicate that the ionic contributions λ_i and κ_i are dominant, see Sections 5 and 6 for further explanation. It is $R_J = 6.9894 \times 10^7$ m.

5.4. Self-diffusion Coefficients

The self-diffusion coefficients of hydrogen $D_{\rm H}$ and helium $D_{\rm He}$ were calculated with the following Green–Kubo formula:

$$D_a = \frac{1}{3N_a}\int_0^\infty dt \sum_{k=1}^{N_a} \langle \boldsymbol{v}_k(0)\cdot \boldsymbol{v}_k(t)\rangle. \qquad (18)$$

In practice, the calculation of self-diffusion coefficients requires less extensive simulations than viscosities or thermal conductivities. Consequently, the same simulation runs (with 108 hydrogen and 10 helium atoms, $Y \approx 0.275$) were used here as well. We estimate that our diffusion coefficients are generally accurate within 5% to 20%, depending on the species and density.

6. TRANSPORT PROPERTIES: RESULTS

In the following, we present the results for the transport properties calculated at the thermodynamic states (P, T) along the Jupiter adiabat. The density ϱ and the heat capacity c_p from Section 4 will also find application in this section. Our main results are compiled in Table 2. The error bars are mostly due to statistical fluctuations unless noted otherwise.

6.1. Viscosities

We display the ab initio results for the dynamic shear η and longitudinal viscosity η' and the kinematic shear viscosity $\nu = \eta/\varrho$ along the Jupiter adiabat in Figure 6. Note that the density is taken from the linear-mixing EOS and therefore contains the mass fraction of heavy elements.

The dynamic shear viscosity η decreases systematically with the radius. In the very outer regions, we find a plausible agreement with extrapolated low-density shear viscosities for pure hydrogen (Stiel & Thodos 1963). Many of our values are higher than the data of Stiel & Thodos (1963) because the H–He fluid becomes correlated in the interior of Jupiter, which leads to increased viscosities further inward.

The longitudinal viscosity η' decreases with the radius, but reaches a minimum near 0.9 R_J and then rises strongly as hydrogen molecules form in the outer envelope. In the metallic regime, the ratio between the longitudinal and shear viscosities approaches a value of $\eta'/\eta \approx 5/3$, which is also frequently found in monoatomic fluids (Malbrunot et al. 1983; Hoheisel 1987). In molecular systems this ratio can be much higher (Emanuel 1990), which is consistent with our data. We did not calculate longitudinal viscosities outside of 0.95 R_J because the required convergence of the respective correlation functions could not be reached within our computational limits at such low densities.

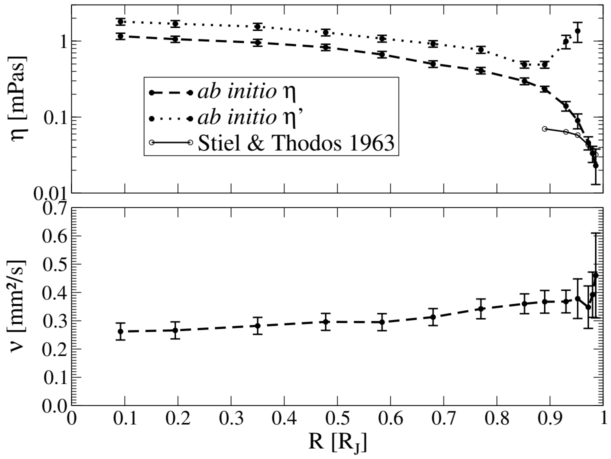

Figure 6. Upper panel: dynamic shear (dashed line) and longitudinal viscosity (dotted line) along Jupiter's adiabat. The thin solid line represents low-density values from Stiel & Thodos (1963). Lower panel: kinematic shear viscosity $\nu = \eta/\varrho$.

The kinematic shear viscosity ν rises very slightly with the radius. It adopts an almost constant value of $\sim$0.3 mm^2 s^{-1} in the entire interior; see Figure 6. Thus, a common qualitative approximation of a constant kinematic viscosity in the dynamo-generating region (Wicht & Tilgner 2010) is largely fulfilled. The respective values for the viscosities along the adiabat are given in Table 2.

6.2. Electrical Conductivity

First, we study the variation of the electronic contribution to the electrical and thermal conductivities with the helium

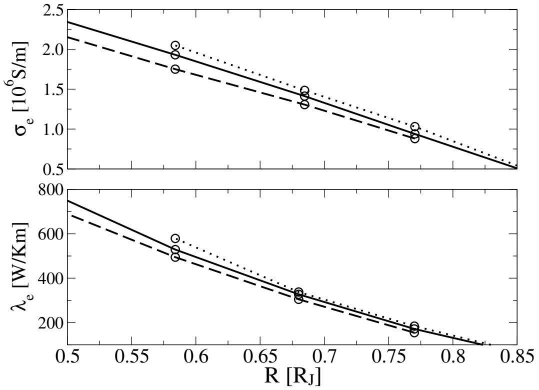

Figure 7. Dependence of the electrical (top) and the thermal (bottom) conductivity on the concentration of helium: $Y_1 \approx 0.238$ (dotted line), $Y \approx 0.275$ (solid line), and $Y_2 \approx 0.311$ (dashed line). These calculations were performed with the PBE functional.

concentration along the Jupiter adiabat. These quantities are potentially not as insensitive to the stoichiometry as η, λ_i, or diffusion coefficients and its influence needs some assessment.

Several calculations are performed for three different helium concentrations using the PBE functional. The general trends are displayed in Figure 7 and the correct absolute values for the conductivities can be obtained by scaling with the HSE:PBE ratios shown in Figure 5. In particular, we have chosen 216 hydrogen and 20 helium atoms to represent the mean helium fraction ($Y \approx 0.275$), 222 hydrogen and 17 helium atoms ($Y_1 \approx 0.238$) for the outer layer, and 208 hydrogen and 24 helium atoms ($Y_2 \approx 0.311$) for the inner layer, respectively. The electrical and thermal conductivities of the H–He mixtures are mainly determined by the hydrogen subsystem. They decrease systematically with the helium concentration, similar to what was found by Lorenzen et al. (2011).

For all considered concentrations, the dependence of σ_e and λ_e on the helium abundance is relatively small. In a case where the influence of the helium concentration on the conductivity has to be accounted for, both this work and that of Lorenzen et al. (2011) can be used to scale the conductivities in the vicinity of the mean helium fraction. The discontinuity of the helium concentration at the layer boundary is a characteristic attribute of three-layer models by definition, however, it is relatively small in our models: from $Y_1 = 0.238$ in the outer envelope to $Y_2 = 0.291$ (J11-4a) or 0.311 (J11-8a) in the inner envelope. Therefore, and also due to the high computational demands, we restrict our following calculations with the HSE functional solely to the mean helium fraction ($Y \approx 0.275$).

The main results for the electrical conductivity $\sigma = \sigma_e$ and the magnetic diffusivity $\beta = 1/\mu_0\sigma$, where μ_0 is the vacuum permeability, were obtained with the HSE functional (Heyd et al. 2003, 2006). They are displayed in Figure 8. The most prominent feature is the transition from nonmetallic to metallic-like conduction ($\sigma \geqslant 2 \times 10^4\,\mathrm{S\,m^{-1}}$; see Redmer & Holst 2010) at about 0.9 R_J, which corresponds to a pressure level of 0.5 Mbar. The transition is continuous because Jupiter's adiabat lies above the critical point of the first-order liquid–liquid phase transition in hydrogen predicted by Morales et al. (2010) and Lorenzen et al. (2010); see Figure 3.

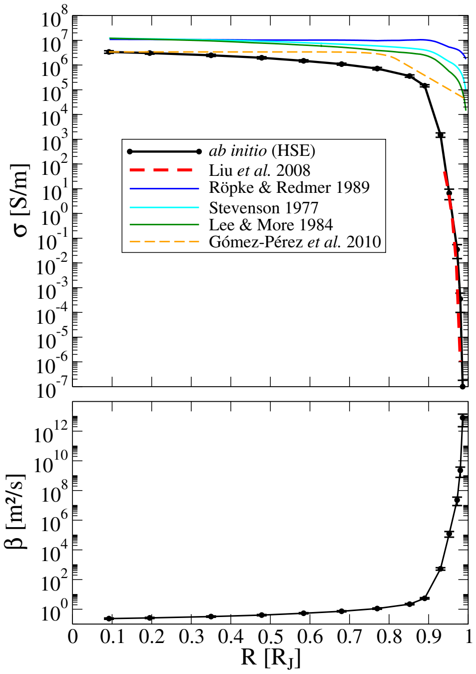

Figure 8. Upper panel: electrical conductivity along Jupiter's adiabat calculated with the HSE functional assuming a constant mean He fraction of $Y \approx 0.275$. Comparison with different models and estimations is made (Stevenson & Salpeter 1977; Lee & More 1984; Röpke & Redmer 1989; Liu et al. 2008; Gómez-Pérez et al. 2010); see the text for further details. Lower panel: magnetic diffusivity $\beta = 1/\mu_0\sigma$ along Jupiter's adiabat calculated with the HSE functional.

Various interpolation formulae have been constructed for the electrical conductivity based on limiting cases, e.g., the Spitzer theory (Spitzer & Härm 1953) for fully ionized classical plasmas, and the Ziman theory (Ziman 1961) for degenerate plasmas; see Röpke (1988) and Röpke & Redmer (1989). We compare our ab initio results with such transport theories developed for strongly coupled plasmas (Röpke & Redmer 1989; Lee & More 1984) assuming a fully ionized hydrogen plasma with a density that is equal to its partial density in our H–He mixture. We also compare our results with the model of Stevenson & Salpeter (1977) which takes into account the influence of helium. The formula of Stevenson & Salpeter (1977) is derived from the Ziman theory by employing hard sphere static structure factors. The model of Lee & More (1984) is based on the relaxation-time approximation for the Boltzmann equation which is solved for arbitrary degeneracy. Desjarlais (2001) generalized this approach to partial ionization later. Partial ionization is relevant for the metal-to-nonmetal transition region in Jupiter and by far most challenging for transport theory since the chemical composition (ionization degree) and the effective interactions between the various species (i.e., electrons, ions, atoms, molecules, molecular ions, etc.) have to be determined within an appropriate theoretical treatment. Advanced chemical models have been developed for this purpose; see Redmer (1997). These rely on assumptions for the discrimination between free and bound electrons as well as on effective pair potentials, which becomes questionable in the warm dense matter regime along Jupiter's adiabat.

We avoid such difficulties by applying a strictly physical picture of electrons and nuclei. Hence, we are able to give accurate predictions for the electrical conductivity over a range of 14 orders of magnitude, from metallic-like conduction in the deep interior to nonmetallic values in the outer envelope.

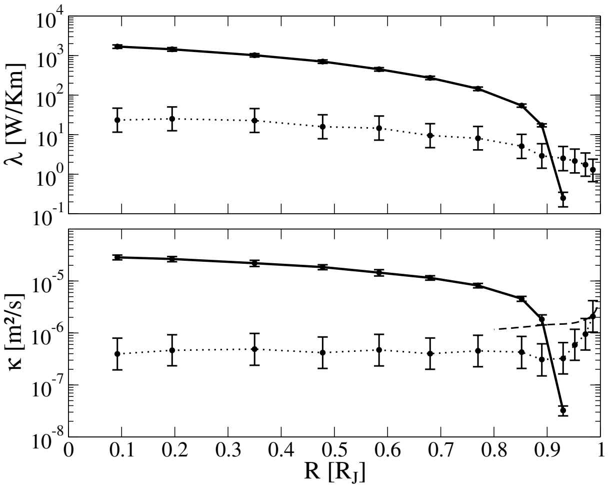

Figure 9. Upper panel: thermal conductivity of the electrons λ_e derived with the HSE functional (solid line) compared with the ionic contribution λ_i (dotted line). Lower panel: thermal diffusivity of the electrons κ_e (solid line) and the respective ionic contribution κ_i (dotted line). The dashed line is an estimate of Stevenson & Salpeter (1977) for the molecular contribution to the thermal diffusivity.

Compared to the ab initio values, the conductivities of the plasma models are higher by about a factor of five even in Jupiter's deep interior. The main reason is that the models do not take into account the electron scattering at helium atoms in the real mixture, which reduces the conductivity correspondingly; see Lorenzen et al. (2011). Furthermore, they were developed for fully ionized plasmas and cannot predict the steep decrease of the conductivity at about 0.9 R_J that we find in consequence of the metal-to-nonmetal transition in hydrogen. Our calculations show that the assumption of full ionization of the hydrogen subsystem is only justified inside about 0.8 R_J.

In contrast, our ab initio results are in excellent agreement with a simple semiconductor model for the conductivity in Jupiter's outer regions as given by Liu et al. (2008). There, experimental shock-wave data for dense fluid hydrogen (Nellis et al. 1992, 1996; Weir et al. 1996) had been used to fit an assumed linear decrease of the band gap with the density.

For additional comparison, Figure 8 contains a hypothetical conductivity profile that assumes a polynomial behavior in the conducting region and an exponential decrease toward the surface of the planet (Gómez-Pérez et al. 2010). This profile is scaled to match our innermost value of 3.39×10^6 S m^{-1}. The simple formula proposed by Gómez-Pérez et al. (2010) accounts for the metallic conductivity regime in the deep interior but cannot reproduce the superexponential decrease of the conductivity toward the outer region of the planet.

6.3. *Thermal Conductivity*

The electronic and ionic contributions to the thermal conductivity λ_e and λ_i and the respective thermal diffusivities $\kappa_e = \lambda_e/\varrho c_p$ and $\kappa_i = \lambda_i/\varrho c_p$ are shown in Figure 9. All of these quantities are calculated for the mean helium fraction ($Y \approx 0.275$) throughout the planet.

The electronic contribution behaves very similarly to the electrical conductivity shown in Figure 8. It decreases strongly at the transition from the metallic to the molecular fluid. The Wiedemann–Franz law is fulfilled in the metallic regime, while strong deviations occur in the transition and molecular regime, similar to what was found in an earlier work for pure hydrogen (Holst et al. 2011).

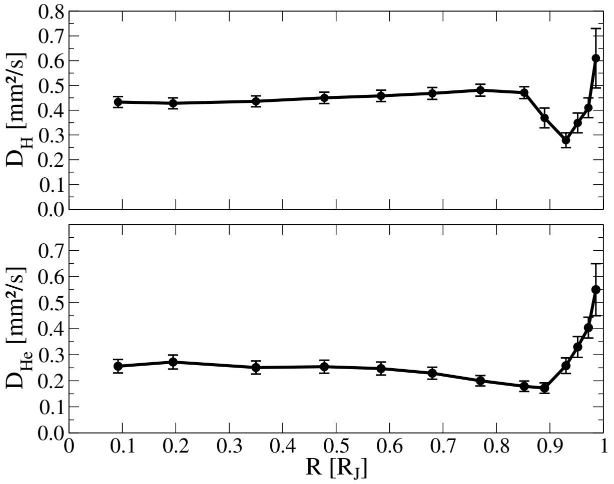

Figure 10. Self-diffusion coefficients of hydrogen (upper panel) and helium (lower panel) inside Jupiter.

The ionic contribution λ_i shows a rather small variation with the radius but decreases steadily. At a radius of 0.9 R_J, where electrons become increasingly localized at the nuclei, the ionic contribution becomes dominant. Because of the approximations made in the calculations of λ_i its error was generally set to be a factor of two.

A similar picture can be drawn for the thermal diffusivity since it behaves correspondingly to the thermal conductivity. The only qualitative difference is that κ_i rises in the very outer parts of the planet. There it approaches an early estimation of Stevenson & Salpeter (1977) for the molecular contribution of a gaseous H–He mixture.

The numerical values for $\lambda = \lambda_e + \lambda_i$ and $\kappa = \kappa_e + \kappa_i$ are given in Table 2. The total thermal diffusivity κ never drops below 10^{-7} m^2 s^{-1}.

6.4. *Diffusion Coefficients*

The self-diffusion coefficients for the hydrogen D_{H} and helium D_{He} nuclei are displayed in Figure 10. In the metallic interior, the diffusion coefficient of hydrogen is about twice as high as the diffusion coefficient of helium, and both show relatively small variations with the radius. This behavior changes drastically as the formation of hydrogen molecules sets in near 0.9 R_J. This process is accompanied with an increase in the scattering cross sections of hydrogen and leads to a drop of D_{H} to the same values as D_{He}. Outside this transition area, both diffusion coefficients rise systematically due to a decreasing density of the H–He mixture.

The overall behavior of the diffusion coefficients is consistent with the results for the electrical and thermal conductivities, which are likewise governed by the metal-to-nonmetal transition in the material. Table 2 contains the numerical values for D_{H} and D_{He}.

7. CONCLUSIONS

In summary, we have applied ab initio simulations to calculate thermodynamic and transport properties along Jupiter's adiabat. These data cover a range of 0.1–0.98 Jupiter radii and are consistent with recent Jupiter models based on the same method and that fulfill the observational constraints (Nettelmann et al. 2012). The data given here can stimulate the development of interior as well as dynamo models that require realistic thermodynamic and transport properties.

For instance, they can be used in magnetohydrodynamic simulations to understand the origin of Jupiter's magnetic field, albeit it is clear that such dynamo simulations will not be able to directly employ all of the results given here without rescaling them first. The reasons for this are of a computational nature, mostly because small-scale turbulence which has its origin, e.g., in small Ekman and Roberts numbers, cannot be completely resolved with the power of today's supercomputers. However, the data presented here can serve as a foothold in the common practice of rescaling the linear into their respective turbulent transport properties (Rüdiger & Hollerbach 2004; Wicht & Tilgner 2010), now allowing one to keep well-founded relative dependencies of the dimensionless numbers with the radius (Gómez-Pérez et al. 2010).

Numerical models for the dynamics in the nonmetallic outer part and in the dynamo region typically assume that heat capacities, the thermal expansion coefficient, and diffusivities are independent of depth (Jones et al. 2011). Our results suggest that this assumption is roughly satisfied in the deep metallic interior. However, the decrease in the electrical conductivity by one order of magnitude inside the metallic regime might already be relevant for dynamo models. Beyond that, the huge radial gradients in the molecular region will have a pronounced impact on the dynamics. Possible implications concern the zone where convection sets in first and remains most vigorous but also the depth of the observed zonal winds (Liu et al. 2008).

Lastly, while standard giant planet models assume an adiabatic, convective interior, the high thermal diffusivity together with a possible presence of a compositional gradient might suppress large-scale convection (Chabrier & Baraffe 2007; Leconte & Chabrier 2012). Such a scenario would have important implications for Jupiter's temperature profile and for core-erosion processes (Wilson & Militzer 2012). Our results can aid future investigations of such problems.

We thank S. Stellmach and B. Holst for inspiring and fruitful discussions and the referee for reviewing the manuscript. This work was supported by the Deutsche Forschungsgemeinschaft (DFG) within the SFB 652 and the SPP 1488. The calculations were performed at the North-German Supercomputing Alliance (HLRN) facilities and at the IT and Media Center of the University of Rostock.

REFERENCES

Alfè, D., & Gillan, M. J. 1998, Phys. Rev. Lett., 81, 5161
Allen, M. P., & Tildesley, D. J. 1989, Computer Simulation of Liquids (Oxford: Oxford University Press)
Assael, M. J., Assael, J.-A. M., Huber, M. L., Perkins, R. A., & Takata, Y. 2011, J. Phys. Chem. Ref. Data, 40, 033101
Baldereschi, A. 1973, Phys. Rev. B, 7, 5212
Bernu, B., & Vieillefosse, P. 1978, Phys. Rev. A, 18, 2345
Bertolini, D., Demmel, F., & Tani, A. 2007, Phys. Rev. B, 76, 094204
Blöchl, P. E. 1994, Phys. Rev. B, 50, 17953
Braginsky, S. I., & Roberts, P. H. 1995, Geophys. Astrophys. Fluid Dyn., 79, 1
Caillabet, L., Mazevet, S., & Loubeyre, P. 2011, Phys. Rev. B, 83, 094101
Celliers, P. M., Loubeyre, P., Eggert, J. H., et al. 2010, Phys. Rev. Lett., 104, 184503
Chabrier, G., & Baraffe, I. 2007, ApJ, 661, L81
Chabrier, G., Saumon, D., Hubbard, W. B., & Lunine, J. I. 1992, ApJ, 391, 817
Christensen, U. R., & Aubert, J. 2006, Geophys. J. Int., 166, 97
de Groot, S. R., & Mazur, P. 1984, Non-Equilibrium Thermodynamics (New York: Dover)
Desjarlais, M. P. 2001, Contrib. Plasma Phys., 41, 267
Desjarlais, M. P. 2003, Phys. Rev. B, 68, 064204
Emanuel, G. 1990, Phys. Fluids A, 2, 2252
Fortov, V. E., Ilkaev, R. I., Arinin, V. A., et al. 2007, Phys. Rev. Lett., 99, 185001
French, M., Hamel, S., & Redmer, R. 2011, Phys. Rev. Lett., 107, 185901
French, M., Mattsson, T. R., Nettelmann, N., & Redmer, R. 2009, Phys. Rev. B, 79, 054107
French, M., Mattsson, T. R., & Redmer, R. 2010, Phys. Rev. B, 82, 174108
French, M., & Redmer, R. 2009, J. Phys.: Condens. Matter, 21, 375101
Gastine, T., & Wicht, J. 2012, Icarus, 219, 428
Gillan, M. J., Alfè, D., Brodholt, J., Vočadlo, L., & Price, G. D. 2006, Rep. Prog. Phys., 69, 2365
Gómez-Pérez, N., Heimpel, M., & Wicht, J. 2010, Phys. Earth Planet. Inter., 181, 42
Greenwood, D. A. 1958, Proc. Phys. Soc., 71, 585
Guillot, T. 2005, Annu. Rev. Earth Planet. Sci., 33, 493
Hafner, J. 2008, J. Comput. Chem., 29, 2044
Hamel, S., Morales, M. A., & Schwegler, E. 2011, Phys. Rev. B, 84, 165110
Hansen, J. P., & McDonald, I. R. 1976, Theory of Simple Liquids (London: Academic)
Heimpel, M., & Aurnou, J. 2007, Icarus, 187, 540
Heimpel, M., Aurnou, J., & Wicht, J. 2005, Nature, 438, 193
Heyd, J., Peralta, J. E., Scuseria, G. E., & Martin, R. L. 2005, J. Chem. Phys., 123, 174101
Heyd, J., Scuseria, G. E., & Ernzerhof, M. 2003, J. Chem. Phys., 118, 8207
Heyd, J., Scuseria, G. E., & Ernzerhof, M. 2006, J. Chem. Phys., 124, 219906
Hoheisel, C. 1987, J. Chem. Phys., 86, 2328
Holst, B., French, M., & Redmer, R. 2011, Phys. Rev. B, 83, 235120
Holst, B., Redmer, R., & Desjarlais, M. P. 2008, Phys. Rev. B, 77, 184201
Hubbard, W. 1966, ApJ, 146, 858
Ichimaru, S., & Tanaka, S. 1985, Phys. Rev. A, 32, 1790
Jones, C., Boronski, P., Brun, A., et al. 2011, Icarus, 216, 120
Kaspi, Y., Flierl, G. R., & Showman, A. P. 2009, Icarus, 202, 525
Kietzmann, A., Holst, B., Redmer, R., Desjarlais, M. P., & Mattsson, T. R. 2007, Phys. Rev. Lett., 98, 190602
Kirk, R. L., & Stevenson, D. J. 1987, ApJ, 316, 836
Knudson, M. D., Desjarlais, M. P., & Dolan, D. H. 2008, Science, 322, 1822
Knudson, M. D., Desjarlais, M. P., Lemke, R. W., et al. 2012, Phys. Rev. Lett., 108, 091102
Knudson, M. D., Hanson, D. L., Bailey, J. E., et al. 2004, Phys. Rev. B, 69, 144209
Kresse, G., & Furthmüller, J. 1996, Phys. Rev. B, 54, 11169
Kresse, G., & Hafner, J. 1993, Phys. Rev. B, 47, 558
Kresse, G., & Hafner, J. 1994, Phys. Rev. B, 49, 14251
Kresse, G., & Joubert, D. 1999, Phys. Rev. B, 59, 1758
Kubo, R. 1957, J. Phys. Soc. Japan, 12, 570
Kubo, R., Toda, M., & Hashitsume, N. 1991, Nonequilibrium Statistical Mechanics (Berlin: Springer)
Leconte, J., & Chabrier, G. 2012, A&A, 540, A20
Lee, Y., & More, R. 1984, Phys. Fluids, 27, 1273
Liu, J., Goldreich, P., & Stevenson, D. 2008, Icarus, 196, 653
Lorenzen, W., Holst, B., & Redmer, R. 2009, Phys. Rev. Lett., 102, 115701
Lorenzen, W., Holst, B., & Redmer, R. 2010, Phys. Rev. B, 82, 195107
Lorenzen, W., Holst, B., & Redmer, R. 2011, Phys. Rev. B, 84, 235109
Malbrunot, P., Boyer, A., Charles, E., & Abachi, H. 1983, Phys. Rev. A, 27, 1523
Matousek, S. 2007, Acta Astronaut., 61, 932
Mermin, N. D. 1965, Phys. Rev., 137, A1441
Militzer, B. 2006, Phys. Rev. Lett., 97, 175501
Militzer, B. 2009, Phys. Rev. B, 79, 155105
Monkhorst, H. J., & Pack, J. D. 1976, Phys. Rev. B, 13, 5188
Morales, M. A., Pierleoni, C., Schwegler, E., & Ceperley, D. M. 2010, Proc. Natl Acad. Sci. USA, 107, 12799
Morales, M. A., Schwegler, E., Ceperley, D., et al. 2009, Proc. Natl Acad. Sci. USA, 106, 1324
Nellis, W. J., Mitchell, A. C., McCandless, P. C., Erskine, D. J., & Weir, S. T. 1992, Phys. Rev. Lett., 68, 2937
Nellis, W. J., Weir, S. T., & Mitchell, A. C. 1996, Science, 273, 936
Nettelmann, N., Becker, A., Holst, B., & Redmer, R. 2012, ApJ, 750, 52
Nettelmann, N., Holst, B., Kietzmann, A., et al. 2008, ApJ, 683, 1217
Nosé, S. 1984, J. Chem. Phys., 81, 511
Paier, J., Marsman, M., Hummer, K., et al. 2006, J. Chem. Phys., 124, 154709
Perdew, J. P., Burke, K., & Ernzerhof, M. 1996, Phys. Rev. Lett., 77, 3865
Redmer, R. 1997, Phys. Rep., 282, 35
Redmer, R., & Holst, B. 2010, in Metal-to-Nonmetal Transitions, ed. R. Redmer, B. Holst, & F. Hensel (Springer Series in Material Sciences, Vol. 132; Berlin: Springer), 63

Röpke, G. 1988, Phys. Rev. A, 38, 3001
Röpke, G., & Redmer, R. 1989, Phys. Rev. A, 39, 907
Rüdiger, G., & Hollerbach, R. 2004, The Magnetic Universe: Geophysical and Astrophysical Dynamo Theory (Weinheim: Wiley VCH)
Saumon, D., Chabrier, G., & van Horn, H. M. 1995, ApJS, 99, 713
Schubert, G., & Soderlund, K. M. 2011, Phys. Earth Planet. In., 187, 92
Spitzer, L., & Härm, R. 1953, Phys. Rev., 89, 977
Stanley, S., & Glatzmaier, G. 2010, Space Sci. Rev., 152, 617
Stevenson, D. J. 1982, Annu. Rev. Earth Planet. Sci., 10, 257
Stevenson, D. J., & Salpeter, E. E. 1977, ApJS, 35, 221
Stiel, L. I., & Thodos, G. 1963, Ind. Eng. Chem. Fundam., 2, 233
Stixrude, L., & Jeanloz, R. 2008, Proc. Natl Acad. Sci. USA, 32, 11071
Subramanian, N., Goncharov, A. F., Struzhkin, V. V., Somayazulu, M., & Hemley, R. J. 2011, Proc. Natl Acad. Sci. USA, 108, 6014
Tamblyn, I., & Bonev, S. A. 2010, Phys. Rev. Lett., 104, 065702
Vasavada, A. R., & Showman, A. P. 2005, Rep. Prog. Phys., 68, 1935
Vorberger, J., Tamblyn, I., Militzer, B., & Bonev, S. A. 2007, Phys. Rev. B, 75, 024206
Weir, S. T., Mitchell, A. C., & Nellis, W. J. 1996, Phys. Rev. Lett., 76, 1860
Wicht, J., & Tilgner, A. 2010, Space Sci. Rev., 152, 501
Wilson, H. F., & Militzer, B. 2012, ApJ, 745, 54
Ziman, J. 1961, Phil. Mag., 6, 1013

PHYSICS OF PLASMAS **24**, 092306 (2017)

Electronic transport in partially ionized water plasmas

Martin French and Ronald Redmer
Universität Rostock, Institut für Physik, D-18051 Rostock, Germany

(Received 27 March 2017; accepted 17 July 2017; published online 18 August 2017)

We use *ab initio* simulations based on density functional theory to calculate the electrical and thermal conductivities of electrons in partially ionized water plasmas at densities above 0.1 g/cm^3. The resulting conductivity data are then fitted to analytic expressions for convenient application. For low densities, we develop a simple and fully analytic model for electronic transport in low-density plasmas in the chemical picture using the relaxation-time approximation. In doing so, we derive a useful analytic expression for electronic transport cross sections with neutral particles, based on a model potential. In the regime of thermal ionization, electrical conductivities from the analytic model agree with the *ab initio* data within a factor of 2. Larger deviations are observed for the thermal conductivity, and their origin is discussed. Our results are relevant for modeling the interior and evolution of water-rich planets as well as for technical plasma applications. *Published by AIP Publishing*. [http://dx.doi.org/10.1063/1.4998753]

I. INTRODUCTION

Electronic transport properties are key quantities to characterize systems with free charge carriers such as plasmas. However, making accurate predictions for the electrical and thermal conductivities of dense multi-component plasmas is still a great challenge since suitable quantum kinetic equations have to be derived and solved.[1,2] Traditional methods for the calculation of transport properties of dense plasmas are based on the chemical picture: the concentration of the free charge carriers is derived from mass-action laws for a given density ϱ and temperature T, and their mobility is determined from the scattering processes with all particle species, for example, ions, electrons, and neutral atoms.[3–5] Although this approach is successful for weakly coupled plasmas, the strong interactions due to long-ranged Coulomb forces heavily complicate the problem at higher densities.[6,7] In particular, the discrimination between free and bound states becomes increasingly involved because short-lived bound states may appear, and the scattering processes can no longer be treated by using effective two-particle interactions between the various species.

During the last two decades, computational approaches that derive electronic transport coefficients of dense plasmas from *ab initio* electronic structure calculations with density functional theory (DFT) have become increasingly successful.[8–15] These methods calculate the electronic properties directly from the Coulomb interactions between all particles and do not require a distinguishment between the bound and free states. Still, such calculations become computationally very costly toward the weakly coupled regime at low density or high temperature. Although the electronic conductivity of water plasma has been systematically investigated[16,17] at densities above 1 g/cm^3, only relatively few *ab initio* data have been published for lower densities.[16] Similar studies on the thermal conductivity have not been made yet at all.

In this paper, we calculate the electrical and thermal conductivities of partially ionized water plasmas at temperatures between 4000 and 50 000 K and densities between 0.1 and 9 g/cm^3 using *ab initio* simulations. We give empirical fit functions which make our results easily available for applications in this parameter domain. Furthermore, we develop an analytic model for electronic transport in low-density water plasmas based on the chemical picture and investigate to which extent the results of both approaches overlap. Note that we consider only electrons as mobile charge carriers here. Contributions from protons or other nuclei, which are also significant under certain conditions,[16–18] are not included here but will be investigated in future work.

In addition to the basic investigation of electron transport in dense plasmas, our research is also motivated by astrophysical questions regarding the electrical and thermal conductivities of planetary matter. In particular, recent models for the evolution of the water-rich planet Uranus suggest that a thermal boundary layer is present in its interior, which offers a possible explanation for Uranus' weak luminosity.[19] The stability of such a layer is directly tied to the thermal conductivity inside the planet. Another important problem is the explanation of the non-dipolar and non-axisymmetric magnetic fields of Uranus and Neptune, which possibly operate in thin shells surrounding stably stratified layers.[20,21] The electrical and thermal conductivity profiles through the interiors of the planets, for example, in terms of the magnetic diffusivity and thermal diffusivity, respectively, are needed for the solution of the magneto-hydrodynamic equations. This scheme was elaborated for H-He mixtures[22] and then applied in the calculation of Jupiter's dynamo.[23,24] Apart from that, our results will also help to better understand complex physical processes such as phase transformations, plasma formation, shock-wave propagation, and radiation transport in technical applications, such as underwater electrical wire explosions.[25]

II. *AB INITIO* CALCULATIONS

We perform *ab initio* simulations consisting of finite-temperature DFT[26–28] calculations for the electrons in combination with molecular dynamics (MD) simulations for the nuclei within the Born-Oppenheimer approximation. At each time step, the nuclei are propagated in a simulation box with periodic boundary conditions using forces from a converged FT-DFT calculation. We use the Vienna *Ab initio* Simulation Package (VASP)[29–32] as numerical implementation of the FT-DFT-MD simulation method.

The electronic wave functions are expanded in plane waves and PAW pseudopotentials[33,34] are employed for the electron-nucleus interaction. For the MD simulations, we use the standard PAW potentials for hydrogen (1 active electron, labeled: PAW_PBE H 15Jun2001) and oxygen (6 active electrons, labeled: PAW_PBE O 08Apr2002) with a cutoff energy of 900 eV. All simulations are performed with the exchange-correlation functional of Perdew, Burke, and Ernzerhof (PBE).[35] The motion of the nuclei is thermostated with a Nosé-Hoover thermostat.[36,37] Depending on the density and the temperature, we simulate 8–54 molecules and evaluate the electronic wave function at the Γ point. The simulations were made with time steps between 0.2 and 0.4 fs and ran for 10 000 to more than 100 000 steps. The particularly long times were necessary in the region where water dissociates into various other gas molecules at low density and temperatures below 10 000 K.[38] All our simulation parameters were extensively tested with various convergence tests against more stringent values. Previous calculations for the equation of state and other properties,[16,17,39,40] including electrical conductivity, were made with the same or very similar parameters.

In addition to FT-DFT-MD simulations, the calculation of the electronic transport properties requires the use of linear response theory (LRT). From each of the simulation runs, we select 20–200 configurations of nuclei and perform a subsequent FT-DFT calculation with each of them, whose results are then averaged. These calculations are performed with the hybrid exchange correlation functional of Heyd, Scuseria, and Ernzerhof (HSE)[41,42] (screening parameter $\mu = 0.2\,\text{Å}^{-1}$). The HSE functional is able to calculate the fundamental electronic band gap of many compounds with much higher accuracy than the PBE functional can do,[43] which also influences the electrical and thermal conductivities.[17,22] Reflectivity measurements along the Hugoniot curve of dense water plasmas[44,45] have confirmed respective theoretical results.[46] As in earlier work,[17,46] we use hard PAW potentials for hydrogen (1 active electron, labeled: PAW_PBE H_h 07Sep2000) and oxygen (8 active electrons, labeled: PAW_PBE O_sv 05Jul2007) with a cutoff energy of 800 eV in our LRT calculations.

The following expressions for the Onsager coefficients are evaluated[13]

$$K_n(\omega) = \frac{2\pi(-1)^n}{\Omega\omega} \sum_{\mathbf{k}\nu\mu} \mathrm{Re}\left(\langle \mathbf{k}\nu|\hat{\mathbf{v}}|\mathbf{k}\mu\rangle \otimes \langle \mathbf{k}\mu|\hat{\mathbf{v}}|\mathbf{k}\nu\rangle\right) \times (f_{\mathbf{k}\nu} - f_{\mathbf{k}\mu}) \left(\frac{E_{\mathbf{k}\mu} + E_{\mathbf{k}\nu}}{2}\right)^n \delta(E_{\mathbf{k}\mu} - E_{\mathbf{k}\nu} - \hbar\omega), \tag{1}$$

where ω is the frequency, Ω is the volume of the simulation box, e is the elementary charge, h_e is the enthalpy per electron, $E_{\mathbf{k}\mu}$ and $f_{\mathbf{k}\mu}$ are the eigenvalue and Fermi occupation number of the Bloch state $|\mathbf{k}\mu\rangle$, and $\langle \mathbf{k}\nu|\hat{\mathbf{v}}|\mathbf{k}\mu\rangle$ are matrix elements with the velocity operator. The latter are calculated from the dipole transition matrix elements, $\langle \mathbf{k}\nu|\hat{\mathbf{r}}|\mathbf{k}\mu\rangle$, that are computed by the optical routines of VASP, that is, via: $\langle \mathbf{k}\nu|\hat{\mathbf{v}}|\mathbf{k}\mu\rangle = i(E_{\mathbf{k}\nu} - E_{\mathbf{k}\mu})\langle \mathbf{k}\nu|\hat{\mathbf{r}}|\mathbf{k}\mu\rangle/\hbar$.[47] They contain all nonlocal contributions from the PAW pseudopotentials and from the Hartree-Fock exchange term.[48] The delta function needs to be broadened to a finite width, which is done with a Gaussian representation.

The static electrical conductivity is given by the trace of $K_0(\omega)$ in the limit of zero frequency

$$\sigma_e = \frac{e^2}{3} \lim_{\omega\to 0} \mathrm{Tr}\, K_0(\omega). \tag{2}$$

This expression is also known as the frequency-dependent Kubo-Greenwood formula.[49,50] The thermal conductivity is calculated via the relation

$$\lambda_e = \frac{1}{3T} \lim_{\omega\to 0} \mathrm{Tr}\left[K_2(\omega) - K_1(\omega)K_0^{-1}(\omega)K_1(\omega)\right]. \tag{3}$$

Note that we chose a somewhat different definition of Eq. (1) than the directionally averaged formulas given in Ref. 13. The reduction of indexes serves mainly to make the expressions more easily comparable with those from Sec. III. For the same purpose, we also dropped the enthalpy per electron, h_e, since it only influences the thermopower, which we do not calculate here. More important, all $K_n(\omega)$ are 3×3 tensors, which is necessary in regions where the water plasma is mostly molecular or atomic. Such states often result in highly inhomogeneous configurations of nuclei, in particular, if the particle number in the simulation box is small (8 or 16 molecules). Consequently, the tensors $K_n(\omega)$ have large off-diagonal elements and the directional averaging must be made only after the matrix multiplication in Eq. (3). Otherwise, the results for the thermal conductivity would be less accurate and remain susceptible to the broadening parameter of the delta function in Eq. (1).

The convergence of the LRT calculations with respect to particle numbers and **k** points was thoroughly checked. The Baldereschi point[51] yielded excellent results for the electrical conductivity and was used in all calculations, similar as in the previous work.[17] The thermal conductivity is slightly more sensitive to the choice of the **k**-point grid, so that the respective systematic error of our data for λ_e is about 5% or less, which we nevertheless find sufficient here.

In total, we have calculated 152 data points for the electrical and thermal conductivities. The statistical uncertainties vary in dependence of density and temperature and can be estimated from the scatter of the data in Figs. 3 and 4.

III. ELECTRONIC CONDUCTIVITY MODEL

To compare with our *ab initio* results, we develop a multi-component conductivity model (MCCM) for electronic transport in partially ionized low-density plasmas. The MCCM is based on the relaxation-time approximation for solving the Boltzmann equation of the electronic distribution function in linear response to external perturbations. Elastic, uncorrelated scattering of electrons at fixed scatterers is considered as a mechanism for resistivity. The solution of the Boltzmann equation, see, for example, the work of Lee and More[52] for a detailed derivation, leads to the following Onsager coefficients

$$K_n = -\frac{2m_e}{3\pi^2\hbar^3}\int_0^\infty \mathrm{d}E\,\frac{E^{n+1}}{\sum_s n_s Q_{es}(E)}\frac{\partial f_e^0}{\partial E}, \tag{4}$$

where m_e is the electron mass, E is the kinetic energy of the electrons, and $Q_{es}(E)$ are the transport cross sections (also known as momentum-transfer cross sections) for scattering of electrons at species s with the particle density n_s. The electrical σ_e and thermal conductivities λ_e are then given by

$$\sigma_e = e^2 K_0 \quad \text{and} \quad \lambda_e = \frac{1}{T}\left(K_2 - \frac{K_1^2}{K_0}\right). \tag{5}$$

For convenience, we separate the contributions of each scattering species by introducing the following specific Onsager coefficients:

$$K_{n,es} = -\frac{2m_e}{3\pi^2\hbar^3 n_s}\int_0^\infty \mathrm{d}E\,\frac{E^{n+1}}{Q_{es}(E)}\frac{\partial f_e^0}{\partial E}, \tag{6}$$

from which the total Onsager coefficients can be calculated via

$$K_n^{-1} = \sum_s K_{n,es}^{-1}. \tag{7}$$

Although this way of term separation is generally an approximation, it yields the same results as Eq. (4) in cases where the scattering is dominated by only a single species, or, if the transport cross sections of all species have the same energy dependence. Deviations from the numerically integrated expression (4) are expected when electrons scatter at several species whose transport cross sections have different energy dependences. However, the important advantages are the possibility to evaluate each of the specific coefficients (6) analytically and that the effect of electron-electron scattering can be included directly into the coefficients for electron-ion scattering $K_{n,eI}$ via appropriate correction factors. The direct calculation of electron-electron scattering is not feasible in the relaxation-time approximation.

We evaluate the derivative of the Fermi function in the non-degenerate case, where

$$\frac{\partial f_e^0}{\partial E} = -\frac{n_e}{2k_BT}\left(\frac{2\pi\hbar^2}{m_ek_BT}\right)^{3/2}\exp\left(-\frac{E}{k_BT}\right). \tag{8}$$

The critical quantities in the MCCM are the transport cross sections. For water plasmas, we distinguish between three classes of scatterers: ions (species index I), neutral particles with a large permanent dipole moment (species index D), and other neutral particles (species index N). We will frequently use the first Born approximation to calculate the transport cross sections, see, for example, Ref. 53

$$Q_{es}(E(p)) = \frac{m_e^2}{4\pi\hbar^4p^4}\int_0^{2p}\mathrm{d}q\,q^3|V_{es}(q)|^2, \tag{9}$$

where $p = \sqrt{2m_eE}$ and $V_{es}(q)$ is the Fourier transform of the scattering potential $V_{es}(r)$. In the following, we derive the expressions for the specific Onsager coefficients for each class of scatterers.

A. Electron-ion scattering

Electron-ion scattering is treated with a screened Coulomb potential[7]

$$V_{eI}(q) = -\frac{Z_Ie^2}{\varepsilon_0(q^2/\hbar^2+\kappa_e^2)}, \tag{10}$$

where Z_I is the charge state of the ion and $\kappa_e = e^2n_e/(\varepsilon_0k_BT)$ is the Debye-Hückel screening parameter in the adiabatic approximation (immobile ions). The transport cross section reads

$$Q_{eI}(E) = \frac{Z_I^2e^4}{16\pi\varepsilon_0^2}\frac{\ln\Lambda(E)}{E^2}, \tag{11}$$

with the screened Coulomb logarithm

$$\ln\Lambda(E) = \frac{1}{2}\left[\ln(1+B) - \frac{B}{1+B}\right], \tag{12}$$

where $B(E) = 8m_eE/(\hbar^2\kappa_e^2)$. Further evaluation of Eq. (6) with $Q_{eI}(E)$ follows the usual manner of pulling the screened Coulomb logarithm out of the integral[7] to obtain an analytic expression for the Onsager coefficients for electron-ion scattering

$$\tilde{K}_{n,eI} = \frac{2^{11/2}\pi^{1/2}(n+3)!\varepsilon_0^2(k_BT)^{n+3/2}n_e}{3Z_I^2e^4m_e^{1/2}n_I\ln\Lambda(B_n)}. \tag{13}$$

To preserve the consistency with the exact low-temperature behavior of $\tilde{K}_{n,eI}$, where $Q_{eI}(E=0) = const.$, the screened Coulomb logarithm (12) is evaluated at the following argument which depends on the index n

$$B_n = 8\sqrt{(n+2)(n+3)}\,\frac{m_ek_BT}{\hbar^2\kappa_e^2}. \tag{14}$$

B. Inclusion of electron-electron scattering

The solution of the Boltzmann equation including electron-electron scattering is much more difficult and cannot be done analytically.[6] The influence of electron-electron scattering on the electrical conductivity of weakly coupled plasmas is nevertheless well-understood, whereas its effect on the thermal conductivity has been explored to much lesser extent.[54–59] In practice, the effect of electron-electron scattering is most easily included by introducing correction factors to the Onsager coefficients for electron-ion scattering $\tilde{K}_{n,eI}$. The respective expressions need to be modified as follows:

$$K_{0,eI} = \frac{f_e}{f_I}\tilde{K}_{0,eI}, \tag{15}$$

$$K_{1,eI} = \frac{a_e f_e}{a_I f_I}\tilde{K}_{1,eI} + \frac{5}{2}k_BT\left(\frac{f_e}{f_I} - \frac{a_e f_e}{a_I f_I}\right)\tilde{K}_{0,eI}, \tag{16}$$

$$K_{2,eI} = \frac{L_e f_e}{L_I f_I}\left(\tilde{K}_{2,eI} - \frac{\tilde{K}_{1,eI}^2}{\tilde{K}_{0,eI}}\right) + \frac{K_{1,eI}^2}{K_{0,eI}}. \tag{17}$$

All coefficients without a tilde include the effect of electron-electron scattering. The definitions were chosen according to Redmer[6] and Adams *et al.*,[57] and the relations to the Spitzer-Härm[54] quantities are

$$\frac{f_e}{f_I} = \gamma_E(Z_I), \quad \frac{a_e f_e}{a_I f_I} = \gamma_T(Z_I), \tag{18}$$

$$\frac{L_e}{L_I} = \frac{2.5\,\varepsilon(Z_I)\delta_T(Z_I)}{\gamma_E(Z_I)}. \tag{19}$$

In their seminal paper, Spitzer and Härm[54] gave numerical values for γ_E, γ_T, δ_T, and ε, which depend on the charge of the ion Z_I. A simple parametrization of their values is achieved with expressions of the form

$$C(Z_I) = 1 - \frac{C_0}{Z_I^{C_1}}\exp\left(-C_2 Z_I\right), \tag{20}$$

which reproduce most of the data within 1% or better. All parameters are given in Table I.

C. Electron-dipole scattering

For molecules with a large dipole moment, in our case H_2O and OH, the interaction with plasma electrons can be described with a point-dipole potential

$$V_{eD}(r,\alpha) = -\frac{D_D e\cos\alpha}{4\pi\varepsilon_0 r^2}, \tag{21}$$

where D_D is the dipole moment and α is the angle between the dipole moment and the electron-molecule position vector. The transport cross section for such a potential was calculated by Altshuler in first Born approximation[60] and reads

$$Q_{eD}(E) = \frac{m_e e^2 D_D^2}{12\pi\varepsilon_0^2\hbar^2}\frac{1}{E}. \tag{22}$$

Due to the simple $\sim E^{-1}$ dependence, Eq. (6) can be evaluated without further approximation. The resulting Onsager coefficients are

$$K_{n,eD} = \frac{2^{7/2}\pi^{1/2}(n+2)!\varepsilon_0^2\hbar^2(k_BT)^{n+1/2}n_e}{D_D^2 e^2 m_e^{3/2} n_D}. \tag{23}$$

TABLE I. Fit coefficients for the electron-electron scattering correction factors.

$C(Z_I)$	C_0	C_1	C_2
f_e/f_I	0.440	0.369	0.0458
$a_e f_e/a_I f_I$	0.765	0.271	0.0469
L_e/L_I	0.615	0.318	0.0326

The following values were taken for the dipole moments: $D_{H_2O} = 6.1863\times10^{-30}$ Asm for water[61] and $D_{OH} = 5.5625\times10^{-30}$ Asm for hydroxyl.[62] Comparison with experimental results for $Q_{e,H_2O}(E)$ shows a reasonable agreement within a factor of 2 for energies lower than 4 eV. Some sets of experimental data disagree with each other even by up to an order of magnitude, especially at energies below 1 eV.[63–65] The electronic transport cross section with OH molecules has not been measured yet, but a theoretical calculation[66] indicated a strong similarity to that of water, which also occurs in the point-dipole scattering model.

D. Electron-neutral scattering

We use the following model potential to describe the scattering of electrons at atoms and unpolar molecules:

$$V_{eN}(r) = -\frac{Z_N e^2}{4\pi\varepsilon_0}\left(\frac{1}{r} - \frac{1}{a_N}\right)\exp\left(-r/b_N\right), \tag{24}$$

where Z_N, a_N, and b_N are constants. It is related to the screened Coulomb potential, and the physical motivation for using it here is given in the Appendix. The Fourier transformed potential reads

$$V_{eN}(q) = -\frac{Z_N e^2}{\varepsilon_0}\frac{b_N^2}{a_N}\frac{\left(a_N b_N^2 q^2/\hbar^2 + a_N - 2b_N\right)}{\left(b_N^2 q^2/\hbar^2 + 1\right)^2}. \tag{25}$$

The transport cross section is derived with Eq. (9) and can be written as

$$Q_{eN}(E) = \frac{Z_N^2 e^4}{16\pi\varepsilon_0^2}\frac{\ln A_N(E)}{E^2}, \tag{26}$$

where, in analogy to the screened Coulomb potential, the *atomic logarithm* function is defined as

$$\ln A_N(E) = \left[\frac{\ln(x_N+1)}{2} - \frac{3a_N^2 + 6a_N b_N - 2b_N^2}{6a_N^2} + \frac{4a_N b_N + a_N^2}{2a_N^2(x_N+1)} - \frac{b_N^2 + a_N b_N}{a_N^2(x_N+1)^2} + \frac{2b_N^2}{3a_N^2(x_N+1)^3}\right], \tag{27}$$

where $x_N(E) = 8b_N^2 m_e E/\hbar^2$. The parameters Z_N, a_N, and b_N are determined by fitting Eq. (26) to recommended or experimental data for the transport cross sections.[63,67–69] Figure 1 displays the high fidelity of these fits for H, H_2, He,[70] O, and O_2. The double peak structure in the case of O_2 (also, the weak shoulder in the case of O) was reproduced best by a twofold superposition of the potential, leading to $Q_{eN}(E) = \sum_i Q_{eN,i}(E)$. Physically, this corresponds to two superpositioned charge densities (atomic or molecular orbitals) at which electrons scatter; see the Appendix. The fit parameters for all species are compiled in Table II.

In analogy to electron-ion scattering, we derive the Onsager coefficients for electron-neutral scattering,

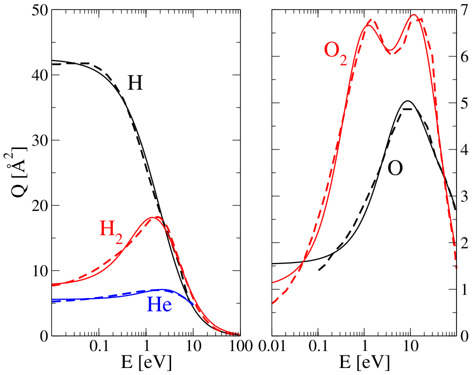

FIG. 1. Experimental or recommended transport cross sections for H,[63] H_2,[67] He,[63] O,[69] and O_2[68] (dashed lines) compared with their fits to Eq. (26) (solid lines). All fit parameters are given in Table II.

$$K_{n,eN} = \frac{2^{11/2}\pi^{1/2}(n+3)!\varepsilon_0^2(k_BT)^{n+3/2}n_e}{3e^4 m_e^{1/2} n_N \sum_i Z_{N,i}^2 \ln A_{N,i}(x_{n,N,i})}, \qquad (28)$$

and evaluate the logarithmic function (27) at

$$x_{n,N,i} = 8\sqrt{(n+2)(n+3)}\, b_{N,i}^2 m_e k_B T/\hbar^2. \qquad (29)$$

Note that the i sum originates from the number of superpositions of the scattering potential (24), which applies here only to the oxygen species. Since it is possible to solve the integral in Eq. (6) numerically with the exact expression (26), we checked that the error introduced by the approximation (7) is never larger than $+14\%$ (for H) and -32% (for O_2) in the case of $K_{0,eN}$, and even lower for the respective coefficients $K_{1,eN}$ and $K_{2,eN}$. The more different neutral species are present in the plasma, the more likely becomes a mutual error compensation in the total coefficients K_n.

TABLE II. Fit coefficients for the transport cross sections of neutral species, where a_B is the Bohr radius.

Species N	Z_N	a_N [a_B]	b_N [a_B]
H	1.28800	20.6740	1.23749
H_2	1.69700	3.69826	1.48086
He	2.53602	2.58939	0.87412
O,1	3.86410	1.65406	0.70269
O,2	25.7430	0.53577	0.23757
O_2,1	0.60920	4.50685	2.00545
O_2,2	8.07077	1.16573	0.58512

E. Numerical assessment of the main approximation

To assess the influence of the approximation (7) in the MCCM, we compare with numerical results from Eq. (4). Electron-electron scattering is excluded here because it does not enter via a transport cross section. The particle densities of all species are taken from the thermal ionization model of Schöttler *et al.*[38]

Figure 2 shows that the numerical results are systematically higher than those of the analytical model, but the deviation is smaller than a factor of 2. In the limits of very low or very high densities, the electrons scatter at only ions or water molecules, respectively, so that the deviations vanish. Especially, the thermal conductivity is somewhat less sensitive to the approximation than the electrical conductivity, which is a sign of slight error compensation between the different specific Onsager coefficients that enter the expression for λ_e.

Moreover, the specific separation of terms in the MCCM allows us to include the electron-electron correction factors into the coefficients $K_{n,eI}$, which is shown by the dotted lines in Fig. 2. This correction reduces the conductivities significantly, especially in the case of the thermal conductivity. The

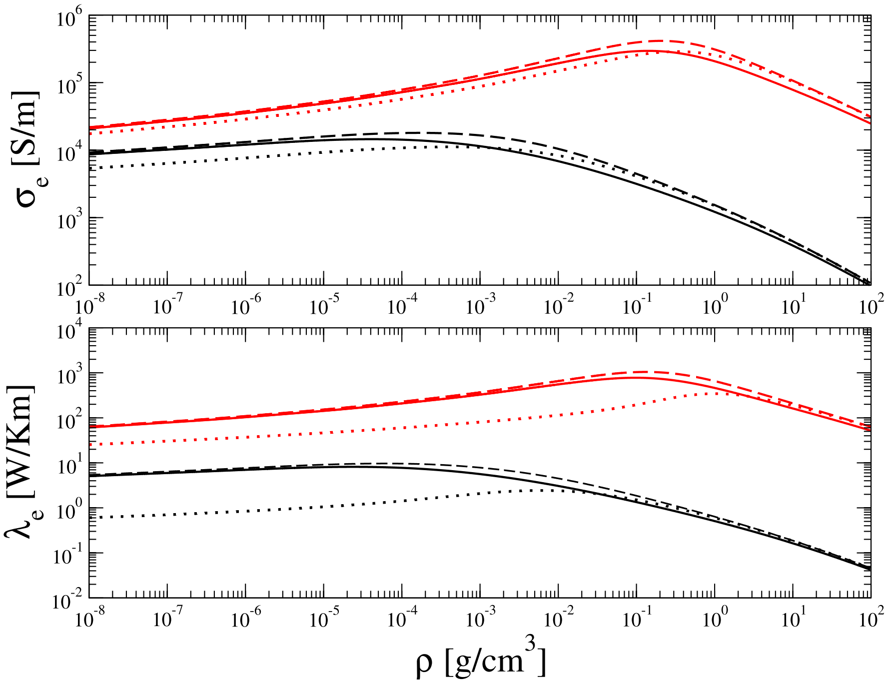

FIG. 2. Electrical and thermal conductivities calculated numerically with Eq. (4) (solid lines) in comparison with results from the analytic model, Eq. (7) (dashed lines). Electron-electron correction factors are not included in these curves. Dotted lines represent results from Eq. (7) with the electron-electron correction factors of Sec. III B. Temperatures are indicated by the color code (black: 20 000 K, red: 100 000 K).

effect is smaller at high temperature because there are more multiply ionized scatters, which enhances the contribution from electron-ion scattering.

F. General summarizing remarks

The MCCM is intended as a simple tool for calculating the electronic contribution to the electrical and thermal conductivities of partially ionized low-density plasmas for which the chemical composition has been determined with mass-action laws. The evaluation of the main Eqs. (5) and (7) is done with the formulas for specific Onsager coefficients, that is, Eqs. (13) and (15)–(17) for Coulomb scatterers, Eq. (23) for dipole scatterers, and Eq. (28) for other neutral scatterers, respectively. Ionic charges and molecular dipole moments, respectively, are the primary input variables in the two former cases. Fit parameters for electron-neutral transport cross sections with H, H_2, He, O, and O_2 are provided here, which are employable for hydrogen-helium-oxygen plasmas of various compositions, including water. Expanding the set of electron-neutral scattering parameters with other atoms or molecules should be straightforward, provided that their transport cross sections are known from either measurements[71,72] or theoretical calculations.[73]

IV. RESULTS AND DISCUSSION

In this section, we present and compare the results of our FT-DFT-MD calculations with that of the MCCM. The concentration of chemical species necessary to evaluate the expressions of the MCCM is taken from the ideal gas model (IGM) of Schöttler *et al.*[38] This model determines the thermal dissociation and ionization of molecules, etc. (H_2O, H_2, O_2, OH, H, O, H^+, O^+,…) via mass-action laws with purely temperature-dependent chemical equilibrium constants for non-degenerate particles. Interaction contributions to the chemical potentials, for example, from the Debye-Hückel limiting law, are not included in order to avoid thermodynamic instabilities (plasma phase transitions),[7] so that the IGM yields a molecular water gas in the high-density limit. At sufficiently low density, where the interaction between the particles is weak, the equation of state of the IGM agrees relatively well with that from the FT-DFT-MD simulations.[38] It is in these regions where one might expect a reasonable agreement of the corresponding conductivities as well. Visual counting of the atomic and molecular species present in the FT-DFT-MD simulations at a density of 0.2 g/cm^3 showed good agreement with the predictions of the IGM. Estimating the free electron density from the FT-DFT-MD simulations would lead to arbitrary results since a clear separation between electronic bound and scattering states cannot be made.

A. Electrical conductivity

The FT-DFT-MD data for the electrical conductivity are displayed in Fig. 3. Our results agree well with earlier calculations[16,17] but cover a larger region with a denser grid that allows for a more detailed view. They show a very nonlinear behavior with density and temperature. The conductivity increases with the temperature, which is a sign that thermal ionization always plays an important role. This effect is strong at low density and at low temperature but becomes very weak above 20 000 K when the density is greater than 2 g/cm^3. The conductivity generally rises with the density, except for the low-density and high-temperature region, where we can identify a region where pressure ionization is weak or absent. Nevertheless, within the FT-DFT-MD approach, it is not possible to fully unravel the interplay between changes in ionization states and scattering properties that lead to the intricate behavior of the conductivity.

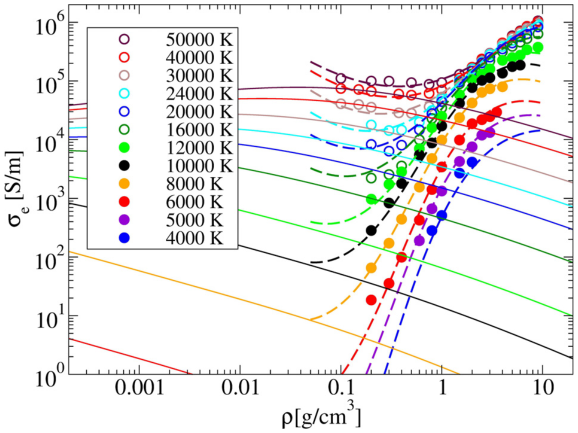

FIG. 3. Electronic contribution to the electrical conductivity for the temperatures indicated in the legend. Circles represent the data from the FT-DFT-MD simulations. Dashed lines show the fit function, Eq. (30), to the data. Solid lines are results from the MCCM; see Sec. III, using particle concentrations from the chemical model of Schöttler *et al.*[38]

Figure 3 also contains the results from the MCCM, which systematically rise with the temperature but mostly decrease with the density. This qualitative difference to the FT-DFT-MD data in the low-temperature and low-density region suggests that elastic scattering of free electrons at atoms and molecules may not be the main process that determines the conductivity there. Transitions from and into bound and quasi-bound states, for example, hopping processes,[74] which become more likely with increasing density, are a possible explanation for rising conductivity at the onset of pressure ionization. Such transitions are included in the FT-DFT, see Eq. (1), but they can hardly be described with simple models in a complex plasma containing many molecular and atomic species. Electron-ion and electron-electron scattering are not important at low temperatures due to the very small concentration of charged species.

As the temperature rises to several 10 000 K, good qualitative agreement emerges between the MCCM and FT-DFT-MD results, which both yield a slight decrease in conductivity with the density. A quantitative difference by a factor of 2 remains, but given the simplicity of the MCCM, this is better than one might expect for a nonideal multi-component plasma. There are definitely many possibilities for improving the MCCM, for example, by using particle compositions from nonideal mass-action laws or by employing improved electron-ion transport cross sections from beyond the first Born approximation.[75–79]

B. Thermal conductivity

The behavior of the thermal conductivity data from the FT-DFT-MD simulation follows similarly nonlinear trends as the electrical conductivity. It shows a much more pronounced increase with the temperature, which persists also in the hot dense plasma region above 2 g/cm^3. This is expected since the thermal conductivity has a temperature dependence that is typically higher by one power in T compared to that of the electrical conductivity.[6,54,80]

The quantitative agreement between the MCCM and the FT-DFT-MD simulation data is somewhat worse than for the electrical conductivity, even in the region characterized by thermal ionization at low density and high temperature. Albeit both electrical and thermal conductivities are, in principle, determined by the same scattering processes, we identify two reasons that could explain the systematically lower values of the MCCM.

First, electron-electron scattering enters the FT-DFT method on a mean-field level in terms of reshaping of the electronic momentum distribution function by the Hartree term. This is fully sufficient for calculations of the electrical conductivity but only partially correct in the case of the thermal conductivity.[59] In general, the maximum influence of electron-electron scattering on transport coefficients occurs in a singly ionized and non-degenerate plasma.[54] In our case, however, the effect is certainly suppressed, mostly due to partial degeneracy,[81] and it should be completely absent at low temperature, where atoms and molecules are the predominant scatterers.

Therefore, a much more reasonable explanation for a growing discrepancy between the MCCM and FT-DFT-MD thermal conductivities toward low temperature is due to different formulations of the heat current. The MCCM assumes that the heat current transports only kinetic energy,[52] whereas the FT-DFT formulation, see Eq. (1), includes also the interaction energy from FT-DFT. The importance of the interaction energy typically increases at lower temperatures compared to the kinetic energy.

To conclude, despite a potential deficiency in capturing the full effect of electron-electron scattering in thermal conductivity calculations with FT-DFT, the FT-DFT-MD results are much more trustworthy than that of the MCCM under the conditions of interest here.

C. Fits of the numerical data

The following empirical function allows for serviceable fits of our FT-DFT-MD data for both electrical and thermal conductivities

$$(\ln\sigma_e, \ln\lambda_e) = a_0 \arctan(a_1 + a_2 x + a_3 y + a_4 xy) + \sum_{i,j} b_{i,j}\, x^i y^j \,, \tag{30}$$

where $x = \ln\varrho$ and $y = \ln T$. The function consists of an arctangent function that captures much of the nonlinear behavior and is supplemented by a polynomial. All coefficients for $\ln\sigma_e$ and $\ln\lambda_e$ are given in Table III. The fit functions are displayed in Figs. 3 and 4. They should not be extrapolated beyond the ϱ-T region that contains the underlying data points displayed in those figures. The decrease of the conductivities at high density is unphysical but no serious problem because there is a transition to the superionic phase of water, which has fundamentally different properties than the dense plasma anyway.[17,39,82] Unfortunately, there is no smooth transition between Eq. (30) and the results from the MCCM at densities below 0.1 g/cm^3.

TABLE III. Fit coefficients for the electrical and thermal conductivities; see Eq. (30). All units are chosen in a way that entering temperatures in K and densities in g/cm^3 lead to results in S/m for σ_e and W/Km for λ_e, respectively.

	$\ln\sigma_e$	$\ln\lambda_e$
a_0	14.85	45.22
a_1	4.39	1.624
a_2	1.249	0.8743
a_3	−0.4551	−0.1757
a_4	−0.09253	−0.07007
$b_{0,-1}$	−661.7	−871.1
$b_{1,-1}$	653.1	449.4
$b_{0,0}$	70.38	82.65
$b_{1,0}$	−138.9	−122.4
$b_{0,1}$	0.891	1.414
$b_{1,1}$	7.047	7.086

V. SUMMARY AND CONCLUSIONS

In conclusion, we have calculated the electronic contribution to the electrical and thermal conductivities in dense, partially ionized water plasmas using FT-DFT-MD simulations and an analytical model (MCCM) in the chemical picture. We investigated the concordance and deviations between the results of both FT-DFT-MD simulations and the MCCM in regions of thermal and pressure ionization. Our analysis suggests that electronic transitions (or scattering) from and into bound electronic states play an important role and lead to continuous pressure ionization at few 1000 K and moderate densities down to at least 0.2 g/cm^3.

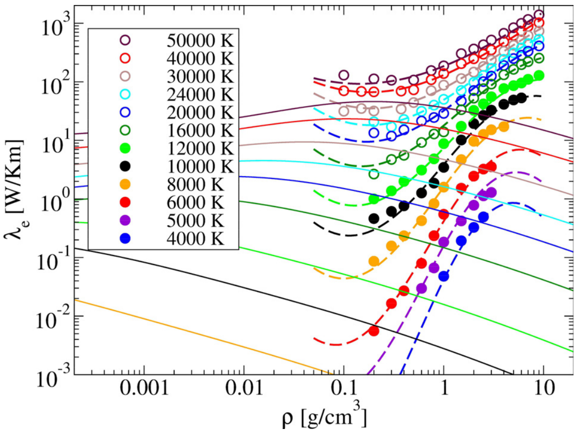

FIG. 4. Electronic contribution to the thermal conductivity for the temperatures indicated in the legend. Circles represent the data from the FT-DFT-MD simulations. Dashed lines show the fit function, Eq. (30), to the data. Solid lines are results from the MCCM, see Sec. III, using particle concentrations from the chemical model of Schöttler *et al.*[38]

The MCCM is intended for application in the weakly coupled, non-degenerate regime. At higher densities, we recommend to use the analytic fit, Eq. (30), to the FT-DFT-MD data instead. Since the results of both approaches do not blend into each other, careful selection must be made on which model to use at certain intermediate densities.

Our results are valuable for practical applications in astrophysics and plasma technology and will aid in improving wide-range conductivity models for multi-component plasmas, albeit several questions concerning the fundamental understanding of electronic transport in plasmas remain. These include achieving a reasonable description of pressure ionization that avoids thermodynamic instablilities in chemical models and examining the scattering processes from and into bound or quasi-bound states. In addition, finding a rigorous way of including electron-electron collisions in calculations of the thermal conductivity with FT-DFT-MD would be very beneficial as well.

ACKNOWLEDGMENTS

The authors acknowledge valuable discussions with S. Rosmej, H. Reinholz, and G. Röpke. This work was supported by the Deutsche Forschungsgemeinschaft (DFG) within the FOR 2440 (Matter under Planetary Interior Conditions—High-Pressure, Planetary, and Plasma Physics), the SPP 1488 (Planetary Magnetism), and the SFB 652 (Strong correlations and collective effects in radiation fields). The calculations were performed at the North-German Supercomputing Alliance (HLRN) facilities, and the IT- and Media Center of the University of Rostock.

APPENDIX: ELECTRON-ATOM POTENTIAL

Starting point is the classical mean-field potential of an electron in the charge density of a hydrogen atom in the ground state, which consists of the nuclear Coulomb potential $V_C(r)$ and the electronic Hartree potential $V_H(r)$. It reads (in atomic units)

$$V_C(r) + V_H(r) = -\left(\frac{1}{r} + 1\right)\exp(-2r). \tag{A1}$$

This simple electron-atom potential was already considered by Born.[83,84] The incorporation of the parameters Z_N, a_N, and b_N into the expression, see Eq. (24), allows for modifications due to exchange and correlation effects and serves to take deviations from the 1 s charge density into account.

Note that we fit experimental data for transport cross sections to the respective expression from the first Born approximation. This lets the parameters Z_N, a_N, and b_N in Table II become mere fit coefficients for Eq. (26), but not true parameters for the potential (24).

[1] D. Zubarev, V. Morozov, and G. Röpke, *Statistical Mechanics of Nonequilibrium Processes* (Akademie-Verlag, Berlin, 1996), Vol. I.

[2] M. Bonitz, *Quantum Kinetic Theory*, 2nd ed. (Springer, Cham, 2016).

[3] W. Ebeling, A. Förster, V. E. Fortov, V. K. Gryaznov, and A. Y. Polishchuk, *Thermophysical Properties of Hot Dense Plasmas* (Teubner Verlagsgesellschaft, Stuttgart, 1991).

[4] J. Aubreton, M. F. Elchinger, and J. M. Vinson, Plasma Chem. Plasma Process **29**, 149 (2009).

[5] K. J. Chung and Y. S. Hwang, Contrib. Plasma Phys. **53**, 330 (2013).

[6] R. Redmer, Phys. Rep. **282**, 35 (1997).

[7] W. Ebeling, V. E. Fortov, Y. L. Klimontovich, N. P. Kovalenko, W. D. Kraeft, Y. P. Krasny, D. Kremp, P. P. Kulik, V. A. Riaby, G. Röpke, E. K. Rozanov, and M. Schlanges, *Transport Properties of Dense Plasmas* (Akademie-Verlag, Berlin, 1984).

[8] M. P. Desjarlais, J. D. Kress, and L. A. Collins, Phys. Rev. E **66**, 025401 (2002).

[9] V. Recoules and J.-P. Crocombette, Phys. Rev. B **72**, 104202 (2005).

[10] S. Mazevet, J. Clérouin, V. Recoules, P. M. Anglade, and G. Zerah, Phys. Rev. Lett. **95**, 085002 (2005).

[11] A. Kietzmann, R. Redmer, M. P. Desjarlais, and T. R. Mattsson, Phys. Rev. Lett. **101**, 070401 (2008).

[12] D. A. Horner, J. D. Kress, and L. A. Collins, Phys. Rev. B **81**, 214301 (2010).

[13] B. Holst, M. French, and R. Redmer, Phys. Rev. B **83**, 235120 (2011).

[14] J. Clérouin, P. Noiret, P. Blottiau, V. Recoules, B. Siberchicot, P. Renaudin, C. Blancard, G. Faussurier, B. Holst, and C. E. Starrett, Phys. Plasmas **19**, 082702 (2012).

[15] D. V. Knyazev and P. R. Levashov, Comp. Mater. Sci. **79**, 817 (2013).

[16] T. R. Mattsson and M. P. Desjarlais, Phys. Rev. Lett. **97**, 017801 (2006).

[17] M. French, T. R. Mattsson, and R. Redmer, Phys. Rev. B **82**, 174108 (2010).

[18] A. C. Mitchell and W. J. Nellis, J. Chem. Phys. **76**, 6273 (1982).

[19] N. Nettelmann, K. Wang, J. J. Fortney, S. Hamel, S. Yellamilli, M. Bethkenhagen, and R. Redmer, Icarus **275**, 107 (2016).

[20] S. Stanley and J. Bloxham, Nature **428**, 151 (2004).

[21] S. Stanley and J. Bloxham, Icarus **184**, 556 (2006).

[22] M. French, A. Becker, W. Lorenzen, N. Nettelmann, M. Bethkenhagen, J. Wicht, and R. Redmer, Astrophys. J., Suppl. Ser. **202**, 5 (2012).

[23] T. Gastine, J. Wicht, L. D. V. Duarte, M. Heimpel, and A. Becker, Geophys. Res. Lett. **41**, 5410, doi:10.1002/2014GL060814 (2014).

[24] C. Jones, Icarus **241**, 148 (2014).

[25] Y. E. Krasik, A. Fedotov, D. Sheftman, S. Efimov, A. Sayapin, V. T. Gurovich, D. Veksler, G. Bazalitski, S. Gleizer, A. Grinenko, and V. I. Oreshkin, Plasma Sources Sci. Technol. **19**, 034020 (2010).

[26] P. Hohenberg and W. Kohn, Phys. Rev. **136**, B864 (1964).

[27] W. Kohn and L. J. Sham, Phys. Rev. **140**, A1133 (1965).

[28] N. D. Mermin, Phys. Rev. **137**, A1441 (1965).

[29] G. Kresse and J. Hafner, Phys. Rev. B **47**, 558 (1993).

[30] G. Kresse and J. Hafner, Phys. Rev. B **48**, 13115 (1993).

[31] G. Kresse and J. Hafner, Phys. Rev. B **49**, 14251 (1994).

[32] G. Kresse and J. Furthmüller, Phys. Rev. B **54**, 11169 (1996).

[33] P. E. Blöchl, Phys. Rev. B **50**, 17953 (1994).

[34] G. Kresse and D. Joubert, Phys. Rev. B **59**, 1758 (1999).

[35] J. P. Perdew, K. Burke, and M. Ernzerhof, Phys. Rev. Lett. **77**, 3865 (1996).

[36] S. Nosé, J. Chem. Phys. **81**, 511 (1984).

[37] W. G. Hoover, Phys. Rev. A **31**, 1695 (1985).

[38] M. Schöttler, R. Redmer, and M. French, Contrib. Plasma Phys. **53**, 336 (2013).

[39] M. French, T. R. Mattsson, N. Nettelmann, and R. Redmer, Phys. Rev. B **79**, 054107 (2009).

[40] M. French, S. Hamel, and R. Redmer, Phys. Rev. Lett. **107**, 185901 (2011).

[41] J. Heyd, G. E. Scuseria, and M. Ernzerhof, J. Chem. Phys. **118**, 8207 (2003).

[42] J. Heyd, G. E. Scuseria, and M. Ernzerhof, J. Chem. Phys. **124**, 219906 (2006).

[43] J. Heyd, J. E. Peralta, G. E. Scuseria, and R. L. Martin, J. Chem. Phys. **123**, 174101 (2005).

[44] M. D. Knudson, M. P. Desjarlais, R. W. Lemke, T. R. Mattsson, M. French, N. Nettelmann, and R. Redmer, Phys. Rev. Lett. **108**, 091102 (2012).

[45] T. Kimura, Y. Kuwayama, and T. Yagi, J. Chem. Phys. **140**, 074501 (2014).

[46] M. French and R. Redmer, Phys. Plasmas **18**, 043301 (2011).

[47] Note that this procedure is only applicable to the off-diagonal matrix elements. It does not yield the correct diagonal matrix elements (electron velocities). However, those do not contribute in Eq. (1).

[48] M. Gajdoš, K. Hummer, G. Kresse, J. Furthmüller, and F. Bechstedt, Phys. Rev. B **73**, 045112 (2006).

[49] R. Kubo and J. Phys, Soc. Jpn. **12**, 570 (1957).
[50] D. A. Greenwood, Proc. Phys. Soc. **71**, 585 (1958).
[51] A. Baldereschi, Phys. Rev. B **7**, 5212 (1973).
[52] Y. T. Lee and R. M. More, Phys. Fluids **27**, 1273 (1984).
[53] F. Sigeneger, S. Arndt, R. Redmer, M. Luft, D. Tamme, W.-D. Kraeft, G. Röpke, and T. Meyer, Physica A **152**, 365 (1988).
[54] L. Spitzer and R. Härm, Phys. Rev. **89**, 977 (1953).
[55] F. J. F. van Odenhoven and P. P. J. M. Schram, Physica A **133**, 74 (1985).
[56] H. Reinholz, R. Redmer, and D. Tamme, Contrib. Plasma Phys. **29**, 395 (1989).
[57] J. R. Adams, H. Reinholz, and R. Redmer, Phys. Rev. E **81**, 036409 (2010).
[58] H. Reinholz, G. Röpke, S. Rosmej, and R. Redmer, Phys. Rev. E **91**, 043105 (2015).
[59] M. P. Desjarlais, C. R. Scullard, L. X. Benedict, H. D. Whitley, and R. Redmer, Phys. Rev. E **95**, 033203 (2017).
[60] S. Altshuler, Phys. Rev. **107**, 114 (1957).
[61] Y. Itikawa, *Molecular Processes in Plasmas* (Springer, Berlin, 2007).
[62] W. Meerts and A. Dymanus, Chem. Phys. Lett. **23**, 45 (1973).
[63] Y. Itikawa, Atom. Data Nucl. Data **14**, 1 (1974).
[64] M. Yousfi and M. D. Benabdessadok, J. Appl. Phys. **80**, 6619 (1996).
[65] J. de Urquijo, E. Basurto, A. M. Ju'arez, K. F. Ness, R. E. Robson, M. J. Brunger, and R. D. White, J. Chem. Phys. **141**, 014308 (2014).
[66] A. M. C. Sobrinho, N. B. H. Lozano, and M.-T. Lee, Phys. Rev. A **70**, 032717 (2004).
[67] J.-S. Yoon, M.-Y. Song, J.-M. Han, S. H. Hwang, W.-S. Chang, B. Lee, and Y. Itikawa, J. Phys. Chem. Ref. Data **37**, 913 (2008).
[68] Y. Itikawa, J. Phys. Chem. Ref. Data **38**, 1 (2009).
[69] L. L. Alves, P. Coche, M. A. Ridenti, and V. Guerra, Eur. Phys. J. D **70**, 124 (2016).
[70] We include helium here because it has an electronic structure (two occupied 1s orbitals) for which the ansatz for the model potential, Eq. (24), is most reasonable. Otherwise, helium does not appear in the calculations made for water.
[71] Y. Itikawa, Atom. Data Nucl. Data **21**, 69 (1978).
[72] M. J. Brunger and S. J. Buckman, Phys. Rep. **357**, 215 (2002).
[73] K. Bartschat, J. Tennyson, and O. Zatsarinny, Plasma Process. Polym. **14**, 1600093 (2017).
[74] R. Redmer, G. Röpke, S. Kuhlbrodt, and H. Reinholz, Phys. Rev. B **63**, 233104 (2001).
[75] G. Röpke and R. Redmer, Phys. Rev. A **39**, 907 (1989).
[76] M. P. Desjarlais, Contrib. Plasma Phys. **41**, 267 (2001).
[77] W. A. Stygar, G. A. Gerdin, and D. L. Fehl, Phys. Rev. E **66**, 046417 (2002).
[78] S. Kuhlbrodt, B. Holst, and R. Redmer, Contrib. Plasma Phys. **45**, 73 (2005).
[79] S. Rosmej, Contrib. Plasma Phys. **56**, 327 (2016).
[80] R. Franz and G. Wiedemann, Ann. Phys. **165**, 497 (1853).
[81] H. Reinholz, R. Redmer, and S. Nagel, Phys. Rev. E **52**, 5368 (1995).
[82] R. Redmer, T. R. Mattsson, N. Nettelmann, and M. French, Icarus **211**, 798 (2011).
[83] M. Born, Nachr. Ges. Wiss. Göttingen, Math.-Phys. Kl. **1926**, 146 (1926).
[84] N. F. Mott and H. S. W. Massey, *Theory of Atomic Collisions* (Oxford University Press, Oxford, 1965).

PRL **107,** 185901 (2011) PHYSICAL REVIEW LETTERS week ending 28 OCTOBER 2011

Dynamical Screening and Ionic Conductivity in Water from *Ab Initio* Simulations

Martin French,[1] Sebastien Hamel,[2] and Ronald Redmer[1]
[1]*Universität Rostock, Institut für Physik, D-18051 Rostock, Germany*
[2]*Lawrence Livermore National Laboratory, Condensed Matter and Materials Division,*
7000 East Avenue, Livermore, California 94550, USA

(Received 19 August 2011; published 25 October 2011)

We present a method to calculate ionic conductivities of complex fluids from *ab initio* simulations. This is achieved by combining density functional theory molecular dynamics simulations with polarization theory. Conductivities are then obtained via a Green-Kubo formula using time-dependent effective charges of electronically screened ions. The method is applied to two different phases of warm dense water. We observe large fluctuations in the effective charges; protons can transport effective charges greater than $+e$ for ultrashort time scales. Furthermore, we compare our results with a simpler model of ionic conductivity in water that is based on diffusion coefficients. Our approach can be directly applied to study ionic conductivities of electronically insulating materials of arbitrary composition, e.g., complex molecular mixtures under such extreme conditions that occur deep inside giant planets.

DOI: 10.1103/PhysRevLett.107.185901 PACS numbers: 66.10.Ed, 61.20.Ja

The process of electrical charge transport in water has attracted much attention since von Grotthuss [1] proposed his mechanism of correlated hydrogen jumps. Especially, *ab initio* simulations have offered new insight into the microscopic dynamical processes of proton transport and into the interaction of the several involved molecular and ionic species [2–4]. As pressure and temperature increase, the dissociation of water molecules allows more protons to contribute to the charge transport which results in a rising conductivity [5–8]. Although theoretical approaches [9–11] to calculate the electrical conductivity of water under extreme conditions can reproduce most of the experimental data well, those models require at least an assumption about the effective charge that is transported by the protons. The unscreened charge of $+e$ is a well motivated [9,10,12] but not the only possible choice here [11,13].

In this work, we present an approach to obtain the electrical conductivity directly from *ab initio* simulations without making assumptions about any involved chemical species that carry defined electrical charges. To accomplish this, we combine density functional theory molecular dynamics simulations (DFT-MD) [14] with state-of-the-art polarization theory [15,16], two well-established *ab initio* calculation techniques. The calculation of the conductivity then involves the evaluation of the Green-Kubo formula for the classical ions that carry time-dependent effective electric charges. Microscopic analyses show that large fluctuations in the effective charge of the protons occur on a femtosecond time scale that play a crucial role in the charge transport in water. Most important, the real power of the method presented here is its direct applicability to more complex systems than water, such as strongly reacting chemicals [17] and molecular mixtures in the deep interior of giant planets [13,18].

Based on the Born-Oppenheimer approximation, our system is described by classical hydrogen ($N_{\mathrm{H}} = 108$) and oxygen ions ($N_{\mathrm{O}} = 54$) that are propagated with forces from the quantum-statistical treatment of the electron system with DFT. We use the exchange correlation functional of Perdew, Burke, and Ernzerhof [19] and the VASP 4.6.28 program package to perform the MD simulations [20–23]. The standard projector augmented wave (PAW) [24,25] potentials (the $1s$ core electrons of oxygen are frozen) are used for the electron ion interaction with a plane-wave cutoff of 900 eV and the electronic wave functions are calculated at the Γ point. These simulation parameters have proven to yield well-converged equation of state data and diffusion coefficients [9,10,26]. The ion temperature is controlled with a Nosé thermostat [27], which we found not to influence the time correlation functions in test simulations.

From basic linear response theory [28] it follows that the electrical conductivity σ is given by a time integral over a current-current autocorrelation function,

$$\sigma = \frac{1}{3Vk_BT}\int_0^\infty dt\langle\vec{J}(t)\cdot\vec{J}(0)\rangle, \qquad (1)$$

where V is the volume, k_BT the thermal energy, and $\vec{J}(t)$ is the total electric current of the system at time t. Equation (1) is known as the Green-Kubo formula, and it was successfully applied in, e.g., classical MD simulations to derive conductivities of molten salts [29]. In our system, the current $\vec{J}(t)$ must basically contain contributions from particles of all three different species, namely, protons, oxygen nuclei, and electrons. Since the Born-Oppenheimer approximation has decoupled the motion of ions and electrons (which are treated statically at every ionic MD step), a direct evaluation of the Green-Kubo formula is not possible because the dynamical information is lacking for the electrons. But as long as the system is nonmetallic, all electronic contributions can theoretically be allocated to ions, which then carry screened effective charges instead of their bare nuclear charges.

The remaining task is now to determine the effective charge of each ion in a consistent way. The literature offers several methods to obtain effective charges from a population analysis of their surrounding electronic states [30], e.g., with a Bader analysis [31]. However, since in a MD simulation all ions are in motion, it is much more reasonable to ask which fraction of its electronic screening cloud remains attached to an ion as it is displaced from its current position. This question is adequately answered by polarization theory [15,16], which allows us to calculate the Born effective charge tensor $\bar{Z}$ via the determination of the change in the electronic polarization induced by a displaced ion. The numerical procedure involves a self-consistent perturbative DFT scheme [16,32]. For instance, this method reproduces the measured mean effective charge of $+0.53$ of hydrogen in liquid water [33] very well [10].

We employ VASP 5.2.8 to calculate the Born effective charge tensor $\bar{Z}(t)$ of every ion at each time step of a MD run. We used a plane-wave cutoff of 400 eV and the Baldereschi point [34] in these particular calculations. This is sufficient to fulfill the charge neutrality condition $2\langle Z_{\mathrm{H}}\rangle = -\langle Z_{\mathrm{O}}\rangle$ for the diagonal elements within 1%. It also results in acceptable numerical costs that amount to about 3 times of the respective MD simulation. In all calculations the time-averaged charge tensors of both ion species are, within the statistical uncertainties, diagonal and contain the same values in any direction. This is consistent with the symmetry of the isotropic and cubic systems that we consider here.

First we examine water at a temperature of 2000 K and a density of 2 g/cm^3. Under these conditions the system still retains its molecular structure but already contains about 20% of dissociated water molecules [10] so that frequent proton jumps occur. Figure 1 displays typical fluctuations of the Born effective charge of an arbitrary hydrogen and oxygen ion. Most interestingly, a hydrogen ion can carry an effective charge greater than $+1$ for short times. Such anomalous (anti-) screening can often be correlated with events at which the hydrogen ion changes its nearest oxygen ion, thus performing a Grotthuss-like proton jump into the respective direction. An explanation for temporarily antiscreened hydrogen ions is given by the breaking of the proton's bond to its oxygen and a jump to the next oxygen ion to form another bond again. During such a process the initial bonding electrons pull back to its oxygen ion while electronic charge density from the second oxygen ion is attracted by the incoming proton to form the new bond. This effectively creates an additional negative current that is directed oppositely to the motion of the proton. Nevertheless, effective charges of $+2$ can occur also without a proton jump; see Fig. 1 near time step 200. We then relate this effect to protons that have already large vibrational amplitudes but do not yet have enough kinetic energy to break their already weakened bond.

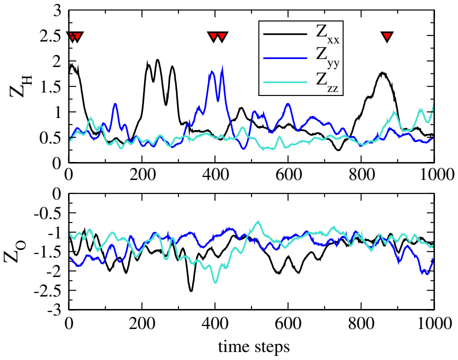

FIG. 1 (color online). Fluctuations in the diagonal Born effective charges for a hydrogen and an oxygen ion. The triangles indicate Grotthuss-like proton jumps (changes of the proton's nearest oxygen neighbor, detectable with a geometric analysis). One time step amounts to 0.3 fs.

Additional simulations show that effective proton charges greater than $+1$ occur also in other phases of water. Figure 2 shows distributions of the Born effective charges distinguished by diagonal and off-diagonal components for both ion species in fluid and superionic water. The diagonal components are distributed over relatively broad intervals and have pronounced non-Gaussian tails to high charge values. The off-diagonal components accumulate around zero. To analyze and understand the microphysics that generates such charge distributions in greater detail would go well beyond the scope of this work. Instead, we aim to put the key aspect here on the calculation of the ionic conductivity in the respective systems.

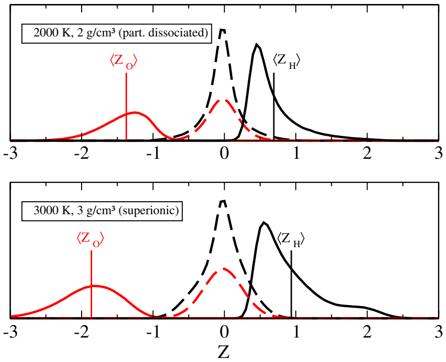

FIG. 2 (color online). Distribution of Born effective charges in partially dissociated (top) and superionic water (bottom) in arbitrary units. Solid lines represent diagonal components, dashed lines off-diagonal components. Protons are displayed in black, oxygen ions in red (gray in print version). The average values of the diagonal components are indicated as well.

The total current $\vec{J}(t)$ in Eq. (1) is expressed as a time derivative of the polarization, and is thus given by the time-dependent Born effective charge tensor via

$$\vec{J}(t) = e\sum_{i=1}^{N} \bar{Z}_i(t)\cdot\vec{v}_i(t), \tag{2}$$

where $\vec{v}_i$ is the velocity of the ith ion and N is the total number of ions. For a simulation of 15 ps duration (50 000 time steps) at 2000 K and 2 g/cm^3 we calculate the current-current correlation function $C(t) = \langle\vec{J}(t)\cdot\vec{J}(0)\rangle/3e^2$ and the respective time integral and display the results in Fig. 3. Depending on how the time-dependent charges are treated, significantly different results are obtained. In particular, the complex mechanism of charge transfer in water does not allow us to use only constant average values of the Born effective charges, $Z_H = \langle Z_H\rangle = 0.69$ and $Z_O = \langle Z_O\rangle = -1.37$ (dashed black line). It is necessary to include their full time dependence into the correlation function to obtain converged results (full black line). Interestingly, the use of predefined constant charges can yield the same conductivity as is found with the fully time-dependent charge tensors, but only if they have values of $Z_H = 1$ and $Z_O = -2$ (blue line, gray in print version). The usually assumed picture of protons transporting their unscreened charges is thus not in contrast to our findings. Nevertheless, this work shows that the processes of charge transport in water involve a complex interplay of ionic movements and changes in the electronic polarization of their surrounding.

In a second simulation of 60 000 time steps we examine superionic water [26,35] at 3000 K and 3 g/cm^3 and found the correlation functions to behave similarly to those shown in Fig. 3. In the same way as above, constant charges of $Z_H = 1$ and $Z_O = -2$ yield the same conductivity as the time-dependent ones.

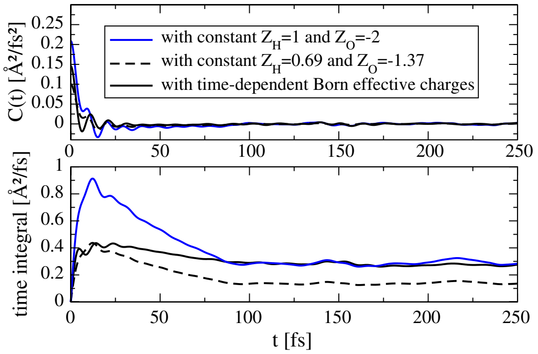

FIG. 3 (color online). Upper: current-current correlation function for water at 2000 K and 2 g/cm^3. Depending on the treatment of the effective charges, different results are obtained, see text for further explanations. Lower: the respective time integrals of the functions from the upper figure.

In general, the time correlations in the current-current correlation function fade on the same time scale as they do in velocity autocorrelation functions. Thereafter the time integral is stable for a certain period before statistical fluctuations take over at long times. Several 10 000 time steps are necessary to obtain converged conductivities with this method.

Furthermore, the Green-Kubo formula (1) can be decomposed into autocorrelation and crosscorrelation terms. When constant charges are assigned to all particles, the contributions from autocorrelations can be expressed by diffusion coefficients which leads to the Nernst-Einstein relation. The crosscorrelation terms contain contributions from the formation of associated species, such as water molecules, and are usually negative. Mattsson and Desjarlais [9] introduced a simple but well-motivated approximation scheme for this term (originally neglecting the relatively small contribution of the oxygen ions [10]). This leads to

$$\sigma' = \frac{e^2 N_H D_H}{V k_B T} + \frac{(2e)^2 N_O D_O}{V k_B T}\left(1 - \frac{3}{2}\gamma\right), \tag{3}$$

where D_i are diffusion coefficients, which can be obtained with much less numerical effort than a reasonably converged current-current correlation function. The factor γ denotes the fraction of hydrogen ions bound to oxygen ions and has to be approximated. The term proportional to γ represents the deviation from the Nernst-Einstein relation in Eq. (3).

With such a model most of the experimental ionic conductivities [5,7,8] in warm dense water can be reproduced well [10]. Nevertheless, the performance of Eq. (3) can now be checked against our more general approach. For our simulations in partially dissociated and superionic water we display the results of both methods in Table I. The agreement is very good in fluid water but not in superionic water where the model of Mattsson and Desjarlais reduces to an Einstein equation for the protons ($D_O = 0$). Therefore all crosscorrelations are omitted

TABLE I. Electrical conductivities from the current-current autocorrelation function (1) calculated with time-dependent Born effective charges, σ, and with constant charges of +1 for hydrogen and −2 for oxygen, $\sigma_{+1,-2}$. These are compared with those derived from Eq. (3), σ' (γ is taken from Ref. [10]). For additional comparison, the conductivity using Eqs. (1) and (2) with time-dependent Bader charges, σ_B, instead of Born effective charges is given as well. Bader charges [31] do not capture electronic polarization effects and should not be used to calculate conductivities. All conductivities along with estimated errors are given in $1/\Omega$ cm.

T (K)	ϱ (g/cm^3)	σ	$\sigma_{+1,-2}$	σ'	σ_B
2000	2.0	30 ± 3	30 ± 3	28 ± 2	11 ± 1
3000	3.0	140 ± 15	140 ± 15	91 ± 3	55 ± 5

which leads to an underestimation of the conductivity by about 50%. We checked that, although the oxygen ions themselves are immobile, correlation terms between protons and oxygen ions are important here. It is thus necessary to follow our more general approach for a quantitatively accurate description of the ionic conductivity in the superionic phase of water. Moreover, this method is directly applicable to more complex systems such as chemically reacting mixtures that contain several different ion species [13,17,18].

Finally, we note that the theoretical basics of our approach do not allow its application to electronically conducting systems. However, we expect that reasonable total conductivity values can yet be obtained for matter with thermally activated electrons by treating them at nonzero temperature also in Born effective charge calculations. The electronic contribution from the Kubo-Greenwood formula usually becomes dominant quickly at higher temperatures [9,10] and will suppress errors arising from a simultaneous inconsistency in the calculation of the Born effective charges.

In summary, we demonstrated that ionic conductivities can be calculated *ab initio* from a combination of DFT-MD simulations and polarization theory. This allows us to include the electronic contribution to the current in a rigorous way when evaluating the Green-Kubo formula. The application to water reveals that the charge transfer processes involve a complex interplay between ionic motion and changes in the electronic polarization, albeit the common assumption of a proton transporting its unscreened charge of $+e$ during Grotthuss-like hopping processes is, to some extent, in line with our findings. We show that a simple conductivity model based on diffusion coefficients works well in fluid water but is not sufficient for the superionic phase. Our approach is capable of giving insight into the time-dependent mechanisms of charge transport in much more complex systems, especially in such where chemical reactions are taking place. It could furthermore aid in parametrizing continuum solvation or semiempirical conductivity models.

We thank B. Holst and W. Lorenzen for helpful discussions. This work was supported by the DFG within the SFB 652 and the SPP 1488 and by the North-German Supercomputing Alliance HLRN. This work was performed under the auspices of the U.S. Department of Energy under Contract No. DE-AC52-07NA27344. Computing support for part of this work came from the Lawrence Livermore National Laboratory (LLNL) Institutional Computing Grand Challenge program.

---

[1] C. J. T. de Grotthuss, Ann. Chim. **LVIII**, 54 (1806).

[2] D. Marx, M. E. Tuckerman, J. Hutter, and M. Parrinello, Nature (London) **397**, 601 (1999).

[3] M. E. Tuckerman, D. Marx, and M. Parrinello, Nature (London) **417**, 925 (2002).

[4] D. Marx, Chem. Phys. Chem. **7**, 1848 (2006).

[5] S. D. Hamann and M. Linton, Trans. Faraday Soc. **62**, 2234 (1966).

[6] W. B. Holzapfel, J. Chem. Phys. **50**, 4424 (1969).

[7] A. C. Mitchell and W. J. Nellis, J. Chem. Phys. **76**, 6273 (1982).

[8] R. Chau, A. C. Mitchell, R. W. Minich, and W. J. Nellis, J. Chem. Phys. **114**, 1361 (2001).

[9] T. R. Mattsson and M. P. Desjarlais, Phys. Rev. Lett. **97**, 017801 (2006).

[10] M. French, T. R. Mattsson, and R. Redmer, Phys. Rev. B **82**, 174108 (2010).

[11] N. Goldman, E. J. Reed, I.-F. W. Kuo, L. E. Fried, C. J. Mundy, and A. Curioni, J. Chem. Phys. **130**, 124517 (2009).

[12] E. Schwegler, G. Galli, F. Gygi, and R. Q. Hood, Phys. Rev. Lett. **87**, 265501 (2001).

[13] R. Chau, S. Hamel, and W. J. Nellis, Nature Commun. **2**, 203 (2011).

[14] D. Marx and J. Hutter, *Ab Initio Molecular Dynamics* (Cambridge University Press, New York, 2009).

[15] R. Resta, Rev. Mod. Phys. **66**, 899 (1994).

[16] S. Baroni, S. de Gironcoli, A. Dal Corso, and P. Giannozzi, Rev. Mod. Phys. **73**, 515 (2001).

[17] C. J. Wu, L. E. Fried, L. H. Yang, N. Goldman, and S. Bastea, Nature Chem. **1**, 57 (2009).

[18] M.-S. Lee and S. Scandolo, Nature Commun. **2**, 185 (2011).

[19] J. P. Perdew, K. Burke, and M. Ernzerhof, Phys. Rev. Lett. **77**, 3865 (1996).

[20] G. Kresse and J. Hafner, Phys. Rev. B **47**, 558 (1993).

[21] G. Kresse and J. Hafner, Phys. Rev. B **49**, 14 251 (1994).

[22] G. Kresse and J. Furthmüller, Phys. Rev. B **54**, 11 169 (1996).

[23] J. Hafner, J. Comput. Chem. **29**, 2044 (2008).

[24] P. E. Blöchl, Phys. Rev. B **50**, 17 953 (1994).

[25] G. Kresse and D. Joubert, Phys. Rev. B **59**, 1758 (1999).

[26] M. French, T. R. Mattsson, N. Nettelmann, and R. Redmer, Phys. Rev. B **79**, 054107 (2009).

[27] S. Nosé, J. Chem. Phys. **81**, 511 (1984).

[28] R. Kubo, J. Phys. Soc. Jpn. **12**, 570 (1957).

[29] J. P. Hansen and I. R. McDonald, Phys. Rev. A **11**, 2111 (1975).

[30] F. Martin and H. Zispe, J. Comput. Chem. **26**, 97 (2005).

[31] R. F. Bader, *Atoms in Molecules: A Quantum Theory* (Oxford University Press, Oxford, 1990).

[32] R. W. Nunes and X. Gonze, Phys. Rev. B **63**, 155107 (2001).

[33] J. Neuefeind, C. J. Benmore, B. Tomberli, and P. A. Egelstaff, J. Phys. Condens. Matter **14**, L429 (2002).

[34] A. Baldereschi, Phys. Rev. B **7**, 5212 (1973).

[35] C. Cavazzoni, G. L. Chiarotti, S. Scandolo, E. Tosatti, M. Bernasconi, and M. Parrinello, Science **283**, 44 (1999).

IOP Publishing New J. Phys. 21 (2019) 023007 https://doi.org/10.1088/1367-2630/ab0613

New Journal of Physics
The open access journal at the forefront of physics

Deutsche Physikalische Gesellschaft DPG
IOP Institute of Physics

Published in partnership with: Deutsche Physikalische Gesellschaft and the Institute of Physics

OPEN ACCESS

RECEIVED
16 November 2018

REVISED
9 January 2019

ACCEPTED FOR PUBLICATION
11 February 2019

PUBLISHED
28 February 2019

PAPER

Thermal conductivity of dissociating water—an *ab initio* study

Martin French
Universität Rostock, Institut für Physik, Albert-Einstein-Str. 23-24, D-18059 Rostock, Germany
E-mail: martin.french@uni-rostock.de

Keywords: thermal conductivity, *ab initio* simulations, water

Abstract

The thermal conductivity of partially dissociated and ionised water is calculated in a large-scale study using density functional theory (DFT)-based molecular dynamics (MD) simulations. In doing so, the required heat current of the nuclei is calculated by mapping the effective particle interactions from the DFT-MD simulations onto classical pair potentials. It is demonstrated that experimental and theoretical thermal conductivity data for liquid heavy water and for ice VII are well reproduced with this efficient procedure. Moreover, the approach also allows for an illustrative interpretation of the characteristics of the thermal conductivity in the dense chemically reacting fluid. The thermodynamic conditions investigated here range from densities between 0.2 and 6 g cm^{-3} and temperatures between 600 and 50 000 K, which includes states highly relevant for understanding the interiors of water-rich planets like Uranus and Neptune and exoplanets of similar composition.

1. Introduction

Gaining accurate knowlegde of the thermodynamic and transport properties of water and water-rich molecular mixtures at high pressures and high temperatures is key to understanding the interior structure, thermal evolution, and magnetic fields of icy giant planets [1–3]. For example, a major unsolved puzzle is the existence of a thermal convection barrier deep inside the ice giant Uranus, which may explain its unusually low luminosity [4]. Furthermore, it is unknown to which degree the icy cores of Jupiter or Saturn are eroded and dissolved into their envelopes [5]. But quantitative planetary evolution models that include both convective and diffusive heat transport [6, 4] require reliable thermal conductivity data, which are not yet available at the relevant conditions.

Direct measurements of the thermal conductivity of materials at extreme pressures and temperatures are highly challenging since undesirable influences of convection, radiation, and heat flux through the confining device have to be inhibited [7]. Much of the progress has therefore been achieved on good conducting metals [8, 9]. For example, the thermal conductivity of iron was recently measured up to pressures of 140 GPa and temperatures of 3000 K using laser-heated diamond anvil cells [10]. The most extreme conditions at which thermal conductivity of water was measured, so far, were only 3.5 GPa at temperatures less than 700 K [11].

This work describes an efficient procedure to calculate the thermal conductivity with *ab initio* computer simulation techniques. The method is then applied to generate a large data base for the thermal conductivity of water that spans a density range between 0.2 and 6 g cm^{-3} and temperatures between 600 and 50 000 K.

During the last two decades, *ab initio* calculations based on finite-temperature density functional theory (FT-DFT) in combination with molecular dynamics (MD) simulations have become a reliable tool for accurate predictions of thermodynamic properties of matter under extreme conditions [12, 13]. The prefix FT emphasises that the electron system is consistently treated at a nonzero (finite) temperature [14], which is typically equal to the temperature of the nuclei.

The calculation of the thermal conductivity with FT-DFT-MD techniques requires a distincted treatment of the contributions from electronic heat conduction and from heat transport via the nuclei. The former is gained by evaluating the electronic Onsager coefficients using the Kohn–Sham eigenvalues and orbitals from the FT-DFT [15], which was recently accomplished also for partially ionised water [16].

The latter is tremendously more difficult to derive because a rigorous calculation of the nuclear heat current is complicated and has been achieved yet only for one-component fluids in ground-state DFT-MD simulations [17, 18]. The reason is that the underlying Born–Oppenheimer approximation decouples the dynamics of electrons and ions. The electron–nucleus interactions then need to be properly reintroduced into the definition of the microscopic nuclear heat current so that it contains the dynamical information relevant for the time scale of nuclear motion. Furthermore, the numerical formalism inherently suffers from rather poor convergence behaviour of the time correlation functions in the Green–Kubo formula, which is another reason for the absence of any large-scale *ab initio* studies on nuclear thermal conductivity of fluid systems to date.

2. Theoretical method and simulation procedure

To calculate the nuclear heat current in the FT-DFT-MD simulations with an efficient but yet sufficiently accurate procedure, we map all effective interactions between the nuclei on radial pair potentials. This allows us to employ an established expression for the heat current in the Green–Kubo formula for the thermal conductivity λ_{nuc} [19–21]:

$$\lambda_{\text{nuc}} = \frac{1}{3Vk_{\text{B}}T^2}\int_0^\infty \mathrm{d}t\ \langle \mathbf{J}'_q(t)\cdot \mathbf{J}'_q(0)\rangle, \tag{1}$$

where V is the volume of the simulation box, T the temperature, k_{B} is Boltzmann's constant, and $\mathbf{J}'_q(t)$ is the modified heat current vector at time t. Note that expression (1) is exact for one-component systems but omits a small correction from thermodiffusion [20] in the multi-component case. The appendix contains additional considerations on different formulations of the heat current and phenomenologial transport equations, including a comparison with an alternative variant that takes thermodiffusion terms into account. It is shown that both variants lead to the same results within the statistical error.

In general, the heat current $\mathbf{J}'_q(t)$ can be written as sum of a kinetic part $\mathbf{J}'_{q,\text{kin}}(t)$ and an interaction part $\mathbf{J}'_{q,\text{int}}(t)$. The kinetic part is easily calculated from the particle velocities $\mathbf{v}_i(t)$ via:

$$\mathbf{J}'_{q,\text{kin}}(t) = \sum_{i=1}^{N}\left(\frac{m_i\mathbf{v}_i^2(t)}{2} - \frac{5}{2}k_{\text{B}}T\right)\mathbf{v}_i(t), \tag{2}$$

where m_i is the mass of particle i, N is the total particle number, and $\frac{5}{2}k_{\text{B}}T$ is the average kinetic enthalpy per particle. The interaction part for pairwise interacting particles can be written as:

$$\begin{aligned}\mathbf{J}'_{q,\text{int}}(t) = &\sum_{i=1}^{N}(E_{F,i}(t) - h_{F,a})\mathbf{v}_i(t)\\ &+ \frac{1}{2}\sum_{\substack{i,j\\ i\neq j}}^{N}(\mathbf{F}_{ij}(r_{ij}(t))\cdot\mathbf{v}_i(t))\mathbf{r}_{ij}(t),\end{aligned} \tag{3}$$

where $\mathbf{F}_{ij}(t)$ and $\mathbf{r}_{ij}(t)$ are force and distance between particles i and j, respectively. The interaction energy of a particle reads:

$$E_{F,i}(t) = \frac{1}{2}\sum_{\substack{j\\ i\neq j}}^{N} V_{ij}(r_{ij}(t)). \tag{4}$$

The partial interaction enthalpy of particle i of species a is taken as:

$$h_{F,a} \approx \langle h_{F,i}\rangle = \frac{1}{2}\sum_{\substack{j\\ i\neq j}}^{N}\left\langle V_{ij}(r_{ij}) + \frac{1}{3}\mathbf{F}_{ij}(r_{ij})\cdot\mathbf{r}_{ij}\right\rangle. \tag{5}$$

The above expression neglects nonideal mixing contributions to $h_{F,a}$ but simplifies the calculations [22, 23]. Nonideal mixing effects on equation of state quantities were found to be very small in calculations of water–ammonia–methane mixtures under similar conditions [24]. Nevertheless, avoiding this approximation is possible, and a comparison with results from an exact expression for λ_{nuc} was made, see the appendix. The very good agreement shows the suitability of the approach described here for dense water plasmas.

The following ansatz for the potential between the nuclear species a and b is made:

$$V^{ab}(r) = \sum_{l=0}^{C^{ab}} c_l^{ab}r^{E_l^{ab}}\exp\left[\alpha^{ab}\left(\frac{r}{L} - \frac{1}{2}\right)^{-1}\right], \tag{6}$$

where $r = r_{ij}$ is the radius and $E_l^{ab} = \gamma^{ab}l + \delta^{ab}$. The exponential term [25] in equation (6) serves to smoothly truncate the potential at half of the simulation box length L. It allows for the evaluation of all expressions that enter equation (3) within the minimum image convention [21] and for systematic convergence tests with the system size. Extensive tests have shown that there are universally suitable choices possible for some of the parameters, i.e. $\alpha^{ab} = 0.1$, $\gamma^{ab} = 0.5$, and $\delta^{ab} = -4$. To allow the potential (6) to reach its converged shape, which depends on density ϱ and temperature T, the cutoff parameter C^{ab} needs to be set typically to numbers between 10 and 20. Potential and thermal conductivity both converge very similarly with C^{ab}.

After the completion of an FT-DFT-MD simulation run, the coefficients c_l^{ab} are fitted by matching the force fields $\mathbf{F}_{ij}(r_{ij}) = -\nabla V_{ij}(r_{ij})$ to the forces on the particles at each 20th (or 50th for very long simulations) time step, which fully determines the potentials (6) for that particular simulation run. This mathematical task can be formulated as a linear least-squares optimisation problem, and its exact solution is determined with means of linear algebra.

After the pair potentials are parametrised, equation (1) is evaluated using the particle trajectories of the same FT-DFT-MD simulation run. This is a very important point to take note of because it ensures that the correlation function of the heat current in equation (1) is evaluated using the ensemble (trajectories) $\langle \ldots \rangle$ generated in the FT-DFT-MD simulation[1]. The whole procedure is labelled here as DFT-MD+GKFF method[2].

The formalism described above is now applied to various FT-DFT-MD simulations of warm dense water performed with the VASP code [26–28] and the PBE exchange correlation functional [29]. Most of the simulation parameters were set to values well-proven for calculating equation of state and diffusion coefficients [30–33]. The major modification here is the large extension in simulation time, so that now between 50 000 and 250 000 time steps (typical length of a time step: 0.3–0.5 fs) are simulated. This large increase is necessary to converge the time correlation function in equation (1) and reach a statistical uncertainty for the λ_{nuc} data of about 10%–20%.

3. Results and discussion

At first, we perform a special benchmark simulation in order to make a direct comparison with the sole example for rigorous calculation of the thermal conductivity of water made with DFT-MD so far [17]. In that work, Marcolongo *et al* derived a special variant of density functional perturbation theory [34, 35] that can describe the heat flow contribution of bound electrons via the energetic polarisation induced by nuclei in motion. Combining this formalism with a ground-state DFT-MD run enabled them to calculate the nuclear thermal conductivity for electronically insulating systems, which is adequate for liquid water. However, this elaborate procedure enhances the computing time of a DFT-MD simulation run by significant factor, similarly as occurs in analogous calculations of ionic conductivities [36, 37].

Our benchmark simulation is performed with liquid heavy water (64 molecules) at the same density of 1.11 g cm^{-3} and same temperature of 385 K as reported by Marcolongo *et al* [17]. The resulting integrated thermal conductivity from the DFT-MD+GKFF approach is displayed in the upper panel of figure 1. After about 100 fs the short-time correlations have decayed and the final value of 0.7 ± 0.1 W Km^{-1} is reached. This number is in excellent agreement with the result from Marcolongo *et al* [17] of 0.74 ± 0.12 W Km^{-1} and also with the experimental value of about 0.68 W Km^{-1} [38].

As second example we compute the thermal conductivity of ice VII at room temperature and at 4 densities using proton-ordered[3] crystal structures of 54 and 128 molecules. The experimental thermal conductivity of ice VII, which was measured up to pressures of 22 GPa [39, 40], is reproduced very well, see lower panel of figure 1. The same plot also shows that the DFT-MD+GKFF approach produces converged values for the thermal conductivity already with 54 molecules in the simulation box. Success at this crucial convergence test indicates that the mapping of the long-ranging forces between charged ice nuclei on short-range pair potentials is adequate for calculating the heat current. This can be understood through the structure of equation (3), which requires the force fields only to reproduce well the fluctuations of virial and energy terms around average values. These fluctuations are mainly determined by the effective interactions on short-range (particle collisions). Accurate reproduction of the total average pressure or Ewald energy, which are more influenced by the long-range character of the Coulomb forces, is not required.

In general, the interatomic potentials (6) look unspectacular for the molecular and fully dissociated fluid states, i.e. they show characteristic repulsive and/or attractive properties. Their behaviour in the partially

---

[1] An obvious alternative, i.e. performing a subsequent classical MD simulation with the derived potentials, would lead to a different ensemble because the radial force fields cannot reproduce the DFT forces exactly. This would significantly worsen the results because such an error would then also propagate into the other relevant dynamic quantities (positions, velocities).

[2] GKFF stands for Green–Kubo (with) force fields. The prefix FT is omitted for simplification, albeit all simulations were made with thermally excited electrons.

[3] Proton order was assumed for simplicity and to enable unambiguous convergence checks with increasing particle number. The thermal conductivity of solids is mainly due to the acoustic phonons, so that the influence of proton disorder is probably small.

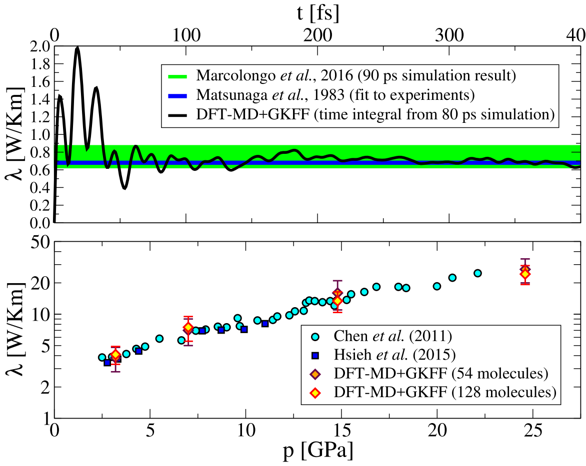

Figure 1. Upper: thermal conductivity of heavy water at 1.11 g cm^{-3} and 385 K from this work (black line) in comparison with the result of Marcolongo *et al* [17] (green stripe) and the measured value [38] (blue line). Lower: thermal conductivity of ice VII at T = 300 K in comparison with experiments [39, 40]. Pressures for the DFT-MD+GKFF points were calculated with an equation of state [41].

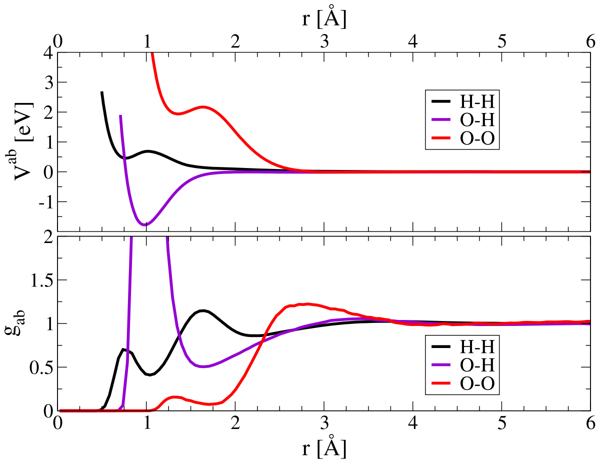

Figure 2. Interatomic potentials (upper panel) and pair correlation functions (lower panel) for partially dissociated water at 1 g cm^{-3} and 6000 K. The length of the simulation box is 11.73 Å.

dissociated region is worth explicit discussion, see figure 2 (upper panel), which shows an example at a density of 1 g cm^{-3} and a temperature of 6000 K. This state represents a reacting dense oxyhydrogen gas mixture, where very short-lived H_2 and O_2 molecules are present as indicated by the pair correlation functions in figure 2 (lower panel). The most prominent attractive well occurs in V^{OH} at the typical length of an intramolecular O–H bond. In addition, both V^{HH} and V^{OO} have shallow valleys at the distances of the diatomic bond lengths of H_2 and O_2 molecules, respectively. These valleys can be reached only by particles that overcome significant potential barriers even higher than the valley depths. All this illustrates the endothermic character of the dissociation reaction of water molecules in this supercritical fluid state.

The main effort of this work is directed towards a general understanding of the thermal conductivity of fluid water across large density and temperature ranges. For such purpose, we first evaluate equation (1) by plugging in the kinetic part of the heat current, equation (2), only. The respective results, λ_{kin}, are shown as dots connected with dashed lines in figure 3. The values rise systematically with temperature but they are relatively independent of the density, especially below 3000 K, where water is largely molecular [30, 32]. This behaviour is somewhat surprising and it suggests that the change in correlations between the water molecules with increasing density does not lead to drastic effects on distribution of their velocities. The averaged values of λ_{kin} for the

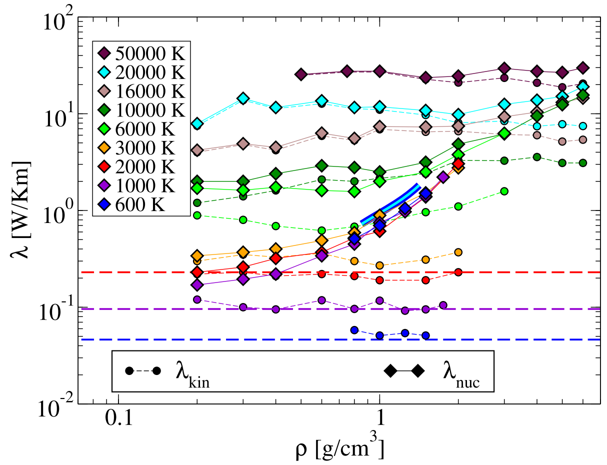

Figure 3. Thermal conductivity of the nuclei from the DFT-MD+GKFF method. Values for λ_{kin} and λ_{nuc} are represented by circles (connected with dashed lines) and diamonds (connected with solid lines), respectively. The thick dashed lines indicate the low-density limits for molecular water at 600, 1000, and 2000 K [42, 43]. Temperatures are indicated via the colour code in the legend. The blue/cyan stripe is the curve from Abramson *et al* [11] scaled to $T = 600$ K.

temperatures 600, 1000, and 2000 K are in good concordance with the known low-density limiting values of the thermal conductivity for molecular water gas [42, 43].

Several interesting changes occur when λ_{nuc} is calculated with the complete heat current that includes both kinetic and interaction part. For molecular water (below $T \leqslant 3000$ K), systematic deviations from λ_{kin} arise as the thermal conductivity acquires a pronounced increase with the density. At densities larger than 1 g cm^{-3}, this leads to a merging of the λ_{nuc} curves for 600 K $\leqslant T \leqslant$ 3000 K with no significant effect of temperature. An absent or weak temperature dependence of λ_{nuc} is common for many liquids [44]. Liquid water at few 100° Celsius is a known exception because its thermal conductivity increases, and this can be understood quantitatively through an excess contribution from the dissociation of hydrogen bonds [45, 46]. It is still debated if and at which density and temperature this rise in thermal conductivity eventually levels off [11, 46, 47]. Our results indicate that this happens somewhat below 600 K, which was observed earlier in classical MD simulations [47]. The only experiment made at these conditions, however, reported of a $\lambda_{\mathrm{nuc}} \sim \sqrt{T}$ behaviour that persists up to more than 600 K [11], but this unusual scaling law[4] has not yet been independently confirmed.

On the other hand, the accuracy of FT-DFT-MD in the description of hydrogen bonds might not yet be sufficient to fully understand the temperature dependence of the thermal conductivity in liquid water, either due to the exchange correlation functional [48] or the classical treatment of the ionic motion. Despite the very good agreement with the measurements in the examples shown in figure 1, our four 600 K data points for λ_{nuc} are lower by 20%–30% than recommended reference values [42]. Still, the density dependence of our thermal conductivites above 1 g cm^{-3} is very well in line with that measured by Abramson *et al* [11], see figure 3. This indicates that the increase in strength of the repulsive molecular interactions under compression is captured well in the DFT-MD+GKFF approach.

A prominent increase in λ_{nuc} emerges at temperatures greater than 3000 K, where water dissociates into atoms or smaller molecules. Figure 3 shows this especially at 6000 and 10 000 K, where λ_{nuc} does not reach the limiting values of λ_{kin} at the lowest density considered here. The reason is the large contribution due to the dissociation reactions of the molecules that enters the interaction part, $\mathbf{J}'_{q,\mathrm{int}}(t)$, through the shape of the potentials (6), as described above on the basis of figure 2. This contribution is analoguous to that from hydrogen-bond dissociation in the liquid, but much larger in number because the intramolecular bonds have greater dissociation energies. Therefore, this effect is more commonly included in chemical models of dilute dissociating gases as an excess term [49, 50]. At $T \geqslant 16\,000$ K, water is fully dissociated and λ_{nuc} is dominated by the kinetic part $\mathbf{J}'_{q,\mathrm{kin}}(t)$, so that it approaches λ_{kin} again at low densities.

For practical purposes, the generated data for the nuclear thermal conductivity are fitted to an analytic expression, which we recommend to use for $T \geqslant 1000$ K:

---

[4] Although a $\lambda_{\mathrm{nuc}} \sim \sqrt{T}$ scaling law exists for gases of hard spheres (derived within the Chapman–Enskog kinetic theory) [19], this is mere coincidence because underlying assumptions of that theory do not hold for liquid water.

Table 1. Fit coefficients for equation (7). All units are chosen in such a way that entering temperatures in K and densities in g cm^{-3} leads to results W Km^{-1} for λ_{nuc}.

j	0	1	2	3
a_j	1.054 31	−0.457 948	−7708.55	1692.09
c_{0j}	338.278	−108.114	11.3921	−0.393 551
c_{1j}	−45.8201	16.7430	−1.925 84	0.071 2254
c_{2j}	−0.944 639	0.161 103	−0.006 783 51	0.0

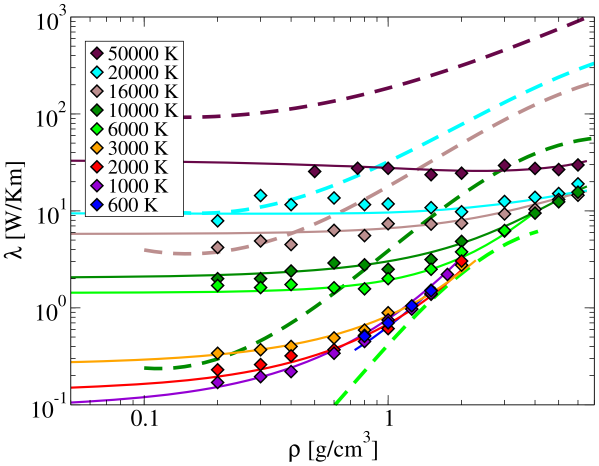

Figure 4. Nuclear thermal conductivity from the DFT-MD+GKFF method (diamonds) and the corresponding fit curves from equation (7) (solid lines). Dashed lines represent the electronic thermal conductivity from [16]. Temperatures are consistently indicated via the colour code in the legend.

$$\ln\lambda_{\mathrm{nuc}} = \sum_{i,j} c_{ij}\,\varrho^i y^j + a_0\exp\left\{-s_0(y-y_0)^2 - \frac{\varrho}{\varrho_0}\right\} + a_1\ln(\varrho+1) + \frac{a_2}{T} + a_3\frac{\ln(\varrho+1)}{T}, \qquad (7)$$

where $y = \ln(T/\mathrm{K})$, $\varrho_0 = 1.117$ g cm^{-3}, $y_0 = 8.5$, $s_0 = 5.636$, and all other coefficients are given in table 1. Figure 4 shows the representation of this fit together with the data points. The fit function is purely empirical and designed to become solely temperature-dependent in the low-density limit.

The nuclear thermal conductivity from equation (7) is intended to be added to the electronic contribution λ_{el} from [16]. Figure 4 also includes λ_{el} for comparison. The nuclear contribution is naturally dominant at low temperatures, and it can remain comparable to λ_{el} even up to $T \approx 20\,000$ K. This is very different from the electrical conductivity, which becomes dominated by electronic transport already near 5000 K [30, 32]. Temperatures in the interiors of Uranus and Neptune are typically less than 6000 K, so that the thermal conductivity of water inside both planets is caused mainly by the interactions between the nuclei. This should also apply to possibly occurring superionic phases [51], which have similar proton diffusion coefficients as the fluid but strongly reduced electronic conductivity [30, 32, 52].

4. Summary

We have presented an efficient approach for calculating the nuclear thermal conductivity with DFT-MD simulations via the determination of effective radial force fields directly from the simulations. One can expect the method to perform generally well for anharmonic crystalline, glassy and superionic solids, dense atomic gases, liquids, and plasmas. Molecular and chemically reacting systems like water can be treated as well if their structure is not too complex. It remains to be explored up to which accuracy liquids consisting of much larger polyatomic molecules can also be described. For such cases, the DFT-MD+GKFF approach could be further expanded and improved straight-forwardly, for example, by using many-body potentials [53] or tight-binding coefficients [54] to describe non-radial interactions between the particles.

Compared to more rigorous techniques for thermal conductivity calculations with DFT-MD that employ different variants of polarisation theory [17, 18], the DFT-MD+GKFF method has three main advantages. First, it does not enhance the computing time of DFT-MD runs at all because λ_{nuc} is calculated within a fast post-processing procedure. Second, the partial enthalpy per particle can be calculated directly from the force fields, either approximately via equation (5) or with exact expressions similar to those in [22]. Third, expressing the heat current as time derivative of polarisation of the electronic system is formally possible only when the material is an electronic insulator. Since the DFT-MD+GKFF circumvents the use of polarisation theory, it is certainly first choice for applications to semimetals and materials with thermally excited electrons.

Finally, we have made novel predictions for the nuclear thermal conductivity of fluid water across a large density-temperature region. Deeper insight into its characteristic changes with density and temperature was achieved by discussing the effective interactions between the particles and their influence on the microscopic heat current. Some of our qualitative predictions, e.g. the existence of a large, mostly temperature-independent region in the dense molecular (or weakly dissociated) fluid will require experimental verification. Apart from that, a fit formula is given for convenient implementation of our results in applications.

Acknowledgements

The author acknowledges valuable discussions with R Redmer and support from the Deutsche Forschungsgemeinschaft (DFG) within the FOR 2440 (Matter under Planetary Interior Conditions—High-Pressure, Planetary, and Plasma Physics). The *ab initio* simulations were run at the North-German Supercomputing Alliance (HLRN) facilities and at the IT- and Media Center of the University of Rostock.

Appendix. Phenomenological equations and microscopic expressions for the thermal conductivity

This section contains additional information on formulations of the transport equations used to calculate the thermal conductivity.

Starting point is the entropy production density from heat and mass transfer in the centre-of-mass frame [20]:

$$\sigma_s = -\frac{\mathbf{j}_q}{T} \cdot \frac{\nabla T}{T} - \sum_a \mathbf{j}_a \cdot \nabla\left(\frac{\mu_a}{T}\right), \tag{A.1}$$

where $\mathbf{j}_q$ are heat current density, $\mathbf{j}_a$ mass-diffusion current densities of the species a, and μ_a the specific chemical potentials, respectively. This equation has the form $\sigma_s = \sum_l \mathbf{j}_l \cdot \mathbf{X}_l$, which allows for the derivation of linear phenomenological transport equations for the currents $\mathbf{j}_l$ generated by forces $\mathbf{X}_l$ that weakly perturb a thermodynamic equilibrium state [20]:

$$\mathbf{j}_i = \sum_i L_{ik} \mathbf{X}_k, \tag{A.2}$$

where L_{ik} are Onsager coefficients, which are scalar quantities in an isotropic system. Several different choices for $\mathbf{j}_l$ and $\mathbf{X}_l$ are possible, and they lead to different phenomenological equations that, in principle, describe the same physics but are more or less convenient to handle in certain cases [20, 55].

A.1. Thermal conductivity in variant *A*

For a two-component system in centre-of-mass frame, where $\mathbf{j}_1 = -\mathbf{j}_2$, equation (A.1) immediately leads to the transport equations:

$$\frac{\mathbf{j}_q}{T} = -L_{qq}\frac{\nabla T}{T} - L_{q1}\nabla\left(\frac{\mu_1 - \mu_2}{T}\right), \tag{A.3}$$

$$\mathbf{j}_1 = -L_{q1}\frac{\nabla T}{T} - L_{11}\nabla\left(\frac{\mu_1 - \mu_2}{T}\right). \tag{A.4}$$

The thermal conductivity λ is usually measured in a stationary state, where $\mathbf{j}_1 = \mathbf{j}_2 = 0$, that is reached after applying a temperature gradient and after the development of a concentration gradient [20]. Fourier's law for heat conduction is then derived by eliminating the gradient term containing the chemical potentials:

$$\mathbf{j}_q = -\lambda_A \nabla T = -\left(L_{qq} - \frac{L_{1q}^2}{L_{11}}\right)\nabla T. \tag{A.5}$$

With the above choice of currents and forces, we can derive the following microscopic expression for the thermal conductivity using linear response theory [19–21]:

$$\lambda_A = \frac{V}{3k_\mathrm{B}T^2}\left[\int_0^\infty \mathrm{d}t\ \langle \mathbf{j}_q(t)\cdot\mathbf{j}_q(0)\rangle - \frac{\left(\int_0^\infty \mathrm{d}t\ \langle \mathbf{j}_1(t)\cdot\mathbf{j}_q(0)\rangle\right)^2}{\int_0^\infty \mathrm{d}t\ \langle \mathbf{j}_1(t)\cdot\mathbf{j}_1(0)\rangle}\right]. \tag{A.6}$$

This expression can be directly evaluated in MD simulations, but its structure requires the calculation of three correlation functions. Both terms in the large bracket are of equal importance and they are subtracted from each other, which is a rather unfavourable structure for error propagation. The microscopic mass current density of species 1 reads:

$$\mathbf{j}_1(t) = \frac{1}{V}\sum_i^{N_1} m_i\mathbf{v}_i(t), \tag{A.7}$$

where N_a is the particle number of species a and m_i is the mass of particle i. For a system with pairwise interacting particles, the heat current density is defined as:

$$\mathbf{j}_q(t) = \frac{1}{2V}\sum_{i=1}^{N}\left(m_i\mathbf{v}_i^2(t) + \sum_{\substack{j\\ i\neq j}}^{N} V_{ij}(r_{ij}(t))\right)\mathbf{v}_i(t) + \frac{1}{2V}\sum_{\substack{i,j\\ i\neq j}}^{N}(\mathbf{F}_{ij}(r_{ij}(t))\cdot\mathbf{v}_i(t))\mathbf{r}_{ij}(t). \tag{A.8}$$

A.2. Thermal conductivity in variant *B*

Instead of directly proceeding with equation (A.1), it is useful to group the all terms with explicit temperature gradients together and rewrite the equation as follows [20]:

$$\sigma_s = -\frac{\mathbf{j}_q'}{T}\cdot\frac{\nabla T}{T} - \sum_a \mathbf{j}_a\cdot\frac{\nabla(\mu_a)_{T,p}}{T}, \tag{A.9}$$

where the modified heat current density reads:

$$\mathbf{j}_q' = \mathbf{j}_q - \sum_a \frac{h_a}{m_a}\mathbf{j}_a. \tag{A.10}$$

Here the partial enthalpies

$$h_a = \left(\frac{\partial H}{\partial N_a}\right)_{T,p,\{N_{b\neq a}\}} \tag{A.11}$$

appear as additional quantities. The phenomenological equations of our two-component system then read (using again $\mathbf{j}_1 = -\mathbf{j}_2$):

$$\frac{\mathbf{j}_q'}{T} = -L_{qq}'\frac{\nabla T}{T} - L_{1q}'\frac{\nabla(\mu_1-\mu_2)_{T,p}}{T}, \tag{A.12}$$

$$\mathbf{j}_1 = -L_{1q}'\frac{\nabla T}{T} - L_{11}'\frac{\nabla(\mu_1-\mu_2)_{T,p}}{T}. \tag{A.13}$$

In these equations, the driving forces are now temperature gradient and gradients in chemical potential at constant T and p. The thermal conductivity λ in the stationary state acquires the same form as in variant A and reads:

$$\mathbf{j}_q = -\lambda_B\nabla T = -\left(L_{qq}' - \frac{(L_{1q}')^2}{L_{11}'}\right)\nabla T. \tag{A.14}$$

A major advantage in variant B is that L_{qq}' now contains the main contribution to λ. The small reduction from the second term is due to thermodiffusion and amounts only to very few percent at maximum [20], and we can therefore neglect it. The microscopic equation for $\lambda_B \approx L_{qq}'$ from linear response theory then requires only the calculation of a single correlation function:

$$\lambda_B = \frac{V}{3k_\mathrm{B}T^2}\int_0^\infty \mathrm{d}t\ \langle \mathbf{j}_q'(t)\cdot\mathbf{j}_q'(0)\rangle, \tag{A.15}$$

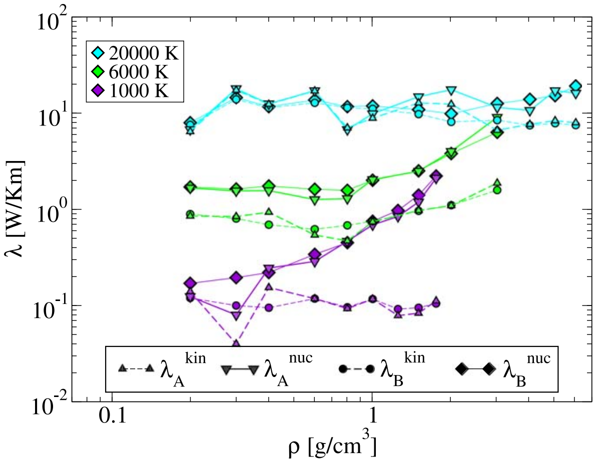

Figure A1. Thermal conductivity of the nuclei from the DFT-MD+GKFF method in variants A and B as indicated in the lower legend. Temperatures are consistently indicated via the colour code in the upper legend.

with the microscopic current density

$$\mathbf{j}_q'(t) = \mathbf{j}_q(t) - \frac{1}{V}\sum_a \left(\frac{\partial H}{\partial N_a}\right)_{T,p,\{N_{b\neq a}\}} \sum_i^{N_a} \mathbf{v}_i(t). \tag{A.16}$$

A difficulty in this variant is the determination of the partial enthalpies, whose direct calculation with MD simulations is relatively involved [22, 56], especially in simulations at constant volume. However, it is possible to approximate the thermodynamic derivative with the mean enthalpy per particle of the same species:

$$\begin{aligned}\left(\frac{\partial H}{\partial N_a}\right)_{T,p,\{N_{b\neq a}\}} &\approx \langle h_a\rangle = \langle h_i\rangle \\ &= \frac{5}{2}k_\mathrm{B}T + \frac{1}{2}\sum_{\substack{j\\ i\neq j}}^{N}\left\langle V_{ij}(r_{ij}) + \frac{1}{3}\mathbf{F}_{ij}(r_{ij})\cdot\mathbf{r}_{ij}\right\rangle.\end{aligned} \tag{A.17}$$

This approximation neglects nonideal mixing contributions to the partial enthalpies and has performed very well in thermal conductivity calculations for Lennard–Jones mixtures [23, 57].

A.3. Comparative validation of both variants against each other

In brief, we made two small and reasonable approximations in variant *B*, whereas variant *A* is a formally exact procedure. Moreover, note that systematic differences between both variants may come into effect only in a multi-component fluid system with inter-species diffusion, i.e. neither if water is fully molecular (where $\mathbf{j}_1 \parallel \mathbf{j}_2 = -\mathbf{j}_1$, which can only be fulfilled if both currents are zero) nor in a solid state (where $\mathbf{j}_1 = 0$ and $\mathbf{j}_2 = 0$).

Now we calculate both λ_A and λ_B for three representative isotherms and compare the results in figure A1. Distinguishment between kinetic (superscript: kin) and total (kinetic plus interaction, superscript: nuc) thermal conductivities is also made, just as described in the main text.

The chosen isotherms are 1000 K (fully molecular water up to to least 1.25 g cm^{-3}, see [58]), 6000 K (chemically reacting water at low densities, dense plasma at high densities), and 20 000 K (fully dissociated water at low densities, dense plasma at high densities). The most noticeable difference between λ_A and λ_B is the much larger scattering in the values of λ_A compared to that of λ_B. The reason is that equation (A.6) contains a difference of two equally important terms in the bracket, each of which contributes significantly to the statistical uncertainty. This effect seems to be especially strong when the interaction contribution to the heat current is small (or set to zero as in $\lambda_{A,B}^{\mathrm{kin}}$). There are no significant differences between the corresponding data sets of λ_A and λ_B.

In conclusion, the well-controllable approximations made in variant *B* do not introduce significant systematic errors into the resulting values for λ_B. In contrast, although the λ_A values are derived from formally exact equations, they are spoiled by much larger statistical uncertainties. Since the high computational cost of DFT-MD simulations limits the possibility of reducing the statistical error to arbitrary smallness, variant *B* is clearly the preferred path to follow in thermal conductivity calculations with the DFT-MD+GKFF method. This will hold even more strongly for systems that contain more than two nuclear species because λ_A would then be given by a more complex arrangement of correlation functions, whereas the expression (A.15) can remain the same, regardless of the number of species. All of the main results in this work are derived within variant B, i.e. $\lambda_{\mathrm{nuc}} = \lambda_B$.

Of course, it would be generally desirable to calculate the partial enthalpies (A.11) exactly, e.g. similar as in [22, 56]. This may be required for systems where nonideal mixing effects in the thermodynamic functions are not as small as those in warm dense water and other planetary ices [24].

ORCID iDs

Martin French https://orcid.org/0000-0001-8050-9816

References

[1] Guillot T 2005 *Annu. Rev. Earth Planet. Sci.* **33** 493–530

[2] Fortney J J and Nettelmann N 2010 *Space Sci. Rev.* **152** 423

[3] Schubert G and Soderlund K M 2011 *Phys. Earth Planet. Inter.* **187** 92–108

[4] Nettelmann N, Wang K, Fortney J J, Hamel S, Yellamilli S, Bethkenhagen M and Redmer R 2016 *Icarus* **275** 107–16

[5] Moll R, Garaud P, Mankovich C and Fortney J J 2017 *Astrophys. J.* **849** 24

[6] Leconte J and Chabrier G 2012 *Astron. Astrophys.* **540** A20

[7] Ross R G, Andersson P, Sundqvist B and Backström G 1984 *Rep. Prog. Phys.* **47** 1347

[8] Mills K C, Monaghan B J and Keene B J 1996 *Int. Mater. Rev.* **41** 209

[9] McKelvey A *et al* 2017 *Sci. Rep.* **7** 7015

[10] Konôpková Z, McWilliams R S, Gómez-Pérez N and Goncharov A F 2016 *Nature* **534** 9

[11] Abramson E H, Brown J M and Slutsky L J 2001 *J. Chem. Phys.* **115** 10461

[12] Gillan M J, Alfe D, Brodholt J, Vocadlo L and Price G D 2006 *Rep. Prog. Phys.* **69** 2365–441

[13] Knudson M D, Desjarlais M P, Lemke R W, Mattsson T R, French M, Nettelmann N and Redmer R 2012 *Phys. Rev. Lett.* **108** 091102

[14] Mermin N D 1965 *Phys. Rev.* **137** A1441–3

[15] Holst B, French M and Redmer R 2011 *Phys. Rev.* B **83** 235120

[16] French M and Redmer R 2017 *Phys. Plasmas* **24** 092306

[17] Marcolongo A, Umari P and Baroni S 2016 *Nat. Phys.* **12** 80

[18] Kang J and Wang L W 2017 *Phys. Rev.* B **96** 020302

[19] Hansen J P and McDonald I R 1976 *Theory of Simple Liquids* (London: Academic)

[20] de Groot S R and Mazur P 1984 *Non-Equilibrium Thermodynamics* (New York: Dover)

[21] Allen M P and Tildesley D J 1989 *Computer Simulation of Liquids* (Oxford: Oxford University Press)

[22] Sindzingre P, Ciccotti G, Massobrio C and Frenkel D 1989 *Chem. Phys.* **129** 213

[23] Vogelsang R, Hoheisel C, Sindzingre P, Ciccotti G and Frenkel D 1989 *J. Phys.: Condens. Matter* **1** 957

[24] Bethkenhagen M *et al* 2017 *Astrophys. J.* **848** 67

[25] Stillinger F H and Weber T A 1985 *Phys. Rev.* B **31** 5262–71

[26] Kresse G and Hafner J 1993 *Phys. Rev.* B **47** 558–61

[27] Kresse G and Hafner J 1994 *Phys. Rev.* B **49** 14251–69

[28] Kresse G and Furthmüller J 1996 *Phys. Rev.* B **54** 11169–86

[29] Perdew J P, Burke K and Ernzerhof M 1996 *Phys. Rev. Lett.* **77** 3865–8

[30] Mattsson T R and Desjarlais M P 2006 *Phys. Rev. Lett.* **97** 017801

[31] French M, Mattsson T R, Nettelmann N and Redmer R 2009 *Phys. Rev.* B **79** 054107

[32] French M, Mattsson T R and Redmer R 2010 *Phys. Rev.* B **82** 174108

[33] Schöttler M, Redmer R and French M 2013 *Contrib. Plasma Phys.* **53** 336

[34] Resta R 1992 *Ferroelectrics* **136** 51–5

[35] Baroni S, de Gironcoli S, Dal Corso A and Giannozzi P 2001 *Rev. Mod. Phys.* **73** 515–62

[36] French M, Hamel S and Redmer R 2011 *Phys. Rev. Lett.* **107** 185901

[37] Sun T and Wentzcovitch R M 2012 *Chem. Phys. Lett.* **554** 15

[38] Matsunaga N and Nagashima A 1983 *J. Phys. Chem. Ref. Data* **12** 933

[39] Chen B, Hsieh W P, Cahill D G, Trinkle D R and Li J 2011 *Phys. Rev.* B **83** 132301

[40] Hsieh W and Deschamps F 2015 *J. Geophys. Res.—Planets* **120** 1697–707

[41] French M and Redmer R 2015 *Phys. Rev.* B **91** 014308

[42] Huber M L, Perkins R A, Friend D G, Sengers J V, Assael M J, Metaxa I N, Miyagawa K, Hellmann R and Vogel E 2012 *J. Phys. Chem. Ref. Data* **41** 033102

[43] Hellmann R, Bich E, Vogel E, Dickinson A S and Vesovic V 2009 *J. Chem. Phys.* **131** 014303

[44] Woolf J R and Sibbitt W L 1954 *Ind. Eng. Chem.* **46** 1947

[45] Eigen M 1952 *Z. Elektrochem.* **56** 176

[46] Dietz F J, de Groot J J and Franck E U 1981 *Ber. Bunsenges. Phys. Chem.* **85** 1005

[47] Bresme F and Römer F 2013 *J. Mol. Liq.* **185** 1

[48] Boese A D 2015 *Chem. Phys. Chem.* **16** 978–85

[49] Butler J N and Brokaw R S 1957 *J. Chem. Phys.* **26** 1636

[50] Aubreton J, Elchinger M F and Vinson J M 2009 *Plasma Chem. Plasma Process* **29** 149–71

[51] Redmer R, Mattsson T R, Nettelmann N and French M 2011 *Icarus* **211** 798

[52] French M, Desjarlais M P and Redmer R 2016 *Phys. Rev.* E **93** 022140

[53] Fan Z, Pereira L F C, Wang H Q, Zheng J C, Donadio D and Harju A 2015 *Phys. Rev.* B **92** 094301

[54] Slater J C and Koster G F 1954 *Phys. Rev.* **94** 1498

[55] Erpenbeck J J 1989 *Phys. Rev.* A **39** 4718–31

[56] Sindzingre P, Ciccotti G, Massobrio C and Frenkel D 1987 *Chem. Phys. Lett.* **136** 35

[57] Vogelsang R and Hoheisel C 1987 *Phys. Rev.* A **35** 3487–91

[58] French M and Redmer R 2009 *J. Phys.: Condens. Matter* **21** 375101

The Astrophysical Journal, 881:81 (7pp), 2019 August 10 https://doi.org/10.3847/1538-4357/ab2d21

Viscosity and Prandtl Number of Warm Dense Water as in Ice Giant Planets

Martin French and Nadine Nettelmann
Institut für Physik, Universität Rostock, Albert-Einstein-Str. 23-24, D-18059 Rostock, Germany
Received 2019 May 3; revised 2019 June 17; accepted 2019 June 25; published 2019 August 14

Abstract

The thermophysical properties in water-rich planets are important for understanding their radius, luminosity, and magnetic field. Here we calculate the shear viscosity, isobaric heat capacity, and Prandtl number of warm dense fluid water using ab initio simulations. More specifically, the density (0.2–6 g cm^{-3})–temperature (1000–50,000 K) conditions considered here include states present in mini-Neptune to Neptune-sized planets. As a general result, we find that $\mathrm{Pr} \gtrsim 1$ in their deep interiors if they are adiabatic, whereas $\mathrm{Pr} \lesssim 1$ if they are super-adiabatic. Our results lend some support to the suggestion of turbulent convection at $\mathrm{Pr} \approx 1$ to explain the peculiar magnetic fields of Uranus and Neptune. Finally, we argue that double-diffusive convection in these Ice Giants would require fine-tuning of the compositional-to-superadiabaticity ratio R_{crit}^{-1} within a small factor of 2; instead we conclude that compositional gradients in Uranus and Neptune would be diffusive in nature and thus primordial heat could still be trapped inside.

Key words: dense matter – planets and satellites: interiors – plasmas

1. Introduction

Over 1200 exoplanets in the sub-Neptune to Neptune-like size range of 1.7–4.0 R_{Earth} have been detected.[1] Many more are expected to be revealed by current and upcoming space missions such as *TESS* and *PLATO*.

Planets in this size range are thought to harbor significant amounts of volatiles, like water, and rocks mixed into a gaseous atmosphere as required to explain observed mass–radius relations (Valencia et al. 2013; Zeng & Sasselov 2014; Thomas & Madhusudhan 2016) or emission and transmission spectra (Morley et al. 2017). In order to understand the thermal structure of such planets, here collectively labeled *ice giant planets*, and if they can sustain a magnetic field (Tian & Stanley 2013), the thermophysical properties of water play a major role, although further effects such as atmospheric composition (Kite & Ford 2018) and ohmic heating efficiency (Pu & Valencia 2017) can greatly influence the temperatures in the deep interior as well.

For *ice giant planets*, the viscosity and the Prandtl number of water are particularly important quantities because they enter a number of characteristic parameters like the Rayleigh number, the Ekman number, or the critical density ratio R_{crit}^{-1}. Those parameters determine the dynamical behavior of the fluid in the presence of buoyancy, rotation, or mean molecular weight gradient (see Stevenson & Salpeter 1977; Soderlund et al. 2013, and references therein). Interior dynamics, in turn, determine the heat flow and the dynamo operation in a rotating planet; thus, ultimately, the values of viscosity and Prandtl number can influence the observable luminosity and magnetic field of a planet.

The luminosity and the magnetic fields of Uranus and Neptune exhibit peculiarities that are not explained by a fully homogeneous interior of vigorous convection. Instead, the magnetic field of Uranus and Neptune has been suggested to be generated in a thin shell atop a stably stratified deep interior (Stanley & Bloxham 2004, 2006; Redmer et al. 2011), or to operate in an interior of three-dimensional turbulent rather than columnar convection (Soderlund et al. 2013). The style of convection seems to be driven by the value of the Prandtl number with a transition between columnar and turbulent convection near $\mathrm{Pr} = 1$ (Soderlund et al. 2013).

Moreover, the low luminosity of Uranus may be due to an inhomogeneous transition zone between the H/He-rich outer envelope and the ice-rich interior (Nettelmann et al. 2016) although atmospheric properties may play a role as well (Friedson & Gonzales 2017; Kurosaki & Ikoma 2017). A zone of mean molecular weight gradient may occur near $r \approx 0.8R_p$ as predicted for Uranus and Neptune both by adiabatic (Podolak et al. 1991; Fortney et al. 2013; Nettelmann et al. 2013) and not-necessarily adiabatic structure models (Helled et al. 2011; Podolak et al. 2019) or deeper inside as favored by early thermal evolution models (Hubbard et al. 1995). At present it is unclear whether such a zone would be accompanied by convection as a result of strong thermal forcing, or by suppression of convection in the form of double-diffusive convection or pure diffusion. The nature of the dynamic regime depends on the viscosity and Prandtl number.

Neither the viscosity nor the thermal conductivity of a molecular fluid at the relevant pressures of 10–500 GPa and temperatures of several thousand degrees kelvin can presently be determined with experiments. However, we are nowadays able to make theoretical predictions for these quantities with ab initio electronic structure calculations due to the steadily growing power of high-performance computing facilities.

In this paper we calculate the shear viscosity η, heat capacity c_p, and Prandtl number of warm dense fluid water as in the interior of Ice Giant planets using ab initio simulations. This paper extends and makes use of recent work on thermal transport properties of water for conditions in the interiors of Uranus and Neptune (French & Redmer 2017; French 2019).

In Section 2 we describe the ab initio simulation method, in Section 3 we present our results for viscosity, specific heat capacity, and Prandtl number. In Section 4 we discuss possible implications of our results for the occurrence of double-diffusive convection and turbulent convection in Uranus and Neptune. Section 5 concludes the paper.

---

[1] exoplanets.org (Han et al. 2014).

2. *Ab initio* Simulations

We performed ab initio molecular dynamics (MD) simulations for the ions (hydrogen and oxygen nuclei) using forces calculated with a finite-temperature density functional theory (FT-DFT) treatment of the electrons in our system (Hohenberg & Kohn 1964; Kohn & Sham 1965; Mermin 1965). This procedure is implemented in the Vienna ab initio simulation package (VASP) Kresse & Hafner (1993a, 1993b, 1994); Kresse and Furthmüller (1996) and it yields the pressure tensor $p_{ij}(\varrho, T)$, and internal energy $u(\varrho, T)$ in dependence of density ϱ and temperature T as equation of state (EOS) quantities.

The PBE (Perdew et al. 1996) functional was employed in our FT-DFT-MD simulations to approximate electronic exchange-correlation effects. We use the standard PAW pseudopotentials (Blöchl 1994; Kresse & Joubert 1999) provided with VASP (hydrogen PAW-sphere radius: 0.52 Å, oxygen PAW-sphere radius: 0.72 Å) with a plane-wave cutoff of 900 eV. These settings were extensively tested in earlier work (French et al. 2009, 2010) and yield well-converged EOS data and transport properties.

All of the simulation runs from this work were already used in recent calculations of the nuclear contribution to the thermal conductivity (French 2019). They were run for 50,000–250,000 time steps with typical time step lengths of 0.3–0.5 fs. Such long simulations are well-suited for the evaluation of time correlation functions of p_{ij} that enter the Green–Kubo expression for the shear viscosity. Particle numbers were varied between 8 and 54 molecules, depending on density and temperature. All simulations with densities of 1 g cm^{-3} and higher were run with 54 molecules. For densities above 3 g cm^{-3}, we used the Baldereschi $\boldsymbol{k}$ point (Baldereschi 1973), whereas the Γ point was sufficient for lower densities. The temperature was controlled with a Nosé–Hoover thermostat (Nosé 1984; Hoover 1985). We consider only the simulations in the fluid state here.

3. Results

3.1. Viscosity

We calculate the shear viscosity with the following Green–Kubo expression (Allen & Tildesley 1989; Kubo et al. 1991; Alfè and Gillan 1998):

$$\eta = \frac{V}{3k_{\rm B}T}\int_0^\infty dt \sum_{ij}\langle(p_{ij}(0) - \langle p_{ij}\rangle)(p_{ij}(t) - \langle p_{ij}\rangle)\rangle, \quad (1)$$

where V is the volume of the simulation box, $k_{\rm B}$ is the Boltzmann constant, and $ij = \{xy, yz, zx\}$ indicates the off-diagonal components of the pressure tensor. The calculated data are shown in Figure 1. The uncertainty is predominantly of statistical nature and amounts to about 10%–20%, albeit there are a few outliers. At low densities, the viscosity rises systematically with temperature, which is a behavior typical for gases because interparticle collisions become more frequent with temperature. Interaction effects between the particles lead to a strong increase with the density, which is more pronounced the lower the temperature is. This behavior is qualitatively similar to what is observed in diamond anvil cell experiments at lower temperatures (Abramson 2007).

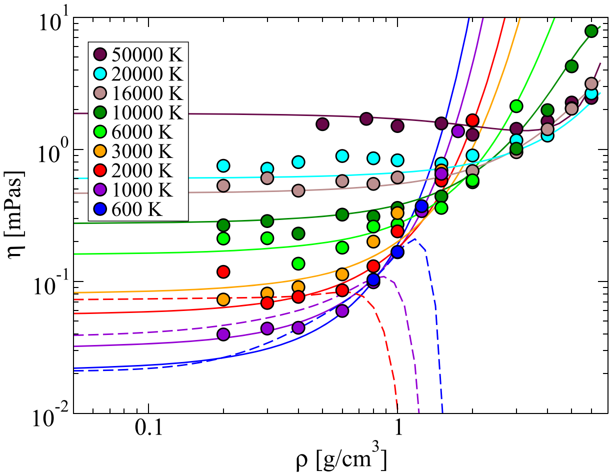

Figure 1. Calculated shear viscosity of fluid water. Numerical values from Equation (1) are shown as circles. Solid lines represent the fit from Equation (2). Temperatures are indicated via the color code. The dashed lines are results from Huber et al. (2009).

Table 1
Fit Coefficients for Equation (2)

i	j	C_{ij}
0	0	−12.77
0	1	−0.1032
0	2	0.06499
1	0	3.38
1	1	−0.5129
1	2	0.01799
2	−1	51.17
2	0	−8.923
2	1	0.3831
3	−3	−58.49
3	0	0.05828

Note. All units are chosen in such a way that entering temperatures in K and densities in g cm^{-3} leads to results in Pas for η.

The following fit function was found to give a good overall representation of the data:

$$\ln\eta = \sum_{i,j} C_{ij}\,\varrho^i y^j, \quad (2)$$

where $y = \ln(T/{\rm K})$. The coefficients C_{ij} are listed in Table 1.

Figure 1 also includes a comparison with the reference correlation given by Huber et al. (2009), which is derived from available experimental data. Their fit formula is valid up to temperatures between 1000 and 2000 K and pressures of 1 GPa, but does not extrapolate well to higher pressures (densities $\gg$1 g cm^{-3}). Still, our data points that lie in the validity region of the reference correlation agree with it within the reported uncertainties.

The general region of applicability of our fit, Equation (2), reaches from a density of 0.2–6 g cm^{-3} and from a temperature of 1000 to 50,000 K. Application at somewhat lower temperatures is possible but the region near the critical point should be avoided, see Huber et al. (2009) for explanations. Also excluded are conditions where water forms ices or superionic phases; in those phases, the viscosity will be orders of magnitude larger than in the fluid phases.

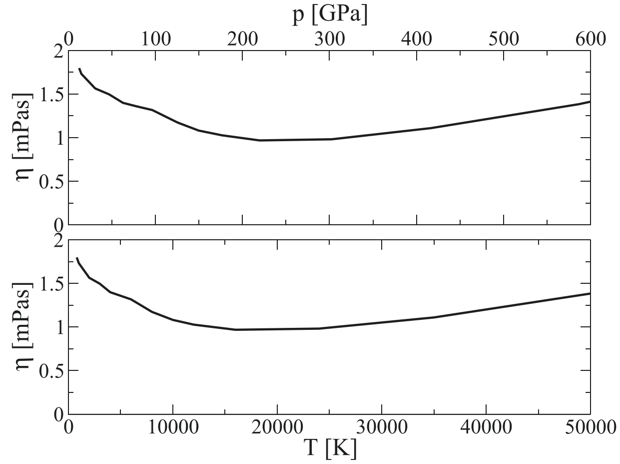

Figure 2. Shear viscosity of water along the principal Hugoniot curve. Thermodynamic conditions are taken from French & Redmer (2009).

Of considerable interest is the viscosity along the principal Hugoniot curve. Such states can be generated in shock wave experiments. The direct measurement of viscosities at shocked states is highly challenging (Miller & Ahrens 1991), and different techniques can yield results that differ by six orders of magnitude (from mPas to kPas) at GPa pressures, see the compilation by Abramson (2015).

In Figure 2, we display our viscosities in dependence of pressure and temperature at principal Hugoniot states taken from French & Redmer (2009). We predict values between 1 and 2 mPas and only slight changes of the viscosity until at least 600 GPa. These values support viscosities estimated indirectly through measurements of ionic mobilities, which are also in favorable agreement with those from diamond anvil cell experiments obtained at pressures of a few GPa (Abramson 2015).

3.2. Heat Capacity

We calculate the isobaric heat capacity c_p, formally defined and more conveniently rewritten as:

$$c_p = \left(\frac{\partial(u + p/\varrho)}{\partial T}\right)_p = \left(\frac{\partial u}{\partial T}\right)_\varrho + \frac{T}{\varrho^2}\left(\frac{\partial p}{\partial T}\right)_\varrho^2 \left(\frac{\partial \varrho}{\partial p}\right)_T \qquad (3)$$

using data tables for $p(\varrho, T)$ and $u(\varrho, T)$ from FT-DFT-MD simulations.

To the internal energy we add a correction term that accounts for quantum effects of nuclear motion. This is important for temperatures of a few 1000 K, where water is mostly molecular or partially dissociated. A purely classical description of the molecular vibration would lead to a significant overestimation of the heat capacity. The procedure (Berens et al. 1983) requires the calculation of the nuclear power spectrum and has been used successfully in previous calculations of the EOS for the ices VII and X (French & Redmer 2015) and for superionic phases (French et al. 2016), and the respective formulas are given in those references.

Table 2
Fit Coefficients for Equation (4)

i	0	0	0	1	1	1.2
j	0	1	2	0	1	2
C_{ij}	41.9	−10.3	0.6813	8.715	−1.393	0.0324

Note. All units are chosen so that entering temperatures in K and densities in g cm^{-3} yields c_p in J gK^{-1}.

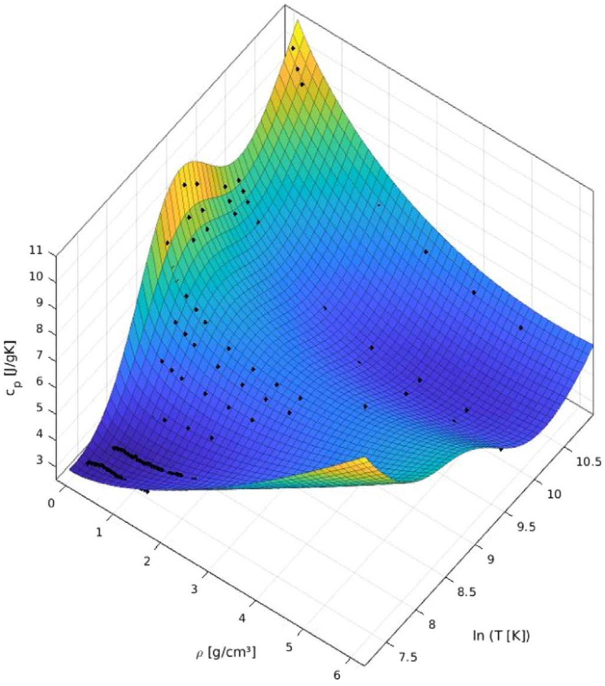

Figure 3. Heat capacity c_p from Equation (4) with some of the underlying data shown as black dots.

Furthermore, to avoid errors in the numerical computation of the partial differentiations in Equation (3) that would arise from a direct interpolation of the EOS data tables for $u(\varrho, T)$ and $p(\varrho, T)$ due to their statistical noise, we use the ansatz by French et al. (2016) to parameterize an analytical free energy function $f(\varrho, T)$ from which the material parameters can be calculated analytically. Unfortunately, we were not able to capture the complete characteristic behavior that occurs due to both dissociation and ionization well enough in a global function $f(\varrho, T)$. Therefore, we split each of the EOS tables for u and p into two smaller tables, one for low T and low ϱ and the other vice versa, also including sufficient mutual overlap. Each of these tables were then used to parameterize a function $f(\varrho, T)$ that could accurately preserve the thermodynamic features in their respective regions. A new data set for the heat capacity c_p was then created from these potential functions via Equation (3).

The generated data set $c_p(\varrho, T)$ was then combined with two additional isotherms (1500 and 2000 K) from the Wagner & Pruß (2002) EOS for molecular water and fitted to the following expression:

$$c_p = \sum_{i,j} c_{ij}\,\varrho^i y^j + \frac{a_0}{x^{1/4}} \exp\{-s_0(y - y_0)^2\}, \qquad (4)$$

where $y = \ln(T/\mathrm{K})$, $y_0 = 8.9$, $a_0 = 3.036$, $s_0 = 1.335$, and all other coefficients are given in Table 2.

The results of Equation (4) are shown in Figure 3. The heat capacity has a prominent ridge near 10,000 K that is caused by the thermal dissociation of molecules into atoms. This ridge is more pronounced at low densities. A similar increase that

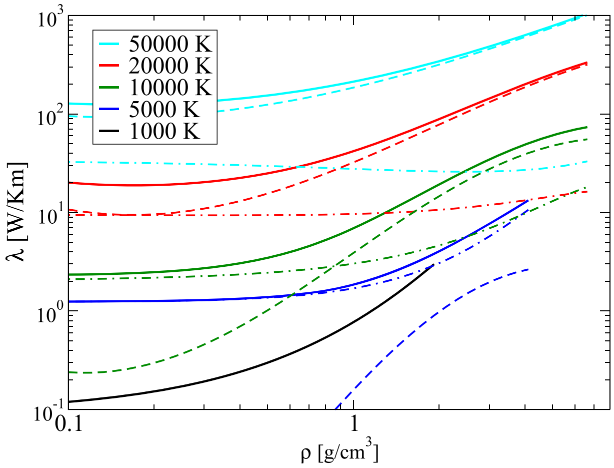

Figure 4. Electronic (dashed lines) from French & Redmer (2017) and nuclear (dotted–dashed lines) from French (2019) thermal conductivity and their sum (full lines).

results from thermal ionization occurs at higher temperatures. The declining of these ridges with the density is due to the increasing importance of pressure dissociation (and ionization) over thermal dissociation (and ionization) that changes the internal energy more strongly with the density than with temperature. Note that the increase in c_p seen at low temperature and high density in Figure 3 is an artifact. Transitions to superionic and ice phases occur there, so that no data for heat capacity of the fluid exist in that region.

In general, the accuracy achieved with Equation (4) is 10% or better and its region of applicability coincides with that of Equation (2) for the viscosity. The only exception is that c_p is affected more strongly by the presence of a critical point. For that reason, we recommend to directly use the values from Wagner & Pruß (2002) below 1500 K and below 1 g cm^{-3}. Their EOS was designed to accurately describe the thermodynamics of water in the vicinity of its critical point.

3.3. Thermal Conductivity

The thermal conductivity has been calculated previously with DFT-MD simulations, where the contributions from electrons, λ_e (French & Redmer 2017), and nuclei, $\lambda_{\rm nuc}$ (French 2019), were treated individually, and each of them were parametrized with analytical formulas. We can rely on those expressions here and need only to add both λ_e and $\lambda_{\rm nuc}$ together to obtain the total thermal conductivity λ.

Figure 4 displays the thermal conductivity and its individual contributions. The electronic thermal conductivity is hardly important below 5000 K. However, pressure ionization causes it to surmount the nuclear contribution at high density once the temperature gets high enough.

Note that the radiative contribution $\lambda_{\rm rad}$ to the thermal conductivity is negligible. It can be derived from the Rosseland mean opacity (Kippenhahn & Weigert 1991), which was estimated with ab initio calculations along the principal Hugoniot curve of water in earlier work (French & Redmer 2011). Below 10,000 K, $\lambda_{\rm rad}$ does not exceed values of 10^{-3} W Km^{-1}, and, thus, remains at least two orders of magnitude smaller than the minimum contributions from nuclei and electrons in Figure 4. In particular, λ_e increases much more strongly with T than $\lambda_{\rm rad}$ does until at least 50,000 K, where $\lambda_e \gg \lambda_{\rm rad} = 2 \times 10^{-2}$ W Km^{-1} (at a density of 3.24 g cm^{-3}).

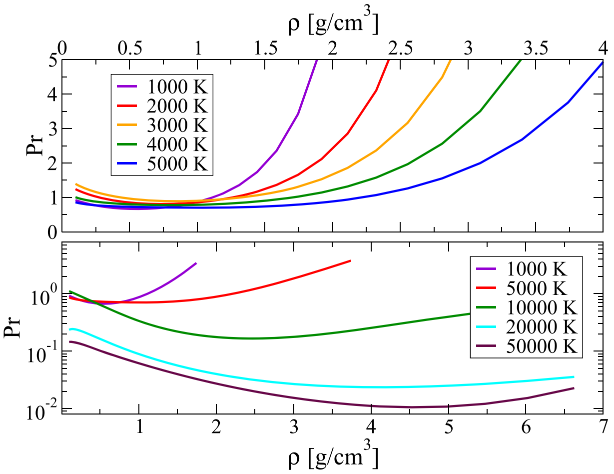

Figure 5. Calculated Prandtl number of warm dense fluid water using viscosity and heat capacity from this work and thermal conductivities from French & Redmer (2017) and French (2019).

3.4. Prandtl Number

The Prandtl number is calculated from the expressions for the thermal conductivity λ (French & Redmer 2017; French 2019), shear viscosity η, and heat capacity c_p as

$$\mathrm{Pr} = \frac{\eta c_p}{\lambda}. \tag{5}$$

The overall uncertainty of the calculated Pr is estimated to 30%–40%. Figure 5 displays several isotherms of the Prandtl number. For temperatures of a few 1000 K, the Prandtl number is close to 1 at low density and increases strongly at densities above 1 g cm^{-3}. This increase is mainly caused by a rising viscosity, also visible in Figure 1.

At higher temperatures, the Prandtl number takes values significantly below 1. The reason for this is the strongly rising thermal conductivity as water becomes ionized and electronically conducting, see Figure 4. Since ionization is also driven by pressure, it also affects the density behavior of Pr.

4. Implications for Ice Giant Planets

In this section we discuss our results for the viscosity and Prandtl number with respect to the magnetic field and potential presence of a semiconvective region in Uranus and Neptune.

4.1. Magnetic Field and Pr

In Figure 6 we plot our calculated Pr values for pressure–temperature conditions along the same three representative Uranus models as in Bethkenhagen et al. (2017). If the transition between the outer H/He envelope and the icy deep interior remains adiabatic and thus the deep interior is cool (a few 1000 K, black and red curves in Figure 6), our Pr values are of the order of 1 and thus may be supportive toward the suggestion of three-dimensional turbulent convection; on the other hand, the deep interior heat flow of these models is around the observed one (Nettelmann et al. 2016) and thus the models do not support the second requirement found by

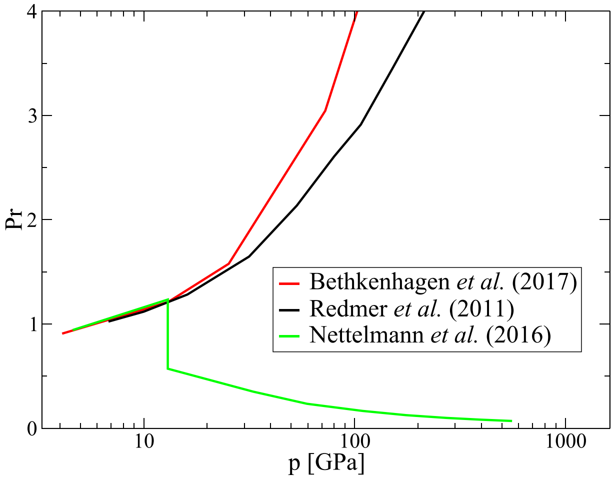

Figure 6. Prandtl number of warm dense fluid water at conditions in the interior of Uranus (Redmer et al. 2011; Nettelmann et al. 2016; Bethkenhagen et al. 2017).

Soderlund et al. (2013) of a much stronger than observed heat flow in the deep interior in order to drive convection in the presence of high $\mathrm{Pr} \gtrsim 1$. Nevertheless, the icy Uranus model in Figure 6 (red curve) represents the coolest possible adiabatic Uranus model. Therefore, the Pr values along that model may place an upper bound to the values in the real planets unless they are subadiabatic and entirely free of super-adiabatic zones.

If otherwise the transition between the outer H/He envelope and the icy deep interior becomes highly super-adiabatic (green curve in Figure 6) and thus the deep internal temperatures stay high (up to 10,000 K), the Prandtl number falls to values of 0.1. Since Pr decreases with temperature, we can also estimate a minimum possible Pr value. We find $\mathrm{Pr} \approx 0.03$ for a core temperature of ≈20,000 K, which may have occurred right after formation if the gravitational energy from contraction was converted into heat without significant loss of heat during the accretion shock. The latter assumption is supported by the convergence of hot-start and cold-start formation models for sub-Jupiter mass planets (Mordasini 2013). Prandtl number values of the order of 0.01–0.1 are Jupiter-like (Nettelmann et al. 2015; Wicht et al. 2018) and suggest that columnar convection could occur in warm ice giants. Moreover, the heat flow of such a model is slightly reduced compared to the adiabatic case. For such warm temperatures, ices (H_2O, CH_4, NH_3) will be in electrically conducting fluid phases. Whether or not in such a case the heat flow can be transported by thermal conduction and thus the deep interior would become stably stratified as suggested by Stanley & Bloxham (2004, 2006) will be investigated in a subsequent paper.

4.2. *Double-diffusive Convection and* $R_{\rm crit}^{-1}$

A double-diffusive region in a planet can occur, for instance, when a compositionally stably stratified region in which the mean atomic weight increases with depth is heated from below. Such a region has been suggested in order to explain the excess luminosity of Saturn (Leconte & Chabrier 2013) or the inflated radius of some hot Jupiters (Chabrier & Baraffe 2007); a thin double-diffusive region may occur in Jupiter in conjunction with H/He phase separation, loss of helium to deeper layers, and thus an increasing helium abundance with depth, leading to reduced heat loss from the deeper interior (Nettelmann et al. 2015; Mankovich et al. 2016). In Uranus and Neptune, structure models predict an increase of ice and rock mass fraction with depth (Podolak et al. 1991, 2019; Hubbard et al. 1995; Helled et al. 2011; Nettelmann et al. 2013). If these inhomogeneous regions were double-diffusive, they could significantly alter the cooling behavior of Uranus and Neptune and thus offer an option to explain simultaneously the low luminosity of Uranus and the brightness of Neptune.

Given a stabilizing mean molecular weight gradient and a growing temperature gradient, a semiconvective fluid will eventually transition into the overturning convective regime. This happens when the condition $1 < R_\rho^{-1}$ is violated, where $R_\rho^{-1} = (\alpha_\mu/\alpha_T)\, \nabla_\mu/(\nabla_T - \nabla_{\rm ad})$ is the ratio of mean molecular weight gradient $\nabla_\mu = d \ln \mu/d \ln p$ to the excess temperature gradient over the adiabatic temperature gradient, $\nabla_{\rm ad} = (d \ln T/d \ln p)_{\rm ad}$, α_T and α_μ being partial derivatives of density with temperature and mean molecular weight μ, respectively. The criterion $1 > R_\rho^{-1}$ for the onset of convective instability can equivalently be written $\nabla_T > \nabla_L$ with $\nabla_L \coloneqq \nabla_{\rm ad} + (\alpha_\mu/\alpha_T)\, \nabla_\mu$. For $\nabla_T = \nabla_{\rm rad}$ this is the Ledoux criterion of convective instability (Merryfield 1995).

If, alternatively, we let the actual temperature gradient decrease for a given mean molecular weight gradient, a semiconvective fluid eventually transitions into the purely diffusive dynamic regime. As a criterion for that transition, the violation of the condition $R_\rho^{-1} < R_{\rm crit}^{-1}$ has been derived from linear stability analysis for a system of salt in water (Walin 1964) and been applied to the discussion of the semiconvective regime in gas planets (Stevenson & Salpeter 1977; Rosenblum et al. 2011; Leconte & Chabrier 2012; Nettelmann et al. 2015). It reads:

$$R_{\rm crit}^{-1} = \frac{1 + \mathrm{Pr}}{\tau + \mathrm{Pr}}, \tag{6}$$

where $\tau = D/\kappa_T$ denotes the ratio of interspecies diffusivity D in a multicomponent system, say an aqueous salt solution or hydrogen dissolved in water, to the bulk thermal diffusivity $\kappa_T = \lambda/c_p\rho$. The regime where the conditions are favorable for the double-diffusive instability is thus given by $1 < R_\rho^{-1} < R_{\rm crit}^{-1}$. Note that for high opacity/low thermal conductivity, i.e., if $\nabla_{\rm rad} \gg \nabla_T$ the condition for the transition to the purely diffusive regime can differ significantly from the Ledoux stability criterion $\nabla_{\rm rad} < \nabla_{\rm ad} + \nabla_L$ as it was applied, e.g., by Vazan et al. (2015) to the evolution of Jovian planets.

For low viscosity, $\mathrm{Pr} \ll 1$, and $R_{\rm crit}^{-1} \simeq \tau^{-1}$ is usually much larger than 1: $\kappa/D \approx 10^8$ in massive stars (Merryfield 1995), $\approx 10^6$ in low-mass RGB stars (Dennissenkov 2010), and $\approx 10^2$ in Jupiter (French et al. 2012): a semiconvective regime can occur. On the contrary, for high viscosity we have $\mathrm{Pr} \gg 1$ and $R_{\rm crit}^{-1} \gtrsim 1$: the semiconvective regime $1 < R_\rho^{-1} < R_{\rm crit}^{-1}$ disappears.

To calculate the $R_{\rm crit}^{-1}$ values in Uranus and Neptune we need to have an estimate of τ. While the $\kappa_T = \lambda/c_p\rho$ is calculated here directly, for D only self-diffusion coefficients for protons and oxygen ions are available (French et al. 2010; Soubiran & Militzer 2015; Bethkenhagen et al. 2017), but those are of limited value here. Since typically, $\tau < 1$, and values $\tau \ll \mathrm{Pr}$ are negligible, we allow τ to vary within a reasonable range of $0.01 \leqslant \tau \leqslant$ to 0.5 in the following discussion.

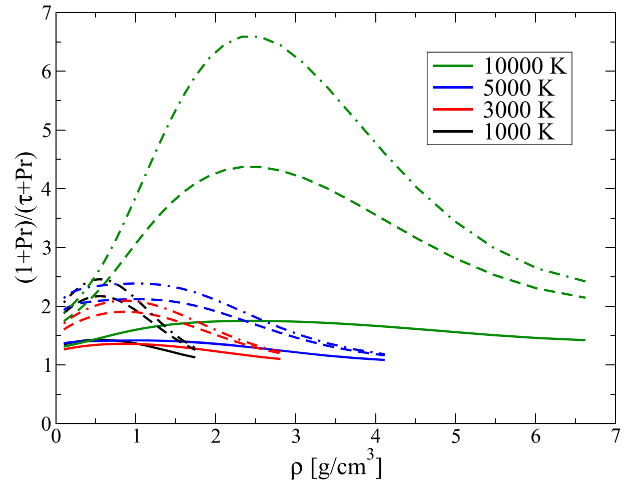

Figure 7. Critical density ratio (6) for different values $\tau = 0.5$ (full lines), $\tau = 0.1$ (dashed lines), and $\tau = 0.01$ (dotted–dashed lines).

Using the Prandtl numbers of Figure 5, we find $R_{\rm crit}^{-1}$ values of 1–2.5 for the deep interior of Uranus and Neptune if they were fully adiabatic (black, red, and blue curves in Figure 7). Thus a small parameter range for the occurrence of double-diffusive convections is available but perhaps unlikely to be realized. Due to Pr < 1 for $T \gtrsim 5000$ K, the parameter space for double-diffusive convection grows if there is a strong thermal boundary layer (TBL) that prevents the cooling of the deep interior (blue to green curves in Figure 7). In other words, hot interiors might promote cooling and mixing through double-diffusive convection to some extent while the assumption of cooled down interiors raises the question of how they lost the heat through the compositional gradient zone if double-diffusive convection, and even more so overturning convection, are suppressed. From these estimates we conclude that primordial heat is still trapped in the deep interior of Uranus and Neptune.

Finally, we compare our $R_{\rm crit}^{-1}$ values with the R_ρ^{-1} values for the warm Uranus model of Nettelmann et al. (2016; green line in Figure 6), which has a strong TBL. Using the parameter values for α_μ, α_T, ∇_μ from that work and choosing superadiabaticity values ($\Delta T - \Delta T_{\rm ad}$) of 100, 1000, 2500, and 4000 K over the pressure range Δp over which ∇_μ stretches, we find $R_\rho^{-1} = 140, 20, 12, 10 \gg R_{\rm crit}^{-1}$ on the inner, icy side of the compositional gradient zone and 4–10 times larger R_ρ^{-1} values on the outer H/He-rich side. Therefore, we conclude that the compositional gradient zone of three-layer ice Uranus and Neptune models, however stretched it may be, remains in the purely diffusive regime.

5. Conclusions

We have calculated the shear viscosity η, isobaric heat capacity c_p, and Prandtl number Pr $= \eta c_p/\lambda$ of dense fluid water on a grid of densities ranging from 0.2 to 6 g cm^{-3} and temperatures from 1000 to 50,000 K using ab initio simulations and thermal conductivity values λ from French & Redmer (2017) and French (2019). The combined data is intended for application in models of water-rich planets in the mini-Neptune to Neptune size range, which we collectively label *Ice Giant planets*.

We find Pr $\simeq 1$ for a wide range of ρ–T conditions including the cool outer envelopes of Uranus and Neptune; at densities $\gtrsim$2.5 g cm^{-3} as in the deep interior of Uranus and Neptune Pr rises with density at moderate temperatures to values of 1–10 because η increases with ρ in dense water due to correlation effects; Pr decreases to values of 0.01–1 at high temperatures of 10–50,000 K because then λ strongly increases due to ionization.

Our results lend some support to the suggestion by Soderlund et al. (2013) of turbulent convection at Pr ≈ 1 to explain the magnetic fields of Uranus and Neptune. However, since cool, adiabatic models do not explain the luminosity of Uranus, we suggest the presence of a thermal boundary layer on-top the dynamo region of moderate superadiabaticity in order to keep both Pr sufficiently high and the heat flow sufficiently low. Whether such models allow for enough thermal driving to sustain turbulent convection in the deep interior remains to be investigated.

Based on our Prandtl number values, we conclude that double-diffusive convection in Uranus and Neptune would require a compositional-to-superadiabaticity ratio R_ρ^{-1} within a small factor of 2 because we obtain $R_{\rm crit}^{-1} \lesssim 2.5$ and $1 < R_\rho^{-1} < R_{\rm crit}^{-1}$ is the regime favorable to double-diffusive convection; comparing our R_ρ^{-1} values furthermore to possible compositional and temperature gradients in Uranus and Neptune we find $R_\rho^{-1} \gg R_{\rm crit}^{-1}$ and thus argue that heat is transported by diffusion across compositional gradient zones. Therefore, primordial heat could still be trapped inside.

We thank M. Bethkenhagen, R. Redmer, and L. Scheibe for valuable discussions. N.N. acknowledges the hospitality of the ISSI in Bern, Switzerland. This work was supported by the Deutsche Forschungsgemeinschaft (DFG) within the Research Unit FOR 2440 (Matter under Planetary Interior Conditions—High-Pressure, Planetary, and Plasma Physics). The ab initio simulations were run at the North-German Supercomputing Alliance (HLRN) facilities and at the IT- and Media Center of the University of Rostock.

ORCID iDs

Martin French https://orcid.org/0000-0001-8050-9816
Nadine Nettelmann https://orcid.org/0000-0002-1608-7185

References

Abramson, E. H. 2007, PhRvE, 76, 051203
Abramson, E. H. 2015, ShWav, 25, 103
Alfè, D., & Gillan, M. J. 1998, PhRvL, 81, 5161
Allen, M. P., & Tildesley, D. J. 1989, Computer Simulation of Liquids (Oxford: Oxford Univ. Press)
Baldereschi, A. 1973, PhRvB, 7, 5212
Berens, P. H., Mackay, D. H. J., White, G. M., & Wilson, K. R. 1983, JChPh, 79, 2375
Bethkenhagen, M., Meyer, E. R., Hamel, S., et al. 2017, ApJ, 848, 67
Blöchl, P. E. 1994, PhRvB, 50, 17953
Chabrier, G., & Baraffe, I. 2007, ApJL, 661, L81
Dennissenkov, P. 2010, ApJ, 723, 563
Fortney, J., Mordasini, C., Nettelmann, N., et al. 2013, ApJ, 775, 80
French, M. 2019, NJPh, 21, 023007
French, M., Becker, A., Lorenzen, W., et al. 2012, ApJS, 202, 5
French, M., Desjarlais, M. P., & Redmer, R. 2016, PhRvE, 93, 022140
French, M., Mattsson, T. R., Nettelmann, N., & Redmer, R. 2009, PhRvB, 79, 054107
French, M., Mattsson, T. R., & Redmer, R. 2010, PhRvB, 82, 174108
French, M., & Redmer, R. 2009, JPCM, 21, 375101

French, M., & Redmer, R. 2011, PhPl, 18, 043301
French, M., & Redmer, R. 2015, PhRvB, 91, 014308
French, M., & Redmer, R. 2017, PhPl, 24, 092306
Friedson, A., & Gonzales, E. 2017, Icar, 297, 160
Han, E., Wang, S., Wright, J., et al. 2014, PASP, 126, 827
Helled, R., Anderson, J., Podolak, M., & Schubert, G. 2011, ApJ, 726, A15
Hohenberg, P., & Kohn, W. 1964, PhRv, 136, B864
Hoover, W. G. 1985, PhRvA, 31, 1695
Hubbard, W. B., Podolak, M., & Stevenson, D. J. 1995, in Neptune and Triton, ed. D. P. Cruishank (Tucson, AZ: Univ. Arizona Press), 109
Huber, M. L., Perkins, R. A., Laesecke, A., et al. 2009, JPCRD, 38, 101
Kippenhahn, R., & Weigert, A. 1991, in Stellar Structure and Evolution, ed. M. Harwit et al. (Berlin: Springer)
Kite, E., & Ford, E. 2018, ApJ, 864, 75
Kohn, W., & Sham, L. J. 1965, PhRv, 140, A1133
Kresse, G., & Furthmüller, J. 1996, PhRvB, 54, 11169
Kresse, G., & Hafner, J. 1993a, PhRvB, 47, 558
Kresse, G., & Hafner, J. 1993b, PhRvB, 48, 13115
Kresse, G., & Hafner, J. 1994, PhRvB, 49, 14251
Kresse, G., & Joubert, D. 1999, PhRvB, 59, 1758
Kubo, R., Toda, M., & Hashitsume, N. 1991, Nonequilibrium Statistical Mechanics (Berlin: Springer)
Kurosaki, K., & Ikoma, M. 2017, AJ, 153, 260
Leconte, J., & Chabrier, G. 2012, A&A, 540, A20
Leconte, J., & Chabrier, G. 2013, NatGe, 6, 347
Mankovich, C., Fortney, J., & Moore, K. 2016, ApJ, 832, 113
Mermin, N. D. 1965, PhRv, 137, A1441
Merryfield, W. 1995, ApJ, 444, 318
Miller, G. H., & Ahrens, T. J. 1991, RvMP, 63, 919
Mordasini, C. 2013, A&A, 558, A113
Morley, C., Knutson, H., Line, M., et al. 2017, ApJ, 153, 86
Nettelmann, N., Fortney, J. J., Moore, K., & Mankovich, C. 2015, MNRAS, 447, 3422
Nettelmann, N., Helled, R., Fortney, J., & Redmer, R. 2013, P&SS, 77, 143
Nettelmann, N., Wang, K., Fortney, J. J., et al. 2016, Icar, 275, 107
Nosé, S. 1984, JChPh, 81, 511
Perdew, J. P., Burke, K., & Ernzerhof, M. 1996, PhRvL, 77, 3865
Podolak, M., Helled, R., & Schubert, G. 2019, MNRAS, 487, 2653
Podolak, M., Hubbard, W., & Stevenson, D. J 1991, in Uranus, ed. J Bergstrahl, E. Miner, & M. Matthews (Tucson, AZ: Univ. Arizona Press), 29
Pu, B., & Valencia, D. 2017, ApJ, 846, 47
Redmer, R., Mattsson, T. R., Nettelmann, N., & French, M. 2011, Icar, 211, 798
Rosenblum, E., Garaud, P., Traxler, A., & Stellmach, S. 2011, ApJ, 731, 61
Soderlund, K. M., Heimpel, M. H., King, E. M., & Aurnou, J. M. 2013, Icar, 224, 97
Soubiran, F., & Militzer, B. 2015, HEDP, 17, 157
Stanley, S., & Bloxham, J. 2004, Natur, 428, 151
Stanley, S., & Bloxham, J. 2006, Icar, 184, 556
Stevenson, D. J., & Salpeter, E. E. 1977, ApJS, 35, 239
Thomas, S., & Madhusudhan, N. 2016, MNRAS, 458, 1330
Tian, B. Y., & Stanley, S. 2013, ApJ, 768, 156
Valencia, D., Guillot, T., Parmentier, V., & Freedman, R. 2013, ApJ, 775, 10
Vazan, A., Helled, R., Kovetz, A., & Podolak, M. 2015, ApJ, 803, 32
Wagner, W., & Pruß, A. 2002, JPCRD, 31, 387
Walin, G. 1964, TellA, 16, 389
Wicht, J., French, M., Stellmach, S., et al. 2018, Magnetic Fields in the Solar System, Vol. 448 (Cham: Springer), 7
Zeng, L., & Sasselov, D. 2014, ApJ, 784, 96

Eidesstattliche Erklärung

Hiermit erkläre ich, dass ich die vorliegende Arbeit selbständig und ohne fremde Hilfe verfasst und keine außer den angegebenen Hilfsmitteln und Quellen benutzt habe. Alle inhaltlich oder wörtlich aus anderen Werken entnommenen Stellen wurden als solche kenntlich gemacht.

Rostock, den 30.6.2021

Martin French

Danksagung

Die Erarbeitung der hier zusammengestellten Forschungsergebnisse wäre nicht gelungen ohne die Mitarbeit von zahlreichen Kolleginnen und Kollegen, mit denen ich in den vergangenen Jahren zusammenarbeiten durfte.

Allen voran gebührt mein größter Dank meinem langjährigen Mentor Ronald Redmer, welcher mir schon seit meiner Zeit als Promotionsstudent die vielen spannenden Fragestellungen des Forschungsgebietes „warme dichte Materie“ näher brachte. Der große Freiraum, den er mir bei allen Forschungsarbeiten ließ, sowie seine kontinuierliche, wohlwollende Förderung und Unterstützung während all den Jahren waren von unschätzbarem Wert.

Herzlich bedanken möchte ich mich auch bei allen aktuellen und ehemaligen Mitgliedern der AG Statistische Physik an der Universität Rostock, mit denen viele der gemeinsamen Veröffentlichungen der letzten Dekade entstanden sind, insbesondere bei Nadine Nettelmann, Bastian Holst, Winfried Lorenzen, Andreas Becker, Mandy Bethkenhagen, Daniel Cebulla, Manuel Schöttler, Bastian Witte und Jean-Alexander Korell. Gleichermaßen bedanke ich mich bei den auswärtigen Mitautoren Sebastien Hamel (LLNL, USA), Johannes Wicht (MPS Göttingen) und Gerd Steinle-Neumann (BGI Bayreuth) für die gelungene Zusammenarbeit.

Ebenso großer Dank gebührt auch den ehemaligen Kollegen von den Sandia National Laboratories (USA): Thomas Mattsson, Michael Desjarlais, Marcus Knudson, Luke Shulenburger und Kyle Cochrane, bei denen ich ein sehr interessantes und lehrreiches Jahr verbringen konnte.

Bei der Deutschen Forschungsgemeinschaft bedanke ich mich für die Förderung der Drittmittelprojekte (DFG-SPP 1488 und DFG-FOR 2440), im Rahmen derer die meisten der hier zusammengestellten Arbeiten entstanden sind.

Sehr wichtig zu erwähnen sind an dieser Stelle auch die Hochleistungsrechenzentren, an denen der Großteil der numerischen Rechnungen durchgeführt wurde, hier vor allem der HLRN, das XSEDE Programm (USA) sowie das ITMZ der Universität Rostock.

Letztlich möchte ich mich noch einmal ausdrücklich bei Wolf-Dietrich Kraeft, Ronald Redmer, Gerd Steinle-Neumann, Nadine Nettelmann und Mandy Bethkenhagen ganz herzlich dafür bedanken, dass sie die vorliegende Arbeit im Vorfeld gelesen und mir so viele wertvolle Hinweise dazu gegeben haben.